La détection des signaux radiofréquence et la génération des nombres aléatoires avec les jonctions tunnel magnétique perpendiculaire

Ahmed Sidi El Valli

▶ **To cite this version:**

Ahmed Sidi El Valli. La détection des signaux radiofréquence et la génération des nombres aléatoires avec les jonctions tunnel magnétique perpendiculaire. Physique [physics]. Université Grenoble Alpes [2020-..], 2022. Français. NNT : 2022GRALY056 . tel-03986221

HAL Id: tel-03986221

https://theses.hal.science/tel-03986221

Submitted on 13 Feb 2023

HAL is a multi-disciplinary open access archive for the deposit and dissemination of scientific research documents, whether they are published or not. The documents may come from teaching and research institutions in France or abroad, or from public or private research centers.

L'archive ouverte pluridisciplinaire **HAL**, est destinée au dépôt et à la diffusion de documents scientifiques de niveau recherche, publiés ou non, émanant des établissements d'enseignement et de recherche français ou étrangers, des laboratoires publics ou privés.

THÈSE

Pour obtenir le grade de

DOCTEUR DE L'UNIVERSITÉ GRENOBLE ALPES

École doctorale : PHYS - Physique
Spécialité : Nanophysique
Unité de recherche : Spintronique et Technologie des Composants

La détection des signaux radiofréquence et la génération des nombres aléatoires avec les jonctions tunnel magnétique perpendiculaire

Radiofrequency signal detection and random number generation with perpendicular magnetic tunnel junctions

Présentée par :

Ahmed SIDI EL VALLI

Direction de thèse :

Ursula EBELS Université Grenoble Alpes	Directrice de thèse
Liliana BUDA-PREJBEANU Professeur des Université, Université Grenoble Alpes	Co-directrice de thèse

Rapporteurs :

DAFINE RAVELOSONA
Directeur de recherche, CNRS DELEGATION ILE-DE-FRANCE SUD
GIOVANNI FINOCCHIO
Professeur associé, Università degli Studi di Messina

Thèse soutenue publiquement le **6 octobre 2022**, devant le jury composé de :

VINCENT CROS Directeur de recherche, CNRS DELEGATION ILE-DE-FRANCE SUD	Examinateur
DAFINE RAVELOSONA Directeur de recherche, CNRS DELEGATION ILE-DE-FRANCE SUD	Rapporteur
GIOVANNI FINOCCHIO Professeur associé, Università degli Studi di Messina	Rapporteur
FLORENCE PODEVIN Professeur des Universités, GRENOBLE INP	Présidente
SEBASTIEN PETIT-WATELOT Maître de conférences, UNIVERSITE DE LORRAINE	Examinateur
RICARDO FERREIRA Ingénieur de recherche, International Nanotechnology Laboratory	Examinateur

Invités :

PHILIPPE TALATCHIAN
Ingénieur Docteur, CEA CENTRE DE GRENOBLE

“It is a mysterious beast, and yet its practical effect prevails over the whole of science”

-The story of spin, Shinichiro Tomonaga.

ACKNOWLEDGMENT

This is it, the last drops of ink, the last whispers in this work. Written in one page, yet it is the heaviest and the least complete of all. For, all the combinations of words won't suffice to express my gratitude to all the people who were involved in this work.

First of all, I would like to thank sincerely my supervisor Ursula Ebels, for allowing me to perform my PhD thesis in her group and for her trust in me. I am deeply grateful for all her guidance, and instructive advice during the work. She was always available whenever I sought her advice and help. She helped me greatly in improving my writing and presentation skills. Her creativity, perfectionism, and deep knowledge make her an utmost model for me to follow in my scientific career.

The guidance of my co-supervisor, Liliana Prejbeanu-Buda, is greatly appreciated. I would like to express my appreciation for all of her help in particular for the simulation part achieved in this work. I thank her for the valuable discussions, support, and hospitality.

I would like to take the opportunity here as well, to thank sincerely Philippe Talatchian, Vadym Iurchuk, and Artem Litvinenko for all the great discussions we had (serious ones most of the time but also the stand-up comedies at lunch). I thank them greatly also for the training that they gave me on the different RF setups used throughout this work.

I gratefully acknowledge the Nanoscience foundation, ERC magical, and ANR Spinnet for funding my Ph.D. work.

Great gratitude for RF spintronic group and my office mates. Pankaj, Sylvain, Mateo, Ariam, Vladimir, Kyongmo, and Arijit thanks for being such nice team players and office mates. Great gratitude as well for the internships students : Geoffrey, Emilie, and Sultane.

I would like also to thank Ricardo, Laurent, and the Great project members who have fabricated such wonderful devices without which this work will stop literally at chapter 3. I am very grateful to Isabelle who trained me to use the PPMS and VSM setups and to Imadeddine, and the RF team in TIMA-lab for the guidance in the de-embedding and demodulation parts. Thanks for the instructive discussions and advice during the work.

Kyongmo, Ryuhei, and Eric thanks for the fruitful discussions and the jokes in the RF lab. I would like to thank as well Rui Ma for performing together the measurements with MTJ-CMOS devices.

Sincere thanks to my committee of suivie de thése, Olivier Klein, and Lucian Prejbeanu your advice and evaluation were fruitful. Great thanks to my thesis defense jury as well, for taking the time to evaluate my work and to come for the defense in person : Florence Podevin, Vincent Cros, Dafiné Ravelosona, Giovanni Finnocchio, Sebastien Petit-Watelot, and Ricardo Ferreira.

Thanks to all Ph.D. students and post-docs in Spintec for sharing their experiences and for the joy in the lab. I thank Celine and Adriana for their help with administration issues. Finally, I would like to thank all Spintec staff for their help and support during these years.

Ultimately, I would like to express my deepest thanks to my family, my parents, and my sisters, who have encouraged and supported me with their unconditional love. Thanks very much for standing behind me with your endless love and support.
Thank you all!

Ahmed SIDI EL VALLI
12 Oct 2022, Grenoble

To my father, my mother, and my sisters

ABSTRACT

Nanoscale magnetic tunnel junctions (MTJ) are promising candidates for nonvolatile memories, radiofrequency and unconventional computing applications. Transfer of spin angular momentum, from an injected spin polarized current, can drive three types of responses in these MTJs: (i) resonance via an rf current, (ii) auto-oscillations via a dc current, and (iii) switching between two states via dc current.

In this thesis, we investigate the first response scheme for rf signal detection for low power wireless sensor nodes as well as the third response scheme for random number generation. Both studies make use of the same MTJ that are characterized by a strong interfacial perpendicular magnetic anisotropy (iPMA) of the free layer and the pinned layer. Such perpendicular MTJ (pMTJ) are currently seen by industrial partners as the most promising MTJ configuration for magnetic memory applications, because they can be made very small (down to 20nm diameter). Of interest for our studies here is that their internal fields are easily tunable through the variation of the device shape, because the ratio of the anisotropy energy due to IPMA and the demagnetization energy depends sensitively on the magnetic layer thickness and diameter. For the devices used here, the free layer thickness was varied from t=1.4nm to 1.8nm. The first part of the thesis is a detailed analysis of the rf signal detection, to optimize the output DC voltage signal, as a function of magnetic layer thickness, diameter, as well as a function of the applied magnetic field orientation, and the absence or presence of dc currents (passive vs. active active). It is found that, first, the passive rf detection signal of these pMTJs increases the more the iPMA compensates the demagnetizing energy. This can be achieved through a reduction of the device diameter, which additionally enhances the STT efficiency and reduces the effect from a serial resistance that will be present for MTJs co-integrated with CMOS. Secondly, in the active detection it is found that the detection frequency band can be tuned over several GHz through a dc current. This tuning is attributed to Joule heating and opens strategies for wide band frequency detection. The second part of the thesis demonstrates that a spin polarized DC current can bring these pMTJs into a superparamagnetic state at zero external magnetic field. Such bitstreams will be of interest for random number generation schemes. Zero field operation will be facilitating the co-integration of these pMTJs with CMOS. The two parts of the thesis are accompanied by a thorough study of the static magneto-resistance loops as a function of applied field angle, DC current and temperature as well as by the modeling of the results based on LLG.

Keywords : Perpendicular magnetic tunnel junctions, Spin torque nanodiodes, Superparamagnetism, Magnetization dynamics, TRNG.

Table of Contents

LIST OF FIGURES

LIST OF TABLES

General Introduction

Less than 2 centuries ago, statements such as wireless communication at the speed of light would have made some great science fiction. Yet here we are, almost all equipped with telephones, computers, and exchanging messages all over the globe. Largely, thanks to the continuous advancements in solid state physics, and electrodynamics.

Moreover, the large accessibility to wireless communication systems, inspired the elaboration of more sophisticated data modulation techniques to avoid interference and to overcome the noise [1]. In addition to a marvelous enhancement of the data rates, that went from 64 kilobytes per second (kbps) in 2000 using the 2G technology, to 1 Gbps in 2020 using the 5G technology [2].

Furthermore, a major advantage of wireless communication systems is their on-board batteries. They allow them to be mobile, and importantly to be implemented in isolated areas far from stable power sources, such as forests, oceans, and outer space. These remote wireless systems are called the wireless sensor networks (WSN), and they are important for a wide range of applications in medicine, security and science [3]. Made of wirelessly coupled sensors and actuators, they can effectively detect a default in their surroundings and autonomously fix it or report on it. However, their autonomy is limited by the capacity of their batteries. Especially when wireless sensor networks (WSN) are in isolated areas battery replacement becomes a difficult task. Thus, one of the main targets in optimizing these networks is to reduce their energy consumption in order to boost the battery autonomy. The latter can be done in many different ways, either through the software by developing faster algorithms [4], or through the hardware by implementing energy efficient components [5]. In this work the focus is on the latter type of solutions. Especially, the components used in communication, because the transmission and the reception of information makes for ~ 84 % of the energy consumption in WSN while the processing and the sensing combined consume only ~ 16 % of the total energy [6]. Moreover, since the transmission of information is intermittent and short in time, a large portion of the energy consumed in the communication modules is due to the reception path. For, along with the energy lost in the demodulation process, the continuous listening of the receiver ,also called idle mode, wastes energy in-between communication sessions.

To overcome this issue one of the efficient solutions, is to implement in the wireless sensor network a wake-up receiver, with the mission to switch off the reception path when the system is not communicating and to switch it on only when required [7]. This will be the more efficient, if the wake-up receiver is made of passive components, and can listen continuously for the wake-up signal without any energy consumption. Therefore, a good wake-up receiver should be passive, and simultaneously sensitive to incident rf signals with ultra-low power, in order to optimize the energy used in the transmission path as well.

This work is a contribution to the quest for a passive and highly sensitive microwave diode that can fulfill the role of an ultra-low power wake-up receiver. It focuses specifically on spintronic devices called: the spin-torque nano-diodes. They convert microwave voltages to dc voltages using the spin transfer torque and the tunneling magnetoresistance effects.

They are expected to be a good candidate for ultra-low power applications such as wake-up receivers. Their sensitivity to low microwave power was demonstrated to be higher than that of typical Schottky diodes [8]. Moreover, they are CMOS compatible, frequency selective, and they operate at microwave frequencies that go from hundreds of MHz to tens of GHz.

In the endeavor to explore and further optimize the spin-torque nano-diodes, in this work the focus is on the spin-torque nano-diodes based on perpendicular magnetic tunnel junctions (pMTJs). The advantage of pMTJs for this task is their strong perpendicular magnetic anisotropy. It allows the optimization of the internal properties of the spin-torque nano-diode via the thickness and the device diameter, which can be as small as 20 nm.

The pMTJs studied in this work were developed within the European Horizon project GREAT that took place between 2016 to 2019. Its main goal was to develop a single stack allowing to perform memory, analog logic and rf functions on the same wafer. The GREAT project approach was to focus on a standard perpendicular magnetic tunnel junction structure, optimized for the memory function, and then tune their internal properties to achieve the performances needed for rf and sensor applications.

To study the spin-torque nano-diodes based pMTJs here, first a thorough static characterization is conducted to understand the internal magnetic states of the ferromagnetic layers, followed by a microwave based characterization to test the diode effect and to understand the magnetization dynamics.

Furthermore, another phenomenon that was discovered during the characterization of the devices is reported in the last chapter. It consists of the first demonstration of perpendicular superparamagnetic tunnel junctions, tunable by current, and fully operating at zero external bias magnetic field. They are of interest for unconventional computing, and applications relying on truly random number generators [9].

The manuscript is organized as follows :

Chapter 1 provides a short introduction to the fundamental phenomena involved in this work and reviews the advancement made on spin-torque nano-diodes. It starts by presenting the main spintronic concepts such as the spin polarization, the tunneling magnetoresistance, the spin transfer torque and the magnetization dynamics. Next, it introduces the spin torque diode effect and reviews their state of art.

Chapter 2 presents the composition of the pMTJs stack used in the study, and follows with a presentation of all the different experimental techniques used throughout this work. The presentation of the experimental techniques follows the order of the chapters. It start by presenting the setups used for the static characterization, followed by those for rf measurements and finally the time dependent analysis setup.

Chapter 3 focuses on the theoretical concepts and presents the derivations of different equations and formalisms used throughout this work to explain the experimental results. It starts by treating the static equilibrium of the magnetization through the total magnetic energy density. This is followed by the derivation of an analytic formula for the rf-to-dc conversion voltage for the pMTJs where the polarizing layer is oriented out-of-plane, via the linearization of the LLG equation. This derivation is then extended to include the effects of an additional dc current (for active detection) and the coupling to another magnetic layer. In the last part of chapter 3, a presentation of the analytic derivations of the Neel-Brown was included to account for the superparamagnetic state.

Chapter 4 is dedicated to the static characterization of the magnetic tunnel junctions with strong perpendicular magnetic anisotropy. This characterization includes the size dependence, as well as the consequences of introducing a dc current into the junctions. For this, the equilibrium states of the magnetizations of both the free and the polarizing layers are studied as a function of the layer diameter and thickness, external magnetic field, temperature and Joule heating, spin transfer torque and VCMA.

Chapter 5 is dedicated to the characterization of the passive rf-to-dc conversion. The magnetization dynamics of both the free and polarizing layers are explored electrically through magneto-resistance measurements without any additional dc current (for passive detection). The experimental characterization includes all free layer thicknesses (1.4 nm, 1.6 nm, and 1.8nm) under in-plane and out-of-plane magnetic field biases, in addition to the different MTJ nominal diameters (20 nm, 40 nm, 80nm, 100nm, and 150 nm).

Chapter 6 dedicated to the characterization of the active microwave signal detection. The aim of the chapter is to explore how the dc current affects the performance of the pMTJ-based spin-torque nano-diodes. They are characterized in the presence of a dc current for all the thicknesses and diameters that were discussed in Chapter V. Moreover, it contains a characterization of the FMR modes of the free and the polarizing layers and their current dependence through the Joule heating and the STT.

Chapter 7 is dedicated to the characterization perpendicular superparamagnetic tunnel junctions operating at zero field. The investigations are carried out by first analyzing the static magnetoresistance measurements of the different free layer thicknesses and diameters to understand their effect on the signal. Thereafter, the analysis is extended to characterize the stochastic variations of the resistance in real-time and their voltage dependence.

Summary and perspectives summarizes the theoretical and experimental results that were obtained in this work, and gives an outlook on the next steps and perspectives.

Background and State of the Art

1.1 Introduction to Spintronics

Spintronics is a branch of physics and technology concerned with both the charge and the spin of electrons. Like the revolution in semiconductors, it developed due to the great advancements in thin film deposition techniques and the unraveling of the physical phenomena occurring at the interfaces of multilayered thin films. However, unlike the conventional electronics where the electron charges are the major actor to manipulate the current flow, for spintronics it is the electron spin.

Ever since the discovery of the giant magnetoresistance (GMR) effect, by A. Fert and P. Grünberg [10], [11] [12], spintronics as a field took-off with a fast speed. The GMR effect demonstrated that the resistivity of two magnetic layers, separated by a thin non-magnetic layer, depends strongly on the orientation of their respective magnetizations. This, along with the nano-size of GMR devices, had, and still has a strong impact on the data storage industry. When used as read heads for hard disc drives (HDD), the GMR devices allow the development of HDD with much smaller memory cells. Hence, it permits the fabrication of memories with much higher densities, to meet the ever growing needs for higher storage capacity.

The following development of the tunneling magnetoresistance (TMR) at room temperature, by J. S. Moodera et al. [13], enlarged the latter fields of applications. It offered much higher changes in resistance by inserting an insulator as the non-magnetic spacer layer separating the two magnetic layers. The devices bear the name magnetic tunnel junctions (MTJ). In addition to their better sensitivity as memory read heads (or magnetic field sensors), MTJs were established as memory cells themselves in the form of non-volatile magnetic random access memories (MRAM). They are foreseen as potential candidates for future memory architectures, and may succeed the currently used semiconductor memories (SRAM, DRAM, flash…etc.) [14].

Moreover, the prediction of the spin transfer torque (STT) by Slonczewski and Berger [15], [16], added more functionality and advantages to the MRAM devices. It permitted the manipulation of the magnetic states of the MTJ layers directly by an electric current, which increased the writing and the reading speed of MRAMs, and reduced their overall energy consumption [17].

Another major consequence of the discovery of the spin transfer torque is its ability to excite steady state oscillations of the magnetization whose frequency can be tuned by the electrical current [18]–[21]. Through the tunneling magnetoresistance, these oscillations are converted into electrical signals with frequencies in the microwave range, thus, paving the way for MTJs to be used as low power nano-oscillators.

In this manuscript, the magnetic tunnel junctions (MTJ) and the spin transfer torque (STT) effect are the basic concepts to describe the spin torque diode effect. They are introduced in the following sections within a general formalism. For the readers seeking more depth on the subjects they are referred to references such as [17], [22]–[24].

1.1.1 Ferromagnetism in 3d transition metals

Magnetic materials are the backbone of spintronics, especially ferromagnetic materials because they have, intrinsically, a strong spontaneous magnetization. The origin of the spontaneous magnetizations for isolated atoms can be portrayed in the classical magnetostatic formalism [25]. For instance, as in a single loop solenoid, an electron orbiting the atomic nucleus will naturally have an orbital momentum that generates a magnetic moment, see Figure *1.1.1*.

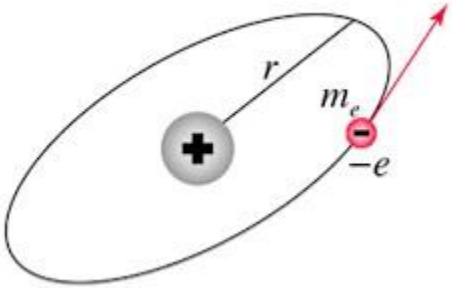

Figure 1.1.1 : Illustration of an electron orbiting the nucleus. Adapted from [26].

The obtained magnetic moments can be expressed by the following relation [25]:

$$\vec{\mu} = -\frac{e}{2m_e}\,\vec{L} \tag{1.1.1}$$

where $\vec{\mu}$ is the magnetic moment, e is the electron charge (absolute value), m_e the electron mass, and $\vec{L}$ the angular momentum. Moreover, picturing the electrons classically as a uniformly charged point particle that rotates around its own center of mass, it will generate an additional magnetic moment called the spin angular momentum. It is described by a similar relation as the orbital magnetic moment. However, this classical description is not quite complete, because at the atomic level, the quantum mechanics is supreme. The angular momentum is quantized by the Planck constant, and interestingly the spin magnetic moment is twice larger than expected from Eq. 1.1.1. The quantum mechanics, and especially the Stern-Gerlach experiment [27], demonstrated that the spin of the electron is an intrinsic property just like the charge and the mass. The corrected formula of the magnetic moment is expressed by :

$$\vec{\mu} = -g\,\mu_B\,\vec{s} \tag{1.1.2}$$

where g is the Landé factor (equal to 2 for spin, and 1 for orbit), $\mu_B = \frac{e\hbar}{m_e}$ the Bohr magneton, $\hbar$ the reduced Planck constant, and $\vec{s}$ the angular momentum (for the electrons spin $: \pm 1/2$). Hence the quantum mechanical nature of the electrons make the total magnetic moment to be dominated by the spin. Moreover, since the electrons have a mass that is thousand times smaller than the nucleus, they are the dominant source of the magnetic moment of the atom (see Eq. 1.1.2).

For the isolated atoms with more than one electron, the filling of the atomic orbitals is governed by Hund's rules [25] that favor a constructive addition of the magnetic moments. The Hund's rules stem from the combination of the Pauli exclusion principle and the Coulomb law. The former forces the electrons with the same spin to stay apart, and the latter promotes the same behavior due to their charge similarity. A direct consequence of Hund's rules is that all the atoms with partially filled orbitals have a non-negligible total magnetic moment, which is the case for a majority of atoms. However, this is the case only for isolated atoms, or rare earth metals [25]. Once the atoms form a solid state body, the angular moments are usually quenched because the electrons become delocalized and form bands. At room temperature, only Fe, Ni, and Co have a spontaneous magnetization. Their specificity lies in their electronic band structure. In these metals, the electrons occupying the highest energy level (Fermi level : E_F) have an asymmetry in the densities of states (DOS) of spin-up (+1/2) and spin-down (-1/2) electrons, see Figure *1.1.2*, namely the electrons from the 3d orbitals, due to their strong exchange coupling (spin interaction), hence the nomenclature 3d transition metals[17], [22], [24]. For the 4s orbital electrons their spin-up and down densities are uniformly distributed and hence do not contribute to the net magnetic moment.

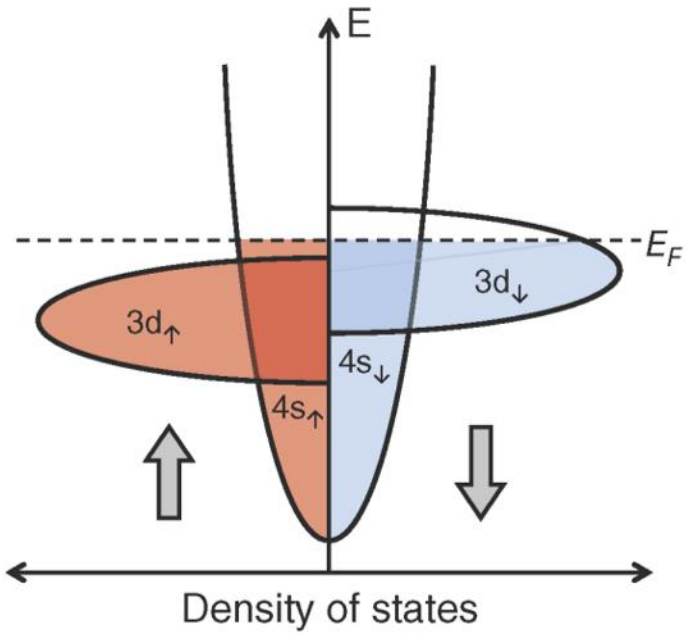

Figure 1.1.2 : Illustration of the band structure of 3d transition metals. Adopted from [17].

The disparity in spin orientations in the 3d transition metal is the reason behind there spontaneous magnetization. The magnetization here refers to the density of magnetic moments in a volume.

Moreover, since the electrons at the fermi level are directly involved in the electrical conductivity, these metals can act as a spin filter (polarized). The conduction in these metals is carried out by the delocalized 4s electrons. When the 4s electrons pass through the metal, they are scattered by the 3d localized electrons having the same energy and spin orientation. The difference of the density of state at the Fermi level implies a different scattering probability depending on the spin orientation.

The spin polarization (P) can be evaluated through the formula :

$$P = \frac{N^{\uparrow} - N^{\downarrow}}{N^{\uparrow} + N^{\downarrow}} \tag{1.1.3}$$

where $N^{\uparrow}$ is the density of states of spin-up electrons and $N^{\downarrow}$ is the density of states of spin-down electrons.

The next section deals with the consequences of this spin polarization.

1.1.2 Tunneling magnetoresistance

The magnetic tunnel junctions (MTJ) are nowadays one of the most known spintronic devices. They are made of two ferromagnetic layers separated by a thin insulating layer. The electronic transport between the two magnetic layers occurs through the quantum tunneling effect [28], where the electrons have a non-negligible probability of tunneling through an energy barrier. The solutions from the Schrödinger equation show that the transmission probability of the electrons through an energy barrier decays exponentially with the barrier thickness (d) : $T \propto e^{-\kappa d}$, with κ the decay rate. Furthermore, in MTJ-like junctions, the tunneling current is proportional to the number of the free electrons at the Fermi level in the emitting layer, and the number of the vacant states at the Fermi level in the receiving layer. It is called the Fermi golden rule (see Eq. 1.1.4). The net tunneling current under an applied bias voltage is approximately [17] :

$$I \propto [D_1(E)f_1(E)] \cdot T(E) \cdot \left[D_2(E - eV)\left(1 - f_2(E)\right)\right] \tag{1.1.4}$$

where $D_i(E)f_i(E)$ is the number of electrons and $D(E)$ the density of states, $f(E)$ the Fermi-Dirac distribution, and i refers to the first or second magnetic layer. Eq. 1.1.4 implies as well that the conductance G is proportional to the product of the densities of states (D_1 and D_2).

For magnetic materials, where up and down electrons have different densities, the tunneling occurs through two separate channels. One channel for the electrons of majority spins and the other channel for those of minority spins. This model is often referred to as Mott model [29], [30], see Figure *1.1.3* for an illustration ($N_i^j = D_i^j(E)f_i(E)$).

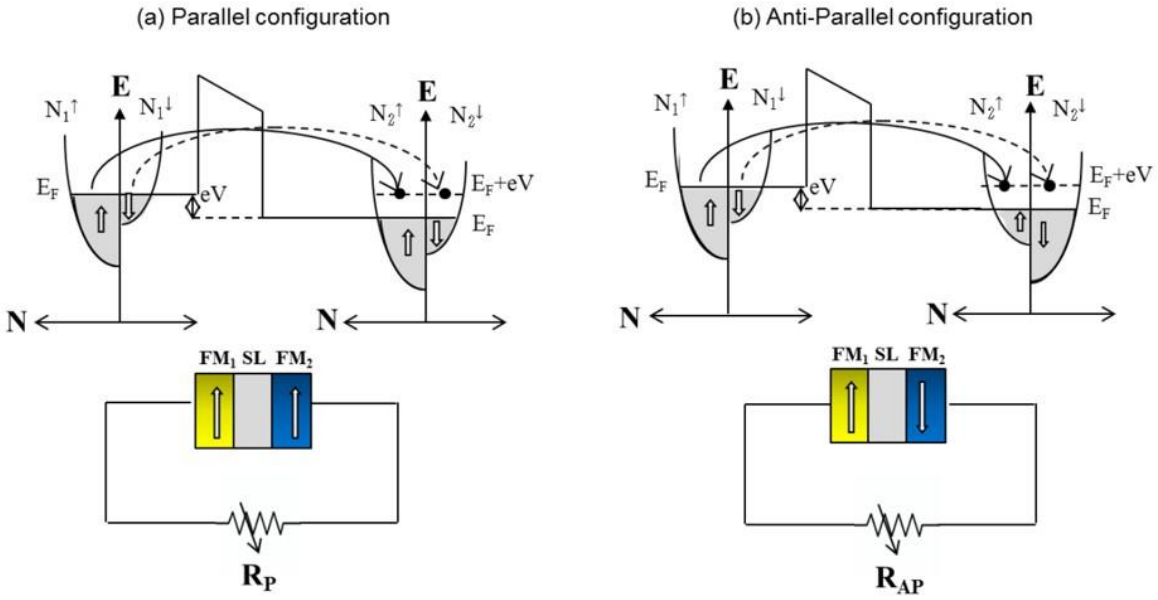

Figure 1.1.3 : (a) The illustration of the tunneling between two magnetic layers with similar band structures (parallel). (b) The same as (a) but with an asymmetrical band structures (anti-parallel). Adapted from [31].

Moreover, the electrons tunneling within the two channels experience different resistivities depending on whether the magnetization of the two magnetic layers have the same orientation or not. For instance, in the case where they are parallel, the conductance from Eq. 1.1.4 predicts higher conductivity, while for the case where they are anti-parallel the conductivity is lower, see Figure *1.1.3*(a)-(b). This can be summarized by the following expressions:

$$G_p \propto D_1^{\uparrow} D_2^{\uparrow} + D_1^{\downarrow} D_2^{\downarrow} \tag{1.1.5}$$

$$G_{ap} \propto D_1^{\uparrow} D_2^{\downarrow} + D_1^{\downarrow} D_2^{\uparrow} \tag{1.1.6}$$

where G_p and G_{ap} are the conductances for the parallel and anti-parallel configurations respectively, and $D_i^{\uparrow\downarrow}$ is the density of state of majority spins (↑ up) and minority spins (↓ down). The change in the resistance between parallel and anti-parallel can be estimated by the tunneling magnetoresistance ratio defined as :

$$TMR = \frac{G_p - G_{ap}}{G_{ap}} \tag{1.1.7}$$

The first experimental observation of the tunneling magnetoresistance was reported in 1972 by Jullière [32]. It was observed in an MTJ made of Fe/GeO/Co and at a temperature of 4.2 K. The TMR ratio was about 14%. However, the development in thin film deposition techniques within the following decades allowed for major enhancements of the TMR. It was found in 1995 by J. Moodera et al. [13], that using Al_2O_3 as an insulating barrier the TMR yields a ratio of 20-70%, at room temperature.

Using the two channel model in Eq. 1.1.6-7, Jullière was able to explain the TMR with a good accuracy by defining the spin polarization as :

$$P_i = \frac{D_i^{\uparrow} - D_i^{\downarrow}}{D_i^{\uparrow} + D_i^{\downarrow}} \tag{1.1.8}$$

which gives a TMR that depends on the spin polarization of the two magnetic layers, expressed as [32]:

$$TMR = \frac{2P_1P_2}{1 - P_1P_2} \tag{1.1.9}$$

However, despite the early success of Julliére's model it failed to predict the experimental observations of the TMR dependence on the characteristics of the insulating barrier [33]. This is due to the omission of the effect of the electron band structure on the tunneling process. The first correction to the model was done by Slonczewski, where through a more rigorous calculation of the TMR he demonstrated analytically that the tunneling depends on the wave vectors, i.e. the velocity of the electrons [34], which indicates that the electrons from the 4s or 3d orbitals have different probabilities of tunneling. The corrected polarization formula is expressed as [17]:

$$P = P_0 \frac{\left(\kappa^2 - k_{F,\uparrow}k_{F,\downarrow}\right)}{\left(\kappa^2 + k_{F,\uparrow}k_{F,\downarrow}\right)} \tag{1.1.10}$$

where P_0 is Julliére polarization in Eq. 1.18, κ the decay rate, and $k_{F,\uparrow\downarrow}$ the wave vectors at Fermi level of the spin majority and minority. Therefore if the electrons with majority spins are traveling faster ($\propto dE/dk$) the spin polarization can be enhanced.

A major breakthrough in the TMR improvement, was first provided from first principle calculations [33], [35], [36]. Butler, Mathon, et al. [35], [36], demonstrated that for an MTJ made of Fe (001) electrodes and a crystalline MgO barrier the TMR can reach 1600%. The major TMR enhancement comes from the coherent tunneling process occurring in these junctions. The matched crystallography of the electrodes and the barrier, preserves the symmetry of the electron orbitals and leads to a strong spin filtering, see Figure *1.1.4*(a)-(b) for an illustration. In Fe (001) and all 3d transition metals, the tunneling electrons are from three Bloch states [17]: Δ_1 (hybridized s-p-d states), Δ_2 (d states), and Δ_5 (p-d states), and only the spin majority electrons are in the Δ_1 states. As illustrated in Figure *1.1.4*(b), the calculation predicts that the Δ_1 electrons have by large the highest tunneling probability and thus the overall spin polarization is almost 1. This process is called the spin filtering. It was demonstrated experimentally and the TMR ratio at room temperature was pushed to values as high as 604 % [33], [37].

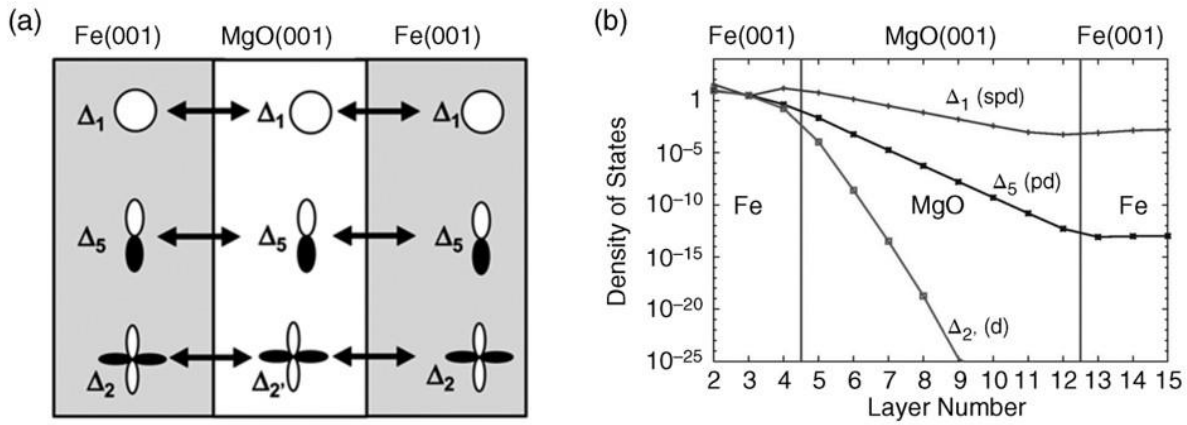

Figure 1.1.4 : (a) The illustration of the conservation of the orbital symmetry in Fe|MgO|Fe junctions. (b) The density of states as a function of the number of atomic layers in Fe|MgO|Fe. Adapted from [33].

Similar barriers such as $SrTiO_3$ show a large TMR, however, so far the MgO as a barrier gives the highest TMR in magnetic tunnel junctions.

The TMR, in general, as an effect shows how the electrical transport can be altered by the magnetic state of a host material, but what about the reciprocal effect? Can the magnetic state be modified by the incoming electrons ?

The answer to these question is the focus of the next section.

1.1.3 Spin transfer torque

In the last two sections, it was shown that if a flow of free electrons (current) passes through a ferromagnetic layer, they become spin polarized. When they penetrate the ferromagnetic layer they start precessing around the local magnetization of the layer. Dephasing of the electron spin precession after a certain distance from the interface leads to a loss of the transverse angular momentum. This transverse moment, via the exchange interaction, is transferred to the local magnetization. As a consequence this angular momentum transfer applies torque on the local magnetization, referred to as the spin transfer torque (STT). For incident non-polarized electrons, no net torque is accumulated and in average it does not have an effect on the magnetization. However, if the incident electrons are polarized the spin transfer torque incites the magnetization to align itself with the incident electrons' angular momentum. For a magnetic tunnel junction, the incident electrons are first polarized by a ferromagnetic polarizing layer, then tunnel coherently through the MgO barrier and reach the interface of the second ferromagnetic layer strongly polarized along the magnetization of the first ferromagnetic layer. Therefore, if the second ferromagnetic layer is not collinear with the first ferromagnetic layer, the spin transfer torque tends

to align it with the incident electrons polarization axis, see Figure *1.1.5* for an illustration[16], [22], [23].

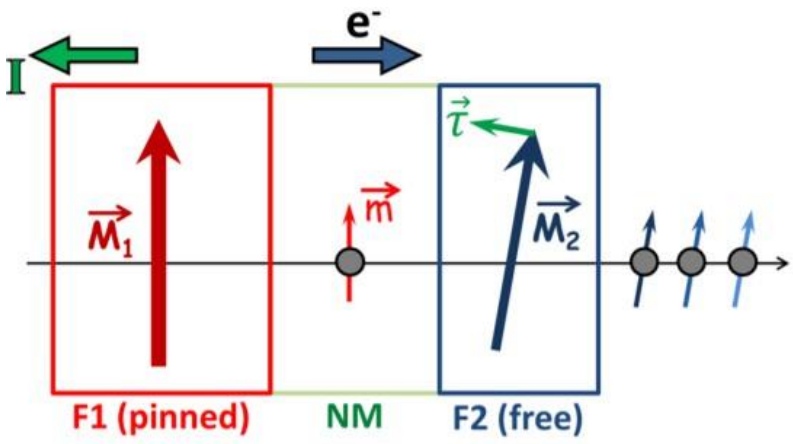

Figure 1.1.5 : Illustration of the spin transfer torque effect in magnetic tunnel junctions. Adapted from [17]. $\overrightarrow{M_1}$ and $\overrightarrow{M_2}$ are the pinned and free layer magnetizations respectively, and $\vec{m}$ the electrons magnetic moment, and $\vec{\tau}$ the STT.

The spin transfer torque (STT) was first predicted in 1996 independently by Slonczewski and Berger [15], [16]. Slonczewski predicted that it can be used to either switch the local magnetization of a layer or to induce steady state oscillations. The spin transfer torque was observed experimentally first in 1998 by Tsoi et al. [19], and first experiments demonstrating the switching of the magnetization were provided by J. Sun [38] in 1999.

The STT is generally made of two components, longitudinal and transverse. The longitudinal torque is for most MTJs the dominant one and depending on its sign it can compensate the magnetization damping. Therefore, it is called the damping-like torque. On the other hand, the transverse STT component acts more like an external bias magnetic field and is therefore called the field-like torque [39]. It usually can be neglected since its maximum value reported is at most ~30% of the damping-like torque. The spin transfer torques acting on the normalized magnetization $\vec{m}_2$ are expressed by the following expressions [17], [22]:

$$\tau = \tau_{\parallel} + \tau_{\perp} = \gamma a_j \left(\vec{m}_2 \times (\vec{m}_2 \times \vec{m}_1)\right) + \gamma\, b_j (\vec{m}_2 \times \vec{m}_1) \qquad (1.1.11)$$

where $\tau_{\parallel}$ is the damping-like term and $\tau_{\perp}$ is the field-like term and a_j and b_j are respectively the corresponding STT prefactors that are proportional to the incident spin polarized current (see section 1.1.5), γ is the gyromagnetic factor.

The effects of the spin transfer torque on the magnetization dynamics will be discussed in section 3.2 of chapter 3, and experimentally throughout the chapters 4 to 7.

They will be analyzed for the switching of the magnetization and the excitation of steady state oscillations due to a spin polarized dc current as well as for forced resonance excitations due to a spin polarized rf current.

1.1.4 Perpendicular magnetic anisotropy (PMA)

Besides the concepts relating to the spin polarized transport, it will be important to understand the magnetization state of a ferromagnetic layer. This is determined by the total energy, which has several contributions as discussed below. One important contribution to the total energy is the crystalline anisotropy energy that can act in thin films such as to align the magnetization perpendicular to the film plane. It arises from the spin-orbit interaction in the crystal [25]. More generally the magnetic anisotropy depends on the ferromagnetic material shape [40], crystallography [25], and/or interface [41], [42] which altogether contribute to determine the equilibrium direction of the magnetization. For the magnetic materials and alloys used for spintronic applications, such as memories, the anisotropy is usually selected to be uniaxial and to favor only two states along the same axis. The energy density such a uniaxial anisotropy is given by [43] :

$$E_u = K_u \sin^2(\theta) \tag{1.1.12}$$

Where K_u is the magnetic anisotropy energy constant, and the θ the angle of the magnetization direction with the easy axis. Notice the energy has only two minima when θ is 0 or π.

In thin magnetic films, when the anisotropy energy is lowest for an out-of-plane orientation of the magnetization one speaks about the perpendicular magnetic anisotropy (PMA). The latter proved to be enormously useful for the endeavor to fabricate magnetic tunnel junctions in the sub 20 nm scale. Not only it allows a higher memory density, but it also lowers the switching current compared to in-plane magnetized MTJs and thus lowers the overall energy consumption.

The perpendicular magnetic anisotropy (PMA) can have both bulk and surface origin, and in both cases it counteracts the shape anisotropy arising from the magnetic self-demagnetizing energy. For the bulk case, the PMA is called magnetocrystalline anisotropy and it originates from the spin-orbit interaction in the crystal [44]–[46]. It was found to be strongly present in ferromagnetic and heavy metal alloys such as Fe (or Co) and Pt (or Pd), which are ordered in the crystallographic phases $L1_0$ and $L1_1$ [14], [47], [48], where $L1_0$ refers to a face centered tetragonal crystal structure with Fe (or Co) and Pt (or Pd) stacks alternating along the plane [001]. $L1_1$ is a rhombohedral crystal structure with alternating planes stacked along the plane [111] [47].

Although the perpendicular magnetocrystalline anisotropy is strong in the mentioned alloys, its biggest flaw is it dependence on the volume of the magnetic layer. Hence for thin films it is weak and cannot be counted on to reach the sub-20 nm MTJs. Luckily, as the thin films get thinner there are interface phenomena that take the lead and subsequently generate a perpendicular anisotropy that becomes stronger as the thickness decreases.

It is referred to as the interfacial perpendicular anisotropy (iPMA) [41], [42]. It is strongly present at the interfaces of ferromagnet/ heavy-metals [49], [50], and the ferromagnet/oxides [41], [51], such as Co/Pt or Co/AlOx, or Co/MgO.

The interfacial anisotropy was first described by Néel in 1954 [52]. Using a pair interaction model he predicted that the broken symmetry at the interface of a magnetic layer creates a magnetic anisotropy distinct from the one in the bulk. Moreover, Néel's prediction was further confirmed using more thorough calculations, such as band structure models, by Gay et al. [53], and Bruno [54], [55]. It was found that at the interface of 3d transition metals, the broken symmetry disrupts the degeneracy (equality) of the 3d electronic states. It creates a split in the energy band, where the out-of-plane orbitals such as d_{z^2} , d_{xz} , and d_{yz} have lower energies compared to the in-plane orbitals : d_{xy}, and $d_{x^2-y^2}$, see Figure *1.1.6* for an illustration [56]. When a heavy metal (Pt, Pd) is deposited on a thin layer of 3d transition metals (Fe, Co, Ni) the hybridization of the 3d orbitals of the latter with the 5d orbitals of the heavy metal leads to the strong interfacial perpendicular anisotropy [50].

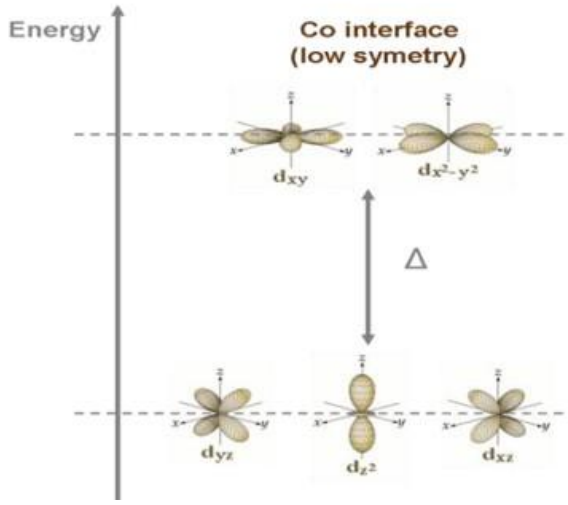

Figure 1.1.6 : Illustration of the band splitting at the interface of a 3d transition metal such as Fe, Co, or Ni. Adapted from [56].

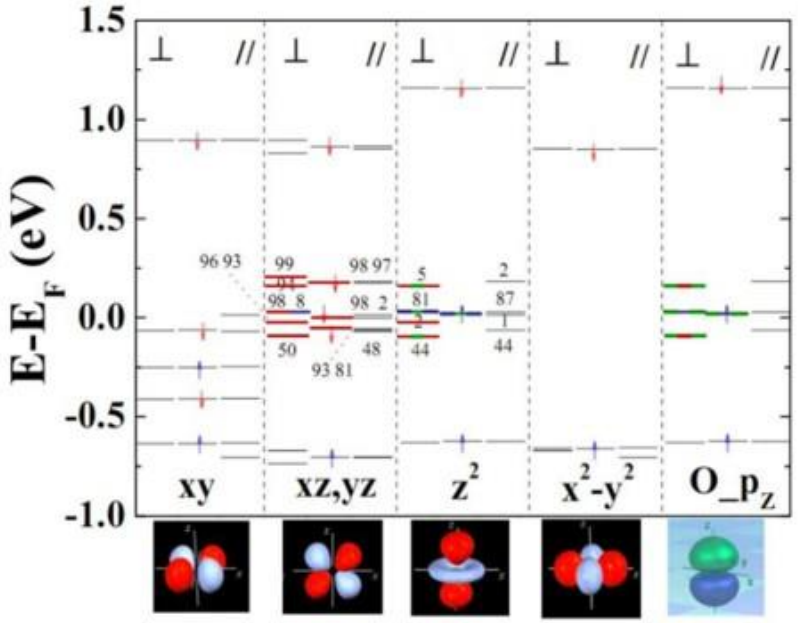

Figure 1.1.7 : The spin-orbit coupling effect at the interface of an Fe layer with an oxide. The middle column correspond to a hybridized state, while the left and right columns correspond to an out-of-plane and in-plane orientations respectively. Adapted from [57].

A further interesting origin of the interfacial perpendicular anisotropy (iPMA) is the interface of a ferromagnet with an oxide such as MgO. The great interest of this phenomenon is that it permits to combine the spin filtering discussed above with a strong perpendicular anisotropy, thus yielding strongly scalable magnetic tunnel junctions that have high spin polarization [14].

The physical origin of the interfacial magnetic anisotropy at the ferromagnet/oxide interface was investigated using first-principle calculations and it was attributed to the hybridization of the 3d out-of-plane orbitals of the ferromagnet and the 2p orbitals of the oxide's oxygen atoms [57], [58]. The summary of the calculations made by Yang et al. in [57] are shown in Figure *1.1.7*, where it can be seen that near the Fermi level only the energy states from the hybridization of the 3d out-of-plane orbitals and the $2p_z$ of the oxygen are present.

1.1.5 Magnetization dynamics

The underlying equation of motion for the magnetization is the Landau-Lifshitz-Gilbert (LLG) equation [15], [59], [60], see Eq. 1.1.13. It consists, generally, of conservative and dissipative terms. The conservative one involves the free energy of the magnetic layer through the effective magnetic field $\vec{H}_{eff}$, where it sums the contributions of the different free energy terms. The conservative term simply states that a non-collinearity between the magnetization and the effective field yields a torque that pushes the magnetization to precess around the effective field infinitely long, see *Figure 1.1.8*(a).

The intrinsic dissipative term accounts for the magnetization relaxation towards its energy minimum. It is defined as a friction "torque", in analogy to and by mathematical definition of that of a friction force, see *Figure 1.1.8*(b). Additional torques due to other phenomena, such as the spin transfer torque, are then added to the equation, see *Figure 1.1.8*(c).

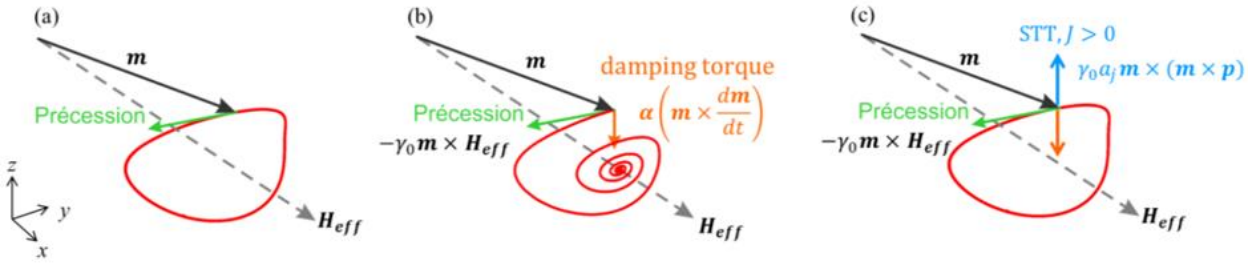

Figure 1.1.8 : (a) The magnetization dynamics for the conservative precession. (b) The magnetization dynamics for the dissipative precession. (c) The magnetization dynamics excited by the spin transfer torque. Adapted from [61].

The LLG equation, including the spin transfer torque, is expressed as follows :

$$\frac{\partial \vec{m}}{\partial t} = -\gamma\left(\vec{m} \times \vec{H}_{eff}\right) + \alpha\left(\vec{m} \times \frac{\partial \vec{m}}{\partial t}\right) + \gamma\, a_{\parallel}\, \vec{m} \times (\vec{m} \times \vec{p}) + \gamma\, a_{\perp}\, \vec{m} \times \vec{p} \qquad (1.1.13)$$

where $\vec{m}$ is the normalized magnetization of the free layer $\frac{\vec{M}}{M_s}$, M_s is the saturation magnetization γ the gyromagnetic ratio, $\vec{H}_{eff}$ is the effective field around which the magnetization precesses, α is the Gilbert damping constant, $\vec{p}$ is the normalized magnetization of the polarizer $\frac{\vec{P}}{M_s}$, $a_{\parallel} = \tilde{a}J$ and $a_{\perp} = \beta a_{\parallel}$ are respectively the STT damping-like and field-like torque prefactors.

The damping-like prefactor is defined by $\tilde{a}J = \frac{\hbar}{-2e}\frac{\eta}{\mu_o M_s t_{FL}}$, with $\hbar$ the reduced Planck constant, e the electric charge, η the spin polarization efficiency, and J (A/m^2) the current density.

The effective field contains several contributions $\vec{H}_{eff} = \vec{H}_{ueff} + \vec{H}_{bias} + \vec{H}_{int}$, including the effective anisotropy field $\vec{H}_{ueff}$ (the difference between the perpendicular anisotropy field H_u and the self-demagnetization field H_d, $\vec{H}_{ueff} = \vec{H}_u - \vec{H}_d$), $\vec{H}_{bias}$ from an external magnetic biasing field, and an interaction field $\vec{H}_{int}$ due to the interaction between layers, that can be due to exchange interaction or dipolar interaction. The different terms of the energy density and the effective field, as well as the spin transfer torque effect on the magnetization dynamics will be discussed in details in chapter 3.

1.2 State of the art of the spin-torque nano-diodes

The magnetization oscillations introduced in the previous sub-section is converted through the tunneling magnetoresistance into electrical voltage signals, and thus can be used for nano-electronic applications. Depending on the spin transfer torque excitation, the induced magnetization dynamics can lead to either a dc or an rf signal, or both simultaneously. If the STT excitations are driven by a dc current, above a certain threshold the magnetization is driven into auto-oscillations, where the oscillation frequency can be tuned via the dc current amplitude. For this operational mode, the magnetic tunnel junctions are referred to as spin-torque nano-oscillators (STNO). They have been extensively studied in the previous years for potential applications in low power telecommunications and for neuromorphic computing. A review can be found in references [21], [62].

A second operational mode is the rf signal rectification, where an rf current excites resonantly the magnetization oscillations leading through the tunneling magnetoresistance to an oscillating resistance. When the rf current frequency is close to the intrinsic resonance frequency of the magnetic layer, the combination of the oscillating resistance and current leads to a dc output voltage. This rectification phenomenon is called the spin-torque nano-diode effect, and it is the subject of this thesis. A detailed discussion on the rectification voltage will be presented in Chapter 3.

1.2.1 Resonant uniform MTJ-based spin-toque nano-diodes

The spin-torque nano-diodes based on magnetic tunnel junctions, have been attracting attention recently because of their nanoscale size, GHz operation, and high sensitivity to low radio-frequency power [63]–[67]. The effect was first reported by Tulapurkar et al. [68] in 2005. They used an in-plane magnetized tunnel junction where the magnetization of the free and polarizing layer are uniformly magnetized and oriented in-plane, see Figure *1.2.1*. The sensitivity of their diodes in the passive case, where only an rf current is applied, was approximately 50 mV/mW.

Although, the first experimental sensitivities of the spin-torque nano-diodes were relatively weak, the theoretical studies were predicting high sensitivities. For instance, the analysis of Wang et al. [69] predicted sensitivities of ~ 10^4 mV/mW by tuning the internal magnetic parameters of the free layer, thus opening the door for improvement based on the internal magnetic parameters, the magnetic configuration, and the non-linear magnetization dynamics. The implementation of the interfacial perpendicular magnetic anisotropy (iPMA) in uniformly magnetized magnetic tunnel junctions was of great advantage for the spin torque diodes since it allows easier tuning of the magnetization orientation. Zhu et al. [70] combining the iPMA and the voltage controlled magnetic anisotropy (VCMA) demonstrated a good enhancement of the spin-torque nano-diode outputs, see Figure *1.2.2*(a).

Moreover, using the iPMA to counteract the in-plane demagnetizing field, and the dc current to reduce the damping, Miwa et al [71] achieved a sensitivity of 12×10^3 mV/mW, see Figure *1.2.2*(b). Recently, using the injection locking the sensitivity in uniform MTJs reached 20×10^3 mV/mW, as demonstrated by Sharma et al. [72].

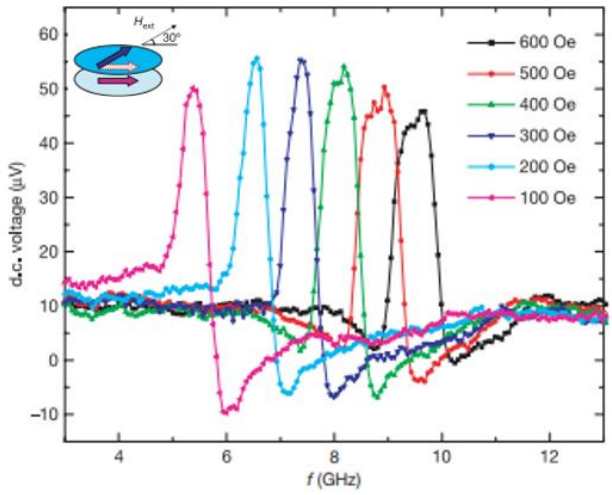

Figure 1.2.1 : The first experimental demonstration of the spin-torque nano-diode effect using in-plane magnetized tunnel junctions. Adapted from [68].

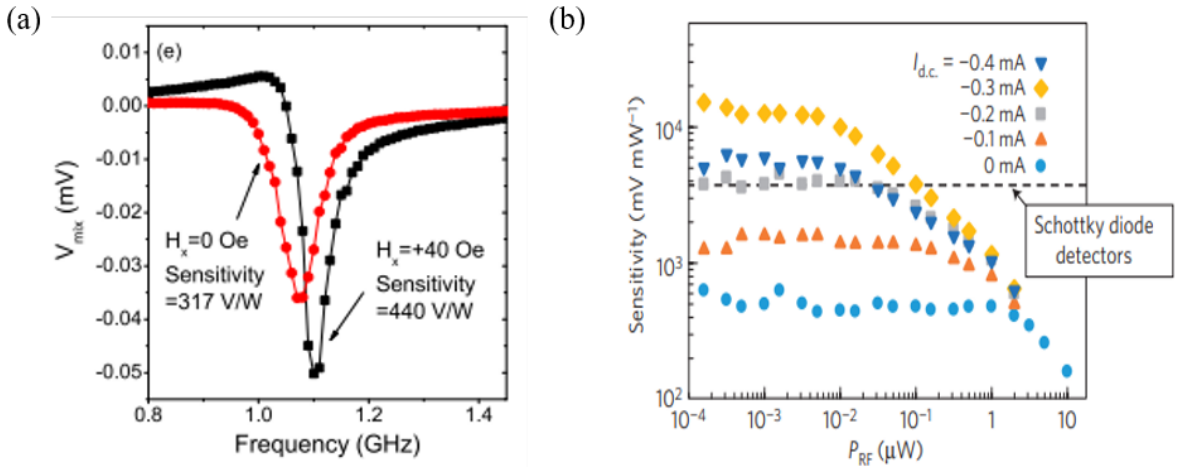

Figure 1.2.2 : (a) Illustration of the enhancement of the spin torque nano-diode output signal by combining the spin transfer torque, iPMA, and the voltage controlled anisotropy, adapted from *[70]*. (b) The enhancement of the sensitivity by spin polarized dc currents, adapted from *[71]*.

1.2.2 Non-resonant uniform MTJ-based spin-toque nano-diodes

Another interesting improvement of the spin-torque nano-diodes output efficiency was the prediction of the non-resonant regime by Prokopenko et al [73], and it's experimental

demonstration by Fang et al. [63]. It arises from the out-of-plane precession (OOP) of the magnetization and was found to be related to the second order magnetic anisotropy. The specificity of this magnetization dynamic regime is its broadband passive operation, unlike the resonant oscillations that are frequency selective. Therefore it is of interest for energy harvesting. The disadvantage of this method is that it requires an rf current power threshold to function, and can cover only a low frequency band (> 3 GHz), see Figure *1.2.3*(a)-(b).

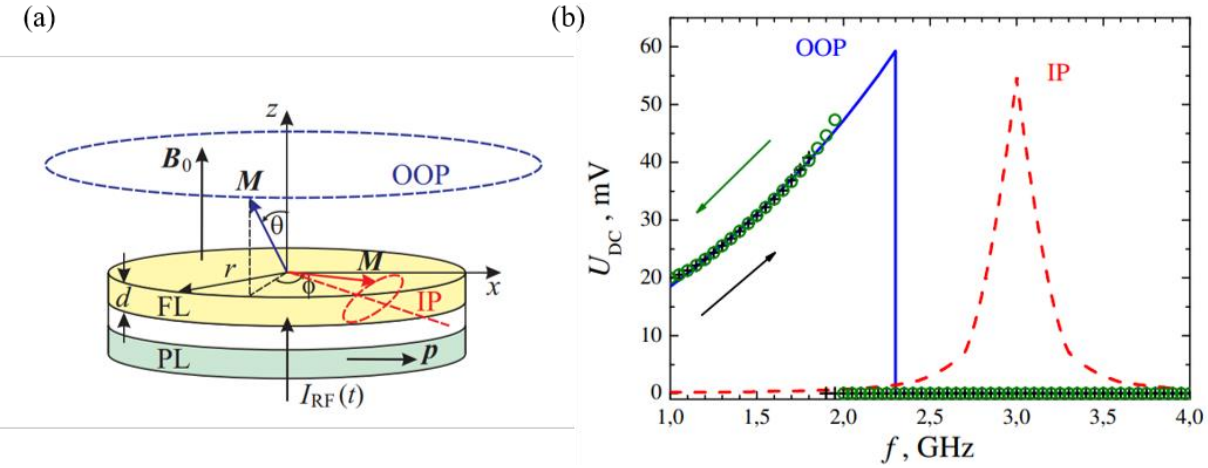

Figure 1.2.3 : (a) Illustration of the broadband magnetization dynamics the OOP, the out-of-plane field can be replaced by the iPMA. (b) The output voltages of a spin torque diode in the OOP broadband regime (Blue) and the IP resonant regime (Red). Adapted from [73].

1.2.3 Vortex MTJ-based spin-toque nano-diodes

In addition to the previous spin torque nano-diodes, alternative enhancements were obtained by exploiting other magnetic configurations, such as the vortex state. In the vortex state of the magnetization, the rf current can drive the vortex core resonantly leading to a spin diode effect in the output. Moreover, adding a dc current simultaneously with the rf current, can lead to the expulsion of the vortex core, yielding a high dc voltage change in the output [74], see Figure *1.2.4*.

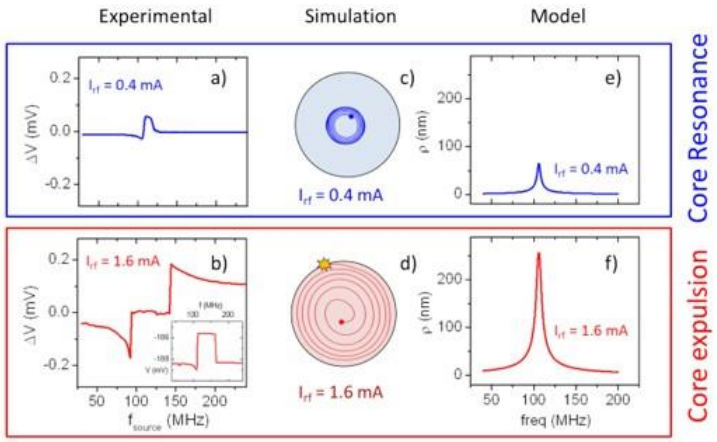

Figure 1.2.4 : Illustration of the operation of vortex spin torque nano-diodes. Adapted from [74].

The sensitivities obtained through the vortex expulsion reached 80×10^2 mV/mW as demonstrated by Tsunegi et al. [75]. However, despite the ultra-high sensitivity of the vortex based spin torque diodes they operate only in the MHz range and still require an external magnetic field, and a dc current to expulse, unlike the uniform MTJs that were demonstrated to operate in the absence of an external magnetic field.

A detailed review of the recent developments of the spin-torque nano-diodes can be found in the references by Finocchio et al. [8], and by Zvezdin et al. [76]. The latter provides a summary table that traces quasi-all the enhancements of the sensitivities of the spin torque diodes.

The work carried out during my PhD is a contribution to the continuous endeavor to improve the spin torque nano-diodes focusing on quasi-uniformly magnetized MTJs with strong iPMA. Unlike the previously reported results, here the polarizing layer is oriented also out-of-plane. These MTJs are referred to as perpendicular magnetic tunnel junctions (pMTJs) and have the advantage of being manufacturable to sub-20 nm diameters, and their magnetic state can easily be tuned trough their free layer thickness. The demonstration of radiofrequency functionalities in these devices makes them multifunctional devices that can operate as memory, sensor, and radiofrequency components. This has been the objective of the Horizon2020 project GREAT, within which the pMTJ devices presented here have been realized. Through this project, we had access to devices of different free layer thicknesses and diameters. The thicknesses were chosen such that the free layer can be oriented either in-plane or out-of-plane. These different pMTJs have been investigated for their spin-torque nano-diode effect in the passive and active regimes, as well as under in-plane and out-of-plane magnetic bias fields. The results are presented respectively in chapters 5 and 6. Before discussing these results, I will provide a detailed discussion on the experimental techniques, the theoretical equations for the expected dc output voltage signal as well as the static hysteresis loops.

Experimental techniques

This chapter introduces the perpendicular magnetic tunnel junctions (pMTJs) and the different experimental techniques used in the upcoming chapters of the manuscript. It starts by presenting the magnetic stack of the pMTJs, followed by the experimental techniques used for the characterization of the static magnetic state and the transport properties (chapter 4), and of the characterization of the dynamic properties (chapter 5-7). The techniques on the magnetization dynamics have been developed prior to this work, details can be found in references [61], [77].

2.1 A brief introduction to the pMTJs under investigation

The pMTJs studied in this work were developed within the European Horizon project GREAT that took place between 2016 to 2019. Its main goal was to develop a single stack allowing to perform memory, analog logic and RF functions on the same wafer. This work concentrates on the RF properties of these devices and especially on the functionality of RF signal detection.

The GREAT project approach was to focus on a standard perpendicular magnetic tunnel junction structure, optimized for the memory function, and then tune their internal properties to achieve the performances needed for RF and sensor applications.

Different strategies are employed for these developments such as changing the effective anisotropy through thickness and diameter variations (RF functionality), or by adding magnets whose field reorients the storage layer magnetization (sensor function). For all functionalities, the targeted spin polarized transport properties were:

- A resistance area product (RA) ranging between 5 and 10Ωμm², which represents a good compromise between the reading path preferring a higher resistance and the performance output in sensing and oscillator applications preferring a lower resistance.
- A tunnel magnetoresistance (TMR) ratio of 100% to maximize the readout signal for the memory and RF functions and the sensitivity of the sensor function.

A second goal was to demonstrate spintronics-CMOS co-integration of the different functionalities with dedicated electrical circuits. Therefore, the devices investigated here have been fabricated on CMOS base wafers whose metallization layer was TaN, onto which the pMTJ stack has been deposited. Tower Jazz provided the CMOS/TaN base wafers, Singulus deposited the magnetic stacks and Spintec carried out the nanofabrication.

2.1.1 pMTJ magnetic stack

The pMTJ stack is a bottom pinned perpendicular magnetized MTJ as illustrated in Figure 2.1.1(a) with the following composition (thickness in nm)[78], [79]:

bottom electrode/ $[Co\ (0.5) / Pt\ (0.2)]_6$ / Ru (0.8) / $[Co\ (0.6) / Pt\ (0.2)]_3$ / Ta (0.2) / Co (0.9) / W (0.25) / FeCoB (1) / MgO (0.8) / FeCoB (t_{FL}) / W (0.3) / FeCoB (0.5) / MgO (0.75)/ top electrode.

The thicknesses of the different layers within the stack are the results of a continuing optimization process of the perpendicular magnetic tunnel junctions carried out at Spintec and at Singulus. The exact stack composition may vary, depending on the deposition tool and materials available. More information on the optimization of pMTJ stacks can be found in [17], [46], [56], [79]–[81].

The major building blocks of the pMTJ stack are successively: the composite free layer marked in green, the tunneling barrier marked in pink, the composite polarizing layer marked in yellow, and the synthetic antiferromagnet (SAF) multilayers marked in cyan.

Free layer (FL): The composite free layer is made of two thin FeCoB layers that are ferromagnetically coupled through a thin Tungsten (W) layer. This composite layer is sandwiched between two thin MgO layers to induce the interfacial perpendicular anisotropy (iPMA) [17]. The purpose of the thin W layer is to pump the diffusing Boron atoms, to avoid them entering the MgO layers, which would degrade the iPMA and the TMR. Since only the thickness of the bottom FeCoB layer was varied (the one closer the polarizing layer), we refer to it as "free layer (FL)". The corresponding thicknesses investigated here are : t_{FL} = 1.8 nm, 1.6 nm and 1.4 nm which is much thicker than the topmost FeCoB layer which is nominally 0.5 nm. This free layer thickness (t_{FL}) influences strongly the competition between the total perpendicular magnetic anisotropy energy (which is the iPMA divided by the thickness) and the demagnetizing energy. For thin films the iPMA dominates and for thick films the demagnetization energy dominates. The thicknesses chosen here are such that they lead to a reorientation of the magnetization direction from out-of-plane (t_{FL} = 1.4 nm) to in-plane (t_{FL} = 1.8 nm).

Polarizing layer (PL): The polarizing layer is a composite layer of Co/W/CoFeB. Its magnetization is expected to be oriented out-of-plane due the iPMA at the FeCoB/MgO interface, as well as the ferromagnetic coupling to the out-of-plane orientated synthetic antiferromagnet (SAF) [80]. The role of the W layer is dual. On the one hand it serves as a Boron pump, but it also ensures the amorphous growth of the FeCoB, needed for a textured growth of the MgO.

Synthetic antiferromagnet multilayers (SAF): The SAF is made of two sets of perpendicularly magnetized $[Co/Pt]_n$ multilayers separated by a thin Ru layer. They are called the bottom SAF layer and top SAF layer and denoted here by B-SAF and T-SAF respectively. The out-of-plane orientation of the overall magnetization in the $[Co/Pt]_n$ multilayers is caused by the strong iPMA at the Co/Pt interfaces [17]. In addition, the Co layers within the $[Co/Pt]_n$ multilayer are coupled ferromagnetically through the indirect exchange coupling. When the thin Ru layer is introduced, it induces an antiferromagnet coupling between the two multilayers. The SAF is used to stiffen the

polarizing layer by coupling ferromagnetically to it. It also compensates the stray fields at the position of the free layer arising from the polarizing layer.

It should be mentioned that the pMTJ stacks have been developed by Singulus, who introduced a Ta (0.2) layer between the last Pt layer of the T-SAF layer and the bottom Co layer of the polarizer. This increases the total thickness of the spacer separating the two Co layers and in consequence it weakens the ferromagnetic coupling between them.

Bottom electrode: The stack was deposited by Singulus on CMOS/TaN base wafers realized by Tower Jazz. The choice of TaN for the last metallization layer is a compromise of having a layer of reduced roughness needed for not degrading the MTJ properties and the materials available at Tower Jazz. The TaN is etched to form the bottom electrode of the pMTJs. Since Ta has a high resistivity compared to Cu, this adds a non-negligible serial resistance to the pMTJ resistance and will have an effect for the diameter dependent properties as will be discussed for the TMR in chapter 4 and the detection signal in chapter 5.

Top electrode The pMTJ stack is covered by a Ru (8nm) capping layer on top of which a thick Ta (150 nm) layer is deposited that serves as a hard mask within the nanofabrication process used at Spintec. Furthermore the Ru layer serves as an etch stop layer and protects generally the MTJs against oxidation.

2.1.2 Nanofabrication of the pMTJ nanopillars

After the deposition of the pMTJ materials on top of the CMOS/TaN basewafer, they were nanofabricated at Spintec into circular nanopillars using e-beam lithography, followed by Ar+ ion etching. The nominal diameters of the nanopillars are D_n = 20, 40, 80, 100 and 150 nm. Here nominal refers to the diameter defined by e-beam lithography. However, SEM imaging shows that the true diameters are approximately 30 nm larger. Hence the real diameter used in the estimation of the static and dynamic properties is $D_r=D_n+30$nm. For convenience though, we refer to the devices with their nominal diameter.

The pMTJ wafers are diced into 5×6 mm^2 chips, where each chip contains 168 devices, as shown in Figure *2.1.1*(b), with different columns for different device diameters. Each chip contains as well two pseudo-devices in the top right fabricated without the pMTJ. These are electrically open and short circuits used for the deembedding of the devices (see section 2.4.1).

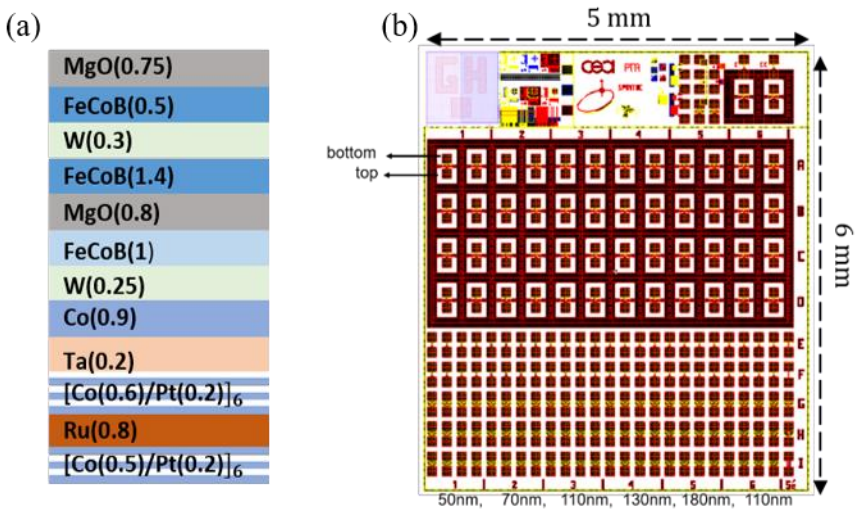

Figure 2.1.1 : (a) The stack of the perpendicular magnetic tunnel junctions used in this study, with the thicknesses in nm in parenthesis. (b) The final chip matrix after the nanofabrication and the wafer dicing. Each chip contains 168 nanopillars with the corresponding diameter mentioned in the bottom of the columns.

2.2 Characterization of the continuous films

Besides the transport properties of the pMTJs concerning the TMR and RA, Singulus did not provide much information on the magnetic properties. Therefore we measured the magnetization hysteresis loops of the continuous films for t=1.4 nm and 1.6 nm. For this a vibrating sample magnetometer (VSM) was used to measure the magnetic moment as a function of an external magnetic field, as well as a function to the field angle to identify the easy and hard axes of the magnetization of the SAF and free layer.

The VSM setup used in this work is from MicroSense® with a sensitivity of 10^{-6} emu and a magnetic field range up to 1.6 Tesla. The measurements are conducted at room temperature. The VSM setup is illustrated in Figure *2.2.1* with the sample sitting in the gap of an electromagnet. The operating principle is the following, the sample holder is vibrated vertically inside the magnet at a constant frequency. The vibrations of the magnetized sample will then, through the Faraday induction law, induce an electric field in a nearby pick-up coil. The resulting voltage is proportional to the magnetic moment of the sample, see [82] for more details.

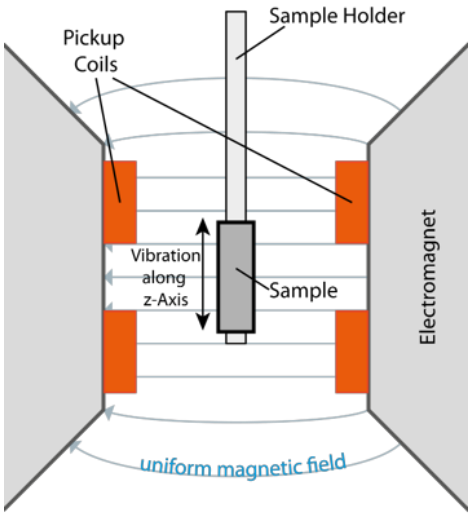

Figure 2.2.1: Schematics of the vibrating sample magnetometer [83].

2.3 Static magneto-transport measurements

The nanofabricated MTJ devices in form of circular nanopillars are characterized for their static and dynamic properties using magneto-transport measurements.

For the static magneto-resistance loops an automated MR tester as well as a physical property measurements system (PPMS) were used. The former provides a statistics of the resistances of the P and AP state, the TMR and coercive fields on wafer level, while the latter is used to study the magnetic and transport properties of single devices as a function temperature, current and magnetic field.

As a result, these measurements allow one to verify the easy axis of the different layers after nanofabrication, and provide the electric properties of these pMTJs such as : the TMR, the STT, the VCMA, and the effect of Joule heating.

2.3.1 Automated MR tester for wafer level characterization

The automated MR tester is used to map electrically the resistance, TMR and coercive fields of all devices on a wafer. It provides the statistics of the device performance, and allows one to give a feedback on the nanofabrication process, for instance if the etching led to shunt resistances or shorts. The automatic MR tester operates by applying a weak dc current (~10 µA), through a GS probe (250 µm pitch), in each device individually by moving the wafer underneath the probes. It then measures the device voltage to determine its resistance. These resistance measurements are conducted at room temperature and in the presence of a variable magnetic field of up to 200 mT.

The magnetic field is generated by an electromagnet. From the hysteresis loops the coercive fields and TMRs are extracted by a MATLAB program. An example of the TMR mapping using the automated MR tester is shown in Figure *2.3.1* for a wafer of pMTJs with a free layer thickness of 1.4nm.

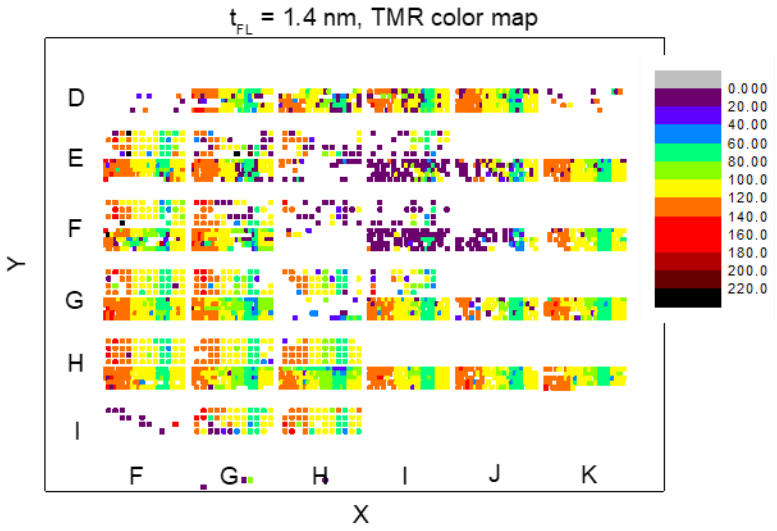

Figure 2.3.1 : Mapping of the TMR values of a pMTJ wafer with a free layer thickness of 1.4 nm. The bias magnetic field is oriented out-of-plane.

2.3.2 Physical property measurement system (PPMS)

The physical property measurement system is one of the key tools for the characterization of spintronic devices. It measures the magneto-resistance to extract different magnetic and transport properties as a function of current, temperature, external magnetic fields, and orientation of the external magnetic field. The temperature can be reduced down to 5 K, and the magnetic field magnitude can go up to 10 Tesla. In this work the PPMS is extensively used in chapter 4 to study the TMR and magnetic properties as a function of temperature and current (or voltage). An illustration of the setup is shown in Figure *2.3.2*. The PPMS measurements are similar to those of the automated MR tester, in the sense that it injects a dc current into the device and measures its voltage to extract the resistance. For the PPMS, the sample is first wire-bonded to the sample holder and then inserted into the thermally insulated chamber of the PPMS. This operation requires careful attention to avoid static current discharges that break the MTJ junction and that occurs frequently.

Inside the PPMS chamber the device is situated in the gap of an electromagnet, and the field angle with respect to the sample is varied by rotating the sample holder using a stepper motor.

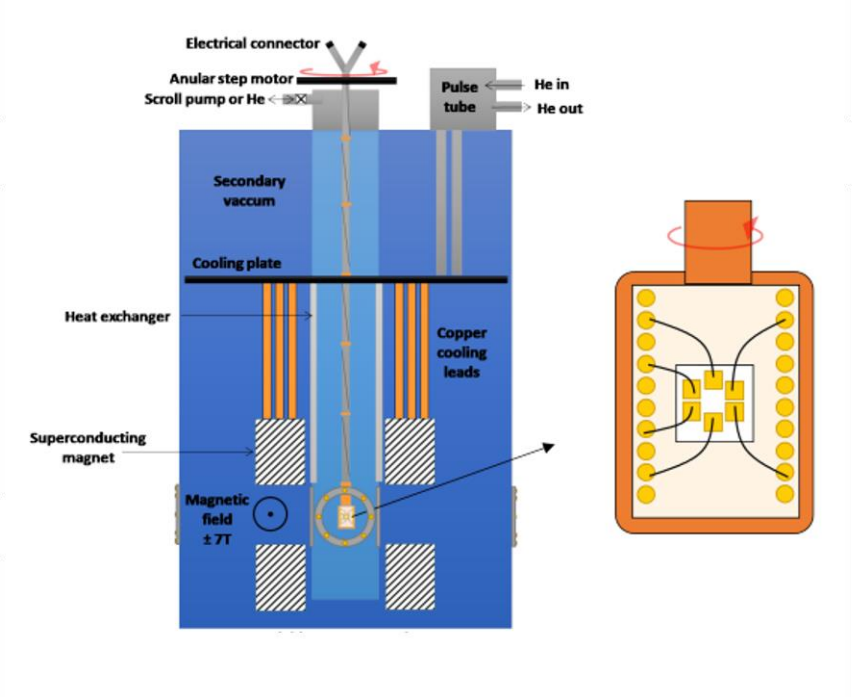

Figure 2.3.2 : Illustration of the physical property measurement system (PPMS) [84].

2.4 Experimental setups for the dynamic characterization in frequency domain

The characterization of the magnetization dynamics makes use of magneto-transport measurements to characterize the small and large angle excitations when driven by a spin polarized rf or dc current. The results are then analyzed for the potential of these pMTJs for rf applications. In the following we describe the experimental techniques used for studying the rf signal detection and the rf signal generation. These experiments need to consider several aspects such as :

- Impedance mismatch since the MTJ resistance is much larger than 50 Ohm.
- The MTJ nanopillar sandwiched between a top and bottom electrode layout can be modeled by an RLC equivalent circuit.
- The frequency dependent response of the measurement setup (attenuation, resonances..etc)

These aspects are important because as the frequency of the input/output signals increase toward the radiofrequency range, many parts of the setup can resonate and sometimes at frequencies close to those expected from an MTJ. Therefore, one has to separate the setup responses from those of the MTJs along with a cautious choice of the rf components with low noise figures and rf resilience.

In addition, the power of the excitation signal for the spin-torque nano-diode studies can as well alter the results either through the impedance mismatch between the rf sources and the loads or-

through Joule heating. A thorough review on transmission line theory and how parasitic lumped elements can affect the rf measurements can be found in reference [85].

2.4.1 Deembedding

To characterize and cancel the effects of the parasitic lumped elements on the measurements, deembedding the pMTJs is an important step before the characterization of the magnetization dynamics.

The aim of the deembedding is to measure the real rf power injected (or generated) in the pMTJs. Because of their high resistance that lies between 500Ω to 3kΩ, depending on the diameter, they are impedance mismatched with respect to the 50Ω setup-components (signal generators, spectrum analyzer etc). Consequently, the rf signals injected into (or generated by) the pMTJs are partially reflected. In addition, following the nanofabrication, the pMTJs are surrounded by a polymer dielectric called Accuflow. It seperates the top and bottom electrodes and can potentially create parasitic capacitances. An illustration of the device in an open circuit, with the potential parasitic lumped elements is shown in Figure *2.4.1*.

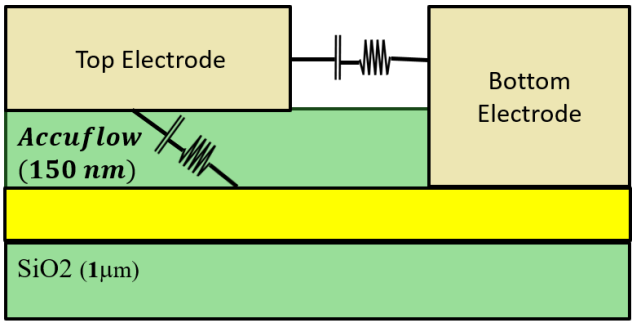

Figure 2.4.1 : Illustration of the device in an open circuit, in the absence of the pMTJ stack.

The deembedding in general works by measuring via a network analyzer the reflection parameters (called S-parameters) of the devices with and without the pMTJ stack and then subtract one from the other to get the pure response from the pMTJ. The subtraction is usually done by converting the S-parameters to transmission parameters and through matrix multiplications remove the parasitic responses and keep only the pMTJ response.

Moreover, the deembedding measurements can be used to determine an electrical equivalent circuit of the parasitic lumped elements by fitting the S-parameters. It is used to locate the source of these lumped elements in the device and predict how to rectify them.

In this work, the S-parameters were measured by a vectorial network analyzer (VNA) with a frequency range between 10 MHz and 40 GHz.

The extracted S-parameters of the pMTJs and the open circuits (see Figure *2.1.1*(b) for their location) are then processed using the software Advanced Design System (ADS) to extract the pure response of the pMTJs and analyze the real power injected in the devices. The deembedding in Figure *2.4.2* shows an example of a device with a nominal diameter of 40 nm and how the experimental results can be altered by the device surroundings. It shows, through the S-parameters that the device in reality reflects the injected power more than what is observed in the experiments prior to the deembedding.

The deembedding results of all pMTJs diameters are used in chapter 5 to determine the maximum voltage of the spin-torque nano-diodes that depends on the real rf power seen by the device and that differs from the power given by the rf signal source.

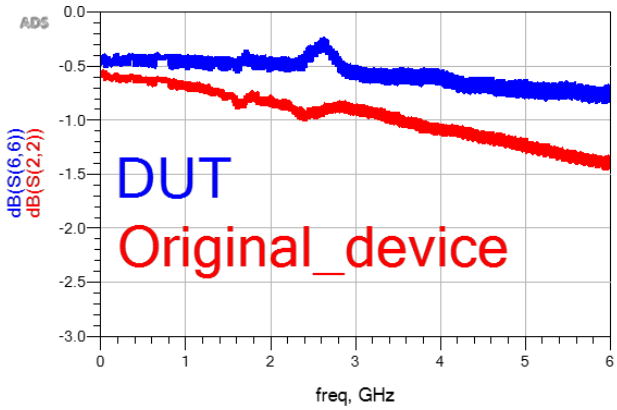

Figure 2.4.2 : The deembedding of a device with a nominal diameter of 40 nm. Here DUT refers to device under test (the isolated pMTJ) and original device refers to the compact pMTJ device with the parasitic lumped elements.

Following the results obtained from the deembedding an equivalent circuit of the pMTJ devices was developed by fitting the S-parameters, as depicted in Figure *2.4.3*(a). The model contains a relatively high parallel capacitance of the order of 170 pF. Although this might very well be due to the incompleteness of the proposed model, it might as well be due to the Accuflow dielectric or/and the air gap between the contact electrodes. To have a clearer idea of the potential origin of this parasitic capacitances, the electric field in the devices in an open circuit phase was simulated using ADS (finite element method), as depicted in Figure *2.4.3*(b), where it shows that the electric field is concentrated in the vertical space between the two electrodes. Therefore, it suggests that the dominant parasitic responses arises potentially from the Accuflow and its contact with the two electrodes. However, as mentioned earlier an improvement of the model might be required to get the full picture of the parasitic elements in the device. In the remaining parts of the manuscript, however, the parasitic elements were removed directly through the deembedding without investigating their nature and origin.

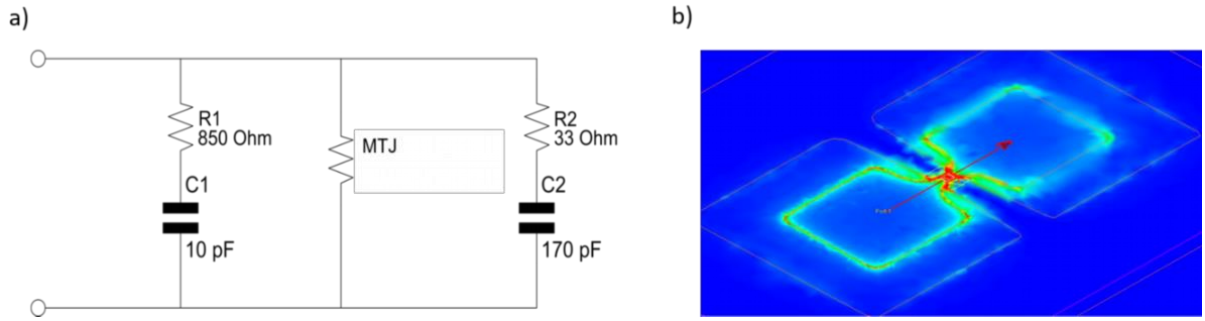

Figure 2.4.3 : (a) The equivalent circuit of the pMTJs. It was obtained by fitting the s-parameters. (b) The electric field from the simulation of the pMTJs device in the absence of the pMTJ stack using the ADS finite element simulator.

2.4.2 Spin torque FMR setup

The experimental setup to measure the spin torque nano-diode effect is called here spin-torque FMR (or ST-FMR). It is a more general name of the setup because it can be used to study the physics of the magnetic layers through the FMR line-shape and line-width, as well as it can be used to investigate the sensitivity of the pMTJs for diode applications. Its operational principle is to inject an rf current to the magnetic device in order to excite via STT, spin orbit torque or other effects (such as Oersted field) the magnetization dynamics. The precession of the magnetization is excited resonantly by the rf current and converted electrically, through the TMR effect, to an oscillating resistance.

The mixture of the rf current and the resulting oscillating resistance yield a voltage in the output with a maximum when the frequency of the rf current matches that of the FMR of the magnetic device. To scan the complete FMR response of the magnetic device there are generally two approaches: one through sweeping the magnetic field, and the other through sweeping the frequency of the rf signal. The first approach consists of fixing the rf signal frequency and varying the magnetic field, and then plot the measured voltage as a function of the external magnetic field. The advantage of this method is the reduction of the rf noise by operating at constant rf signal frequency, however its downside is its low speed and relatively large field steps (for this specific setup). For the second approach the procedure is reversed, the magnetic field magnitude is fixed and the rf signal frequency is swept from hundreds of MHz to tens of GHz, and afterwards the measured voltages are plotted as a function of the rf signal frequency. This method is much faster than the first one, although the varying rf signal leads to a frequency dependent background signal of potentially increases overall noise level. The two methods give generally similar voltages, and they are used both in this work.

The schematics of the setup used in this thesis is shown in Figure *2.4.4*. It consists of a radiofrequency generator with a 50 Ω impedance, that feeds the rf current to the magnetic tunnel junction (MTJ). The produced output voltage is measured by a Keithley 2400 source meter mounted in parallel to the MTJ. To separate between the injected rf current and the produced dc current, a bias-Tee is inserted at the input of MTJ. The rf current is fed from the capacitive gate of the bias Tee and the dc current is collected by its inductive gate. The setup is also equipped with a tunable in-plane magnetic field that is generated using an electromagnet. It is tunable between -150 mT and 150 mT with field steps of 1mT. For the measurement conducted under an out-of-plane magnetic field they were realized using a permanent magnet producing fields at the device of 100-300 mT depending on the distance.

In the setup in Figure *2.4.4*, the source meter is used for two purposes. It is used to measure the output voltage in the passive detection where no dc current is injected. In the case of active detection it also simultaneously injects a dc current (rf + dc).

It is noted that for these ST-FMR experiments, no lock-in amplification was used, unlike other reports in the literature on spin torque FMR [8], [76]. This choice is due to the application oriented approach of this work. The aim is to have a characterization with results as close as possible to that of an implemented diode.

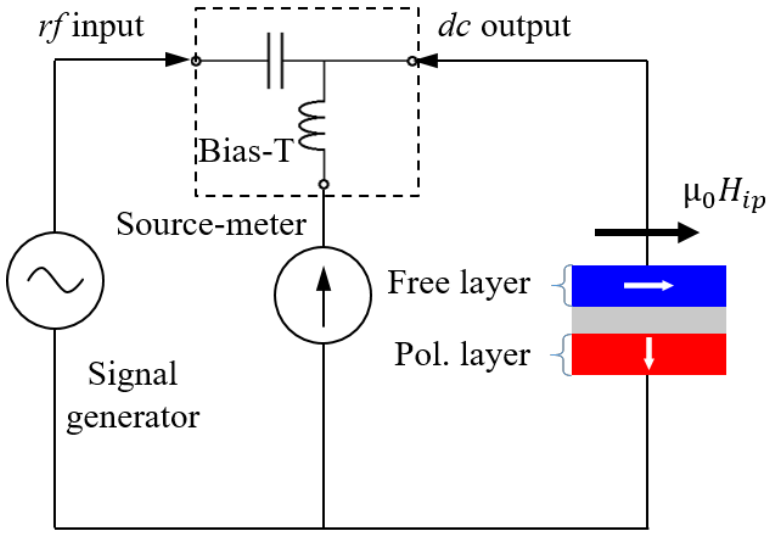

Figure 2.4.4 : Schematics of the spin torque FMR experimental setup

2.4.3 Spin torque rf generation setup

Another important setup for the electrical characterization of the magnetization dynamics is the thermal FMR, called here Spin torque rf generation setup. The thermal FMR complements the spin-torque nano-diode characterization.

It helps to understand the dynamic response of the MTJ layers prior to the injection of the rf current, and importantly in this work, it helped to quantify the Joule heating effect on the magnetization.

It works generally by injecting a weak dc current into the MTJ to read electrically, through the frequency response, the magnetization dynamics induced by thermal fluctuations. It is also used to characterize the auto-oscillation response of the MTJ by increasing the current above a critical threshold value to reach the auto-oscillation regime.

The experimental setup : The experimental setup of the thermal FMR, for an in-plane magnetic bias field, is shown Figure *2.4.5*. It consists of a current source (Keithley 2400) that generates the input dc current, which is injected into the MTJ nanopillar through the inductive port of the bias-Tee. The generated rf signal passes through the capacitive port of the bias-tee. Next, the generated rf signal is amplified using a low noise amplifier. The gain of amplifier used here was 43 dB. After amplification the signal is filtered from low frequency parasitic signals (radio/tv etc) by a high pass filter with a 1 GHz cutoff frequency. The amplified and filtered signal is subsequently fed to a power splitter that divides it into two parts. One part is measured on a spectrum analyzer for the frequency domain analysis, and the other part on a single shot oscilloscope for the time domain analysis. For the spectrum analyzer the resolution band width (RBW) was set to 1 MHz, and the frequency range was 1 GHz to 10 GHz. The FMR linewidths of the pMTJs are usually in the range of hundreds of MHz, therefore the choice of the RBW value here guaranties both the detection of neighboring FMR peaks and a faster measurement (small RBW implies slower sweeping time). For the oscilloscope, the aim is to acquire long time traces to have more accuracy on the signal noise, hence here the sampling rate was selected to be 50 Giga-samples/second, and the bandwidth was set to 16 GHz.

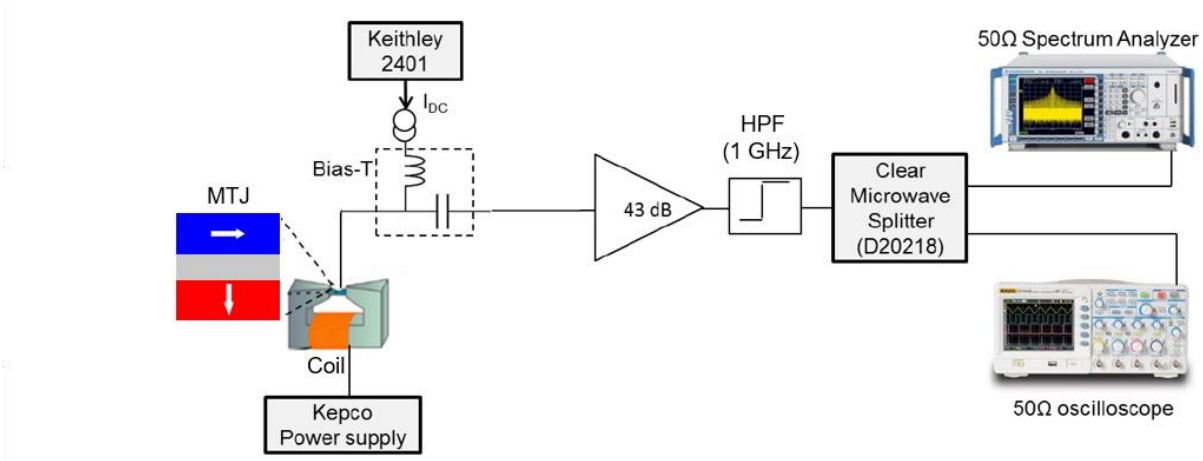

Figure 2.4.5 : The experimental setup of the thermal FMR measurements

Furthermore, an important point is the current sign convention at the sample level to interpret correctly the measurements. For all measurements we used special rf probes of the type GS (ground-signal) of 225µm pitch. The GS probes were placed on the contact pads such that the ground connector of the rf probe contacted the pad of the bottom device of the device, and the signal connector of the rf probe contacted the top electrode pad. Since the bottom electrode is in contact with the polarizing layer (PL) and the top electrode is in contact with the free layer (FL), the following sign convention applies: for positive current the electrons pass first by the polarizing layer and then to the free layer, and can excite the latter. Table 2.4.1 gives a summary of the current sign convention and shows which layer is excited for the case of the free layer and the polarizing layer being magnetized out-of-plane.

		I (A) > 0		I (A) < 0	
		Direct electrons	Reflected electrons	Direct electrons	Reflected electrons
Parallel state	□Free layer	Stabilized			Destabilized
	□Polarizing layer		Destabilized	Stabilized	
Antiparallel state	□Free layer	Destabilized			Stabilized
	□Polarizing layer		Stabilized	Destabilized	

Table 2.4.1 : The current sign convention used in this work, highlighting the STT action on the different layers

***Signal analysis and extraction* :** With the experimental measurements acquired, the next step is to revert, through a software, the modifications added to the signal amplitude by the setup, i.e. amplification or attenuation. The goal is to extract the real signal amplitude coming from the MTJ. The method adapted here to the correct the signal follows these steps :

- *Baseline correction* : The first step is to correct the rf setup noise (baseline) that occurs when sweeping the frequency. It is accomplished by initially measuring the amplified based line of the setup in a condition where the MTJ is not active (zero current and field), and then correct it. The correction starts by normalizing the baseline signal acquired in volt (Bl_0) by the RBW through the following formula :

$$Bl_{norm}(V^2/Hz) = \frac{(Bl_0)^2}{RBW} \tag{2.4.1}$$

and then correct the signal for the added gain from the setup, through the following formula :

$$Bl_{cor}\left(V^2/_{Hz}\right) = Bl_{norm} * 10^{-\frac{gain_{db}}{10}} \tag{2.4.2}$$

- *Spectrum correction:* The second step in the signal correction is the normalization of the measured MTJ signal by the RBW and the gains, similar to eq. 2.4.1 and 2.4.2. Finally, to obtain the power spectral density (PSD) of the device, the corrected baseline-

Bl_{cor} is subtracted from the corrected PSD signal PSD_{cor}: $PSD_{real} = PSD_{cor} - Bl_{cor}$.

- *Fitting the data:* Finally, to extract the center frequency, power and the linewidth of the measured peaks, the signals are fitted using a Lorentzian of the form :

$$Lorentz = \frac{y_0}{(x - x_c)^2 + w} + c \tag{2.4.3}$$

With linewidth equal to $2\sqrt{w}$, x_c the center frequency, and the power obtained via numerical integration of Eq. 2.4.3.

The whole correction procedure is automated using a python (or matlab) program.

Furthermore, the time domain measurements, using the oscilloscope were used to extract real amplitude and phase of the auto-oscillation signal and the corresponding noise spectra, see [31]. However, in this manuscript these studies are not presented.

2.5 Real-time measurements of the stochastic switching of the magnetization

Besides the rf studies in the frequency domain, discussed in Chapter 5 and 6, in Chapter 7 the studies are focused on the random switching of the magnetization, when the pMTJ is in a superparamagnetic state. The experimental characterization aims at acquiring longue real-time traces of the random switching of the magnetization to allow for more accurate statistical analysis. The times traces are measured for different voltages in order to understand how the STT affects the probability of switching of the magnetization.

The experimental setup used here to probe the magnetoresistance variations of the pMTJs in real time is illustrated in Figure *2.5.1*. It consists of a Stanford lock-in amplifier (V_{app}) in series with an ohmique resistance with a value R_0 = 850 Ω, and an oscilloscope in parallel to the MTJ device. The value of R_0 was chosen as the geometrical mean of the parallel and the antiparallel resistances ($\sqrt{R_p R_{ap}}$) to maximize the voltage difference between the two. It was obtained by first expressing the difference in voltage around R_0 in the two cases given by :

$$V_{diff} = \left(\frac{R_0}{R_p + R_0} - \frac{R_0}{R_{ap} + R_0}\right) V_{app} \tag{2.5.1}$$

Thereafter the derivative of V_{diff} with respect to the resistance R_0 is calculated and set to zero, $dV_{diff}/dR_0 = 0$, to extract the maximum resistance. The maximum resistance obtained is exactly the geometrical mean given by : $R_{0_{max}} = \sqrt{R_p R_{ap}}$.

The output voltage of the MTJ is measured using a Tektronix MSO46 oscilloscope that has an input impedance of 1 MΩ and a bandwidth of 10 GHz. The time constant of the setup is estimated to be $\tau_{Rc} \approx 100$ ns. It arises from the parasitic capacitances of the different components of the setup, including the MTJ stack. To minimize the time constant, in this work, short rf cables were used (~ 1 meter), and no filters or other additional rf components were used.

Moreover, to avoid voltage reading errors caused by the time constant, the oscilloscope time-step was selected to be 16 ns/pts to ensure that it is at least five times smaller than the time constant of the setup. In addition, for each voltage point, the magnetoresistance was recorded for at least 1000 seconds, equivalent to 10 million transitions, to have more accurate statistics.

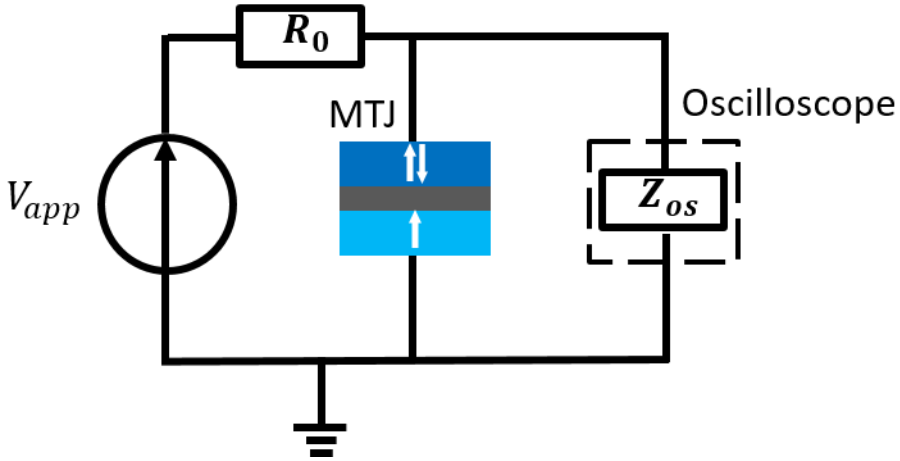

Figure 2.5.1 : The experimental setup used in real-time measurements of the magnetoresistance variation with current (voltage).

Data processing: Once the experimental data have been acquired, the next step is to process and plot the data. The size of the registered data from these measurements is around 4 Tb, with 15 Gb in each file separately. The first step in the analysis, after getting a computer with more than 32 Gb RAM, is to plot the data, as in Figure *2.5.2*(a), and then numerically extract the dwell times of the AP and P states (τ_{ap} and τ_P). The latter represent the time that the magnetization takes before switching to another state. It is extracted numerically by fixing a threshold resistance around 70% of the R_{ap} and monitoring when the resistance goes below or above this threshold. After the extraction of the dwell times their cumulative distribution functions (CDF) are plotted and fitted by the following exponential distribution :

$$CDF(t) = 1 - e^{-\lambda_{p/ap} t} \tag{2.5.2}$$

with $\lambda_{p/ap} = 1/\tau_{p\_ap}$, see Figure *2.5.2*(b). The fitting allows the extraction of the value of τ_{ap} and τ_p and to plot the probability of stabilizing the AP state defined as :

$$P_{ap} = \frac{<\tau_{ap}>}{<\tau_{ap}> - <\tau_p>} \tag{2.5.3}$$

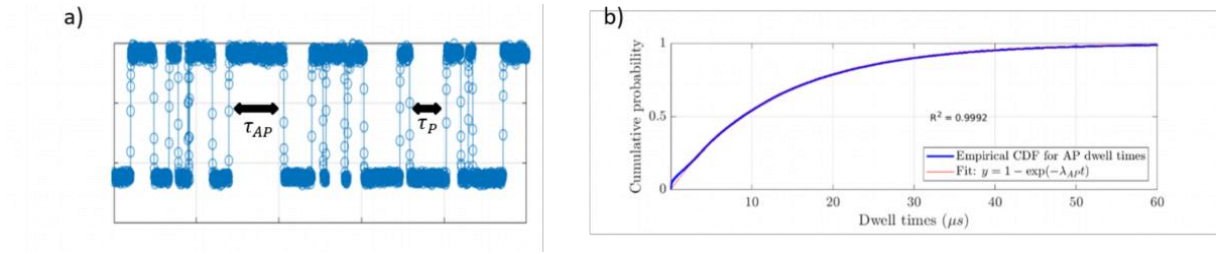

Figure 2.5.2 : (a) An example of a time trace of the stochastic switching of the MTJs. The dwell times are highlighted in black. (b) The plot of the CDF of the dwell times obtained numerically by counting the switching (in blue) and its exponential fit (in red).

Conclusion

In conclusion, the pMTJs studied here are bottom pinned MTJs with a resistance-area (RA) product of $\sim 10\ \Omega.\mu m^2$ and a TMR of $\sim$100 %.

The different experimental techniques used for the static and the dynamic measurements of the pMTJs are : the VSM for the continuous films, the automatic MR tester and PPMS for the static MR characterization of the nanopillars, the deembedding and the ST-FMR for the characterization of the rf-to-dc conversion, the generation setup for characterization of the thermal FMR power spectral densities, and finally the real-time experiments to register the voltage time-traces for the superparamagnetic state.

The results obtained using these experimental setups will be presented in chapter 4 for the static measurements, chapter 5 and 6 for the dynamic measurements, and chapter 7 for the real-time measurements.

Before proceeding to these results, in the next chapter all the theoretical concepts and equations used throughout this work will be presented.

Theoretical analysis of the static and dynamic responses of the pMTJ

This chapter is dedicated to the derivation of formulas and equations needed to understand the physics and/or used to fit the experimental data of this thesis (chapter 4 to chapter 7). The pMTJs under investigation are modelled using a macrospin approach, for three different operating regimes:

- **Static**: The static equilibrium position is derived as a function of the bias applied magnetic field. It provides the reorientation of the magnetization as a function of the field magnitude and direction. By fitting the hysteresis loops it gives a good estimation of the interfacial perpendicular magnetic anisotropy. Furthermore, the obtained static equilibrium positions are the starting point for evaluating the FMR resonance excitations.
- **Dynamic**: The underlying dynamics of the spin-torque nano-diode effect is the ferromagnetic resonance, and hence its derivation and analysis will be needed to investigate the produced dc voltage signal. For this, the dynamic susceptibility expressions will be derived for excitation via spin transfer torque provided by an rf current. The analysis is extended to include the FMR response of the polarizing layer, by including its exchange coupling to the synthetic antiferromagnet.
- **Stochastic**: The stochastic switching of the magnetization, discussed in chapter 7, is generally described by the Neel-Brown model. Here, its derivation from the Fokker-Planck equation is presented followed by an adaptation for the field-free switching demonstrated in this work. The developed model is used in chapter 7 to fit the experimental data and provides explanations for the results and how to improve them.

3.1 Static equilibrium of the Free (or Polarizing) layer

3.1.1 Total energy density and effective field

In a uniformly magnetized ferromagnetic layer, with a uniaxial anisotropy, the static equilibrium state of the magnetization is determined by minimizing the total energy density expressed by :

$$E_t = E_u + E_d + E_{int} + E_{bias} \tag{3.1.1}$$

with E_u the uniaxial magnetic anisotropy energy density, E_{dem} the demagnetizing self-energy density, E_{int} the energy density due to interaction between layers (dipolar or exchange) and E_{bias} the energy density from an external magnetic bias field.

In most situations, we use spherical coordinates, for which the magnetization can be expressed as $\vec{m}_{FL} = \frac{\vec{M}_{FL}}{M_s} = \begin{pmatrix} \sin(\theta) * \cos(\varphi) \\ sin(\theta) * \sin(\varphi) \\ \cos(\theta) \end{pmatrix}$, with M_s the saturation magnetization and θ and φ the azimuthal and zenith angles of the free layer magnetization, see Figure *3.1.1*.

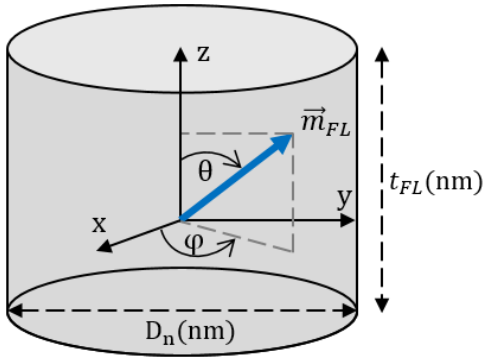

Figure 3.1.1: Illustration of the spherical coordinates of the free layer magnetization (in blue)

The corresponding expressions of the energy densities in spherical coordinates in SI units, are listed below:

1. Considering only interface perpendicular magnetic anisotropy (iPMA), as is the case for the pMTJs, the energy density is given by :

$$E_u = \frac{K_i}{t} * (1 - (\vec{m}_{FL}.\vec{n})^2) = \frac{K_i}{\mathrm{t}} * (1 - (\cos(\theta))^2) \qquad (3.1.2)$$

with K_i the energy constant of the interfacial perpendicular magnetic anisotropy in J/m² and $\vec{n} = \begin{pmatrix} 0 \\ 0 \\ 1 \end{pmatrix}$ the unit vector of the anisotropy direction. For t it is the thickness of the magnetic layer.

2. The self-demagnetizing energy density is defined as:

$$E_d = \frac{\mu_0}{2} M_s^2 \left(\vec{m}_{FL}.\bar{\bar{N}}.\vec{m}_{FL}\right) \qquad (3.1.3)$$

with $\bar{\bar{N}} = \begin{pmatrix} N_x & 0 & 0 \\ 0 & N_y & 0 \\ 0 & 0 & N_z \end{pmatrix}$ the demagnetizing tensor.

In general, the computation of the demagnetizing tensor is the most cumbersome, but for simple geometries (cylinders, cubes, thin films, disks etc.) it can be computed using the formulas of Rhodes and Rowlands [86], [87]. For infinitely thin films we have $N_x = N_{yy} = 0$ and $N_z = 1$, while for finite sized circular elements one has $N_z < 1$ and $N_x = N_y = (1-N_z)/2$.

3. The ferromagnetic layers inside a magnetic stack can interact via dipolar or exchange interaction (exchange coupling to an antiferromagnetic layer or interlayer exchange coupling, as it occurs in $(Co/Pt)_n$ multilayers or Co/Ru/Co trilayers). The corresponding energy density, for instance for the free layer due to dipolar stray fields arising from other layers, is expressed as [24], [40], [88]:

$$E_{int} = E_{dipolar} = -\mu_0 M_s\left(\vec{m}_{FL}.\vec{H}_{dipolar}\right) \tag{3.1.4}$$

In general the dipolar interaction field $\vec{H}_{dipolar}$ can be calculated in different ways. As will be shown in chapter 4, for the description of the free layer, such a dipolar stray field will arise from an unsaturated SAF. Considering the SAF to be fixed and oriented out-of-plane, i.e. its orientation does not change with an external applied bias field H_{bias}, the corresponding dipolar field is constant and adds to the external bias field. Its value is estimated from the offset of the out-of-plane hysteresis loops (see section 4.2 of chapter 4 for details).

$$\vec{H}_{dip} = \left(0,0,H_{dip}\right) \tag{3.1.5}$$

For the exchange interaction energy between the magnetic layers is expressed by [89], [90]:

$$E_{ex} = -J_r\vec{m}_1\vec{m}_2 \tag{3.1.6}$$

where $\vec{m}_1$ and $\vec{m}_2$ the magnetizations of the coupled layer, and $J_r = \frac{J_{rkky}}{\mu_0 M_s t}$ is the interlayer exchange coupling energy density.

Since the interaction fields relevant for this thesis have only an out of plane component, they are refered to as $\vec{H}_{int} = (0,0,H_{int\perp})$

4. The last term to consider for the total magnetic energy density due to an external bias magnetic field is:

$$E_{bias} = -\mu_0 M_s\left(\vec{m}.\vec{H}_{bias}\right) \tag{3.1.7}$$

where the bias field can be applied at any direction $\vec{H}_{bias} = \left\|\vec{H}_{bias}\right\|\begin{pmatrix}\sin(\theta_b) * \cos(\varphi_b)\\ sin(\theta_b) * \sin(\varphi_b)\\ \cos(\theta_b)\end{pmatrix}$. In the experiments discussed in this work, the bias field is applied either in the film plane along the x axis ($\theta_b = \frac{\pi}{2}, \varphi_b = 0$) which is referred to as $H_\parallel$ or out of plane ($\theta_b = 0, \varphi_b = 0$) which is referred to as $H_\perp$.

With this the total magnetic energy density E_t of Eq. 3.1.1 takes the following form in spherical coordinates (for cylindrical layer):

$$\begin{aligned} E_t(\theta,\varphi) = \frac{K_i}{t_{FL}} + \frac{\mu_0 M_s^2}{2}\left[N_x cos(\varphi)^2 + N_y sin(\varphi)^2\right] - \\ \left[\frac{K_i}{t_{FL}} + \frac{\mu_0 M_s^2}{2}\left[N_x cos(\varphi)^2 + N_y sin(\varphi)^2 - N_z\right]\right] * \cos(\theta)^2 \\ - \mu_0 M_s[H_{\parallel} * \sin(\theta) * \cos(\varphi) - (H_{\perp} + H_{int\perp}) * \cos(\theta)] \end{aligned} \tag{3.1.8}$$

For a cylindrical layer where $N_x = N_y$, Eq. 3.1.8 is simplified to the form :

$$\begin{aligned} E_t(\theta,\varphi) = \frac{K_i}{t_{FL}} + \frac{\mu_0 M_s^2}{2}\left[N_x + N_y\right] - \frac{\mu_0 M_s}{2} * H_{ueff} * \cos(\theta)^2 \\ - \mu_0 M_s[H_{\parallel} * \sin(\theta) * \cos(\varphi) - (H_{\perp} + H_{int\perp}) * \cos(\theta)] \end{aligned} \tag{3.1.9}$$

where $H_{ueff} = H_u - H_d$ the effective magnetic anisotropy field, with $H_u = \frac{2(K_i/t_{FL})}{\mu_0 M_s}$, and $H_d = M_s * (N_z - N_x - N_y)$.

To analyze how the different terms of the total energy density affect the magnetization dynamics it is convenient derive from it the effective magnetic field $\vec{H}_{eff}$, and analyze the torque that it exerts on the magnetization. The effective magnetic field is defined by the negative gradient of the total energy density with respect to the magnetization and is correspondingly the vector summation of different fields:

$$\vec{H}_{eff} = -\frac{1}{M_s}\frac{\partial E_t(\theta,\varphi)}{\partial \vec{m}} = \vec{H}_{ueff} + \vec{H}_{int\perp} + \vec{H}_{\perp} + \vec{H}_{\parallel} \tag{3.1.10}$$

The torque exerted by the effective magnetic field will drive the magnetization to precess around it, and the magnetization dynamics in this case can be expressed via the torque equation given by:

$$\frac{\partial \vec{m}}{\partial t} = -\gamma\left(\vec{m} \times \vec{H}_{eff}\right) \tag{3.1.11}$$

with γ the gyromagnetic factor in $\frac{GHz}{T}$ (~28). This expression defines the pressesion without any losses, while it is well known from experiments that the magnetization displays a damped precession towards $\vec{H}_{eff}$. The full torque equation which is the Landau-Lifshitz-Gilbert equation (LLG) has therefore additional terms that were already presented in chapter 1 in the section 1.1.5. However, the analysis of the magnetization dynamics, in the first place, requires the knowledge of the equilibrium position of the magnetization. The method used in this thesis to determine the latter is presented in the following subsection.

3.1.2 Equilibrium position of the magnetization as a function of the bias field

To determine the magnetization equilibrium position, the initial step is to minimize the total energy density of Eq. 3.1.9. This is done by determining the critical points (θ_o, φ_o) for which the first derivatives of the energy density $E_{t_\varphi}(\theta,\varphi) = \frac{\partial E}{\partial \varphi}$, $E_{t_\theta}(\theta,\varphi) = \frac{\partial E_t}{\partial \theta}$ with respect to (θ,φ) are equal to zero [91]. Once the critical points are obtained, they are tested for their stability by computing the determinant *Det* of the second derivatives matrix (Hessian matrix). If the determinant of the Hessian matrix (see Eq. 3.1.12) at (θ_o, φ_o) is positive then the total energy has a local minimum or maximum at that critical point, otherwise if the determinant is negative then this corresponds to a saddle point there[91].

$$Det(Hessian) = E_{t_{\theta\theta}}(\theta,\varphi) * E_{t_{\varphi\varphi}}(\theta,\varphi) - E_{t_{\varphi\theta}}(\theta,\varphi) * E_{t_{\theta\varphi}}(\theta,\varphi) \tag{3.1.13}$$

where $E_{t_{\theta\theta}} \equiv \partial^2 E_t/\partial\theta^2$, $E_{t_{\varphi\varphi}} \equiv \partial^2 E_t/\partial\varphi^2$ and $E_{t_{\varphi\theta}} \equiv \partial^2 E_t/\partial\theta\partial\varphi$ are the second order partial derivatives.

To determine whether the solution is a minimum, the second derivatives of the total energy density $E_{t_{\theta\theta}}$ and $E_{t_{\varphi\varphi}}$ at the critical points need to be positive. When they are negative, the critical point corresponds to a maximum.

The partial derivatives of the total magnetic energy density in Eq. 3.1.9, for both spherical angles are the following :

- First order partial derivatives :

$$E_{t_\varphi}(\theta,\varphi) = \mu_0 M_s * H_\parallel * sin(\theta) * sin(\varphi) = 0 \rightarrow \varphi_0 = \{0\,;\pi\} \tag{3.1.14}$$

$$E_{t_\theta}(\theta,\varphi) = \mu_0 M_S * [\, H_{ueff} * cos(\theta) * sin(\theta) - H_\parallel * cos(\theta) * cos(\varphi) + (H_\perp + H_{int\perp}) * \sin(\theta)] = 0 \tag{3.1.15}$$

- Second order partial derivatives :

$$E_{t_{\varphi\varphi}}(\theta,\varphi) = \mu_0 M_s * H_\parallel * sin(\theta) * cos(\varphi) \tag{3.1.16}$$

$$E_{t_{\theta\theta}}(\theta,\varphi) = \mu_0 M_S * [\, H_{ueff} * cos(2\theta) + H_\parallel * sin(\theta) * cos(\varphi) + (H_\perp + H_{int}) * \cos(\theta)] \tag{3.1.17}$$

$$E_{t_{\theta\varphi}}(\theta,\varphi) = \mu_0 M_s * H_\parallel * sin(\theta) * cos(\varphi) \tag{3.1.18}$$

Unlike Eq. 3.1.13, the solution of Eq. 3.1.12 is not straightforward when both in-plane fields $H_\parallel$ and $(H_\perp + H_{int})$ are present. To solve it for this general case, all the trigonometric functions in Eq. 3.1.15 are transformed to $\cos(\theta)$ to have a single variable $X = \cos(\theta)$.

The transformation allows Eq. 3.1.15 to be rewritten as :

$$E_{t_\theta}(\theta,\varphi) = H_{ueff} * X * \sqrt{1-X^2} - H_{\parallel} * \cos(\varphi) * X + (H_{bias\perp} + H_{int\perp}) * \sqrt{1-X^2} = 0 \quad (3.1.19)$$

Then, Eq. 3.1.19 is transformed algebraically to remove the square root terms, yielding the following 4th order polynomial :

$$X^4 + c_3 * X^3 + c_2 * X^2 + c_1 * X + c_0 = 0 \quad (3.1.20)$$

where $c_3 = 2 * \frac{(H_\perp + H_{dip})}{H_{ueff}}$, $c_2 = \left(\frac{c_3}{2}\right)^2 + \left(\frac{H_\parallel * \cos(\varphi)}{H_{ueff}}\right)^2 - 1$, $c_1 = -c_3$, $c_0 = -\left(\frac{c_3}{2}\right)^2$.

This 4th order polynomial of Eq. 3.1.19 is solved analytically using the Ferrari method [92], which consists of a variable transformation of the sort $Y = X - \frac{c_3}{4}$. After some tedious algebraic developments, the solutions to Eq. 3.1.15 are obtained by the four roots of the polynomial in Eq. 3.1.20 and are noted here by :

$$\theta_0 = \{\cos^{-1}(X_0), \cos^{-1}(X_1), \cos^{-1}(X_2), \cos^{-1}(X_3)\} \quad (3.1.21)$$

The full formulas of the roots $X_{0,1,2,3}$ are given in Annex A.

The critical angles obtained in Eq. 3.1.21, are finally inserted into the second derivatives in Eq. 3.1.16 and Eq. 3.1.17 to determine the minimum equilibrium angle. The latter represents the static orientation of the magnetization.

The method developed here allows to obtain the magnetization equilibrium position in the presence of magnetic fields with two field components $H_\parallel$ and $H_\perp$.

3.2 Magnetization dynamics under a subcritical spin polarized dc current

To understand the action of the spin transfer torque in pMTJs, in this section we first analyze the magnetization response to a spin polarized dc current to determine an expression of the threshold or critical current, where the static equilibrium position becomes unstable.

The starting point is the Landau-Lifshitz-Gilbert (LLG) equation[59], [60] including both spin torque terms, see Chapter 1(section 1.1.5) :

$$\frac{\partial \vec{m}}{\partial t} = -\gamma\left(\vec{m} \times \vec{H}_{eff}\right) + \alpha\left(\vec{m} \times \frac{\partial \vec{m}}{\partial t}\right) - \gamma\, a_\parallel\, \vec{m} \times (\vec{m} \times \vec{p}) + \gamma\, a_\perp\, \vec{m} \times \vec{p} \quad (3.2.1)$$

In order to determine the threshold current of instability, the LLG equation will be linearized.

In the case of the pMTJs, with a perpendicular polarizer the polarization vector is $\vec{p}$ = (0,0,1) and a perpendicular free layer, and considering of a slight non-collinearity between the two, the cross products in Eq. 3.2.1 give :

$$\begin{pmatrix}\dot{m}_x\\ \dot{m}_y\\ \dot{m}_z\end{pmatrix} = \gamma\begin{pmatrix} -\left(H_\perp - H_{ueff}\right)m_y + H_{bias_y}m_z + \frac{\alpha}{\gamma}m_y\dot{m}_z - \frac{\alpha}{\gamma}m_z\dot{m}_y - a_\parallel m_x m_z + a_\perp m_y \\ -H_{||}m_z + \left(H_\perp - H_{ueff}\right)m_x + \frac{\alpha}{\gamma}m_z\dot{m}_x - \frac{\alpha}{\gamma}m_x\dot{m}_z - a_\parallel m_y m_z - a_\perp m_x \\ -H_{||}m_x + H_{||}m_y + \frac{\alpha}{\gamma}m_x\dot{m}_y - \frac{\alpha}{\gamma}m_y\dot{m}_x - a_\parallel(1-m_z^2)\end{pmatrix} \quad (3.2.2)$$

with $\dot{m} = \frac{\partial m}{\partial t}$, and H_{bias_y} is the bias field along the y axis. Here the interaction field $H_{int\perp}$ was included in the out-of-plane bias field $H_\perp$.

For small perturbations the magnetization in the out-of-plane direction is stable (or metastable) and can be approximated to $m_z = \pm 1$ (P, AP) [93]–[95]. Including this in Eq. 3.2.2 allows the projection of the magnetization dynamics to the x-y plane given by :

$$\begin{pmatrix}\dot{m}_x\\ \dot{m}_y\end{pmatrix} = \gamma\begin{pmatrix} -\left(H_\perp - H_{ueff}\right)m_y + a_\perp m_y \mp \frac{\alpha}{\gamma}\dot{m}_y \mp a_\parallel m_x \pm H_{bias_y} \\ \mp H_{||} + \left(H_\perp - H_{ueff}\right)m_x - a_\perp m_x \pm \frac{\alpha}{\gamma}\dot{m}_x \mp a_\parallel m_y\end{pmatrix} \quad (3.2.3)$$

The separation of variables, by replacing $\dot{m}_x$ and $\dot{m}_y$ in the right side of Eq. 3.2.3, gives the following non-homogenous set of ordinary differential equations :

For $m_z = +1$, Eq. 3.2.3 becomes :

$$\begin{pmatrix}\dot{m}_{x+}\\ \dot{m}_{y+}\end{pmatrix} = \bar{\bar{N}}\begin{pmatrix}m_{x+}\\ m_{y+}\end{pmatrix} + \begin{pmatrix}h_x\\ h_y\end{pmatrix} \quad (3.2.4)$$

With the matrix,

$$\bar{\bar{N}} = \begin{pmatrix}\left[-a_\parallel - \alpha\left(H_\perp - H_{ueff} - a_\perp\right)\right] & \left[-H_\perp + H_{ueff} + a_\perp + \alpha a_\parallel\right] \\ \left[H_\perp - H_{ueff} - a_\perp - \alpha a_\parallel\right] & \left[-a_\parallel - \alpha\left(H_\perp - H_{ueff} - a_\perp\right)\right]\end{pmatrix} \quad (3.2.5)$$

and $h_x = -\alpha H_{H_{bias_y}} + H_{bias_y}$, and $h_y = -H_{H_{bias_y}} - \alpha H_{bias_y}$.

The second term in Eq. 3.2.4 is related to the stationary solution (when Eq. 3.2.4 = 0) and can be written in the form :

$$\begin{pmatrix}h_x\\ h_y\end{pmatrix} = \bar{\bar{N}}\begin{pmatrix}m_{x0+}\\ m_{y0+}\end{pmatrix} \quad (3.2.6)$$

With this definition Eq. 3.2.4 can be homogenized by a variable change such as defining a vector $\vec{U} = \vec{m}_+ + \vec{m}_{+0}$, hence the magnetization dynamics around the equilibrium in Eq. 32 is expressed by

$$\begin{pmatrix} \dot{U}_{x+} \\ \dot{U}_{y+} \end{pmatrix} = \bar{\bar{N}} \begin{pmatrix} U_{x+} \\ U_{y+} \end{pmatrix} \tag{3.2.7}$$

The analytic solution to the equation Eq. 3.2.7 is straightforward (using Laplace transform or variable separation), and it requires the diagonalization of the matrix $\bar{\bar{N}}$ [96]. Once the latter is done, the eigenvalues obtained are the following :

$$\lambda_{1,2} = \frac{\gamma}{1+\alpha^2} * (A_+ \pm iB_+) \tag{3.2.8}$$

where $A_+ = \left[-a_\parallel - \alpha\left(H_\perp - H_{ueff} - a_\perp\right)\right]$, and $B_+ = \left[-H_\perp + H_{ueff} + a_\perp + \alpha a_\parallel\right]$.

In addition, their corresponding eigenvectors are $W_{1,2} = (1, \pm i)$. The general solution of Eq. 3.2.4 is thus,

$$\begin{pmatrix} U_{x+} \\ U_{y+} \end{pmatrix} = k_1 \begin{pmatrix} 1 \\ i \end{pmatrix} e^{\lambda_1 * t} + k_2 \begin{pmatrix} 1 \\ -i \end{pmatrix} e^{\lambda_2 * t} \tag{3.2.9}$$

where k_1 a k_2 are constants that depend on the initial conditions.

The complex numbers in the eigenvectors imply that the solution in Eq. 3.2.9 is a set of oscillating functions (sine and cosine), also called spirals. The stability of the solution depends on the real part of the eigenvalues $Re\left(\lambda_{1,2}\right) = A_+$. If A_+ is negative the initial state $m_z = +1$ is stable and the perturbed magnetization will spiral back to its equilibrium position (damped oscillations). However, if A_+ is positive the solution diverges due to the increase of the amplitude with time, and thus the magnetization initial state becomes unstable.

Hence, the magnetization stability condition can be written as follows :

$$Re\left(\lambda_{1,2}\right) = -a_\parallel - \alpha\left(H_\perp - H_{ueff} - a_\perp\right) < 0 \tag{3.2.10}$$

Due to the STT this stability condition will change with the current density *J* since $a_\parallel \sim J$. This is illustrated in Figure *3.2.1*, where the phase portrait is plotted for strong negative current in (a), zero current in (b), and strong positive current in (c).

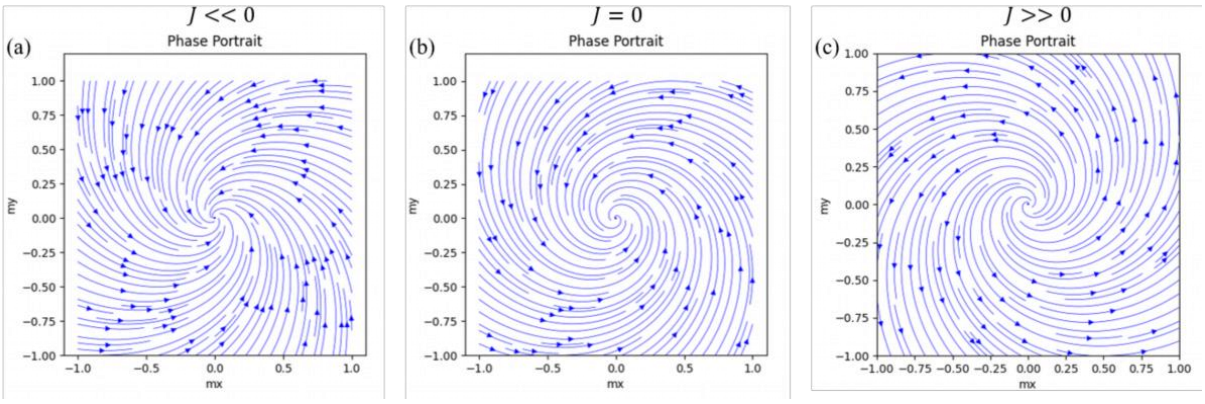

Figure 3.2.1 : (a) the phase portrait of Eq. 3.2.4 for a strong negative current (the value was chosen arbitrarily). (b) the same as (a) but for zero current. (c) the phase portrait of Eq. 3.2.4 for a strong positive current (the value was chosen arbitrarily).

Comparing the zero current phase portrait with the high negative current, shows that the negative current increases the magnetization relaxation rate, while for the high positive current the magnetization equilibrium becomes unstable above a certain threshold current density and the solution diverges.

To extract the critical current density $J_{c_\pm}(J_{c_{P\leftrightarrow AP}})$ at which the magnetization becomes unstable, $a_\parallel$ in Eq. 3.2.10 is replaced by its formula and Eq. 3.2.10 is solved for the current density, which gives

$$J_{c_{P\to AP}} = -\frac{2e}{\hbar} * \frac{\mu_o M_s t_{FL}}{\eta} * \alpha * \left(H_\perp - H_{ueff}\right) * \frac{1}{(1-\alpha\beta)} \tag{3.2.11}$$

$$J_{c_{AP\to P}} = -\frac{2e}{\hbar} * \frac{\mu_o M_s t_{FL}}{\eta} * \alpha * \left(H_\perp + H_{ueff}\right) * \frac{1}{(1+\alpha\beta)} \tag{3.2.12}$$

Above these critical currents, the critical points of the magnetization is becomes unstable.

Finally, in addition to the definition of the critical currents, it is important to compute the magnetization relaxation time, following a perturbation. For the spin-torque nano-diodes, this relaxation time is where the transient and the stationary solutions mix and no net dc voltage is produced. For the pMTJs the magnetization relaxation time is given by :

$$\tau_r = \frac{1}{Re(\lambda_{1,2})} = \frac{1+\alpha^2}{\gamma\left[a_\parallel + \alpha\left(H_\perp - H_{ueff} - a_\perp\right)\right]} \tag{3.2.13}$$

In the passive case ($a_\parallel = a_\perp = 0$), and for typical MTJ parameters, such as $\alpha = 0.01$, $\gamma = 28$ GHz/T [17], and for $(H_{ueff} - H_\perp) \approx 40\ mT$ from the magnetoresistance fitting in chapter 4, the relaxation time is $\tau_r \approx 90\ ns$ ($\frac{1}{\tau_r}$ ≈11 MHz).

3.3 The free layer magnetization dynamics excited by a spin polarized rf current

The goal of this section, is to have at hand the theoretical expressions of the precession amplitude of the ferromagnetic resonance (FMR) of the free layer oscillations in the pMTJ, when excited by an rf spin polarized current. This amplitude will depend on the device shape via the demagnetization factors, the interfacial perpendicular magnetic anisotropy (iPMA), and the spin transfer torque prefactor. Together, with the TMR, they are the most important terms in the derivation of the dc voltage produced by the spin-torque nano-diodes as will be described in the section 3.5.

The theoretical treatment is based on the macrospin model, and uses the linearization approach to obtain an expression of the precession amplitude of the resonance excitations. This approach is justified, since the amplitudes of the resonance excitations remain small. This would be different for large angle steady state auto-oscillations excited under spin polarized dc currents.

The free layer magnetization dynamics, in the presence of an rf excitation current, is described by Eq. 3.2.1, i.e. the Landau-Lifshitz-Gilbert equation [59], [60] including the Slonczewski spin torque terms for an rf current [15].

Different to the previous section, here for convenience the solutions of the linearized LLG equation are derived in the local coordinate system using spherical coordinates [97]. The magnetization dynamics is considered as a small perturbation around the equilibrium, and defined as :

$$\vec{m} = \vec{m}_0 + \partial\vec{m} \tag{3.3.1}$$

where $\vec{m}_0 = \frac{1}{M_S}\begin{pmatrix} M_S \\ 0 \\ 0 \end{pmatrix}$ is the magnetization vector at equilibrium, and $\partial\vec{m} = \frac{1}{M_S}\begin{pmatrix} 0 \\ \delta m_\theta \\ \delta m_\varphi \end{pmatrix}$ is the dynamic magnetization. See Figure *3.3.1* below for the angles θ and φ.

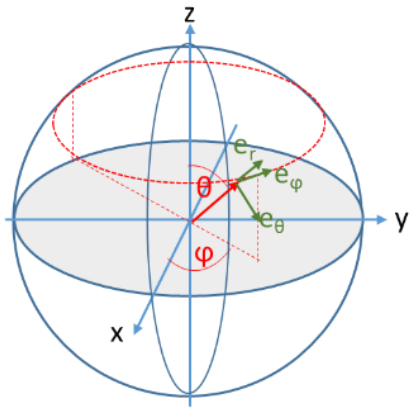

Figure 3.3.1 : Illustration of the local spherical coordinates

As a consequence, the analysis of the perturbed magnetization can be done by projecting the linearized LLG equation into the local plane $m_\theta - m_\varphi$.

The rf excitation is given by the current density $J\left(\frac{A}{m^2}\right) = J_0 * \mathrm{e}^{\mathrm{i}\omega t}$ with $\frac{\omega}{2\pi}$ its frequency and J_0 it's amplitude. It determines the excitation 'field' through the STT terms defined as :

$$\overline{\overline{STT}} = J_0 * [\tilde{a}\vec{m} \times (\vec{m} \times \vec{p}) + \tilde{\alpha}\,\beta\vec{m} \times \vec{p}] \tag{3.3.2}$$

After carrying out all the cross products in the linearized LLG and the Taylor expansion of the effective field, Eq. 3.3.2 takes the following form :

$$\begin{pmatrix} \delta\dot{m}_\theta \\ \delta\dot{m}_\varphi \end{pmatrix} = \begin{pmatrix} \frac{-E_{\theta\varphi}}{M_s \sin(\theta)}\delta m_\theta + \left(\frac{-E_{\varphi\varphi}}{M_s \sin(\theta)^2}\,\delta m_\varphi - \frac{\alpha}{\gamma}\delta\dot{m}_\varphi\right) \\ \left(\frac{+E_{\theta\theta}}{M_s}\delta m_\theta + \frac{\alpha}{\gamma}\delta\dot{m}_\theta\right) + \frac{E_{\theta\varphi}}{M_s \sin(\theta)}\delta m_\varphi \end{pmatrix} + \mathrm{e}^{\mathrm{i}\omega t} * \overline{\overline{STT}} * \begin{pmatrix} p_\theta \\ p_\varphi \end{pmatrix} \tag{3.3.3}$$

The second derivatives of the energy density in Eq. 3.3.3 are those provided in Eq. 3.1.11-15, and for the excitations arising from the spin transfer torque terms, the cross product gives the excitation matrix $\overline{\overline{STT}} = J_0 * \tilde{a} * \begin{pmatrix} 1 & \beta \\ -\beta & 1 \end{pmatrix}$. In Eq. 3.3.3 all the second order terms were neglected due to their small values, i.e. terms ~ $(\delta m_\theta * \delta m_\varphi)$ and α^2 are set to zero.

To solve Eq. 3.3.3, based on the steady state solutions of forced damped systems, a good solution guess (Ansatz) is :

$$\begin{pmatrix} \delta m_\theta \\ \delta m_\varphi \end{pmatrix} = \mathrm{e}^{\mathrm{i}(\omega t)} * \begin{pmatrix} A_\theta \\ A_\varphi \end{pmatrix} \tag{3.3.4}$$

where $\frac{\omega}{2\pi}$ is the frequency of the injected current, ϕ the phase difference between the oscillations of the magnetization and those of the current. For A_θ and A_φ they are the solution amplitudes of the θ and φ components respectively. Inserting Eq. 3.3.4 into Eq. 3.3.3, and carrying out the algebra development, gives :

$$\begin{pmatrix} A_\theta \\ A_\varphi \end{pmatrix} = \bar{\bar{\chi}} * \left[\overline{\overline{STT}} * \begin{pmatrix} p_\theta \\ p_\varphi \end{pmatrix}\right] \tag{3.3.5}$$

where $\bar{\bar{\chi}}$ is the susceptibility tensor corresponding to the variation of the magnetization with the forcing 'field' from the spin transfer torque.

It is given by :

$$\bar{\bar{\chi}} = \frac{1}{det\bar{\bar{R}}}\begin{pmatrix} \left(\frac{i\omega}{\gamma} - \frac{E_{\theta\varphi}}{M_s \sin(\theta)}\right) & -\left(\frac{i\omega}{\gamma}.\alpha + \frac{E_{\varphi\varphi}}{M_s \sin(\theta)^2}\right) \\ \left(\frac{i\omega}{\gamma}.\alpha + \frac{E_{\theta\theta}}{M_s}\right) & \left(\frac{i\omega}{\gamma} + \frac{E_{\theta\varphi}}{M_s \sin(\theta)}\right) \end{pmatrix} \tag{3.3.6}$$

The multiplication of the matrices $\bar{\bar{\chi}}$ and $\overline{\overline{STT}}$, gives:

$$\bar{\bar{\chi}} * \overline{\overline{STT}} = \frac{1}{det\bar{\bar{R}}}\begin{pmatrix} \left(\frac{i\omega}{\gamma} - \frac{E_{\theta\varphi}}{M_s \sin(\theta)}\right) & -\left(\frac{i\omega}{\gamma}.\alpha + \frac{E_{\varphi\varphi}}{M_s \sin(\theta)^2}\right) \\ \left(\frac{i\omega}{\gamma}.\alpha + \frac{E_{\theta\theta}}{M_s}\right) & \left(\frac{i\omega}{\gamma} + \frac{E_{\theta\varphi}}{M_s \sin(\theta)}\right) \end{pmatrix} \begin{pmatrix} 1 & \beta \\ -\beta & 1 \end{pmatrix} \tag{3.3.7}$$

with $det\bar{\bar{R}}$ the determinant of the matrix $\bar{\bar{\chi}}^{-1}$ that can be written as $\frac{1}{det\bar{\bar{R}}} = \big(A(\omega) - \mathrm{i}\, S(\omega)\big) = Ze^{i\sigma}$, where $A(\omega) = \frac{(\omega_0^2 - \omega^2)}{(\omega_0^2 - \omega^2)^2 + (\omega\Delta\omega_0)^2}$ is an antisymmetric Lorentzian, and $S(\omega) = \frac{\omega\Delta\omega_0}{(\omega_0^2 - \omega^2)^2 + (\omega\Delta\omega_0)^2}$ is a symmetric Lorentzian. $\frac{\omega_0}{2\pi}$ is the ferromagnetic resonance frequency of the oscillating magnetization, defined as $\left(\frac{\omega_0}{\gamma}\right)^2 = \frac{E_{\theta\theta}.E_{\varphi\varphi} - E^2{}_{\theta\varphi}}{M^2{}_s \sin(\theta)^2}$, and $\frac{\Delta\omega_0}{2\pi}$ is the corresponding full-width-half-maximum (linewidth), defined as $\frac{\Delta\omega_0}{\gamma} = \frac{\alpha}{M_s}(E_{\theta\theta} + \frac{E_{\varphi\varphi}}{\sin(\theta)^2})$.

Replacing Eq. 3.3.7 into Eq. 3.3.5 the final solution yields for the amplitude of oscillations :

$$\begin{pmatrix} A_\theta \\ A_\varphi \end{pmatrix} = J_0 * \tilde{a} * \gamma^2 * (A(\omega) - \mathrm{i}\, S(\omega)) * \bar{\bar{W}} * \begin{pmatrix} p_\theta \\ p_\varphi \end{pmatrix} \tag{3.3.8}$$

where $\bar{\bar{W}}$ is a 2*2 matrix with the following components :

$$\bar{\bar{W}} = \begin{pmatrix} W_{11} & W_{12} \\ W_{21} & W_{22} \end{pmatrix} \tag{3.3.9}$$

- $W_{11} = \left(\frac{i\omega}{\gamma} - \frac{E_{\theta\varphi}}{M_s \sin(\theta)}\right) + \beta\left(\frac{i\omega}{\gamma}\alpha + \frac{E_{\varphi\varphi}}{M_s \sin(\theta)^2}\right) = |W_{11}|e^{i\varepsilon_{11}}$
- $W_{12} = -\left(\frac{i\omega}{\gamma}.\alpha + \frac{E_{\varphi\varphi}}{M_s \sin(\theta)^2}\right) + \beta\left(\frac{i\omega}{\gamma} - \frac{E_{\theta\varphi}}{M_s \sin(\theta)}\right) = |W_{12}|e^{i\varepsilon_{12}}.$
- $W_{21} = \left(\frac{i\omega}{\gamma}.\alpha + \frac{E_{\theta\theta}}{M_s}\right) - \beta\left(\frac{i\omega}{\gamma} + \frac{E_{\theta\varphi}}{M_s \sin(\theta)}\right) = |W_{21}|e^{i\varepsilon_{21}}.$
- $W_{22} = \left(\frac{i\omega}{\gamma} + \frac{E_{\theta\varphi}}{M_s \sin(\theta)}\right) + \beta\left(\frac{i\omega}{\gamma}.\alpha + \frac{E_{\theta\theta}}{M_s}\right) = |W_{22}|e^{i\varepsilon_{22}}.$

For a fixed out-of-plane polarizer, and a circular nanopillar as for the pMTJs studied here, the solution projected onto the θ axis is equivalent to the magnetization dynamics measured electrically through the TMR (which is the projection onto the z-axis). Therefore, to analyze the experimental results, in the studies conducted in this work only the projection onto the θ-axis is considered.

The equation Eq. 3.3.8 then takes the following form :

$$A_\theta = J_0 * \tilde{a} * \gamma^2 * \big(A(\omega) - \mathrm{i}\, S(\omega)\big) * W_{11} * p_\theta = J_0 * \tilde{a} * \gamma^2 * Z e^{i\sigma} * |W_{11}| e^{i\varepsilon_{11}} \qquad (3.3.10)$$

Developing Eq. 3.3.10 gives the following equation for the magnetization dynamics :

$$\delta m_\theta = A_\theta * e^{i(\omega t)} \qquad (3.3.11)$$

Inserting Eq. 3.3.10 to determine the amplitude A_θ leads to the following expression

$$A_\theta = J_0 * \ \tilde{a} * \gamma * \frac{\omega}{\sqrt{\left(\omega_0^2 - \omega^2\right)^2 + (\omega \Delta\omega_0)^2}} * e^{i\phi} \qquad (3.3.12)$$

and,

$$\phi = \sigma + \varepsilon_{11} = atan\left(\frac{\omega \Delta\omega_0}{\omega_0^2 - \omega^2}\right) + \mathrm{atan}\left(\frac{\omega}{\gamma H_{\parallel}(T)\beta}\right) \qquad (3.3.13)$$

The equations Eq. 3.3.12 and Eq. 3.3.13, unfold most of the interesting features of the magnetization dynamics forced by an rf current.

For instance, at resonance, when the frequency of the frequency of the injected rf current is approaching the ferromagnetic resonance frequency of the magnetization ($\omega \approx \omega_0$), the amplitude in Eq. 3.3.11 becomes :

$$|\delta m_{\theta_0}| = \ J_0 * \ \tilde{a} * \left(\frac{\gamma}{\Delta\omega_0}\right) \qquad (3.3.14)$$

where the phase is $\phi|_{\omega \approx \omega_0} \approx [0 \text{ or } \pi]$, considering $\beta \ll 1$ (i.e. neglecting the field-like torque contribution to the excitation for the pMTJs), and using the rule : atan(1/x) = -atan(x) + $\pi/2$.

Thus, based on Eq. 3.3.14, the amplitude of the free layer magnetization oscillation is determined by the current density amplitude (J_0), the damping-like and field-like spin transfer torque (STT) prefactors respectively $\tilde{a}$ and β, and the inverse of the linewidth $\Delta\omega_0$. These factors are crucial for the optimization of the amplitude of the resonance excitation.

For a zero bias magnetic field, and zero interaction field $H_{int\perp}$, $\omega_0 = \omega$ and $\Delta\omega_0 = \alpha(H_u - H_d)$, so that Eq. 3.3.14 yields :

$$\left|\delta m_{\theta_0}\right| = \frac{I_0}{\pi * r^2} * \ \tilde{a} * \frac{1}{\alpha(H_u - H_d)} \qquad (3.3.14)$$

With I_0 the amplitude of the injected rf current, $r = \frac{D}{2}$ the radius of the free layer, H_u the uniaxial magnetic anisotropy, and H_d the demagnetizing field. Hence, to drive the free layer magnetization to oscillate at high amplitudes, at constant current amplitude I_0, the following criterions must be met :

- High spin polarization $\tilde{a} \propto \eta \to 1$.
- Low magnetic damping $\alpha \to 0$.
- Compensation of the demagnetizing field by the magnetic anisotropy : $(H_u - H_d) \to 0$.
- small free layer radiuses (diameter) $r \to 0$ for high current densities

The first two criteria are dependent on the magnetic materials and their experimental characterization requires changing the free layer materials. Unfortunately, changing the material is out of the scope of this work. However, for a given optimized pMTJ stack, the last two criteria can be characterized by changing the free layer thickness and diameter, and will be explored experimentally in this work.

In the next section, a similar analysis will be carried out to derive the magnetization dynamics of the polarizing layer excited by an rf current.

3.4 The polarizing layer magnetization dynamics excited by a polarized rf current

The polarizing layer differs from the free layer by its coupling to the synthetic anti-ferromagnet. Therefore its magnetization dynamics under a spin polarized rf current might differ from the free layer's one.

To account for the SAF coupling effect on the polarizing layer, the macrospin model developed in the previous section is extended to treat two coupled monodomain layers. This is done by analyzing the dynamics of two coupled LLG equations. Here, the polarizing layer and the top SAF layer are considered to have one pseudo-magnetization that arises from the whole composite polarizing layer. The system considered is illustrated in Figure *3.4.1*, where PL is the composite polarizing layer and B-SAF is the bottom SAF layer.

The dynamics of the two coupled magnetizations $\vec{m}_1$ and $\vec{m}_2$ is given by the following coupled equations :

$$\frac{\partial \vec{m}_1}{\partial t} = -\gamma \left(\vec{m}_1 \times \left(\vec{H}_{eff1} + J_r \, \vec{m}_2 \right) \right) + \alpha \left(\vec{m}_1 \times \frac{\partial \vec{m}_1}{\partial t} \right) - \gamma \, a_{\parallel} \, \vec{m}_1 \times (\vec{m}_1 \times \vec{p}) + \gamma \, a_{\perp} \, \vec{m}_1 \times \vec{p} \quad (3.4.2)$$

$$\frac{\partial \vec{m}_2}{\partial t} = -\gamma \left(\vec{m_2} \times \left(\vec{H}_{eff2} + J_r \, \vec{m}_1 \right) \right) + \alpha \left(\vec{m}_2 \times \frac{\partial \vec{m}_2}{\partial t} \right) - \gamma \, a_{\parallel} \, \vec{m}_2 \times (\vec{m}_2 \times \vec{p}) + \gamma \, a_{\perp} \, \vec{m}_2 \times \vec{p} \quad (3.4.3)$$

Here, $\vec{p}$ is the magnetization of the layer that will polarize the electrons traveling to the free layer in Figure *3.4.1*.

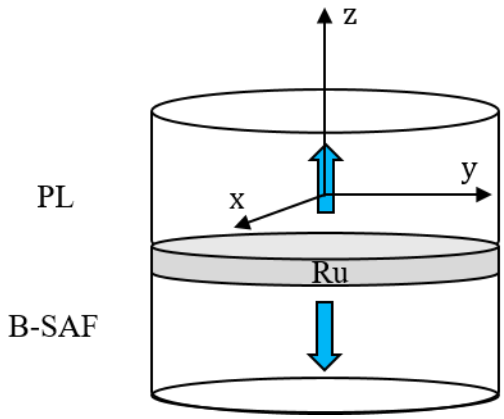

Figure 3.4.1: Illustration of the composite polarizing layer coupled to the magnetization of the bottom layer of SAF through a thin Ru layer.

To solve the system of equations Eq. 3.4.2-3.4.3, the two equations are linearized, and the magnetizations are assumed quasi-stable along the z-axis ($\sim \pm 1$). Thus, for small perturbations, the dynamics of the magnetizations can be probed through the oscillations along the x and y axis. For convenience the system is expressed in Cartesian coordinates. Starting first by solving the system in the absence of current, it gives :

$$\frac{\dot{m}_{1x}}{\gamma} = -\left(H_{\perp} - H_{ueff_1}\right)m_{1y} - J_r\left(m_{1y} + m_{2y}\right) - \alpha\frac{\dot{m}_{1y}}{\gamma} \tag{3.4.4}$$

$$\frac{\dot{m}_{1y}}{\gamma} = \left(H_{\perp} - H_{ueff_1}\right)m_{1x} - J_r\left(m_{1x} + m_{2x}\right) + \alpha\frac{\dot{m}_{1x}}{\gamma} \tag{3.5.5}$$

$$\frac{\dot{m}_{2x}}{\gamma} = -\left(H_{\perp} - H_{ueff_2}\right)m_{2y} - J_r\left(m_{1y} + m_{2y}\right) + \alpha\frac{\dot{m}_{2y}}{\gamma} \tag{3.4.6}$$

$$\frac{\dot{m}_{2y}}{\gamma} = \left(H_{\perp} - H_{ueff_2}\right)m_{2x} - J_r\left(m_{1x} + m_{2x}\right) - \alpha\frac{\dot{m}_{1y}}{\gamma} \tag{3.4.7}$$

where $H_{\perp}$ is the out-of-plane magnetic bias field. In the following, the composite polarizing layer and the bottom SAF layer are assumed to have approximately the same H_{ueff}.

Including the forcing rf current density, the steady state solution of the system is given by :

$$\vec{m} = \vec{A}\, e^{i(\omega t)} \tag{3.4.8}$$

where $\vec{A}\,(A_{1x}, A_{1y}, A_{2x}, A_{2y})$ is the oscillation amplitude, $\frac{\omega}{2\pi}$ the frequency of the forcing current, and ϕ the phase of the oscillating solution.

Inserting Eq. 3.4.8, into 3.4.4 to 3.4.7 and including the spin transfer torque terms from Eq. 3.4.2-3.4.3, one obtains the following solution after variable separation:

$$\vec{A}e^{\phi} = \gamma\, \tilde{a}\, J_0\, \bar{\bar{\chi}}'\ \ \bar{\bar{N}}\, \vec{p}_{x-y} \tag{3.4.9}$$

where χ' is the susceptibility corresponding to the response of the coupled magnetizations to the spin-transfer torque excitations. Its components are the following :

$$\bar{\bar{\chi}}'^{-1} = \begin{pmatrix} -\left(\alpha\widetilde{H} + \tilde{a}\, J_0 P_{z_1} + \frac{i\omega}{\gamma}\right) & -\widetilde{H} & -\alpha J_r & -J_r \\ \widetilde{H} & -\left(\alpha\widetilde{H} + \tilde{a}\, J_0 P_{z_1} + \frac{i\omega}{\gamma}\right) & J_r & -\alpha J_r \\ -\alpha J_r & J_r & \left(\alpha\widehat{H} - \tilde{a}\, J_0 P_{z_2} - \frac{i\omega}{\gamma}\right) & -\widehat{H} \\ -J_r & -\alpha J_r & \widehat{H} & \left(\alpha\widehat{H} - \tilde{a}\, J_0 P_{z_2} - \frac{i\omega}{\gamma}\right) \end{pmatrix} \tag{3.4.10}$$

where $\widetilde{H} = (H_{\perp} - H_{ueff}) + J_r$, and $P_{z_{1-2}}$ are the out-of-plane components of the spin current polarization: free layer for $\vec{m}_1$, and $\vec{m}_1$ for $\vec{m}_2$. For $\bar{\bar{N}}\, \vec{p}_{x-y}$ it is given by :

$$\bar{\bar{N}} = \begin{pmatrix} 1 & -\beta & 0 & 0 \\ \beta & 1 & 0 & 0 \\ 0 & 0 & 1 & -\beta \\ 0 & 0 & \beta & 1 \end{pmatrix} \begin{pmatrix} p_{1x} \\ p_{1y} \\ p_{2x} \\ p_{2y} \end{pmatrix} \tag{3.4.11}$$

To focus on the response from the composite polarizing layer, the general solution is projected onto $\vec{m}_1$ and analyzed for the STT excitations from the free layer. For pMTJs, the field-like torque is expected to be weak (see the experimental results in chapter 5), therefore it is neglected in the further calculations. The final solution of the polarizing layer magnetization dynamics, excited by a quasi in-plane free layer ($P_{z_1} \approx 0$), i.e. $t_{FL} = 1.8\, nm$ and $t_{FL} = 1.6\, nm$, is the following :

$$A_1 = \tilde{a} * J_0 * \gamma * \omega * \frac{(D-\xi) * \left(D^2 - \xi^2 + \frac{\omega^2}{\gamma^2}\Delta\omega^2\right)}{(D+\xi)^2(D-\xi)^2 + 4\Delta\omega^2 \frac{\omega^2}{\gamma^2} D^2} * e^{-i\phi} \tag{3.4.12}$$

with,

$$\phi = \operatorname{atan}\left(\frac{\omega * (D-\xi)}{\frac{\Delta\omega}{2} * \left(\frac{\omega_0^2}{\gamma^2} + \frac{\omega^2}{\gamma^2}\right)}\right) \tag{3.4.13}$$

where $D = \frac{\omega_0^2}{\gamma^2} - \frac{\omega^2}{\gamma^2}$ is the ferromagnetic resonance term in the absence of the interlayer exchange coupling, with $\frac{\omega_0}{2\pi} = \gamma\left(H_\perp - H_{ueff}\right)$ the ferromagnetic resonance frequency of the oscillating polarizing layer and $\Delta\omega = 2\alpha\left(H_\perp - H_{ueff}\right)$ its linewidth. In 3.4.12 and 3.4.13 ξ is the coupling term given by $\xi = 2J_r(H_\perp - H_{ueff})$.

From Eq. 3.4.12, it can be noticed that the coupled system can oscillate at two different resonance frequencies. One resonance at $\omega_- = \sqrt{\omega_0^2 - \gamma^2\xi}$, and another resonance with higher frequency at $\omega_+ = \sqrt{\omega_0^2 + \gamma^2\xi}$. To analyze the sign of the amplitude at those frequencies, Eq. 3.4.12 can be evaluated near the resonance where : $\lim_{D\to\pm\xi}(D^2 - \xi^2) = 0$. The latter gives the following approximation :

$$A_1 \approx \tilde{a} * J_0 * \gamma * \omega * \frac{(D - \xi)}{4D^2} \tag{3.4.14}$$

Interestingly, due to the last factor in Eq. 3.3.14 $(D - \xi)$, it can be seen that the amplitude changes its sign when the excitation frequency becomes larger than $\frac{\omega_-}{2\pi}$. Therefore, the peaks exhibited at the two renonaces have different signs, and thus the two make an asymmetric resonance response. The derived formula, is in agreement with the analysis in ref [89].

With the derivation of the magnetization dynamics excited by a spin polarized rf current, for both the free and the polarizing layers, the final step is to derive the dc voltage of the spin torque nano-diodes in correspondence to the experimental measurements.

3.5 The output voltage of the spin-torque nano-diodes

3.5.1 The passive detection voltage

The rf-to-dc voltage conversion across an MTJ, where only an rf current is injected is given by :

$$V_{rec}(\omega) = \langle V(t)\rangle = \langle Re(I) * Re(R)\rangle = \langle I_0\cos(\omega t) * Re(R(\omega t + \phi))\rangle \tag{3.5.1}$$

where I_0 is the rf current amplitude, ω the rf current frequency, and $R(\omega t + \phi)$ is the oscillating magnetoresistance. Considering the oscillation of the free layer, the latter is given by the Slonczewski TMR conductance formula, defined by [34]:

$$R(\omega t + \phi)^{-1} = G(\omega t + \phi) = \frac{(R_p^{-1} + R_{ap}^{-1})}{2} + \frac{(R_p^{-1} - R_{ap}^{-1})}{2}(\vec{m}_{FL}(\omega t + \phi).\vec{p}) \tag{3.5.2}$$

where R_p and R_{ap} are the parallel and anti-parallel resistances of the MTJ respectively, and θ the angle difference between the free and polarizing layers (considered here to be fixed and aligned along the z-direction).

For the pMTJs, where the polarizing layer magnetization is oriented out-of-plane, and where only the magnetization motion along z is detected electrically, the resistance from Eq. 3.5.1 becomes since $\delta m_z = \delta m_\theta$:

$$R(\omega t + \phi) = R_p \left(\frac{(1 + TMR)}{1 + 0.5TMR} \left(\frac{1}{1 + \frac{\text{TMR}}{2 + TMR} * \delta m_\theta} \right) \right) \tag{3.5.3}$$

with R_p the parallel resistance, $TMR = \frac{R_{ap} - R_p}{R_p}$, and $\delta m_\theta\ (\omega t + \phi)$ from Eq. 3.3.11-12. Expanding Eq. 3.5.3 in Taylor series, and replacing the TMR by the Julliere formula $TMR = \frac{2\eta^2}{1 - \eta^2}$ [32], with η the ratio of the spin polarization, the algebra yields :

$$Re(R(\omega t + \phi)) = R_p * \left(1 + \frac{\eta^2}{1 + 2\eta^2}\right) + R_p * \eta^2 (1 + \eta)^2 * Re[\delta m_\theta\ (\omega t + \phi)] \tag{3.5.4}$$

The parameter η was introduced here to simplify the formula in Eq. 3.5.4 by replacing the TMR factor. However it should be noted that it represents the spin polarization only when the TMR corresponds to the intrinsic one called TMR_o later on in the further analysis in chapters 4 and 5. There, we will see that the TMR obtained from experiments is affected by a serial resistance.

In Eq. 3.5.4 the first term of the resistance is independent of the magnetization dynamics and is due to the static magnetoresistance change. The second term in Eq. 3.5.4 shows clearly that the oscillations of the magnetoresistance are proportional to those of the magnetization. Replacing $\delta m_\theta\ (\omega t + \phi)$ by its real value and inserting the resistance (Eq. 3.5.4) into the voltage equation (Eq. 3.5.1) gives :

$$V(t) = V_{rec} + V_{rf}(t) \tag{3.5.5}$$

With Eq.3.3.11 for δm_θ, the frequency dependent rectification voltage signal is given by the time average

$$V_{rec}(\omega) = < R_p * I_0^2 * \eta^2 (1 + \eta)^2 * \frac{\tilde{a}}{\pi r^2} * \gamma * \frac{\omega}{\sqrt{\left(\omega_0^2 - \omega^2\right)^2 + (\omega \Delta\omega_0)^2}} * \cos(\omega t) * \cos(\omega t + \phi) > \tag{3.5.6}$$

And the time dependent contribution is given by :

$$V_{rf}(t) = I_0 * R_p * \left(1 + \frac{\eta^2}{1 + 2\eta^2}\right) * \cos(\omega t) \tag{3.5.7}$$

The time average of the voltage in Eq. 3.5.5, is given by 3.5.6, since the average of 3.5.7 is zero: the following dc voltage :

$$V_{rec} = < V(t) > = P_{rf_0} * \frac{\tilde{\alpha}}{\pi * r^2} * \eta^2(1+\eta)^2 * \frac{\gamma * \omega}{\sqrt{\left(\omega_0^2 - \omega^2\right)^2 + (\omega \Delta\omega_0)^2}} * \cos(\phi) \quad (3.5.8)$$

where $P_{rf_0} = R_p * I_0^2$ is the electric power in the parallel resistance state. The power injected in the MTJ (P_{rf}) depends on the resistance relative to the orientation of the free layer magnetization (R_0) : $P_{rf_0} = \frac{R_p}{R_0} P_{rf}$.

At the resonance frequency, and in the absence of bias fields, the voltage in Eq. 3.5.8 reaches its maximum, and takes the following form (see Eq.3.3.14):

$$V_{rec_{max}} = \frac{R_p}{R_0} * P_{rf} * \eta^2(1+\eta)^2 * \frac{\tilde{\alpha}}{\pi * r^2} * \frac{1}{\alpha(H_u - H_d)} \quad (3.5.9)$$

The different factors in Eq. 3.5.9, give a good lead on the optimization of the maximum dc voltage produced by the spin torque nano-diodes. To maximize the output dc voltages, without changing the magnetic material, the MTJ should have :

- Smaller diameters to increase the STT amplitude
- Compensation between H_u and H_d through the device shape
- Good impedance matching to insure that the maxiumum power is transmitted to the device, to excite the dynamics and produce the MR signal.

These different criteria, and their consequences will be explored experimentally in chapter 5.

A numerical evaluation of the rectification voltage from Eq. 3.5.8 is plotted in Figure *3.5.1*, for the three free layer thicknesses 1.4 nm, 1.6 nm, and 1.8 nm, and for a diameter of 100 nm. The parameter values are shown in the legend of Figure *3.5.1*. They were adapted from the fitting done in chapter 4.

The simulations show that for an injected power of 0.1 mW the output voltage is in the range of ~100 mV. Moreover, it shows that the output signal increases as the thickness of the free layer drops from 1.8 nm to 1.6 nm, or when the thickness increases from 1.4 nm to 1.6 nm. The latter is a consequence of the inverse dependence of the magnetization oscillations amplitude on the difference between the demagnetizing field and the magnetic anisotropy field (Eq. 3.5.9). As the free layer thickness decreases, the magnetic anisotropy field increases (see Eq. 3.1.2), and thereby it pulls the free layer magnetization out-of-plane against the in-plane demagnetizing field. A more detailed discussion will be presented in chapter 5.

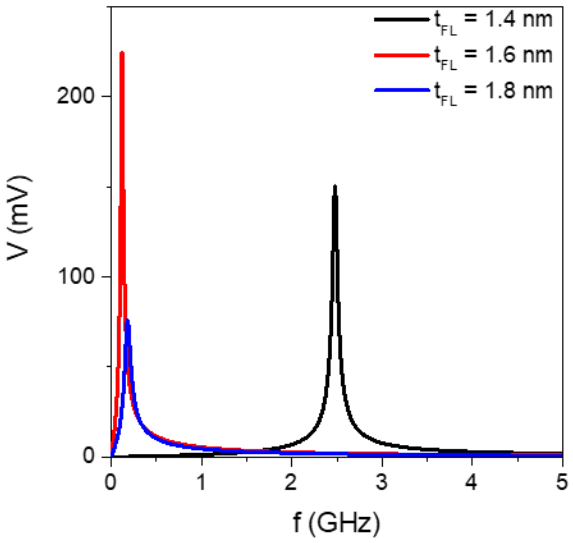

Figure 3.5.1 : Simulation of the dc rectification voltage in the output of a spin torque nano-diode, using Eq. 3.5.8, for the free layer thicknesses of 1.4 nm, 1.6 nm, and 1.8 nm respectively, and a nominal diameter of 100 nm. The parameter values are : $P_{rf} = 0.1\,mW$, $R_p = 850\,\Omega$, TMR = 100%, $\eta = 0.17$, $\alpha = 0.01$, $M_s = 1e6\,A/m$, $K_u = 8.4e-4\,J/m^2$, $\Gamma = 28\,GHz/T$, and $\mu_0 H_{int\perp} = 42\,mT$, $\tilde{a} = 4mT/A$.

To complete the formalism developed here, the sensitivity of spin torque nano-diode must be defined. In this work, it is considered at resonance as :

$$\epsilon = \frac{dV_{rec}}{dP_{rf}} = \frac{R_p}{R_0} * \frac{\tilde{a}}{\pi * r^2} * \eta^2(1+\eta)^2 * \frac{\gamma}{\alpha(H_u - H_d)} \qquad (3.5.10)$$

For the parameters in Figure *3.5.1*, and for a free layer thickness of 1.6 nm and a nominal diameter of 100 nm, the sensitivity is expected to be $\epsilon = 2200\,mV/mW$.

3.5.2 Active detection voltage (subcritical current)

For the active damped precessions of the magnetization, where an additional dc current is injected in the magnetic layer the same approach discussed in section 3.5.1 applies. The obtained formula of the magnetization dynamics is the following:

$$\delta m_\theta = A_\theta * e^{i(\omega t + \phi)} \qquad (3.5.11)$$

where the susceptibility components are modified to include the action of the STT on the damping.

Correspondingly, this leads to a modification of the precession amplitude. For the case of a bias magnetic field along the z direction (or zero bias field),

$$A_\theta = \frac{I_0}{\pi r^2} * \tilde{\alpha} * \gamma * \frac{\omega}{\sqrt{\left(\omega_0^2 - \omega^2\right)^2 + \left(\omega\left(\gamma a_{\parallel_{dc}} - \Delta\omega_0\right)\right)^2}} \tag{3.5.12}$$

and,

$$\phi = atan\left(\frac{\omega\left(\gamma a_{\parallel_{dc}} - \Delta\omega_0\right)}{\omega_0^2 - \omega^2}\right) + \tan\left(\frac{\omega}{\gamma H_\parallel(T)\beta}\right) \tag{3.5.13}$$

While the resonance frequency $\omega_0^2 \sim \omega^2$ is little affected by the dc current, one can see from Eq 3.5.12 that the dc current density reduce the intrinsic damping of the magnetization and in consequence lead to higher oscillation amplitudes for one current sign, but smaller amplitudes for the other sign.

For instance, at resonance, where the magnetization amplitude is at its maximum, Eq. 3.5.12 takes the following form :

$$\left|\delta m_{\theta_0}\right| = \frac{I_0}{\pi r^2} * \tilde{\alpha} * \left(\frac{\gamma}{\gamma a_{\parallel_{dc}} - \Delta\omega_0}\right) \tag{3.5.14}$$

Eq. 3.5.14, clearly highlights the additional enhancement of the resonance amplitude induced by the dc current. The corresponding maximum voltage produced by the spin torque nano-diode is given by :

$$< V >_{max} = \frac{R_p}{R_0} * P_{rf} * \eta^2(1+\eta)^2 * \frac{\tilde{\alpha}}{\pi * r^2} * \frac{\gamma}{\gamma a_{\parallel_{dc}} - \Delta\omega_0} \tag{3.5.15}$$

Although Eq. 3.5.15 predicts that injecting more current, with the right sign, increases the output voltage amplitude, it must be reminded that the formula holds only for small currents. For, as the spin transfer torque magnitude approaches the total compensation of the damping, the magnetization dynamic becomes unstable.

Above the critical dc current, the magnetization might bifurcate into self-sustained oscillations, and the diode becomes inherently an auto-oscillator. In this regime, the spin torque nano-diode can synchronize with the rf current source, leading to a drastic decrease of its own phase noise (injection locking) [98]. This strong reduction of phase noise, translates to less energy dissipation, and thus smaller linewidth and higher power of the auto-oscillator (diode) frequency spectrum [99]. For the spin torque nano-diodes this was observed experimentally in [100]–[102]. An explanation of this phenomena in MTJs is provided in Annex C. Here we do not consider this case.

3.6 Field-Free voltage controlled superparamagnetism in pMTJs

This section bears no direct link to the spin-torque nano-diode effect. It deals with the superparamagnetic behavior of the magnetization and it is related to chapter 7. It presents the derivation of the Neel-Brown model used to fit and explain the experimental measurements in chapter 7.

The first theoretical treatments of monodomain superparamagnetic particles was done by L. Neel in [103], where he proposed an Arrhenius law of the dwell-times at zero external bias field defined as :

$$\tau = \tau_0 e^{\frac{\mathrm{K\,V}}{k_B T}} \tag{3.6.1}$$

where τ is the mean dwell-time, τ_0 the attempt time, K the magnetic anisotropy energy constant (J/m^3), V the particle volume (m^3), k_B the Boltzmann constant and T the temperature (K).

The Neel model was extended by W. F. Brown, where he thoroughly derived it from first principles using the LLG equation [104]. The Brown model consists of adding to the LLG equation a random fluctuating field $\vec{h}(t)$, making it stochastic (Langevin) and afterwards solving it for the mean dwell-times. The random field is supposed to be stationary and its correlation time between two events is much smaller than the time required for a noticeable change in the magnetization. Those conditions are expressed by the time average and time correlation of the thermal fluctuating field $\vec{h}(t)$ given by :

$$\overline{\vec{h}(t)} = 0. \tag{3.6.2}$$

$$\overline{\vec{h}_\iota(t)\vec{h}_\jmath(t')} = \frac{2D}{\gamma^2}\,\delta_{ij}\delta(t - t') \tag{3.6.3}$$

where $\overline{\vec{h}(t)}$ is the time average of the random magnetic field, δ_{ij} Kronecker delta with i and j the cartesian coordinates (x,y,z), and D = $\frac{\alpha\gamma K_B T}{M_s V}$ is the diffusion coefficient.

The LLG equation with the random magnetic field, in the absence of the spin transfer torque, takes the following form :

$$\frac{\partial\vec{m}}{\partial t} = -\gamma\left(\vec{m} \times \left(\vec{H}_{eff} + \vec{h}\right)\right) + \gamma\alpha\left(\vec{m} \times \frac{\partial\vec{m}}{\partial t}\right) \tag{3.6.4}$$

For convenience, in this section the LLG equation in Eq. 3.6.5 is rewritten in the Landau-Lifshitz form (by cross multiplying with $\vec{m}$ and using the triple vector product formula) :

$$\frac{\partial\vec{m}}{\partial t} = -g'\left(\vec{m} \times \left(\frac{\partial E}{\partial\vec{m}} + \vec{h}\right)\right) + h'\,\vec{m} \times \left(\vec{m} \times \left(\frac{\partial E}{\partial\vec{m}} + \vec{h}\right)\right) \tag{3.6.5}$$

where $g' = \frac{\gamma}{1 + \alpha^2}$, and $h' = \alpha g'$. For low damping $\alpha^2 \ll 1$, $g' = \gamma$ and $h' = \gamma\alpha$.

To evaluate statistically the stochastic LLG equation in Eq. 3.6.5, Brown transformed it into the Fokker-Planck equation [105] and solved it for the probability distribution of the fluctuations of the magnetization. He used two methods to do so, with the first one consisting of an expansion of integral equations, in long and tedious calculations using the Wang-Ulenbeck approach described in [106]. However, his second method allows to avoid the long calculations by using the Brownian motion theory used by Einstein in [107], and it is the one considered here.

The approach consists of using the continuity equation of the probability distribution defined as :

$$\frac{\partial W}{\partial t} = -\nabla.\vec{J}_{pr} \tag{3.6.6}$$

where W is the probability distribution, and $\vec{J}_{pr}$ the probability distribution current. The latter has two contributions, one from the drift transport and the other from the diffusion:

$$\vec{J}_{pr} = W\frac{\partial \vec{m}}{\partial t} - D\,\frac{\partial W}{\partial \vec{m}} \tag{3.6.7}$$

Inserting Eq. 3.6.7 into Eq. 3.6.6, and replacing $\frac{\partial \vec{m}}{\partial t}$ by the LLG equation, the development yields the following Fokker-Planck equation :

$$\frac{\partial W}{\partial t} = D\,\Delta W + \gamma\,\vec{m}\cdot\left(\frac{\partial E}{\partial \vec{m}} \times \frac{\partial W}{\partial \vec{m}}\right) + \gamma\alpha\frac{\partial}{\partial \vec{m}}\cdot\left(W\frac{\partial E}{\partial \vec{m}}\right) \tag{3.6.8}$$

where ΔW is the Laplacian of the probability distribution.

To obtain the stationary solutions ($\frac{\partial W}{\partial t} = 0$) of Eq. 3.6.8, the equation is treated in spherical coordinates of the magnetization. For a uniaxial anisotropy, Eq. 3.6.8 is dependent only on the polar angle θ, and it takes the form :

$$\nabla.J_{\theta_{pr}} = 0 \tag{3.6.9}$$

which means that the probability distribution current $J_{\theta_{pr}}$ is constant. The expression of the polar term $J_{\theta_{pr}}$ is given by :

$$J_{\theta_{pr}} = D\sin(\theta)\left[\frac{\partial W}{\partial \theta} + \frac{\gamma\alpha}{D}\frac{\partial E}{\partial \theta}\,W\right] = constant = D * J_{pr} \tag{3.6.10}$$

where $D * J_{pr}$ is just a constant and J_{pr} is a normalization of $J_{\theta_{pr}}$. Notice, the terms inside the bracket can be written as : $e^{-\beta E}\frac{\partial}{\partial \theta}\left(W(\theta,t)\,e^{\beta E}\right)$, with $\beta = \frac{V}{k_B T}$. Integrating over the polar angle θ and solving for the probability distribution W gives :

$$W = J_{pr} * e^{-\beta E}\int \frac{e^{\beta E}}{\sin(\theta)}d\theta \tag{3.6.11}$$

Knowing the probability distribution in Eq. 3.6.11, the next step in determining the mean dwell-times is to use Kramer's transition state theory [108].

The theory assumes a fluctuating population of particles in an energy well that escapes at a certain rate [109]. The escape rate represents the inverse of the dwell-time and the latter is given by:

$$\tau = \frac{N_0}{J_{pr}} \tag{3.6.12}$$

with $N_0 = \int_0^{\theta_m} W \sin(\theta)\, d\theta$ is the number of particles in the well, and θ_m the angle corresponding to the maximum of the well. Inserting Eq. 3.6.11 in Eq. 3.6.12 yields :

$$\tau = \int_0^{\theta_m} e^{-\beta E(\theta)} \sin(\theta) \int_0^{\theta} \frac{e^{\beta E(\theta')}}{\sin(\theta')} d\theta' d\theta \tag{3.6.13}$$

For high energy barriers (> 5 $K_B T$), the particles are concentrated near the local minimum of the energy. Thus the integrals in Eq. 3.6.13 can be approximated using the Laplace method (2nd order Taylor expansion of the energy $E(\theta)$), and using $\sin(\theta') \sim \theta'$. The final result, after carrying out the algebra, gives an Arrhenius Law with the following form :

$$\tau(0) = \tau_n * \left(\frac{1}{\beta E"(0)} * \frac{\sqrt{2\pi}}{\sqrt{\beta |E"(\theta_m)|}\ * \sin(\theta_m)} \right) * \exp(\beta \Delta E) \tag{3.6.14}$$

$$\tau(\pi) = \tau_n * \left(\frac{1}{\beta E"(\pi)} * \frac{\sqrt{2\pi}}{\sqrt{\beta |E"(\theta_m)|}\ * \sin(\theta_m)} \right) * \exp(\beta \Delta E) \tag{3.6.15}$$

where $\Delta E = E(\theta_m) - E(0|\pi)$ is the energy barrier in the absence of an external magnetic field and STT, and τ_n the Néel attempt time.

Including in the energy expression ΔE a magnetic bias field H with a direction collinear to the magnetization $\vec{m}$ its development in Eq. 3.6.14, and Eq. 3.6.15, gives :

$$\tau_{\pm} = \tau_0\ * \exp\left(\beta * \Delta E * \left(1\ \pm \frac{H}{H_u} \right)^2 \right) \tag{3.6.16}$$

where $\pm$ refers to the escape from the minimum at 0 (parallel) or π (antiparallel) respectively, τ_0 is the attempt time corresponding to the Néel attempt time multiplied by the factor in Eq. 3.6.16 , and H_u refers to the magnetic field of the uniaxial magnetic anisotropy.

The spin transfer torque effect can also be included using the same approach as for the bias field in the Neel-Brown model. This was first done by Zhang in [110], and generalized by Tanigushi et al. in [111]. The corresponding mean-dwell times were found to be [112]:

$$\tau_{\pm} = \tau_0\ * \exp\left(\beta * \Delta E * \left(1\ \pm \frac{V_{app}}{V_c} \right)^b * \left(1\ \pm \frac{H + AV_{app} + BV_{app}^2}{H_u} \right)^2 \right) \tag{3.6.16}$$

where V_{app} is the applied voltage, V_c the critical switching voltage (analogous to the critical current derived in Eq. 3.2.1 in section 3.2), A and B are the linear and quadratic terms of the field-like torque respectively, and $\beta = \frac{Volume}{k_B T}$. Tanigushi et al. in [111] reported that the power coefficient b is dependent on the magnitude of the applied voltage. For bias voltages smaller than the critical switching voltage V_c the coefficient is predicted to be $b \approx 1$, while for higher voltages b can be quadratic or a fractional number. Moreover, it is also reported that for in-plane magnetic tunnel junctions $b \approx 1$ and for pMTJs $b \approx 2$ [14]. In this work, it is considered to be equal to 1, because the logarithmic plot of the average dwell times from the experimental results in chapter 7 have a quasi-linear dependence on voltage.

Conclusion

To conclude, in this chapter all the theoretical models that will be used in the upcoming chapters have been derived using a macrospin approach.

For the static state of the magnetization of the different pMTJ layers, an analytic approach was proposed to determine the FL static equilibrium in the presence of both in-plane and out-of-plane fields simultaneously. These results, where then exploited to derive a model for the spin torque diode effect by linearizing the LLG equation. An approximate formula for the magnetization dynamics was established for the free and the polarizing layers under rf current excitation and with and without interaction to the SAF (either dipolar coupling for the FL or interlayer exchange coupling for the PL). In addition, a formula for the voltage produced by the spin-torque nano-diodes was derived for the pMTJs for both passive and active detection.

Finally, to account for the stochastic switching of the superparamagnetic state explored in chapter 7, the derivation of the Neel-Brown model was presented where first only the tuning by a magnetic field was treated, and then the spin transfer toque effect was added.

In the next chapter, the different formulas developed in these sections will be used to fit the different experimental data obtained in this work, and to provide predictions for further improvements.

Static characterization of the magnetic properties of the pMTJs

The pMTJs have a complex magnetic structure, with the SAF, the polarizing layer and the free layer that can change their relative orientations under applied magnetic bias fields, temperature, or electric current. For the dynamic experiments it is important to know, prior to the excitation, what is the initial magnetic state and orientation of the magnetizations of the different layers. For instance, in the spin-torque nano-diode measurements, the excited magnetic layer exhibits small angle oscillations around the magnetization equilibrium. Furthermore, knowing the equilibrium state of the polarizing layer is also important, because it helps to know the spin polarization direction which can have a direct influence on the output voltages of the spin-torque nano-diode.

Therefore, due to their importance, this chapter is dedicated to the characterization of the equilibrium states of the different magnetic layers of the pMTJs. The magnetic equilibrium states, first, are determined for the continuous pMTJ films for different free layer thicknesses. The total magnetic moments are measured for in-plane and out-of-plane magnetic fields, which allows to identify their easy and hard axis. Secondly, following the nanofabrication of the pMTJ nanopillars, the magnetic equilibrium states are characterized through their magnetoresistance using the PPMS measurements. The pMTJs are first measured in weak dc currents, at room temperature, to probe the effects of the magnetic field orientation and magnitude. Subsequently, for the same measurements, the temperature is varied between 20 K and 300 K, to explore its effect on the equilibrium states and the TMR through the hysteresis loop measruements. Finally, the input dc current value is increased (for negative and positive signs), to investigate its action on the magnetic equilibrium states. The analysis includes the effect of the spin transfer torque, the Joule heating, and the voltage controlled magnetic anisotropy.

4.1 Static characterizations of the continuous films and TMR statistical analysis

4.1.1 Continuous film characterizations

Before discussing the magneto-resistance loops of the nanopillar devices, here the magnetization loops of the unpatterned magnetic stacks are presented to determine the orientation of the magnetization of the free and polarizing layers. This is done by measuring their magnetic moments, using a vibrating sample magnetometer (VSM). The dependence of the (normalized) magnetic moments as a function of an out-of-plane magnetic field is shown in Figure *4.1.1*(a) for films with free layer thicknesses of t_{FL} = 1.4 nm (red curve) and t_{FL} = 1.6 nm (black curve).

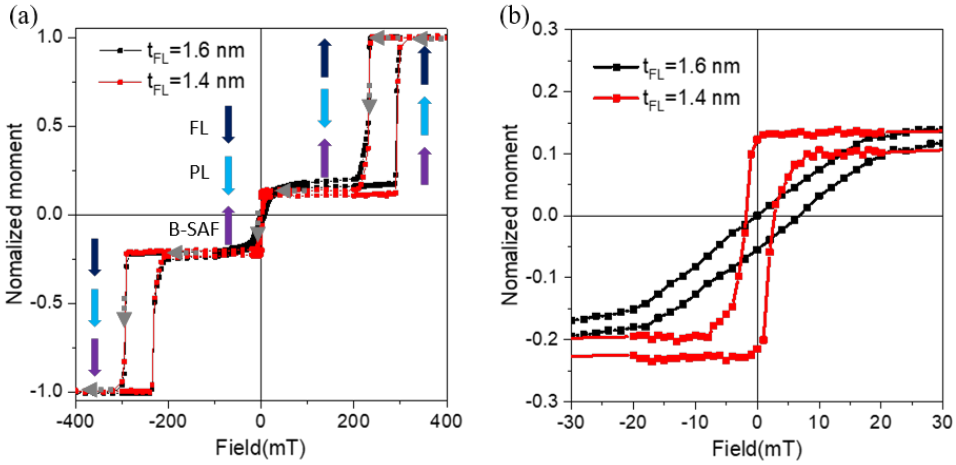

Figure 4.1.1: Vibrating sample magnetometer measurements of the continuous pMTJ films for two free layer thicknesses t_{FL} = 1.4 nm (in red) and t_{FL} = 1.6 nm (in black). (a) The VSM measurements under an out-of-plane magnetic field varied between -400 mT and 400 mT. (b) A zoom of (a) around zero field. B-SAF is the bottom SAF layer, FL the free layer, and PL the composite polarizing layer including the top SAF layer (see section 2.1.1 of chapter 2).

For the free layer thickness t_{FL} = 1.4 nm two hysteretic regions are observed, one around zero magnetic field, with a smaller change in magnetic moment, and another at higher magnetic (positive and negative) fields, with a bigger change in magnetic moment. The hysteresis observed around zero field is attributed to the free layer reversal, because of the softness of the free layer compared to other layers in the stack. For the hysteresis observed in higher out-of-plane magnetic fields, they are attributed to the switching of the polarizing layer and the bottom SAF layer (B-SAF). When decreasing the magnetic field from high positive values to high negative ones, the corresponding switching of the different magnetic layers (FL, PL, B-SAF) is sketched in Figure *4.1.1*(a) by the colored arrows.

The sharp switching of the hysteresis around zero and higher magnetic fields, indicates that the magnetizations of the free, polarizing, and SAF layers all have an out-of-plane easy axes, and thus all their magnetizations are oriented perpendicular to the film plane.

For the free layer thickness t_{FL} = 1.6 nm, this is different for the reversal around zero field. A closer look to the plot in Figure *4.1.1*(a) shows that the reversal is more gradual, with an S-shaped reversal which is the signature that the field direction is a hard axis. This is better seen in the zoom shown in Figure *4.1.1*(b). Here, the change in the easy axis orientation when the free layer thickness increased to t_{FL} = 1.6 nm is caused by the reduction of the volume averaged interfacial perpendicular anisotropy (iPMA) inversely dependent on the thickness. This behavior is confirmed for the nanopillar devices measured by electrical transport measurements using the physical property measurement system (PPMS).

4.1.2 Statistical analysis on wafer level of the tunneling magnetoresistance

After nanofabrication, the tunneling magnetoresistance (TMR) is measured on wafer level of all the fabricated devices using an automated MR tester whose field range is limited to 150 mT. Since the yield on wafer level is not 100%, the TMR measurements help to localize the operating magnetic tunnel junctions in the diced wafer, and thus the ones to be investigated. In addition, such statistical analysis of the MR loops on wafer level provide a feedback for the nanofabrication and magnetic stack optimization. The TMR measurements were carried out under a variable out-of-plane bias magnetic field. From the TMR loops, the parallel (R_p) and antiparallel (R_{ap}) resistances are extracted where the TMR is defined by :

$$TMR = \frac{R_{ap} - R_p}{R_p} \tag{4.1.1}$$

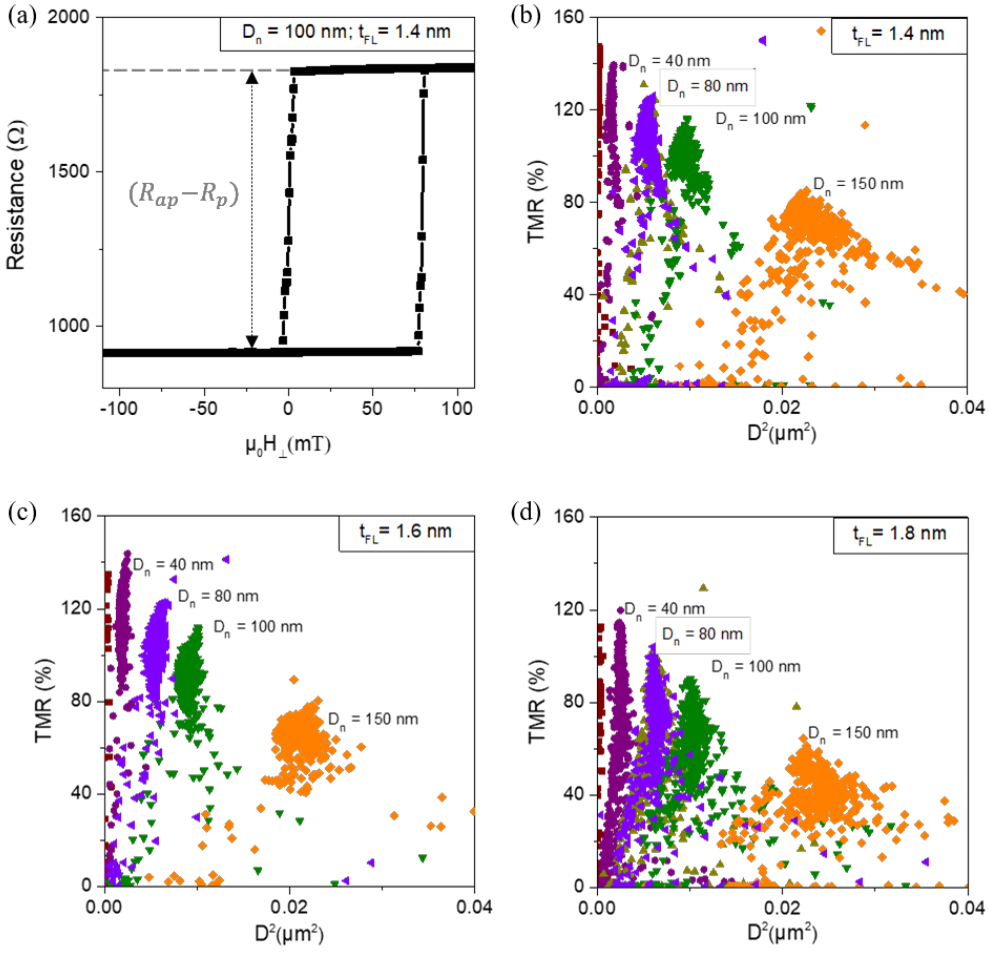

Figure 4.1.2 : (a) A typical magnetoresistance loop of a device with free layer thickness of 1.4 nm and a nominal diameter of 100 nm, plotted as a function of the out-of-plane field. (b) The TMR of all the devices on a wafer with a free layer thickness of 1.4 nm as function of the square of the -diameters (area). (c) & (d) are the same as (b) for the larger free layer thicknesses 1.6 and 1.8 nm respectively.

In Figure *4.1.2*(a) an example of the measured magnetoresistance close to zero field is shown for a device with a free layer thickness of 1.4 nm and a nominal diameter of D_n =100 nm. As expected from the VSM measurements for a device with such a free layer thickness, the magnetization of the free layer is orientated out-of-plane and exhibits a hysteretic behavior typical for an easy axis loop. Nonetheless, the hysteresis loop is not centered around zero field, this issue will be discussed in more detail in the next section.

The statistics of the extracted TMR values, as a function of the squared nominal diameters (area), are plotted in Figure *4.1.2*(b), 2(c), and 2(d) for the three free layer thicknesses 1.4, 1.6 and 1.8 nm respectively. Surprisingly, the maximum TMR of the clusters decreases as the MTJ device area becomes larger. This is observed for all three free layer thicknesses and is not expected from the TMR formula in Eq. 4.1.1.

The reason behind this unexpected behavior is that these pMTJs were deposited on a thick tantalum-nitride TaN bottom electrode (25 nm) that has a relatively high resistance, and which is the same for all diameters (see section 2.1 of chapter 2). This means that the TaN is not part of the MTJ nanopillar and therefore adds a constant serial resistance R_s independent of the nanopillar diameter leading to a modified expression for the measured TMR :

$$TMR = \frac{R_{ap} - R_p}{R_p + R_s} \tag{4.1.2}$$

Eq. 4.1.2 can be rewritten such that the intrinsic TMR_0 in the absence of a serial resistance $TMR_0 = \frac{R_{ap}-R_p}{R_p}$ is rescaled by a diameter dependent factor which reduces the TMR when the diameter increases. In Eq. 4.1.3 ρ_p is the resistivity of the parallel resistance

$$TMR = \frac{R_{ap} - R_p}{R_p} * \frac{1}{1 + \frac{R_s}{R_p}} = TMR_0 * \frac{1}{1 + \frac{R_s}{R_p}} = \frac{TMR_0}{1 + \frac{R_s}{\rho_p * t_{FL}} * \frac{\pi}{4} * D^2} \tag{4.1.3}$$

with $R_p = \rho_p * \frac{t_{FL}}{D_n^2 * (\frac{\pi}{4})}$. Fitting Eq. 4.1.3 shows that the serial resistance is around $R_s = 180\ \Omega$ (see Annex B for the derivations).

The corrections reveal that the pMTJs have an intrinsic $TMR \approx 124\%$, and a resistance-area product RA $\approx 6\ \Omega\,.\,\mu m^2$. The plots of TMR corrected for the serial resistance are shown Figure *4.1.3*(b).

To summarize, the more the pMTJ diameter is reduced, the more the measured TMR approaches the intrinsic TMR. This serial resistance will have an important consequence for the passive detection signal, discussed in chapter 5.

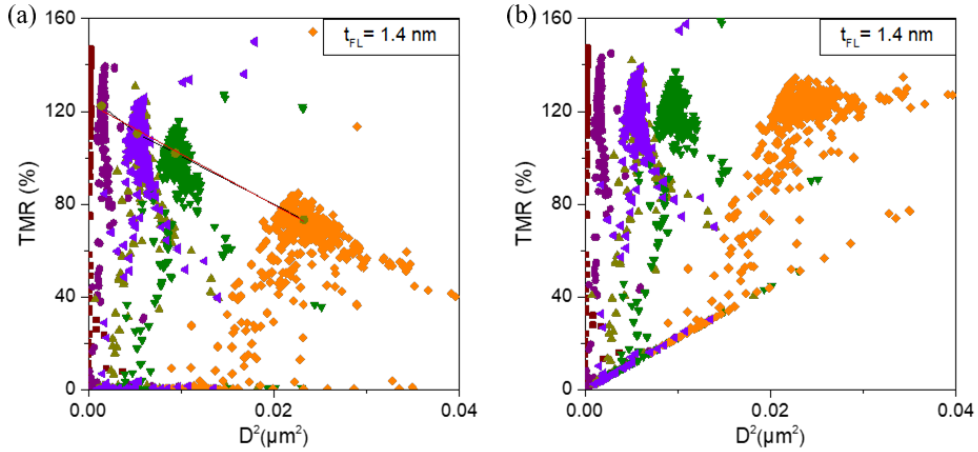

Figure 4.1.3 : (a) Fitting of the TMR distribution as a function of the junctions squared diameter and for a free layer thickness of 1.4 nm. (b) The TMR distribution after correction for the serial resistance from the bottom electrode TaN.

4.2 The pMTJs magnetoresistance at room temperature and low current

This section presents the TMR loops for the different free layer thicknesses, under different field orientations, at room temperature and in low current obtained via PPMS measurements. Fitting these MR loops based on the energy density given by Eq.3.1.9 in section 3.1 of chapter 3, we can extract useful parameters of the pMTJ stacks such as the value of iPMA energy constant K_i. The measurements conducted at room temperature are summarized in the following table (Table 4.2-1) :

Free layer thicknesses	Nominal diameter	Out-of-plane field $\boldsymbol{H}_{\perp}$	In-plane field $\boldsymbol{H}_{\parallel}$
1.4 nm, 1.6 nm, 1.8 nm	100 nm	[− 300 mT, +600 mT]	± 600 mT

Table 4.2-2 : summary of the static measurements at room temperature

The asymmetry in sweeping the out-of-plane magnetic field $H_{\perp}$ is done to avoid the switching of the bottom SAF layer.

4.2.1 The magnetoresistance at room temperature and low current for t_{FL} = 1.4 nm

The free layer reversal with a thickness of 1.4 nm is the first to be treated here, because it can be compared to the VSM magnetization loops of the continuous film shown in Figure *4.1.1*(a). It is easier to interpret for the magnetization orientations and its coercive fields offer a good way to track the static equilibrium and how they are affected by external factors, such as temperature and spin transfer torque, as will be considered in later sections (i.e. 4.3 and 4.4).

For the other free layer thicknesses they are treated in the next subsection 4.2.2. The results from both subsections and the explanations provided will be modeled in 4.2.3 and 4.2. 4.

The magneto-resistance measurements from a free layer with a thickness of 1.4 nm under out- and in-plane magnetic fields are shown in Figure *4.2.1*(a) and Figure *4.2.1*(b) respectively. The out-of-plane magnetic field measurement in Figure *4.2.1*(a) is in agreement with the continuous film measurements, it shows two hysteresis loops corresponding to the switching of the FL and PL layers. Starting from a strong positive magnetic field $\mu_0 H_\perp$ = 600 mT, where all the magnetizations are oriented in the same direction and then decreasing the field, leads to a first switching around 150 mT. The latter is attributed to the PL and T-SAF switching to be anti-parallel to the B-SAF, due to the exchange interaction. If the field is decreased further towards negative values, a second switching occurs near zero field that is attributed to the free layer switching. Further decreasing the field in the negative direction should lead to the switching of the B-SAF layer, however it is invisible in the magnetoresistance measurement. In addition, the field sweeping in the negative direction is stopped at – 300 mT to avoid this switching, and to preserve the B-SAF fixed in one direction. These interpretations are illustrated by the colored arrows in Figure *4.2.1*(a).

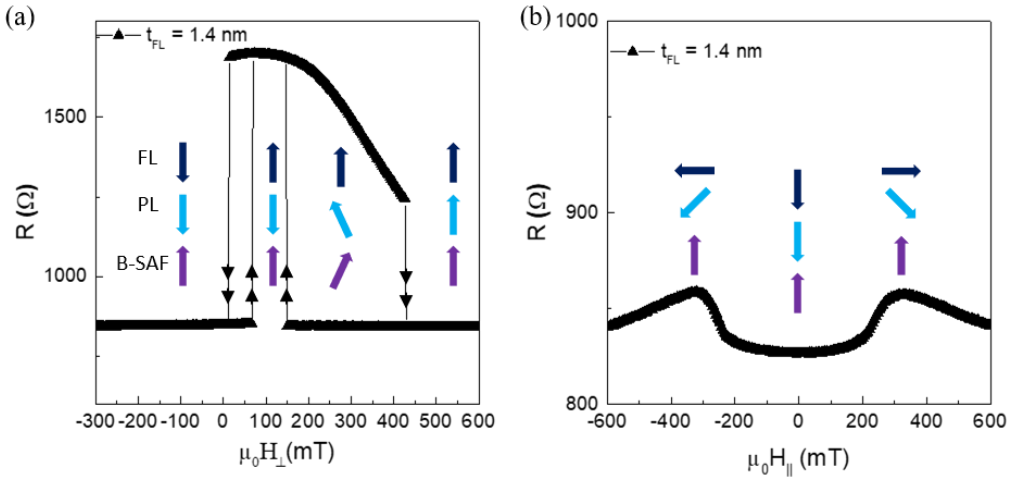

Figure 4.2.1 : (a) Magnetoresistance of pMTJ devices of $t_{FL} = 1.4nm$ and $D_n = 100nm$ measured for an out-of-plane field ($H_\perp$). (b) The same as (a) for in-plane field $H_\parallel$. The colored arrows indicate the orientations of the different magnetic layers and the black arrows shows the field sweeping direction. B-SAF is the bottom SAF layer, FL the free layer, and PL the composite polarizing layer including the top SAF layer (see section 2.1.1 of chapter 2).

If the magnetic field was swept from negative values to positive values, the same explanations for the switching holds. However, for the PL magnetoresistance there is a difference between the two field sweepings. For the positive to negative sweeping, the magnetoresistance seems to have only two states, while in the negative to positive sweeping the PL gradually rotates away from the perpendicular orientation before it switches. The latter is the normal response of SAFs, where the two layers rotate away from their equilibrium direction prior to the switching. For the former behavior where the PL magnetoresistance is constant, it might be due to the dipolar field coupling of the layers oriented all in the same direction at high positive field.

The dipolar field favors the parallel alignment and helps the bias field, while the dipolar field in the antiparallel state supports the reversal to the antiferromagnetic state.

A further observation of Figure *4.2.1*(a) is that the hysteresis loop of the free layer is not centered around zero field. Its center is shifted to the positive fields by $H_{\perp} \sim 40$ mT, due to the not-fully compensated SAF stray field. The positive sign of the stray field indicates that it is coming from the top layer of the SAF.

For the in-plane magnetic field measurements, in Figure *4.2.1*(b), the changes in the magnetoresistance values are generally small, which indicates that the angle between the FL and PL layer magnetization is weakly affected by the in-plane field. Since both layers have an in-plane hard axis, this can be explained by the gradual rotation from out- to in-plane of both magnetizations at similar rates, and thereby keeping the angle between them quasi-constant. However, for higher in-plane magnetic fields above ~ 200 mT, the magnetoresistance starts to increase slightly with the field, has a maximum around 350mT and then starts to decrease. The increase in resistance is attributed to the free layer getting closer to in-plane saturation, where the field of the maximum resistance can be taken roughly as the in-plane saturation field. The following decrease in resistance is then attributed solely to the rotation of the PL magnetization. More analysis on this interpretation will be presented in the fitting subsections.

4.2.2 The magnetoresistance at room temperature and low current for t_{FL} = 1.6 nm and t_{FL} = 1.8 nm

The magnetoresistance loops, for the two free layer thicknesses 1.6 nm, and 1.8 nm, are compared to t=1.4nm in Figure *4.2.2*(a)-(b) for devices with a nominal diameter of $D_n = 100$ nm, and under an out-of-plane ($H_{\perp}$) and in-plane ($H_{\parallel}$) magnetic fields respectively.

The out-of-plane magnetoresistance loops in Figure *4.2.2*(a), show that the increase in the free layer thickness changes the square hysteresis loop observed for t_{FL} = 1.4 nm to an s-shape, indicating that the out-of-plane orientation is a hard axis, where the saturation field increases with increasing thickness. The TMR at zero field is not at 50% because of the stray field from SAF, it reorients the magnetization slightly out-of-plane towards the parallel state.

For the in-plane magnetoresistance loops, in Figure *4.2.2*(b), increasing the free layer thickness changes the shapes of the MR loops. For t_{FL} = 1.6 nm, since the free layer is softer, its reorientation to the in-plane field directions occurs at much smaller field compared to t_{FL} = 1.4 nm (for 1.4nm this is 350mT while for 1.6nm this is <100mT). For higher fields, the free layer is expected to be in-plane and the reduction in resistance is attributed to the rotation of the polarizing layer towards the in-plane direction.

For pMTJs with a free layer thickness of t_{FL} = 1.8 nm, it is expected to have an in-plane easy axis, as shown in the out-of-plane measurements, and therefore the in-plane field measurement reveals only the rotation of the polarizing layer leading to a continuous decrease of the resistance starting at zero field.

These different interpretations of the equilibrium orientations of the free and polarizing layers are discussed more in the next subsections where the magnetoresistance loops are fitted to extract the iPMA value.

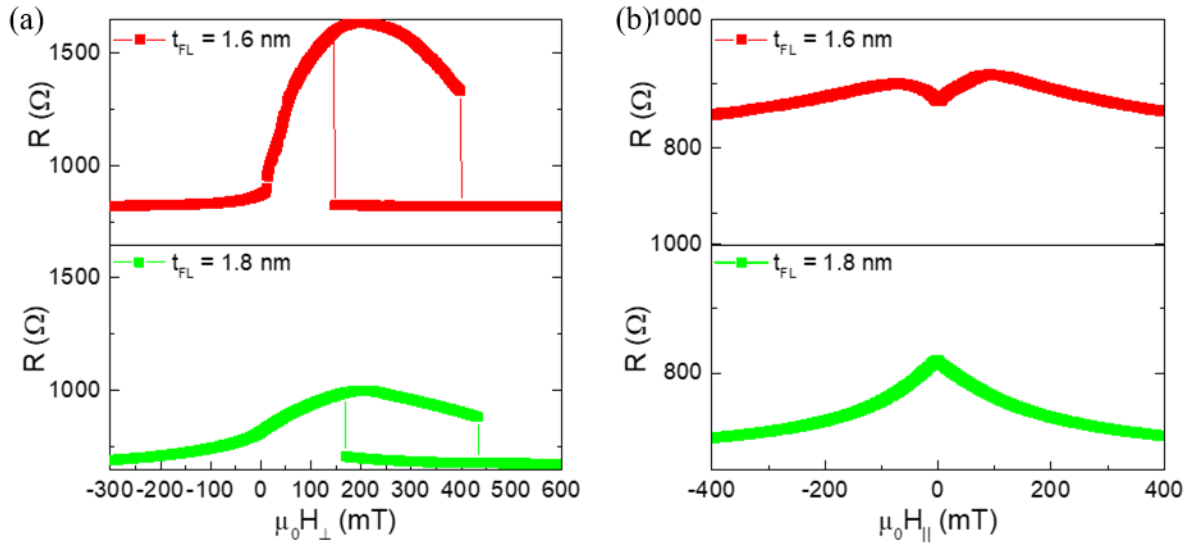

Figure 4.2.2: (a) Magnetoresistance loops of pMTJ devices of $t_{FL} = 1.6\,nm$ (in red) and $t_{FL} = 1.8\,nm$ (in green), with $D_n = 100\,nm$ measured for out-of-plane field ($H_\perp$). (b) The same as (a) for in-plane fields $H_\parallel$. Please note that the resistance scales in (a) and (b)are different

4.2.3 Fitting of the magnetoresistance loops for out-of-plane magnetic fields

Using the total energy density given in section 1.1 of chapter 1, here the magnetoresistance loops are fitted to extract the interfacial perpendicular magnetic anisotropy (iPMA). The approach consists of using the saturation magnetization M_s from published experimental works on similar magnetic tunnel junctions [113], and fitting the magnetoresistance loop to determine the value of the iPMA energy constant. The fitting focuses first on the FL with t_{FL} = 1.4 nm, due to its square hysteresis loop, and afterwards the fitted parameters are tested on the other FL thicknesses to check their validity.

The magnetoresistance loop of the FL obtained through the minimization of its total magnetic energy is shown in Figure *4.2.3*(a) in red. The simulation in Figure *4.2.3*(a) corresponds to a device with a free layer thickness of 1.4 nm and a nominal diameter of 100 nm. For the simulations the real values of the diameters were used ($D \approx D_n$ + 30 nm), it will be the case for all the coming simulations. The coefficient of the interfacial perpendicular magnetic anisotropy K_i was extracted by fitting the experimental measurements obtained from a device with the same thickness and diameter. The volume average anisotropy constant is found to be approximately $K_u = \frac{K_i}{t_{FL}(1.4\ nm)} = 600\ kJ/m^3$, which is in agreement with published iPMA values, i.e. [114]–[116].

The corresponding value of $K_i = 8 * 10^{-4}$ J/m² of the iPMA obtained from the fitting of t_{FL} = 1.4 nm is used to simulate the magneto-resistance loops for the other two free layer thicknesses (1.6 nm, 1.8 nm). In Figure *4.2.3*(b) the simulations (in purple) are compared to the experimental results (red and green respectively). The value of M_s used is $M_s = 10^6\ A/m$.

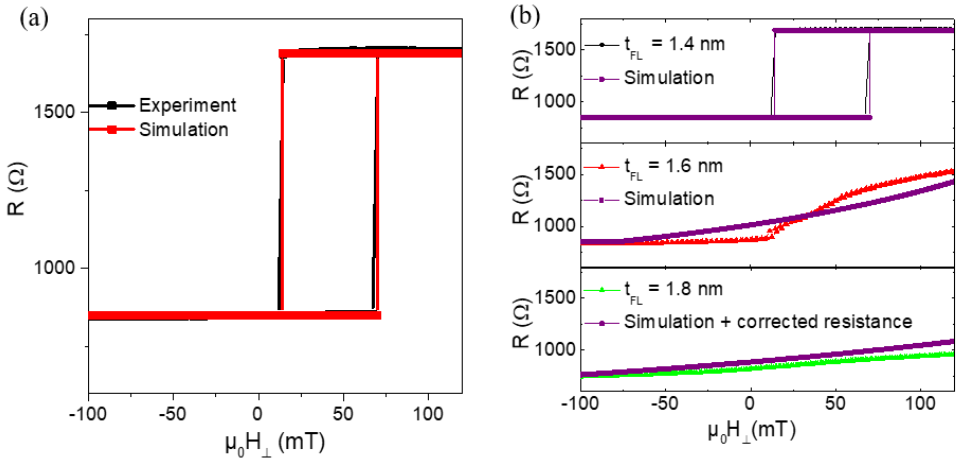

Figure 4.2.3 : (a) Fitting of the out-of-plane magnetoresistance loops of device with free layer thickness of t_{FL} = 1.4 nm and a nominal diameter of D_n = 100 nm. (b) Using the K_i from fits in (a) to simulate the magneto-resistance loops of t_{FL}=1.6 and 1.8 nm using $M_s = 10^6\ A/m$, $K_i = 8.4e-4\ J/m^2$, and $\mu_0 H_{int\perp} = 42\ mT$ for the out-of plane stray field coming from the uncompensated SAF.

The comparison in Figure *4.2.3*(b), between the experimental results and the simulations, shows that the derived model describes well the magnetoresistance loops. It also confirms the interpretation provided earlier on the FL equilibrium orientation, such that the free layer magnetization is oriented out-of-plane for $t_{FL} = 1.4$ nm, intermediate for $t_{FL} = 1.6$ nm, and in-plane for $t_{FL} = 1.8$ nm while the PL was considered to be fixed and out-of-plane.

The free layer orientation is determined by $H_{ueff} = H_u - H_d$ (see Eq. 3.1.9 in section 3.1 of chapter 3), when it is positive then the free layer is oriented out-of-plane and when it is negative the free layer is oriented in-plane. It is dependent on the free layer thickness and diameter through H_u and H_d. For the magnetic anisotropy H_u, it is inversely dependent on the thickness ($K_u = K_i/t_{FL}$), therefore increasing the free layer thickness reduces H_u (see Eq. 3.1.9). For the demagnetizing field H_d, as was discussed in section 3.1 of chapter 3, it is dependent on both the free layer thickness and diameter through the demagnetizing factors (N_x, N_y, N_z). It is proportional to the difference of N_z and $2N_x$ (see Eq. 3.1.9). The dependence of the demagnetizing field factors is shown in Figure 4.2.4(a)-(b) as a function of the FL diameter and for different FL thicknesses.

The demagnetizing factors in Figure 4.2.4 are dominated by N_z and they change very little with the thickness but noticeably with the diameter.

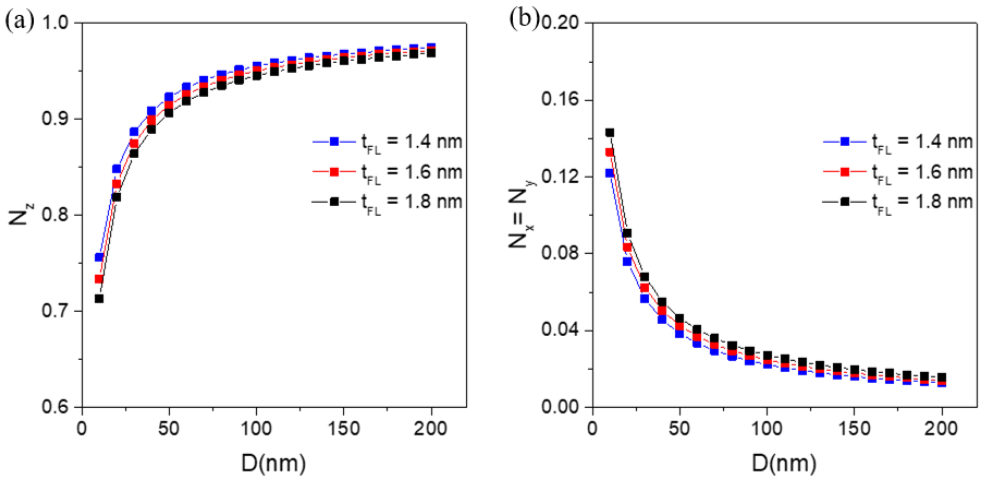

Figure 4.2.4 : (a) The demagnetizing factor N_z plotted as a function of the FL diameter and for the different thicknesses. It was calculated using the method discussed in section 3.1 of chapter. (b) The same as (a) but for the N_x and N_y demagnetizing factors.

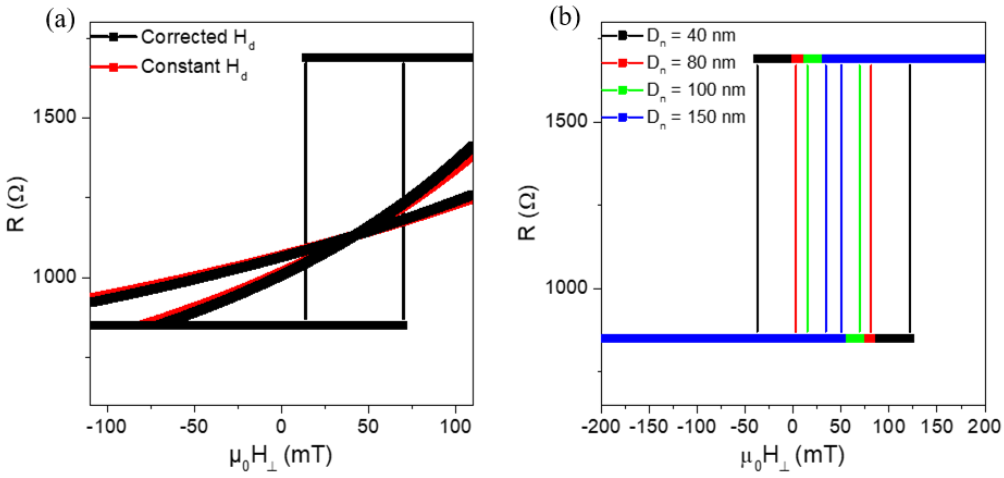

Figure 4.2.5 : (a) Comparison of the simulated FL magnetoresistance loops for three free layer thicknesses (1.4, 1.6, and 1.8 nm) with constant demagnetizing factors in red and by correcting for the demagnetizing factors in black. (b) Simulations of the magnetoresistance of a FL with a thickness of 1.4 nm and nominal diameters varying from D_n = 150 nm to D_n = 40 nm.

The sensitivity of the free layer magnetization orientation to slight changes in its thickness is investigated in Figure 4.2.5(a).

For the red plots the demagnetizing factors were kept constant as the free layer thickness changes, and in the black plots the correct demagnetizing factors are used. The plots confirm that the effect of the demagnetizing field is negligible when the free layer thickness changes from 1.4 nm to 1.8 nm.

Hence, the thickness dependence of the perpendicular anisotropy is the dominant effect behind the reorientation of the free layer magnetization observed in Figure 4.2.5(a).

However, unlike the free layer thickness variations, changing the nanopillar diameter changes noticeably the demagnetizing field and affects the magnetization equilibrium. The effect of the MTJ diameter is simulated in Figure 4.2.4(b) for a FL thickness of 1.4 nm. It can be seen that the coercive field increases noticeably as the nominal diameter decreases from 150 nm to 40nm.

It should be reminded here, that the simulations were conducted using the real diameters ($D \sim D_n + 30$ nm).

4.2.4 Fitting of the magnetoresistance loops for in-plane fields

Next the same fitting procedure is used to analyze the magnetoresistance loops under in-plane magnetic field, shown Figure *4.2.2*(b). Under an in-plane magnetic field, if the polarizing layer is fixed out-of-plane, with a free layer of thickness 1.8 nm (in-plane), the model predicts a constant magnetoresistance. However, the experimental measurements Figure *4.2.3*(b) show a magnetoresistance that continuously decreases. This decrease results from the polarizing layer that is gradually rotating towards the in-plane magnetic field direction.

To include the reorientation of the polarizing layer magnetization in the fitting, its equilibrium is also calculated with the same approach described in section 2.1 of chapter 2. The difference to the FL parameters is that it experiences a much stronger constant out-of-plane field, coming from the interlayer exchange coupling to the SAF and a weaker anisotropy. The parameters used in the simulations are summarized in table *Tableau 4.2.1* :

Layer	M_s (A/m)	K_u (kJ/m^3)= $K_i\left(\frac{1.4nm}{t_{FL}(nm)}\right)$	$\mu_0 H_{int\perp}$(mT)	N_z	$N_x = N_y$
FL	10^6	600	42 mT	0.955835	0.022082
PL	10^6	400	450 mT	0.953882	0.023059

Tableau 4.2.1 : The value of the parameters used in the fitting of the magnetoresistance loops.

The parameters (iPMA and $H_{int\perp}$) of the polarizing layer are obtained by fitting the in-plane magnetoresistance measurements, starting with the free layer thickness $t_{FL} = 1.8$ nm for which the FL magnetization is directed in-plane. The latter guarantees that the variations of the magnetoresistance are due solely to the reorientation of the magnetization of the polarizing layer.

The results of the simulations of different free layer thicknesses, under an in-plane field are plotted in Figure *4.2.6*(a) and the fit parameters are given in Tableau *4.2.1*. They show an overall agreement with the magnetoresistance loops in Figure *4.2.2*(b). It can be seen that for the free layer of thickness 1.4 nm, under in-plane magnetic fields lower than 50 mT, the magnetoresistance is quasi-constant as in the measurements in Figure *4.2.1*.(b). Similarly, for higher magnetic fields, it starts to increase towards a maximum before it decreases.

The behavior of the FL for this thickness is due to the simultaneous rotation of both the FL and the PL magnetizations towards the in-plane field direction. In particular the field range of quasi-constant resistance is caused by the fact that both layers rotate at the same rate as is illustrated in Figure *4.2.6*(b) where the equilibrium angles of both magnetizations, under in-plane field, are plotted.

Moreover, the simulations in Figure *4.2.6*(a), show that increasing the FL thickness reduces the field range of the quasi-constant resistance, which means that the FL saturates in-plane at smaller and smaller fields. This explains the magnetoresistance behavior for the FL thicknesses of 1.6 nm and 1.8 nm.

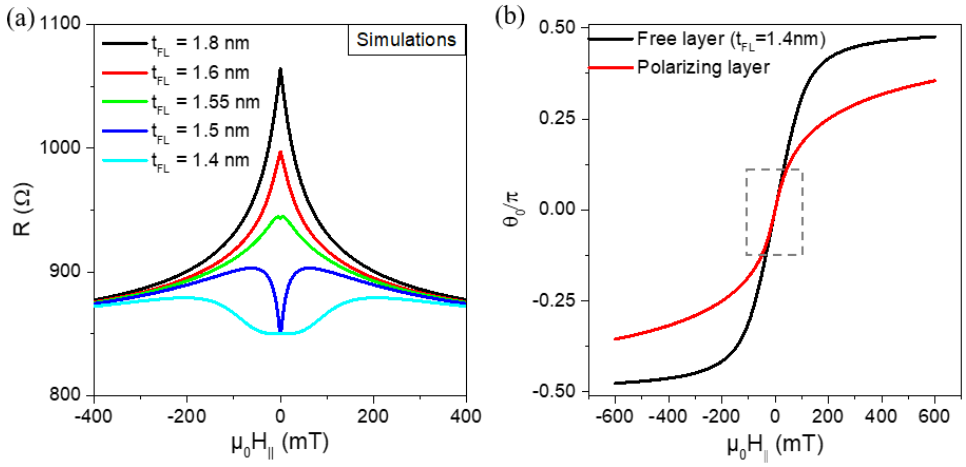

Figure 4.2.6 : (a) Simulations of the magnetoresistance for pMTJs with 100 nm of diameter and for different free layer thicknesses. (b) Comparison of the polar equilibrium angles of the free (in black) and polarizing (in red) layers. For the parameters used here see Tableau 4.2.1.

To conclude, the measured magnetoresistance loops of the different free layer thicknesses, and for two field orientations, were studied using an analytic approach based on the macrospin model. The simulations confirm the orientations of both the free and the polarizing layer magnetizations. The extracted parameters will be used for the magnetization dynamics analysis in chapter 5.

In the next sections, the discussion will be expanded to include the temperature dependence of the magnetization, which will be later on compared to the dependence on an injected dc current to distinguish between effects coming from Joule heating and the spin transfer torque.

4.3 Temperature dependence of the pMTJ magnetoresistance

The study of the temperature dependence of the magnetoresistance for perpendicular magnetic tunnel junctions is an essential step to understand how their internal magnetic parameters are affected by heat. Especially, at room temperature heating in pMTJs can be induced by dc currents or by rf power through Joule heating.

For this purpose, the magnetoresistances corresponding to the three free layer thicknesses were measured as a function of temperature, under both out-of-plane and in-plane magnetic fields.

The discussion starts with the temperature dependence of the free layer magnetization for the thickness of 1.4 nm, under out-of-plane field. Afterwards, the conclusions will be generalized to the other thicknesses 1.6 nm and 1.8 nm. The choice of the free layer of thickness 1.4 nm is because the temperature effect is mostly on the interfacial perpendicular anisotropy (iPMA) and the saturation magnetization. Thus, a magnetic layer with an out-of-plane easy axis, such as $t_{FL} =$ 1.4 nm allows the detection of these changes in the iPMA through the coercive field.

4.3.1 Temperature dependence of the magnetoresistance under out-of-plane field

The results for a device with a nominal diameter of 100 nm are shown in Figure *4.3.1*(a). As the temperature decreases from 300 K to 200 K, the coercive field in Figure *4.3.1*(a) increases indicating that the iPMA is increasing as the temperature decreases. The coercive field was taken as difference between the positive and negative reversal fields of the magnetoresistance loops (as $|(H_{P\text{-}AP} - H_{AP\text{-}P})|$).

Interestingly, the perpendicular magnetic stray field emanating from the not-fully compensated SAF (at the origin of the FL loops shifts) is also changing with temperature between 40 and 50 mT, with an average value of ≈ 42 mT. The parabolic shape could probably be due to the simultaneous variations in the overall parameters of the magnetic layers in the stack, such as the M_s, iPMA, and the exchange coupling.

The temperature dependence of the coercive field arises from the temperature dependence of the anisotropy. In general, the temperature dependence of the uniaxial anisotropy is given by the Callen-Callen law [117]:

$$K_u(T) = K_{u0}\left(\frac{M_s(T)}{M_{s0}}\right)^{\xi} \tag{4.3.1}$$

where K_{u0} is the uniaxial anisotropy coefficient at zero temperature, M_{s0} the saturation magnetization at zero temperature, and $M_s(T)$ the temperature dependent saturation magnetization.

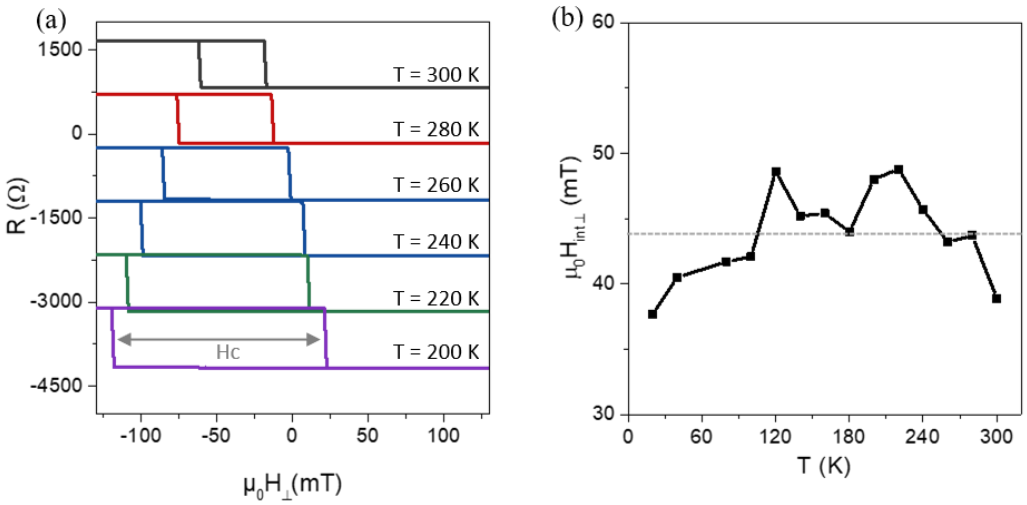

Figure 4.3.1 : (a) Magnetoresistance loops of a pMTJ device with free layer thickness of 1.4 nm and a nominal diameter of 100 nm, as a function of the out-of-plane magnetic field and for temperatures ranging between 200 K and 300 K. The plots are offset vertically for a better illustration. (b) The extracted perpendicular stray field $H_{int\perp}$ from the not-fully compensated synthetic anti-ferromagnet as function of the temperature. It was extracted from the loops in (a) by evaluating the field shift of the loops center from zero.

The power coefficient ξ is usually between 2 and 3 [113]. The temperature dependent saturation magnetization it is given by the Bloch law [45]:

$$M_s(T) = M_{s0}\left(1 - \left(\frac{T}{T_c}\right)^{\frac{3}{2}}\right) \tag{4.3.2}$$

where T_c is the Curie temperature of the magnetic layer (taken as 1200 K [113]), and T the temperature of the sample.

Including the temperature dependencies of Eq. 4.3.1 and Eq. 4.3.2 in the energy minimization procedure from section 3.2 of chapter 3, and using a power coefficient $\xi = 2.5$, yields a good correlation to the experimental measurements of the coercive field H_c as shown in Figure *4.3.2*(a), where the experimental and the simulation results are plotted together. However, below 100 K the coercive field from the experiment is somewhat larger than the simulations.

The temperature dependence of the interfacial perpendicular magnetic anisotropy K_i, corresponding to the simulated coercive fields, is plotted in Figure *4.3.2*(b).

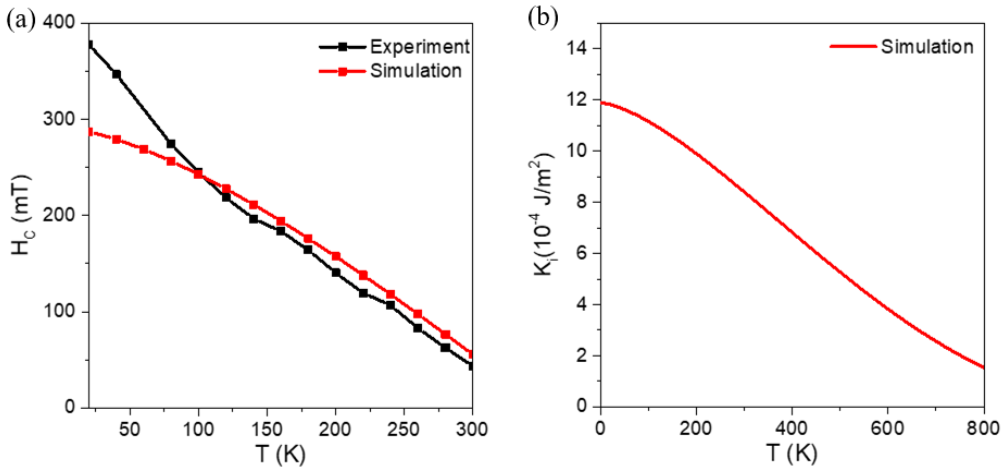

Figure 4.3.2 : (a) coercive field H_c extracted from the experimental results in Figure 4.3.1(a) in black, and the coercive field obtained by macrospin simulations in red. (b) the simulation of the temperature dependence of the interfacial perpendicular magnetic anisotropy using Eq. 4.3.1.

The experimental temperature dependence of the switching fields is summarized in Figure *4.3.3*(a), and also in Figure *4.3.3*(b) that shows the 3D contour plots of the magnetoresistances as a function of temperature and the out-of-plane magnetic field, called the switching diagram. They show that the switching fields are symmetric with the temperature. The latter will serve as a reference for comparison when the STT effects are discussed later on in section 4.4. To note, in Figure *4.3.3*(a)-(b) the hysteresis loops were corrected for the shift caused by the SAF stray field ($H_{int\perp}$).

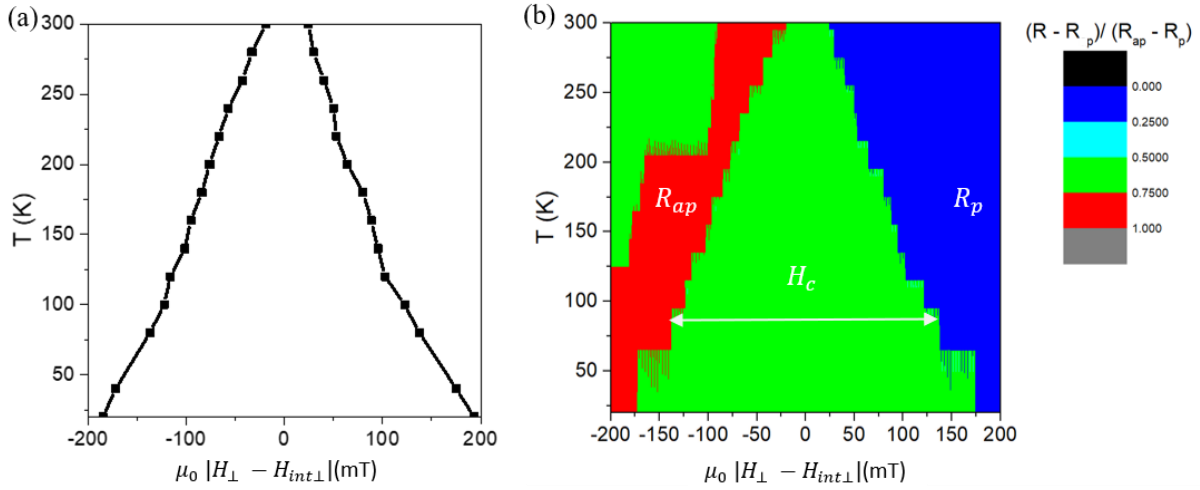

Figure 4.3.3 : (a) The positive (transition from AP to P) and negative (transition from P to AP) switching fields of the FL are plotted as a function of the temperature and out-of-plane field, where the loop shift was subtracted. (b) The switching diagram representing the 3D contour plot of the magnetoresistance as a function of temperature and the out-of-plane magnetic field.

4.3.2 Temperature dependence of the TMR

The temperature has also a strong effect on the tunneling magnetoresistance (TMR) of the junctions. This phenomenon has been thoroughly studied in the past [118]–[120]. However, its characterization remains an important step, because the TMR is necessary to probe the magnetic state electrically and the amplitude of the measured dynamic signals scales with the TMR.

The temperature dependence of the resistances (R_p and R_{ap}) and the TMR are shown in Figure *4.3.4* (a)-(b). The TMR decreases from 170% at 20 K to 100% at 300 K, which is mainly due to a strong variation of the resistance in the AP state, while the P state resistance does not change.

To understand this phenomenon, many models have been proposed in the past, in which some have good agreement with experiments. In general, the dependence of the tunneling conductance (resistance) on temperature can be classified into two groups : one for spin-independent tunneling, and another for spin-dependent tunneling.

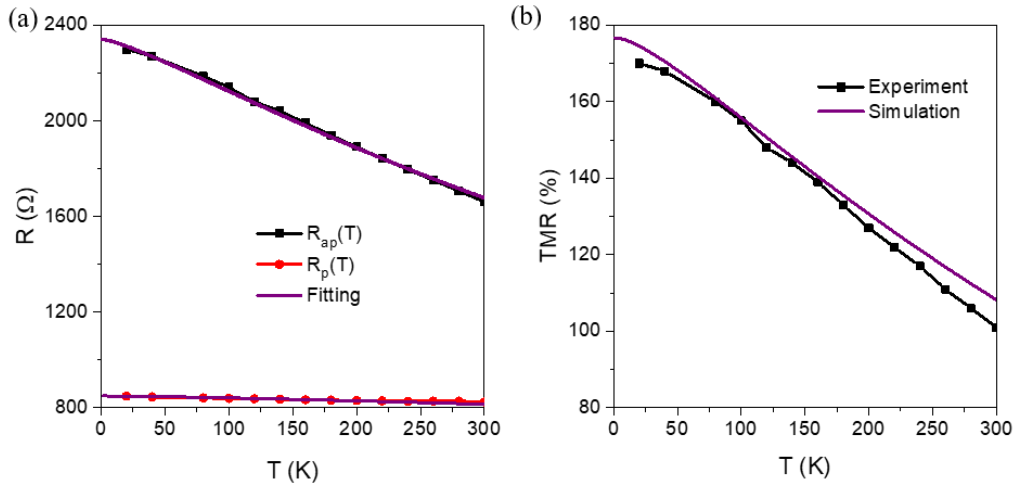

Figure 4.3.4 : (a) the temperature dependence of the parallel and anti-parallel resistance respectively in black and red, along with the fitting from the analytical model in purple. The fitting parameters are : Q = 0.07, $E_m = 121\,meV$, S = 3/2, $\xi = 0.3$, and $E_C = 0.14\,meV$. (b) The temperature dependence of the measured TMR in black and the fitted TMR from (a) in purple.

For the spin-independent tunneling, the temperature dependence is caused by the thermal smearing of the Fermi level. It excites electrons to energy states above the Fermi level (called hot electrons), which can then tunnel through a lower energy barrier, and thus the conductance increases, see Figure 3 in [121]. The increase in the tunneling conductance due to thermal smearing is expressed by the following conductance formula, first derived in [122] :

$$G(T) = G_0 * \frac{CT}{\sin(CT)} \tag{4.3.3}$$

with $C = 1.387 * 10^{-4} * d/\sqrt{\phi}$, where d is the barrier thickness in (Å) and ϕ the barrier height in (eV). The barrier height of MgO is $\phi \approx 3.5$ eV [118]. Hence, for pMTJs with an MgO thickness of 1 nm the formula predicts a smearing effect on resistance around $\left(\frac{G(T)}{G_0}\right)^{-1} \approx 1.75\%$. Thus, the smearing effect in the pMTJ is very weak, however, it will be included in the overall fitting.

The weakness of the thermal smearing indicates that the TMR decrease with temperature is dominated by the spin dependent tunneling. Two models have been proposed for this, with the first one linked to the spin polarization [120], while the second one linked to magnon generation [119]. For the model based on the spin polarization, it considers the spin polarization to be proportional to the saturation magnetization (exchange field), and hence it could be approximated by the Bloch law in Eq. 4.3.2. However, the model does not predict the weak and strong temperature dependencies of the parallel and anti-parallel resistances respectively. Contrary to the magnon generation model proposed by Zhang et al. in [119] that predicts the difference in the temperature dependencies of R_p and R_{ap}. For low voltages, their formalism is simplified and the temperature dependence of the resistance is expressed by the formulas given in [118]:

$$R_p(T) = R_p(0) * \left[1 + Q * \xi * \frac{2S}{E_m} * k_B T * ln\left(\frac{k_B T}{E_C}\right)\right]^{-1} \quad (4.3.4)$$

$$R_{ap}(T) = R_{ap}(0) * \left[1 + Q * \frac{2S}{E_m} * \frac{1}{\xi} * k_B T * ln\left(\frac{k_B T}{E_C}\right)\right]^{-1} \quad (4.3.5)$$

with Q standing for the efficiency of the magnon generation, S the spin parameter, $E_m(meV) = \frac{3k_B T_C}{S+1}$, with T_C the Curie temperature, $E_C(meV)$ is the magnons generation cut-off, and $\xi = \frac{\rho_p * \rho_{ap}}{\rho_p^2 + \rho_{ap}^2}$ the ratio of the density of states. The model predicts that the antiparallel resistance changes are more important than the parallel resistance changes, because of their inverse dependence on ξ that is less than one.

The combination of the magnon generation model with the weak smearing effect gives a good fitting of the experimental temperature dependence of the TMR as seen in Figure *4.3.4*(a). The values of the parameters in Eqs. 4.3.4 and 4.3.5 are included in the legend of Figure *4.3.4*(a). These results, will allow the TMR temperature dependence to be included in the analytical modeling of the pMTJs.

4.3.3 Temperature dependence of the magnetoresistance under in-plane field

In the following the acquired understanding of the magnetization temperature dependence in an out-of-plane magnetic field, for $t_{FL} = 1.4\,nm$, is generalized to the in-plane magnetic field measurements.

In Figure *4.3.5*(a) are plotted the measurements of the magnetoresistance in an in-plane magnetic field, and for temperatures increasing from 200 K to 300 K.

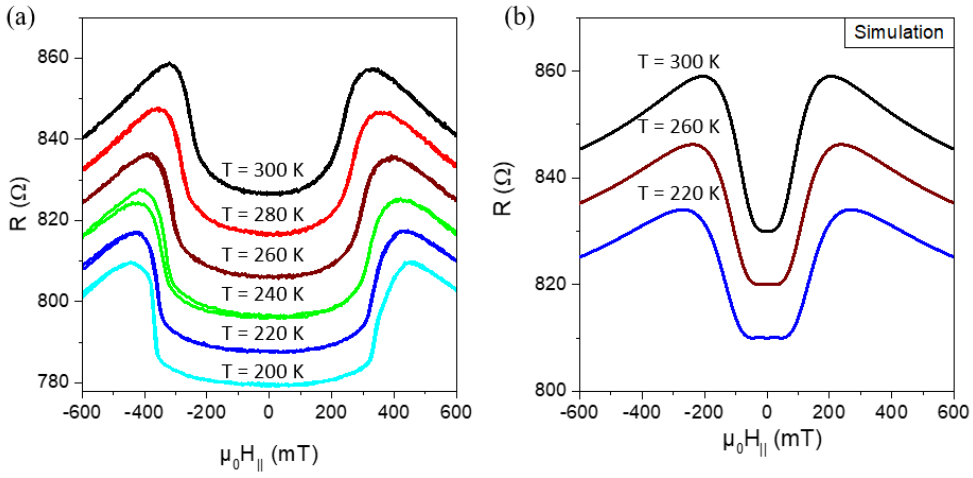

Figure 4.3.5 : (a) Measurements of the magnetoresistances of a device with $t_{FL} = 1.4\,nm$ and $D_n = 100\,nm$, as a function of an in-plane magnetic field and temperature. (b) Simulation of the magnetoresistance of a device with the same dimensions as in (a) as a function of an in-plane magnetic field and temperature. The plots are offset vertically for a better illustration.

As the temperature increases the central region, with quasi-constant resistance, reduces in size. This is a direct consequence of the reduction of the iPMA by the increasing temperature. It reduces the iPMA of the free and the polarizing layers simultaneously, and leads them to rotate more easily towards the in-plane magnetic field. This is qualitatively confirmed by the simulations in Figure *4.3.5*(b). Here, the simulations were done using the same macrospin model used above in section 4.2 to describe the magnetoresistance under an out-of-plane magnetic field, and with the same parameters values.

4.3.4 Temperature dependence of the magnetoresistance for t_{FL} = 1.6 nm and t_{FL} = 1.8 nm

For the other two thicknesses of the free layer, t_{FL}=1.6 nm and 1.8 nm, the same conclusions of the temperature dependence as for 1.4 nm can be drawn. Figure *4.3.6*(a) and (b) show the measurements of the magnetoresistances, for the free layer thicknesses 1.6 nm and 1.8 nm for out-of-plane magnetic fields. For t_{FL}=1.6nm, as the temperature decreases from 300 K to 200 K, the iPMA increases until it becomes stronger than the demagnetizing field, so that the free layer reorients towards the out-of-plane direction which becomes the easy axis. This occurs around T = 260 K, where the loop shape changes to a square hysteresis loop. For t_{FL} = 1.8nm, the loops remain S-shaped, indicating that in this temperature range the increase in anisotropy is not enough to reorient the free layer magnetization.

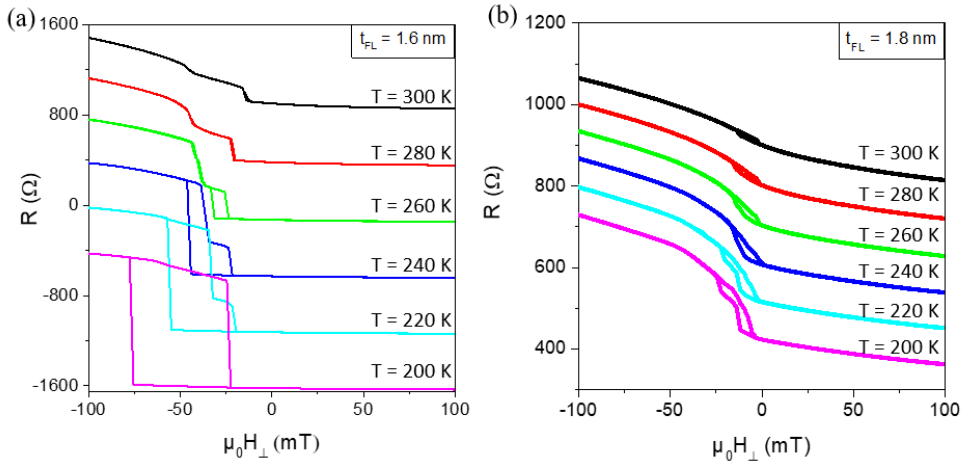

Figure 4.3.6 : (a) Measurements of the magnetoresistance of a device with $t_{FL} = 1.6\ nm$ and $D_n = 100\ nm$, under an out-of-plane field and for different temperatures. The plots are offset vertically for a better illustration. (b) The same as in (a) for a device with $t_{FL} = 1.8\ nm$.

To conclude, the overall analysis done so far permitted the determination of the initial conditions of the magnetizations of the free and polarizing layers. The static behavior of the free layer magnetization is well understood in the framework of the macrospin model.

In spintronics the applications requires an external bias current (voltage) to control the magnetization state. This essential parameter will be the subject of the next section.

4.4 Current dependence of the perpendicular magnetic tunnel junctions

The application of an external bias current (voltage) to a magnetic tunnel junction unfolds a number of diverse and interesting phenomena. It can modify the magnetization state through the self-heating (Joule heating), or through the transfer of spin angular momentum. In addition to these two effects that act through the injected current, there are other effects that act through the electric field (voltage) known as “voltage controlled magnetic anisotropy” (VCMA). The distinction between these effects is not straightforward.

To distinguish the different effects, we first analysis here the magnetic hysteresis loops. In chapter 6 the analysis will be supported by ferromagnetic resonance experiments.

4.4.1 Current dependence of the reversal of the free layer t_{FL} = 1.4 nm

The discussion starts with the current dependence for the free layer with a thickness of 1.4 nm under out-of-plane field and the conclusions can be used to explain the dependencies for the other thicknesses.

The magnetoresistance hysteresis loops for the free layer reversal for positive and negative currents are shown in Figure *4.4.1*(a) and Figure *4.4.1*(b) respectively. Here the measurement temperature was set to 200 K so that it can be compared with the pure temperature (T) dependence presented in the previous section. In addition, for convenience, the measurements are carried out upon applying a DC current instead of voltage.

For small bias currents below |I| = 0.3 mA, the hysteresis loops in Figure *4.4.1*(a)-(b) show a similar dependence. But for higher current values, clearly, the coercive field reduces much more for the case of the negative currents. The coercive field is defined as $|(H_{P\text{-}AP} - H_{AP\text{-}P})|$ where $H_{P\text{-}AP}$ ($H_{AP\text{-}P}$) is the reversal field for transition from P to AP (AP to P). The variation of the coercive field with the current is summarized in Figure *4.4.2*(a), where an asymmetry in current sign is evident. For a current of the magnitude |I| = 0.5 mA, there is a difference of 45 mT in the coercive field between the two current signs.

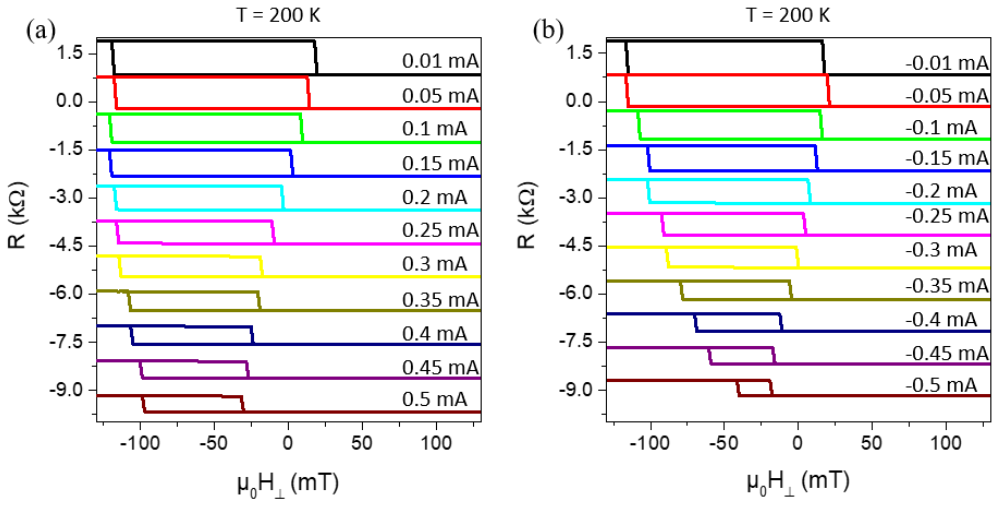

Figure 4.4.1 : (a) The magnetoresistance loops as a function of the out-of-plane magnetic field for different positive bias currents (mA). (b) the same as (a) for negative bias current (mA).

To visualize better, the asymmetry in the coercive field with current sign, Figure *4.4.2*(b) displays the 3D contour plot of the magnetoresistance as a function of the current and the out-of-plane field. The green area corresponds to the bi-stable region of the hysteresis loop, with the switching fields $H_{P\text{-}AP}$ and $H_{AP\text{-}P}$ at its boundaries. The switching fields are asymmetrical with the current sign. The negative current reduces the negative switching field more than the positive current.

The positive current does the inverse, it reduces the positive switching field more. In general, these are expected consequences of the spin transfer torque switching [17], and will be discussed next.

It is reminded, that negative current means that the electrons are flowing from the free layer to the polarizing layer and positive current means that the electrons are flowing from the polarizing to the free layer. The STT therefore is expected to destabilize the anti-parallel state for positive current and to destabilize the parallel state for negative current .

However, the asymmetry does not exclude the presence of other current (or voltage) induced phenomena such as the VCMA and the Joule heating.

To sort out their different contributions to the magnetization switching, they will be addressed separately to predict their effects. Starting with the STT, then the Joule heating, and finally the VCMA.

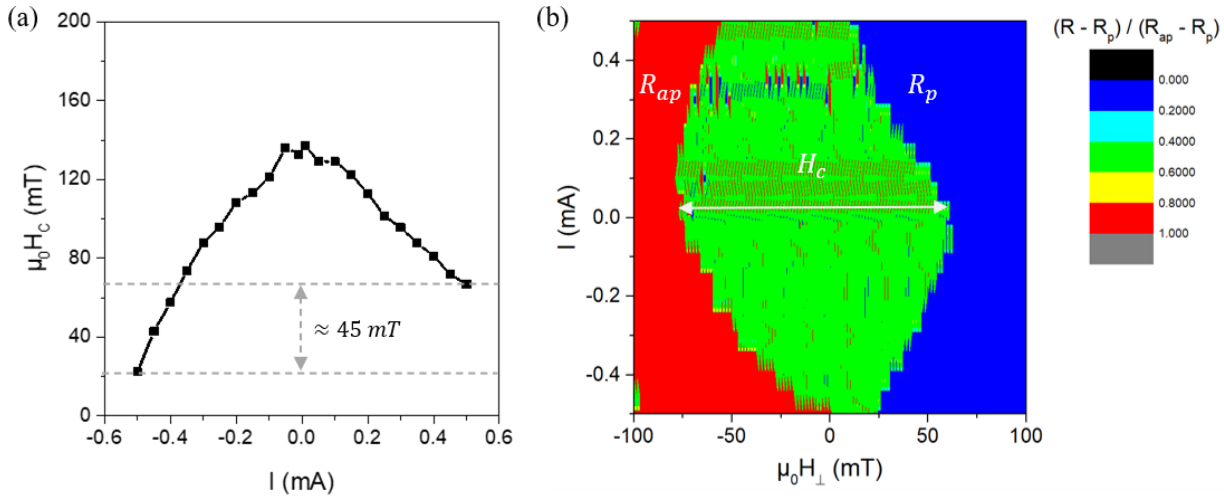

Figure 4.4.2 : (a) The coercive field as a function of the bias current, it is extracted from the measurements shown in Figure 4.4.1. (b) The magnetization switching diagram by plotting the 3D contour of the magnetoresistance loops as a function of current and out-of-plane magnetic field. The switching fields are defined as the boundaries of the green area. Here the stray field coming from the synthetic antiferromagnet was subtracted to center the plots around zero.

4.4.1.1 The characterization of the spin transfer torque

The STT effect on the switching fields can be studied using the linearized LLG equation formalism established in section 3.2 of chapter 3. There it was deduced that the critical currents for the P and AP states have the following expressions :

$$J_{c_{P\to AP}} = -\frac{2e}{\hbar} * \frac{\mu_o M_s t_{FL}}{\eta} * \alpha * \left(H_\perp - H_{ueff}\right) * \frac{1}{(1-\alpha\beta)} \qquad (4.4.1)$$

$$J_{c_{AP\to P}} = -\frac{2e}{\hbar} * \frac{\mu_o M_s t_{FL}}{\eta} * \alpha * \left(H_\perp + H_{ueff}\right) * \frac{1}{(1+\alpha\beta)} \qquad (4.4.2)$$

It is reminded here that α is the damping constant, beta the field-like torque coefficient, η the spin polarization, and $H_\perp$ the out-of-plane field which can include the exchange $H_{int\perp}$. The critical currents from Eq. 4.4.1 and Eq. 4.4.2, as a function of the out-of-plane field $H_\perp$, are plotted in Figure *4.4.3*(a). For this calculation, the coefficient $\alpha\beta \ll 1$ was neglected, and the parameter values are given in the legend of Figure *4.4.3*. In Figure *4.4.3*(a), the coercive field at zero current is indicated by dashed lines, it permits the construction of a Current-Field switching diagram. The latter is plotted in Figure *4.4.3*(b) and it shows that the STT acts on the switching fields (the edges of the hysteresis loop) in an asymmetric manner. In positive current it reduces the positive switching field while keeping the negative one constant, and vice versa in negative current.

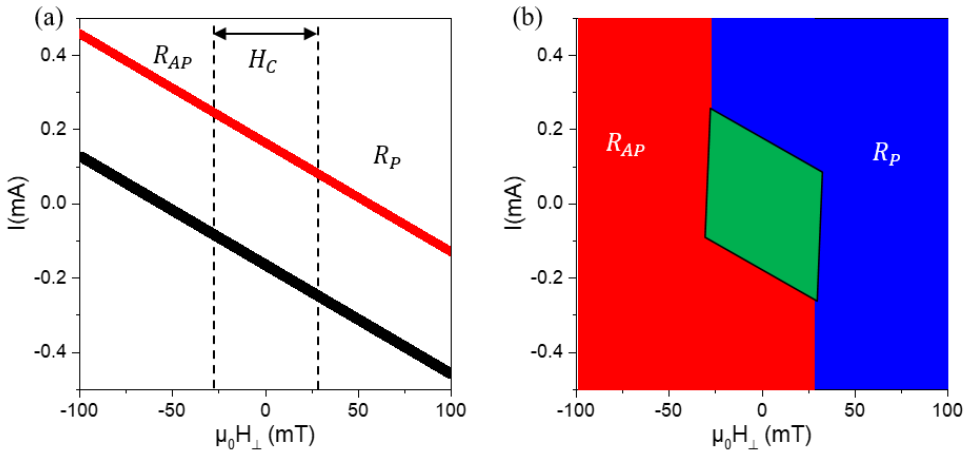

Figure 4.4.3 : (a) Critical currents plotted as a function of the out-of-plane field $H_\perp$, where $J_{c_{P\to AP}}$ is plotted in red and $J_{c_{AP\to P}}$ plotted in black. The parameters used to plot them are the same from the macrospin model see Tableau 4.2.1, for $t_{FL} = 1.4\ nm$, with an approximate value of $a_\parallel = \frac{2e}{\hbar} * \frac{\mu_o M_s t_{FL}}{\eta} \approx R_p * 4\frac{mT}{A}$. The value of $a_\parallel$ is consistent with the values used to fit similar experimental results in ref *[95]*. (b) Schematics of the switching diagram based on Figure 4.4.3(a).

Thus, experimentally, the asymmetric behavior of the switching fields with the current sign can be well explained through the STT effect, contrary to the temperature effect via Joule heating shown in Figure *4.3.3*(a) that is expected to be fully symmetric with the current sign. Therefore to quantify the effect of the STT, focusing on the current variation of one of the two switching fields is enough, i.e. the AP-to-P. The approach used here is the following :

- First, the switching fields corresponding to the reversal AP-to-P are extracted from the measurements for all the current values and signs.
- Next, the switching fields in negative currents are subtracted from those in positive currents.

This procedure should cancel out the symmetric response due to the Joule heating and leave the contribution from the STT. The result is depicted in Figure *4.4.4*(a) where the difference between the switching fields (ΔH_{AP_P}) is plotted as a function of the current amplitude. Considering this difference ΔH_{AP-P} to be produced only by the STT, the STT effect and the Joule heating can be disentangled and discussed separately. The corrected switching field plots are shown in Figure *4.4.4*(b), where the contribution due to STT is in red and due to Joule heating in black. Focusing on the negative current sign and comparing the two phenomena, it can be concluded that the STT effect on the coercive field is the most significant. However, the Joule heating has a noticeable action on the coercive field as well.

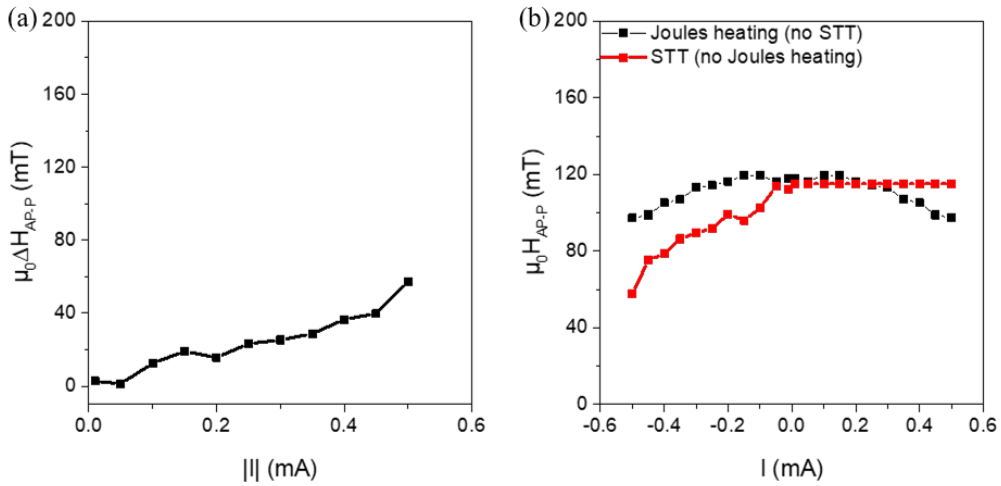

Figure 4.4.4 : (a) The difference between the AP-to-P switching fields in positive and negative current as a function of the current amplitude. (b) The corrected switching fields for the STT without Joule heating (in red), and the corrected coercive fields for Joule heating without STT (in black).

4.4.1.2 The characterization of the Joule heating

The analysis in the previous section on the STT contribution to the magnetoresistance switching, revealed that Joule heating can contribute to the reduction of the switching field as a function of current leading to a symmetric change of the switching field. The aim of this section is to quantify the Joule heating in the pMTJs by the current.

The heat generated by the dc current, will have a direct consequence on the interfacial perpendicular anisotropy (iPMA), and the saturation magnetization (M_s) as both are temeperature dependent as discussed in section 4.3 (Eq. 4.3.1, 4.3.2). Based on these equations we will quantify the expected changes in the magnetic parameters induced by the dc current.

For this we use the approach presented in [113], where the Joule heating in the free layer is modeled for current pulses of duration t_p.

Using the first law of thermodynamics [123] the model explores the heat transfer by conduction in one dimension, and the thermal resistance approach [124]. The latter yields an ordinary differential equation of the temperature changes:

$$C\frac{dT}{dt} = R_p I^2 + Q(T - T_0) \tag{4.4.3}$$

where C is the specific heat of the MTJ, Q is the heat transfer coefficient and T the free layer temperature under current I. The first term on the right-hand-side of Eq. 4.4.3 is the electric power in W, with R_p the parallel resistance and I the injected DC current. The second term stands for the heat transfer with T_0 the temperature at zero current.

Eq. 4.4.3 has a solution of the type :

$$T = T_0 + R_p I^2 * Q * \left(1 - e^{-(Q/C)t_p}\right) \tag{4.4.4}$$

where t_p is the length of the current pulse. The model predicts that the Joule heating can be much reduced using short current pulses. However, for continuous current (dc) such as the ones used here $t_p \to +\infty$, the Joule heating is at its maximum. Eq. 4.4.4 for dc currents takes the following simple form with a quadratic dependence on the injected current:

$$\Delta T = \zeta I^2 \tag{4.4.5}$$

where $\Delta T = T - T_0$ is the temperature increase due to the current, and $\zeta = Q * R_p$.

The next step is to include this current dependent temperature in Eq. 4.3.1 and in Eq. 4.3.2 which take the form :

$$K_u(T_0 + \Delta T) = K_{u0}\left(\frac{M_s(T_0 + \Delta T)}{M_{s0}}\right)^{\xi} \tag{4.4.6}$$

$$M_s(T_0 + \Delta T) = M_{s0}\left(1 - \left(\frac{T_0 + \Delta T}{T_c}\right)^{\frac{3}{2}}\right) \tag{4.4.7}$$

To extract the proportionality factor ζ in Eq. 4.4.6, the following approach is used :

- First, the corrected switching field $\mu_0 \Delta H_{ap-p}$ for the STT in Figure *4.4.4*(b) is plotted as a function of Joule heating ΔT by replacing ΔT with the expression in Eq. 4.4.5 for the current.
- Subsequently, the corrected coercive field from the current measurement is plotted against the coercive field from the temperature measurements.
- Finally, the coefficient ζ, is varied until the two match approximately.

The fitting is shown in Figure *4.4.5*. It gives $\zeta = 150\ K/mA^2$ for a pMTJ with free layer thickness of 1.4 nm and a diameter of 100 nm. The obtained ζ value is relatively close to the one obtained in [113] ($\zeta \sim 200\ K/mA^2$). This rough approximation implies that the injection of a dc current with magnitude I = 0.4 mA increases the temperature of the free layer by $\Delta T = 24\ K$.

From this rough analysis, a good understanding of the magnetoresistances at different currents values can be established. The analysis shows that the STT effect is the dominant one but that the Joule heating has an important effect on the iPMA and the M_s. For the magnetization dynamics this means that in the sub-critical regions, where the dc current is smaller than the critical current, the dc current can still have an effect on the FMR frequency that can be varied by M_s and K_i due to Joule heating.

For the other free layer thicknesses 1.6 nm and 1.8 nm, the Joule heating effect is expected to be roughly similar, although the STT excitation might be different due to their relative reorientations.

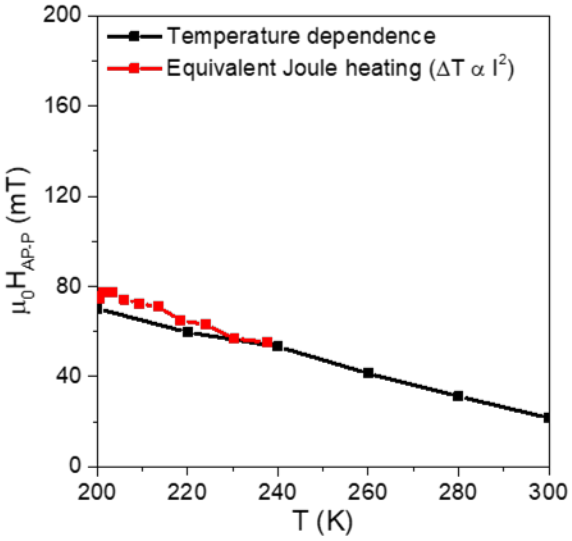

Figure 4.4.5 : (a) The fitting of the switching field AP-P from the temperature measurement by those from the current measurements using Eq. 4.4.5. The measurements are from a pMTJ device with $t_{FL} = 1.4\ nm$, a nominal diameter of $D_n = 100\ nm$ and $R_p = 850\ \Omega$.

4.4.1.3 The voltage controlled magnetic anisotropy (VCMA)

Besides the STT and Joule heating, the changes of the switching field with current might also arise from a VCMA. In the following, we briefly demonstrate that this effect can be neglected for the pMTJs studied here.

The voltage controlled magnetic anisotropy is an interface effect. First principle calculations [125]–[127], show that it arises from the accumulation of spin polarized charges at the interface between a ferromagnetic layer and an insulator.

It is also called the spin dependent screening effect [128]. The accumulation of the spin polarized charges at the interface of the ferromagnetic layer creates a surface magnetization, and changes the spin-orbit coupling via a change in the occupation of the atomic orbitals. Therefore, since the interfacial perpendicular anisotropy (iPMA) is dependent on the spin-orbit coupling it is accordingly changed when a voltage is applied.

Experimentally, the dependence of the iPMA on the voltage was found to be linear [129]. For one sign of the voltage the iPMA increases linearly and for the other sign it decreases. As a consequence, for the VCMA, it is expected that the coercive field changes linearly with the voltage, and its boundaries (switching fields) change symmetrically.

The VCMA is generally represented by the following phenomenological model[129]:

$$\frac{K_i}{t_{FL}} = \frac{K_i(0)}{t_{FL}} - \frac{\xi}{t_{FL}} * \frac{V_b}{t_{ox}} \tag{4.4.8}$$

where $K_i(0)$ is the iPMA energy constant at zero voltage, t_{FL} the free layer thickness, ξ (fJ/V.m) the VCMA efficiency coefficient, V_b the bias voltage, and t_{ox} the thickness of the oxide layer (MgO).

For MgO-based MTJs, the VCMA efficiency coefficient ξ is usually between 30 fJ/V.m and 60 fJ/V.m [129]. However, for the pMTJs investigated here, the FL is surrounded by two MgO barriers, with similar thicknesses, that can compensate their relative effects through the inverse charge accumulation at their interfaces, thereby reducing the overall VCMA of the MTJ.

To evaluate the VCMA using Eq. 4.4.8, an upper estimation of the coefficient ξ = 30 fJ/V.m is used, along with a voltage corresponding to the highest experimental current values of |0.5|mA. For the remaining parameters they are extracted from the macrospin model used before and their values are the following :

$V_b = R_{ap} * (0.5 * 10^{-3}) = 0.8$ V,

$t_{ox} = 1$ nm,

$\frac{K_i(0)}{t_{FL}(1.4\ nm)} = 600$ kJ/m^3.

The calculations yield for the second term in Eq. 4.4.8, a value of $\frac{k_v}{t_{FL}} = \frac{\xi}{t_{FL}} * \frac{V_b}{t_{ox}} = 17$ kJ/m^3, it represents only $\approx 2.8\,\%$ of the zero voltage perpendicular magnetic anisotropy coefficient. However, it can have a drastic consequences on the magnetization state. This is illustrated by the macrospin calculations shown in Figure *4.4.6*(a) for a dc current |I| = 0.5 mA. The coercive field at zero current is reduced to almost zero for negative current sign (red plot), and almost doubled for the positive current sign (green plot). Nevertheless, the results from the simulations in Figure *4.4.6*(a) do not reproduce the experimental results shown in Figure *4.4.6*(b).

In the experimental results, the coercive field at zero current is two times higher than the coercive field at 0.5 mA positive current, and 6 times larger than the one at 0.5 mA negative current. It indicates that the value used for the VCMA efficiency was exaggerated for this pMTJ stack, and that the VCMA effect is generally weak in these MTJ devices.

Further arguments supporting a weak VCMA contribution in the pMTJs will follow later-on using the ferromagnetic resonance analysis.

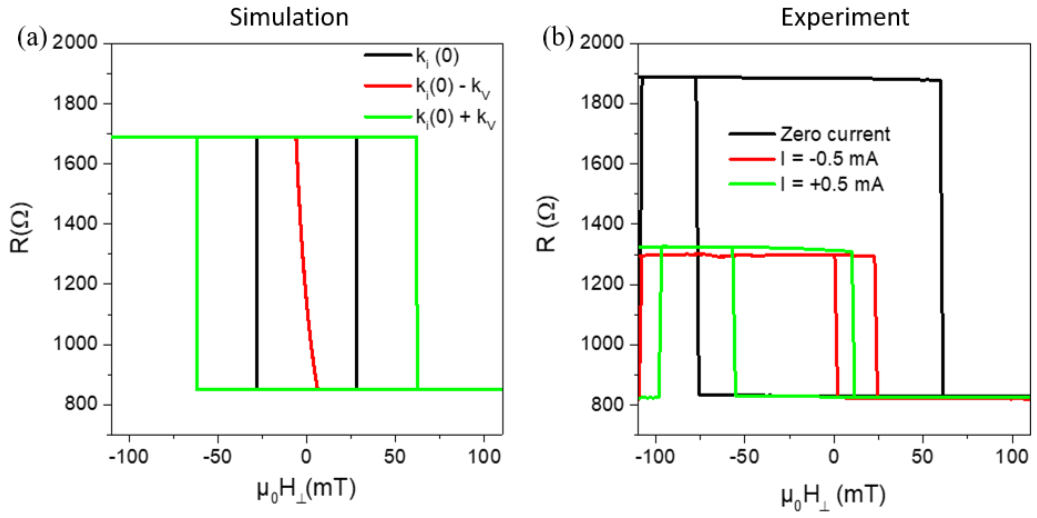

Figure 4.4.6 : (a) Macrospin simulations of the VCMA effect, based on the minimization of the total magnetic energy, and for a dc current |I| = 0.5 mA. (b) Experimental measurements of the magnetoresistance hysteresis loops for low dc current (10 µA, black line) and |I| = 0.5 mA (red and green line).

4.4.1.4 The TMR bias voltage dependence

The injection of a large current density, as shown in the previous section, can cause the magnetization to switch and thereby provides a means to manipulate the magnetic state electrically.

The dc current or dc voltage however also affects the tunneling magnetoresistance (TMR). An example is shown in Figure *4.5.3*(a), for a device with a free layer thickness of 1.4 nm and a diameter of 100 nm, the TMR loses 50% of its initial value by increasing the current magnitude to 0.5 mA.

Interestingly, the bias dependence of the TMR is independent of the current sign, and similar to the TMR temperature dependence : the changes in the TMR are mostly mediated by the anti-parallel state, see Figure *4.4.7*(b).

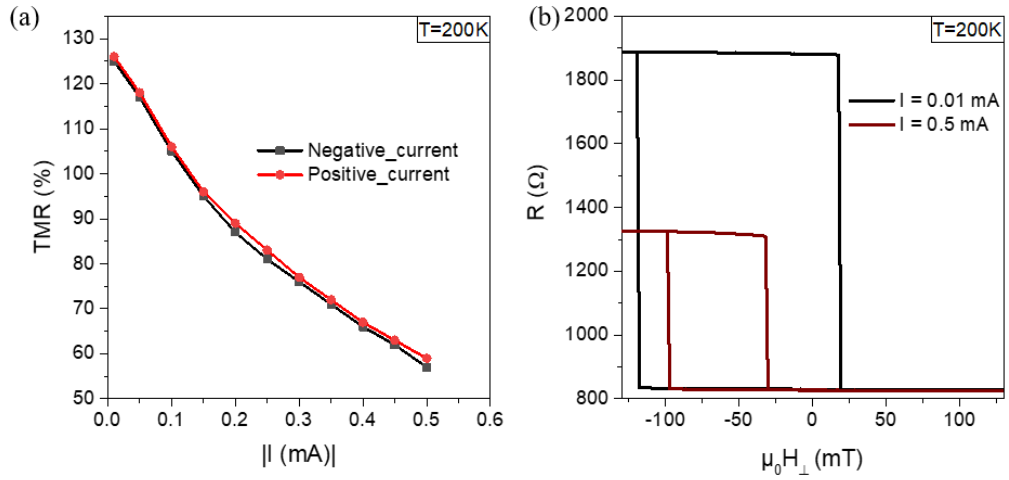

Figure 4.4.7 : (a) TMR dependence on the bias voltage, extracted from the current measurements shown in Figure 4.4.3, for a pMTJ device with a free layer thickness of 1.4 nm and a diameter of 100 nm. (b) Magnetoresistance hysteresis loops for a dc current of magnitude 0.01 mA (in black) and dc current of magnitude of 0.5 mA (in red).

The TMR dependence on the bias current (voltage), was first discovered by [13] and [130]. It is usually attributed to the spin flip (magnon generation) caused by the hot electrons (electrons with energy higher than the Fermi level) at the interface of the free layer. It can be explained by the model presented earlier for the temperature dependence of the TMR [119]. For low voltages, it is approximated by :

$$R_P(V,T)|_{V\to 0} = R_p(V,0) * \left[1 + Q * \xi * \frac{2S}{E_m} * k_B T * ln\left(\frac{k_B T}{E_C}\right)\right]^{-1} \quad (4.4.9)$$

$$R_{AP}(V,T)|_{V\to 0} = R_{ap}(V,0) * \left[1 + Q * \frac{2S}{E_m} * \frac{1}{\xi} * k_B T * ln\left(\frac{k_B T}{E_C}\right)\right]^{-1} \quad (4.4.10)$$

where V is the bias voltage, Q standing for the efficiency of the magnon generation, S the spin parameter, $E_m(meV) = \frac{3k_B T_C}{S+1}$, with T_C the Curie temperature, $E_C(meV)$ the magnon generation cut-off, and $\xi = \frac{\rho_p * \rho_{ap}}{\rho_p^2 + \rho_{ap}^2}$ the ratio of the density of states.

Although, the model provides an explanation for the TMR voltage dependence, Eq. 4.4.9 and Eq. 4.4.10 are limited to very low voltage measurements. Moreover, for the fitting, it requires knowledge of the TMR voltage dependence at very low temperature. The latter is unfortunately missing in this work.

4.5 Current dependence of the reversal of the polarizing layer

The aim of this discussion is to complement the previous analysis by including the current dependence of the reversal of the polarizing layer (PL). This step is as important as the analysis of the free layer (FL), because for the passive spin diode effect, in chapter 5, both the FL and the PL dynamics are detected. More importantly, in the active spin diode measurements, in chapter 6, the PL response is higher than that of the FL.

The PL reversal is investigated here, under an out-of-plane field, and for all the different FL thicknesses. Although, it must be noted that in these measurements the PL reversal is at high out-of-plane fields where the FL should be saturated out-of-plane. Hence, even if the FL orientation at zero field is different for each thickness, in the PL reversal it should be approximately out-of-plane for all the thickness.

4.5.1 Current dependence of the polarizing layer for t_{FL} = 1.4 nm

For a pMTJ with a free layer thickness of 1.4 nm, the PL reversal for different current signs is shown in Figure *4.5.1*(a). Similarly to the FL reversal in Figure *4.4.1*(a), here the magnetoresistance loops show a noticeable asymmetry with the current sign, which indicates the action of the STT. The magnetoresistance shape in negative current, shows a distortion in the spin-flop region that is not present in the positive current measurements. Similar distortions are usually an indicator of the self-sustained oscillations of the magnetization. In this case, it is likely to be the PL that auto-oscillates, because with the negative current the electrons flow from the FL to the PL.

Focusing on one of the switching fields (AP-to-P), as in the previous approach, and plotting it as a function of currents, illustrates well the asymmetry with the current sign, see Figure *4.5.1*(b).

To disentangle the STT and the Joule heating in the PL hysteresis, as in the case of the FL, the switching fields from the positive currents are subtracted from those in the negative current. The result is plotted in Figure *4.5.2*(a) as a function of the current amplitude. The corrected switching fields from the STT alone, and those from the Joule heating alone are also plotted in Figure *4.5.2*(b). The results show that, for a FL thickness of 1.4 nm, the PL reversal is dominated by the STT effect, with an important presence of the Joule heating.

Using the model developed above in Eq. 4.4.5. to convert the current measurements into the Joule heating equivalent and fitting the temperature measurements, gives a $\zeta = 300\ \mathrm{K/mA^2}$. The fitting shows that the Joule heating present in the PL is about two times higher than that induced in the FL, which might be due to the difference in their effective volumes. The fitting is depicted in Figure *4.5.3*.

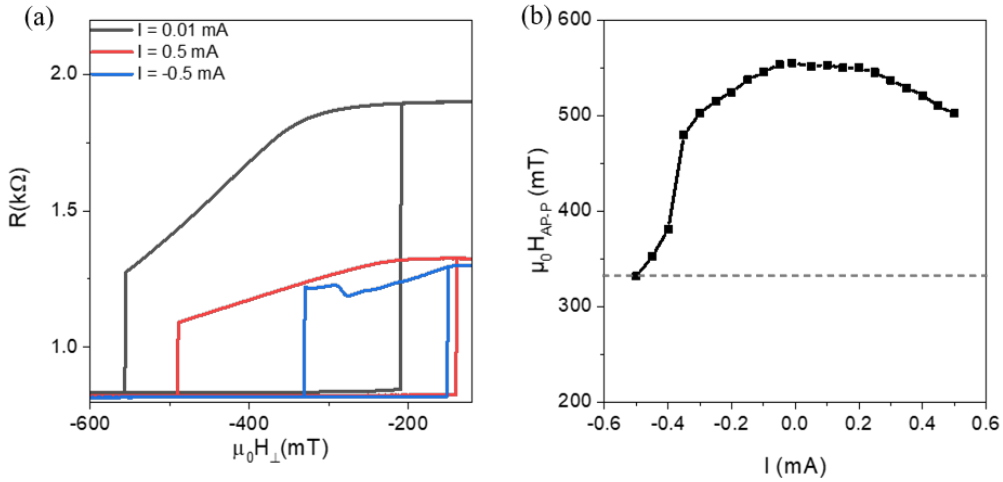

Figure 4.5.1 : (a) The experimental magnetoresistance loops of the PL as a function of the out-of-plane field at T = 200 K and for different dc currents. (b) The AP-to-P switching field from the PL hysteresis loop, plotted as a function of the dc current.

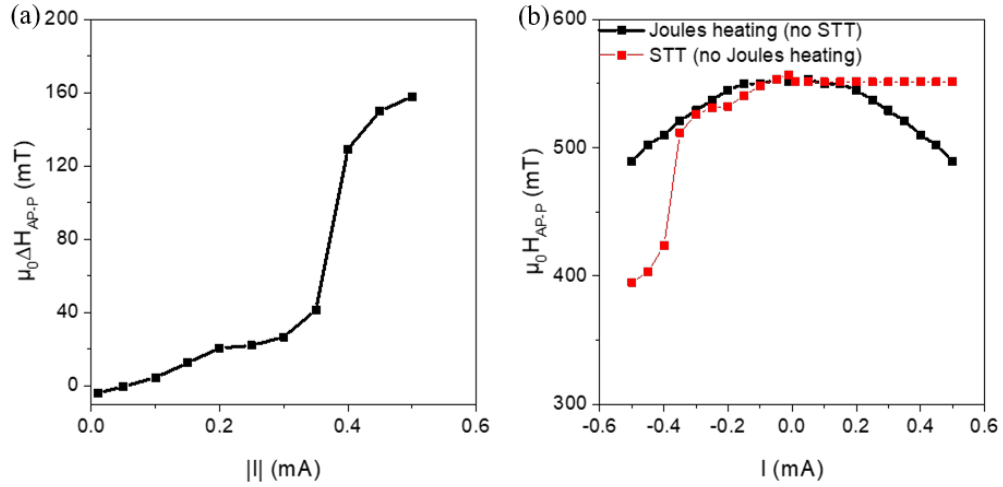

Figure 4.5.2: (a) The difference between the AP-to-P switching fields of the PL in positive and negative current as a function of the current amplitude. (b) The corrected PL switching fields for the STT without Joule heating (in red), and the corrected coercive fields for Joule heating without STT (in black).

Selecting the other switching field P-to-AP for the whole analysis done previously should be generally similar, however the measurements from the PL reversal show a totally different response. The switching field P-to-AP for the PL as a function of the current is almost constant and independent of the current sign or amplitude, see Figure *4.5.4*(a). Although it exhibits a drastic jump at current amplitude |0.4| mA for both signs, which is mostly a heat induced behavior.

The latter jump is also present in the real temperature measurements, which indicates that its source might be the anisotropy, see Figure *4.5.4*(b). However, what is happening exactly is not straightforward due to the complicated structure of the PL layer and its coupling to the SAF. For the jump, it might be a sharp reorientation, or a domain switching, and in both cases it might be related only to this specific device. As for the constant behavior of P-to-AP with the current, it is present in the other thicknesses, and its main source is also not yet fully determined.

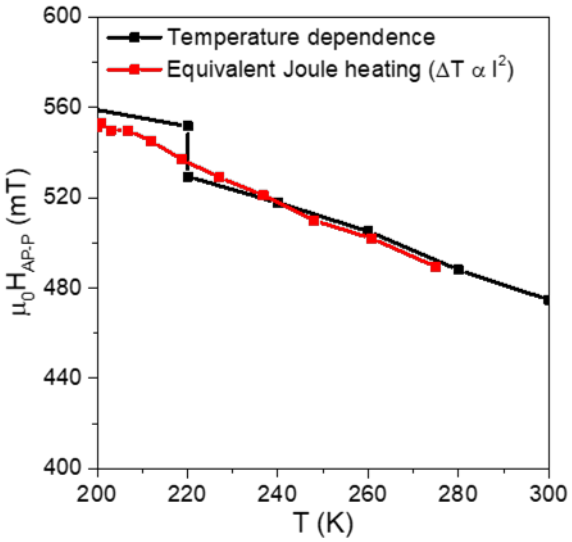

Figure 4.5.3: (a) The fitting of the FL coercive field from the temperature measurements by those from the current measurements using Eq. 4.4.5. The measurements are from a device with $t_{FL} = 1.4\ nm$ and a diameter of $D = 100\ nm$.

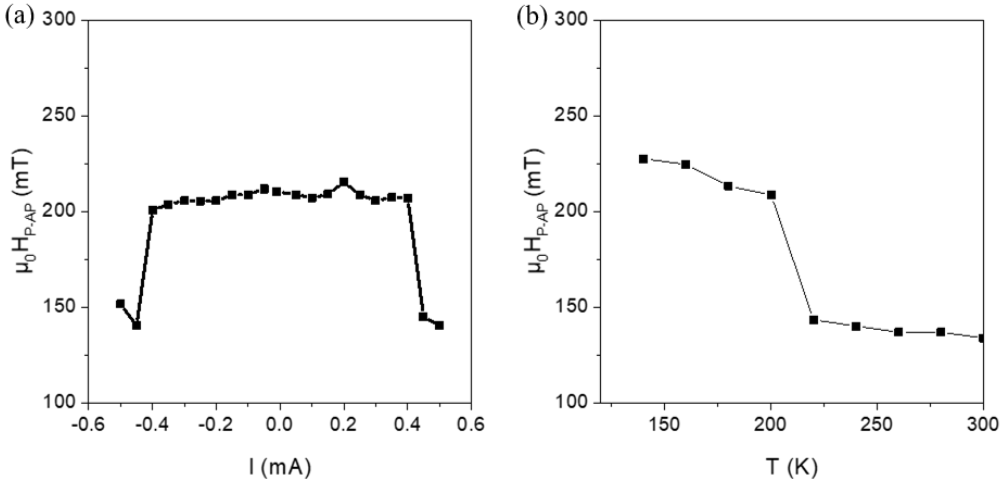

Figure 4.5.4: (a) The P-to-AP switching field from the PL hysteresis loop, plotted as a function of the dc current. (b) the P-to-AP switching field from the PL hysteresis loop plotted as a function of the temperature for input current of 10 μA.

4.5.2 Current dependence of the polarizing layer for t_{FL} = 1.6 nm and t_{FL} = 1.8 nm

The goal of this subsection is to explore the dependence of the PL reversal on the FL thickness. The latter changes the equilibrium orientation of the FL and as a consequence the electrons flowing from the FL to the PL can stabilize different orientations depending on the FL thickness. It is reminded here that the characterization of the PL are done at high out-of-plane magnetic fields where the FL is saturated out-of-plane.

For this analysis the same approach as in section 4.5.1 is used to quantify the STT effect. It starts by extracting the AP-to-P switching fields and then plotting them for all the current signs and amplitudes. The results from a pMTJ with a FL thickness of 1.6 nm are sketched in Figure *4.5.5*(a), and those from one with a FL thickness of 1.8 nm are sketched in Figure *4.5.5*(b). For both devices, the nominal diameters are 100 nm, and the measurements are done at a temperature 200 K to have the same measurement conditions as before in section 4.5.1.

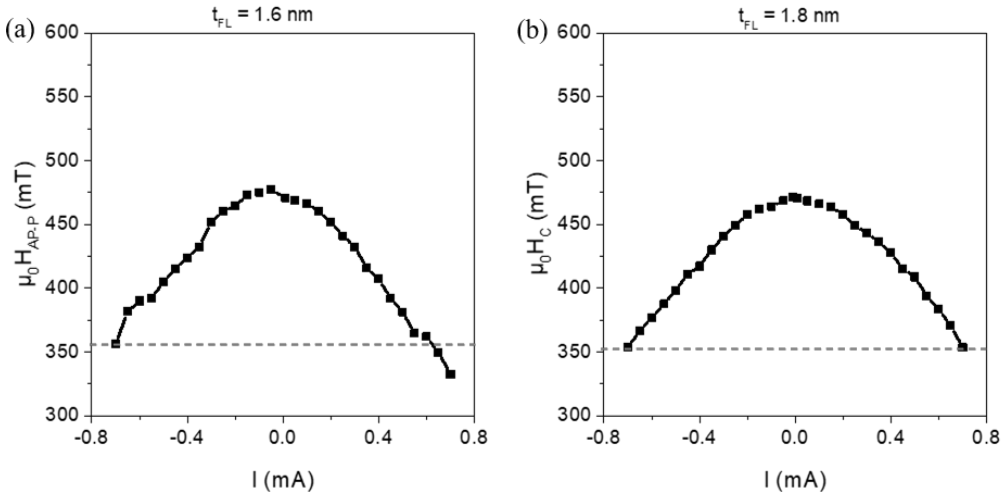

Figure 4.5.5 : The AP-to-P switching field from the PL hysteresis loop, plotted as a function of the dc current, for a FL thickness of (a) 1.6 nm and (b) 1.8 nm.

Starting with the measurements in Figure *4.5.5*(a), for t_{FL}= 1.6 nm, they show that the AP-to-P does have an asymmetry with the dc current sign, however it is weaker compared to t_{FL}= 1.4 nm. In addition, for t_{FL}= 1.6 nm, the AP-to-P changes more with the positive current, while for t_{FL}= 1.4 nm (in Figure *4.5.1*(b)) it changes more with the negative current. Considering the current convention, the latter might mean that for 1.4 nm, the PL switching is mediated directly by the electrons flowing from the FL to the PL, while for 1.6 nm the PL switching is mediated via the reflected electrons (see Table 2.4.1 for the current convention).

For the pMTJ with a FL thickness of 1.8 nm, in Figure *4.5.5*(b), the PL switching field AP-to-P is quasi-symmetric with current sign. Comparing the results for all FL thicknesses, see Fig. 4.5.6, it can be concluded that for the PL, the AP-to-P current sign asymmetry decreases with the increase in the FL thickness. This is illustrated in Figure *4.5.6* where the AP-to-P difference with current sign is plotted for all the FL thicknesses. If the asymmetry is considered as the main STT contribution, and the symmetry to be due to Joule heating, the measurements give the impression that for the PL reversal, the STT efficiency drops for higher FL thicknesses, while the PL Joule heating increases with them. Although it must be reminded that the interpretation considered here for the STT switching is based on a fixed out-of-plane orientation of the free layer for all thicknesses. Therefore, for a high out-of-plane magnetic field, if the FL is not saturated out-of-plane then the formulas derived for the PL switching currents, as in section 4.4.1.1, do not necessarily hold anymore.

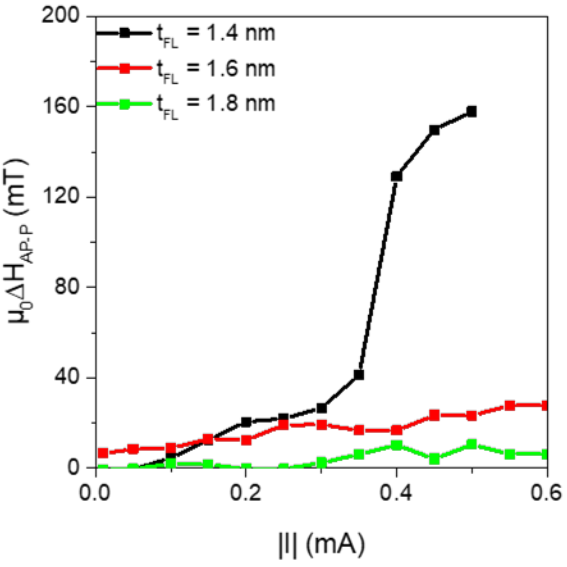

Figure 4.5.6: The asymmetry between the AP-to-P switching fields of the PL as a function of the current amplitude for all the FL thicknesses.

4.6 The current dependence of the magnetoresistance under an in-plane magnetic field.

In section 4.2.1, it was shown that a device with a free layer thickness of 1.4 nm, has an out-of-plane easy axis. Moreover, under an in-plane magnetic field, the magnetizations of the free and polarizing layers exhibit both an in-plane rotation towards the magnetic field direction. Although for relatively weak in-plane fields the reorientation occurs at the same rate, which results in a quasi-constant magnetoresistance with the in-plane field. In this section, the aim is to investigate the current dependence of the magnetoresistance measured under an in-plane magnetic field.

The results, from a pMTJ with a FL thickness of 1.4 nm, and a nominal diameter of 100 nm are depicted in Figure *4.6.1*(a) and Figure *4.6.1*(b) for positive and negative currents respectively. Interestingly, around zero magnetic field and for negative dc currents a pronounced increase in the resistance with the current is observed. The increase is maximum at zero field and decreases with increasing in-plane magnetic field. The latter phenomenon is absent for positive current. This suggests that the spin transfer torque effect is contributing to this peak. It is also consistent with the current sign of the STT (negative current destabilizing the free layer through back reflected electrons). This peculiar behavior can also be observed for the other free layer thicknesses and will be analyzed in detail in chapter 7.

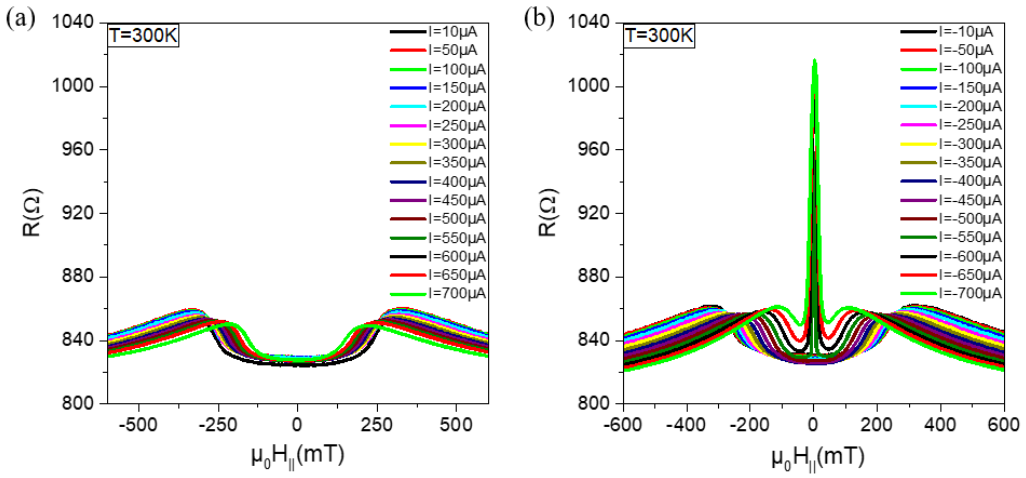

Figure 4.6.1 : (a) The magnetoresistance as a function of an in-plane magnetic field and positive dc current, for a device with a free layer thickness of 1.4 nm and a diameter of 100 nm. (b) the same as (a) for negative dc currents.

Conclusion

To conclude, in this chapter the equilibrium magnetic states of both the free and the polarizing layers were characterized using the VSM for the continuous films and using the PPMS for nanopillar devices. The three free layer thicknesses (t_{FL} =1.4 nm, 1.6 nm and 1.8 nm) were characterized under out-of-plane and in-plane magnetic fields, and for variable temperatures and dc currents. The measurements combined with a macrospin analysis (from chapter 3) helped to identify the equilibrium orientation of the free layer magnetization, to extract the iPMA energy constant and in addition to distinguish between the different phenomena involved when a dc current is injected into the device.

It was found that for $t_{FL} = 1.4$ nm the free layer magnetization is orientated out-of-plane, while for $t_{FL} = 1.6$ nm and $t_{FL} = 1.8$ nm it is orientated in zero field at an intermediate angle and in-plane respectively. Moreover it was found that under dc current the dominant effect is the spin

transfer torque, followed by the Joule heating by $\zeta \approx 150\ \mathrm{K/mA^2}$, and probably a weak voltage controlled anisotropy (VCMA).

The polarizing layer was demonstrated to be out-of-plane at equilibrium and reorients by an in-plane field. The characterization of the polarizing layer reversal revealed that its AP-to-P reversal is dependent on the free layer thickness, while its P-to-AP is almost independent of temperature and current amplitude and sign. The quantification of the Joule heating gives an approximate value of $\zeta \approx 300\ \mathrm{K/mA^2}$.

The understanding of the static behavior of the pMTJs layers will be the background on which the coming chapters are build. In the next chapter, it will be used to investigate the magnetization dynamics under an oscillating electric current, for the passive spin-torque nano-diode effect. Subsequently, it will be used for the investigations of the magnetization dynamics under both dc and oscillating current (active detection), and finally for the stochastic behavior of the magnetization reversal.

Passive radiofrequency detection in pMTJs

In this chapter the pMTJs are explored for the passive spin-torque nano-diode effect, where passive refers to zero dc current. The objective was to define the experimental conditions that lead to the largest output signal for the passive rf-to-dc conversion. The experiments were carried out under in-plane and out-of-plane fields for all the three free layer thicknesses (1.4 nm, 1.6 nm, and 1.8 nm) and for all nominal diameters (20 nm, 40 nm, 80 nm, 100 nm, 150 nm).

The characterization of the rf-to-dc conversion shows dc output voltages in the mV range, with a signal-to-noise ratio (SNR) of 26-39 dB for an input rf power of –25 dBm. Moreover, the sensitivity of the devices to the input rf power was found to be ε ~ 300 mV/mW. The output voltages exhibit a noticeable dependence on the pMTJ size : they increase by a factor of ~ 6 when the nominal diameter is reduced from 150 nm to 20 nm. The latter improvement can be doubled when the FL thickness changes from 1.8 nm to 1.6 nm. This size-dependent enhancement is attributed to different effects: (i) the magnitude of the spin transfer torque that depends inversely on the area of the FL, (ii) the effective anisotropy $H_{ueff} = H_u - H_d$ that depends via the anisotropy on the FL thickness and via the demagnetization field on the diameter (see Figure *4.2.4* and Figure *4.2.5* in section 4.2 of chapter 4), and (iii) the TMR that for these specific devices depends on the diameter. A similar diameter dependence was also observed for the rf-to-dc conversion within the polarizer. The obtained results indicate that the thickness and diameter of the FL are important parameters for the optimization of the spintronic based rf detectors.

Following the rf-to-dc characterizations, the pMTJ devices were tested for rf demodulation using the On-Off-Shift-Keying (OOK) technique. Incoming modulated square signals with frequencies up to 50 kHz were demodulated successfully by the pMTJs.

Finally, in the last section of this chapter a discussion of the asymmetry in the signal shape under an out-of-plane field is included. It is suggested to be due to the exchange coupling between the PL and the SAF.

5.1 Characterization of the passive spin-torque nano-diode effect under an in-plane magnetic field

In this section, the pMTJs with the three free layer thicknesses (1.4 nm, 1.6 nm, and 1.8 nm) are characterized for the spin-torque nano-diode effect under an in-plane magnetic bias field. Moreover, for each FL thickness, the spin-torque nano-diode effect is characterized for a different range of diameters. The results are then analyzed and fitted by the model developed in section 3.3 of chapter 3.

5.1.1 The output signal shape and the identification of the ferromagnetic resonance modes

To start the characterization, we first present results for three perpendicular magnetic tunnel junctions (pMTJ) with the same nominal diameter (D_n = 80 nm), and different free layer thicknesses (1.4 nm, 1.6 nm, 1.8 nm). The pMTJs were exposed to an rf current with a power of -5 dBm and a frequency that was swept from 0.5 GHz to 15 GHz at a given constant in-plane magnetic field. Then the frequency sweeps were repeated for different fields that were varied from 0 mT to 100 mT. The goal of this initial characterization was to understand how the spin-torque nano-diode signal evolves as the free layer thickness (i.e. the free layer orientation) changes. The measured output voltages are plotted in Figure *5.1.1*(a)-(c).

For the free layer with a thickness of 1.4 nm, the output dc voltage in Figure *5.1.1*(a) looks independent of the rf current frequency as well as the in-plane magnetic field. The measurements suggest that the resonance of the magnetization is not detectable electrically. This is mostly caused by the quasi-collinearity of the free and polarizing layer magnetizations for this thickness, under in-plane field. In chapter 4 section 4.2, it was shown that under an in-plane magnetic field below 50 mT, the Fl and Pl are quasi-collinear, i.e. their respective angle changes very little in this field range. Thus, under an in-plane field, the magnetoresistance changes are weak for a free layer with a thickness of 1.4nm.

For the remaining free layer thicknesses, 1.6 nm, and 1.8 nm, their output voltages in Figure *5.1.1*(b)-(c) exhibit resonance responses as a function of the rf current frequency. However, interestingly, at a constant in-plane magnetic field, there are two resonance frequencies, regardless of the free layer thickness. The two resonance frequencies are lying within two distinct frequency ranges, one at lower frequencies 1-5 GHz and the other one at higher frequencies 8-12 GHz. In addition, the dc voltages produced by those two resonances are of opposite signs. The two resonance frequency branches are plotted in Figure *5.1.1*(d) as a function of the in-plane magnetic field, and for both free layer thicknesses.

Figure *5.1.1*(d) shows that as the free layer thickness changes, the lower resonance frequencies vary noticeably, while the higher resonance frequencies are almost the same for both thicknesses. The latter is a strong hint on the origin of the two resonances. Considering the polarizing layer magnetization dynamics to be the origin of the higher resonance frequencies could explain the results because its excitation frequencies will be independent of the free layer thickness.

In addition, the corresponding dc voltage is negative (opposite to the first resonance mode), because it is excited by the back reflected electrons while the free layer is excited by the electrons polarized by it, and vice versa, the two magnetic layers are always excited by currents of opposite signs.

Therefore, the higher resonance frequency branch is attributed to the oscillations of the polarizing layer, while the lower resonance frequency is attributed to the oscillations of the free layer.

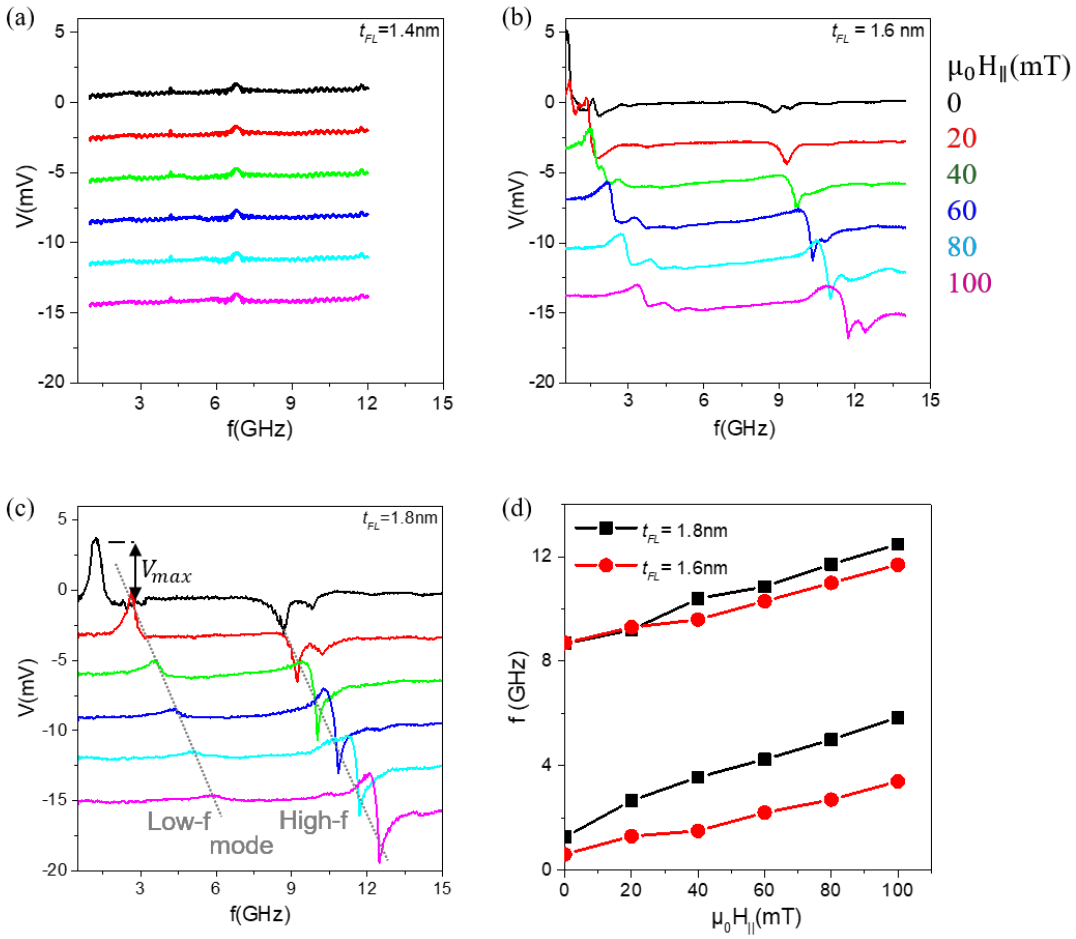

Figure 5.1.1: (a) Experimental results of the dc rectification voltage of a magnetic tunnel junction with a nominal diameter of 80 nm and a free layer thickness of 1.4 nm, upon sweeping the frequency of the rf current injected in the pMTJ at constant in-plane magnetic field $H_{||}$. The corresponding rf power is -5 dBm. (b) and (c) are the same as (a) but for free layers thicknesses 1.6 nm and 1.8 nm respectively. (d) The resonance frequencies extracted from (b) and (c) vs. the in-plane magnetic field $H_{||}$.

The higher resonance frequency of the polarizing layer, as compared to the one from the free layer, is attributed to its coupling to the synthetic antiferromagnetic (SAF) that is considered here to be fixed. Therefore, the Pl experiences a constant out-of-plane interaction field $H_{int\perp}$ that will be stronger than the out-of-plane field that the free layer experiences due to the dipolar field from the non-compensated SAF. To argue more on these assumptions, in Figure *5.1.2*(a)-(b), the resonance frequencies of the magnetizations of the free and polarizing layers are estimated using the macrospin model developed in section 3.3 of chapter 3.

The resonance frequencies from the model have the dependence:

$$f_0 = \frac{\gamma}{2\pi * \sin(\theta_i)} * \sqrt{(H_{\parallel} m_{x0}) * \left(H_{ueff}(2m_{z0}^2 - 1) + H_{\parallel} m_{x0} + (H_{int\perp}) m_{z0}\right)} \qquad (5.1.1)$$

where θ_i is the equilibrium angle of the FL or PL obtained by Eq. 3.1.18 in chapter 3. m_{x0} and m_{z0} represent the static equilibrium position of the magnetization at a given field value, they are obtained from the energy minimization of Eq. 3.1.18 in section 3.1 of chapter 3. The field $H_{int\perp}$ in Eq. 5.1.1 is considered constant and to be due to the stray field from the SAF in the case of the free layer and the exchange coupling of the PL to the SAF in the case of the polarizing layer.

The parameters used in the evaluation of Eq. 5.1.1 are summarized in the following table (Tableau *5.1.1*):

Layer	M_s (A/m)	K_u (kJ/m^3)	$\mu_0 H_{int\perp}$ (mT)	N_z	$N_x = N_y$
FL	$\sim 10^6$	$600 * \left(\frac{1.4nm}{t_{FL}(nm)}\right)$	42	0.949537	0.025232
PL	$\sim 10^6$	xx	xx	0.953882	0.023059

Tableau 5.1.1 : The value of the parameters used in the fitting of the FMR frequencies in Figure 5.1.2 of the FL and PL. The average M_s values for FL and the PL are $1.14 * 10^6$(A/m) and $1.12 * 10^6$(A/m) respectively. Since they are relatively similar, in the calculations both were approximated by 10^6 (A/m).

The parameter values for the FL are those extracted from the fitting of the magnetoresistance loops in section 4.2.3 in chapter 4, while for the polarizing layer they were obtained from the fitting to the experimental data in Figure *5.1.2*(b). Figure *5.1.2*(a) shows the results for the low frequency resonance (free layer), and Figure *5.1.2*(b) for the high frequency resonance (polarizing layer).

For the low frequency resonances, attributed to the dynamics of the free layer magnetization, the simulations reproduce the measured results with a good approximation. In particular, the simulations predict the observed shift of the resonance to lower frequencies when the free layer thickness changes from 1.8 nm to 1.6 nm. Thus, the simulations confirm that the low frequency resonances are those of the free layer magnetization.

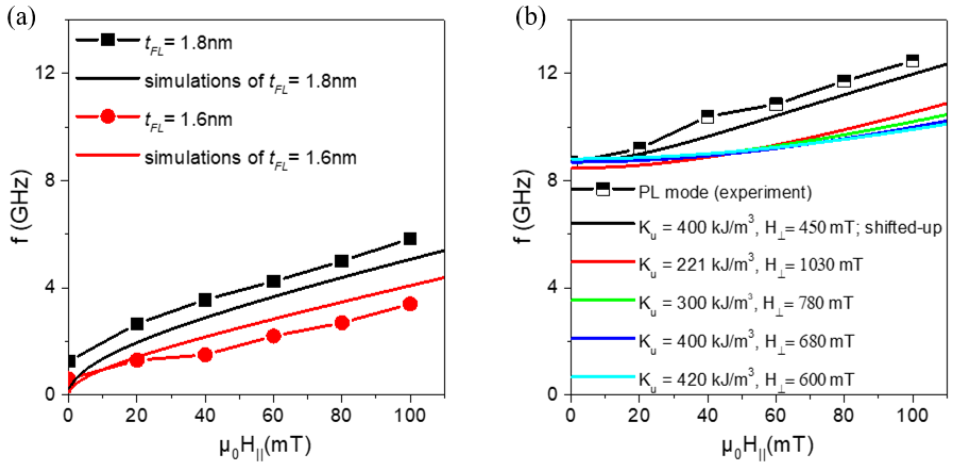

Figure 5.1.2 : (a) Comparison between simulations and the experimentally extracted frequencies vs. applied in-plane field for the ferromagnetic resonance modes of free layers with the same nominal diameter D_n = 80 nm. The simulations are plotted as continuous lines, while the line-point plots are the experimental results. (b) The same as (a) but for the polarizing layer. Here the anisotropy and the out-of-plane field were varied to fit the experiment.

For the polarizing layer mode however, the fitting in Figure *5.1.2*(b) requires different parameters than those obtained in chapter 4 for the free layer. For this, the perpendicular interaction field $H_{int\perp}$ and the anisotropy energy constant $K_u = K_i/t_{Pl}$ were varied. However, the fitting using the model was not as satisfactory as for the FL. For instance, using the PL parameters from section 4.2.3 in chapter 4, resulted in an FMR mode with a similar evolution (slope) vs. the in-plane field, but its frequency is by ~ 5.25 GHz lower than the measured frequency. The result is plotted in Figure *5.1.2*(b) (black line, after shifting it up by 5.25 GHz). In order to obtain frequencies close to the experimental ones, the anisotropy constant $K_u = K_i/t_{PL}$ and the perpendicular interaction field $H_{int\perp}$ were varied using different set of values. The results are plotted in Figure *5.1.2*(b). However as can be seen the increase of frequency with field is much weaker for the simulated results. It is difficult to fit both the anisotropy constant and the out-of-plane coupling field to reproduce the experiments. For instance, a low anisotropy constant requires a high out-of-plane field to have the correct frequency (Figure *5.1.2*(b) in red), and a high anisotropy constant requires a small out-of-plane field (Figure *5.1.2*(b) in cyan). Moreover, the first case (in red) gives FMR modes with slopes that are a little bit higher than those in the second case (in cyan). But the values of the $H_{int\perp}$ are much larger than what one would expect from the exchange coupling of the PL to the SAF.

These different fittings of the PL FMR suggest that the perpendicular anisotropy is weak (compared to the FL) and the perpendicular interaction field is very strong. This may mean that the assumption of a rigid SAF layer and only the polarizing layer being excited is not correct. The results could then be more consistent for an excitation where the PL and the T-SAF make one composite layer that is strongly exchange coupled to the B-SAF.

Furthermore, other effects, that were neglected here, might play a role, such as the dipolar coupling between the FL and the PL, that in addition can change with the in-plane field, due to the rotation of the magnetization. This will require a more detailed numerical modelling.

With the origins of the resonance modes identified, the next step is to characterize the amplitude of the dc voltages produced.

For a free layer with a thickness of 1.8 nm and a nominal diameter of 80 nm, at zero external bias field ($\mu_0 H_{\parallel} = 0$ mT), and for an rf current with a power of -5 dBm, the maximum dc voltage amplitude is $V_{max} \approx 3$ mV, see Figure *5.1.1*(c). It is 2 mV smaller than the maximum dc voltage produced in a free layer with a thickness of 1.6 nm, under the same conditions, $V_{max} \approx 5$ mV. The origins of this enhancement will be explored in the next section.

5.1.2 The maximum output voltage vs. size of the free layer

To start the analysis of the rf-to-dc output voltage amplitude and its dependencies, the approach used in this work consists of fitting the output voltages using the magnetization dynamics equations derived in section 3.3 of chapter 3, and with this to investigate the size dependence of the maximum voltages. The derived voltage formula depends on the rf power, the STT amplitude, and the internal and external fields.

In section 3.3 of chapter 3 the expression corresponding to the rf-to-dc conversion was given by :

$$< V > = \frac{R_p}{R_0} * P_{rf} * \frac{\tilde{a}}{\pi * r^2} * \eta^2 (1+\eta)^2 * \frac{\gamma * \omega}{\sqrt{\left(\omega_0^2 - \omega^2\right)^2 + (\omega \Delta\omega_0)^2}} * \cos(\phi) \qquad (5.1.2)$$

with $\phi = atan\left(\frac{\omega \Delta\omega_0}{\omega_0^2 - \omega^2}\right) + \text{atan}\left(\frac{\omega}{H_{\parallel} m_{x0} * \beta}\right)$, $\Delta\omega_0$ the linewidth given by $\Delta\omega_0 = \gamma * \frac{\alpha}{Ms} * (H_{ueff}(2m_{z0}^2 - 1) + 2H_{\parallel} m_{x0} + (H_{\perp}) m_{z0})$, the resonance frequency ω_0 given by the expression in Eq. 5.1.1, the TMR factor $\eta^2 = \frac{TMR}{2+TMR}$, and R_0 the magnetoresistance relative to the orientation of the free layer magnetization compared to the polarizing layer.

To fit the experimental measurements using Eq. 5.1.2, the parameters are separated into fixed and tunable ones. For the parameters obtained from the static characterization in chapter 4 they are considered fixed values, such as : M_s, H_{ueff}, γ and η (TMR), while the tunable ones are the fit parameters: the spin transfer torque (STT) coefficients $\tilde{a}$ and β, and the damping constant α. The STT field-like torque coefficient β is neglected, because it favors an antisymmetric Lorentzian, while the measurements show clearly that the FL gives a symmetric Lorentzian.

For the remaining fitting parameters, we started the fitting using a value of $\alpha = 0.01$ for the magnetization damping. This value a rough approximation that is generally accepted in macrospin simulations [131]. In particular for an FeCoB free layer, similar to the one studied here, with thicknesses of 1-2 nm, the average magnetization damping constant is $\alpha \approx 0.01$ [132].

In addition, in the model developed in section 3.3 of chapter 3, the resonance linewidth was considered to depend only on the magnetization damping and the internal fields. However, the ferromagnetic resonance linewidth can be broadened by magnon scattering, and in the case of polycrystals, by the random internal fields of its constituent grains [133]–[137]. It is called the inhomogeneous broadening of the ferromagnetic resonance (FMR). To correct for this phenomenon the magnetization resonance linewidth is written as follows :

$$\Delta\omega_r = \Delta\omega_0 + \gamma\Delta H_i \tag{61}$$

where $\Delta\omega_r$ is the total FMR linewidth, and γ the gyromagnetic ratio, and ΔH_i the inhomogeneous broadening of the FMR.

For the spin transfer torque coefficient $\tilde{a}$, it is generally challenging to measure [138], [139], therefore to fit the results it is first approximated from its formula in Eq. 1.1.13 in section 1.1.5 of chapter 1 to get a starting value and then it is tuned for the fitting.

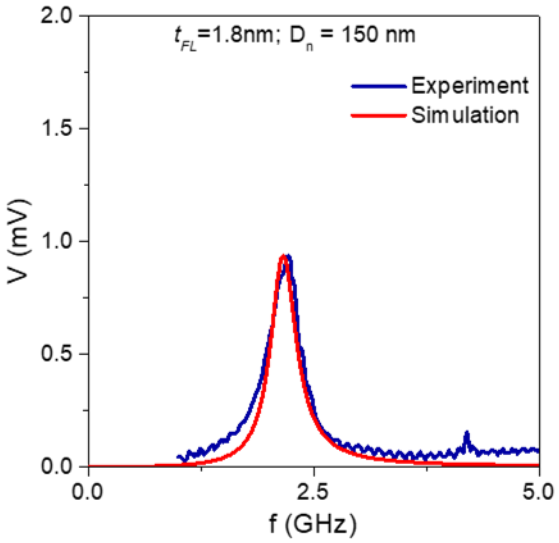

Figure 5.1.3 : Fitting of an experimentally measured FMR response of a free layer magnetization with a thickness of 1.8 nm and a nominal diameter of 150 nm. The fitting was done using Eq. 5.1.2 with the same parameters as in Figure 5.1.2, except for the damping, the FMR inhomogeneous broadening, and the spin transfer torque. These values are given in the text.

For a device with a free layer of thickness 1.8 nm and a nominal diameter of 150 nm, under the same condition as in Figure *5.1.1*(a), the fitting using Eq. 5.1.2 is shown in Figure *5.1.3*. The fitting parameters used in the simulation for the damping, the inhomogeneous broadening, and the spin transfer torque coefficient are respectively : $\alpha = 0.015$, $\Delta H_i = 8$ mT, $\tilde{a} \approx 18\ 10^{-2}$ T/A. For the fitting of the inhomogeneous broadening ΔH_i, here the value of the damping α was fixed, and ΔH_i was varied until the fitting of the FMR linewidth matched. This approach was used because varying α in the fitting process led to large values that are inconsistent with the literature [132].

Although, the magnetization damping and the FMR inhomogeneous broadening values are in accordance with literature [140], the value of the spin transfer torque coefficient is relatively small compared to the values used in literature. Therefore, those three parameter values are not considered as real values, but more as phenomenological ones to reproduce the experimental results, from this magnetic stack specifically. The parameters extracted here will be added to those in Tableau *5.1.1* and they will be used in the next simulations of the maximum voltage.

With the simulation parameters tuned, next the experimental results of the different free layer sizes are explored.

For a free layer with a thickness of 1.8 nm, and various pMTJ diameters, the measured output dc voltage is shown in Figure *5.1.4*(a). Here, the input rf current has a power of P_{rf} = -5 dBm, and the resonance frequencies were extracted from in-plane magnetic field measurements similar to those in Figure *5.1.1*(c).

Interestingly, in Figure *5.1.4*(a), the maximum amplitude of the output dc voltage (V_{max}) increases as the pMTJ diameter decreases. For instance, for a pMTJ with a nominal diameter D_n = 150 nm, the maximum output voltage is V_{max} =1.3 mV, and for a nominal diameter D_n = 20 nm it is V_{max} = 7.3 mV. Thus the output dc voltage is enhanced by a factor of 5.6. Moreover, for all pMTJ diameters in Figure *5.1.4*(a), the maximum voltage amplitude decays as the FMR frequency increases.

The latter effect is predictable by the voltage formula in Eq. 5.1.2 and is related to the magnetic susceptibility (see Eq. 3.3.11). To have higher resonance frequencies requires higher in-plane magnetic fields (see Eq . 5.1.1). As a consequence, for a free layer with a magnetization aligned in-plane, the higher the in-plane magnetic field, the larger the linewidth of the FMR resonance ($\Delta\omega_0 \propto \frac{\alpha}{\gamma} H_{\parallel}$). Thus, the amplitude of the dc voltage, inversely dependent on the linewidth at resonance, will drop with the FMR frequency as shown in the measurement in Figure *5.1.4*(a).

At a fixed FMR frequency, the enhancement of the maximum dc voltage V_{max} as the pMTJ diameter scales down, is observed for all FMR frequencies. Therefore, to understand the origin of this phenomenon, the FMR frequency can be fixed for the analysis, and thereafter the conclusions can be generalized to all FMR frequencies.

For the upcoming analysis, the chosen FMR frequency, for all free layer sizes, is f_0 = 2 GHz. This frequency was selected to be close to the frequencies of the Industrial-Scientific-Medical (ISM) band, which permits to investigate simultaneously the potential of the spin-torque nano-diodes for applications in such a band.

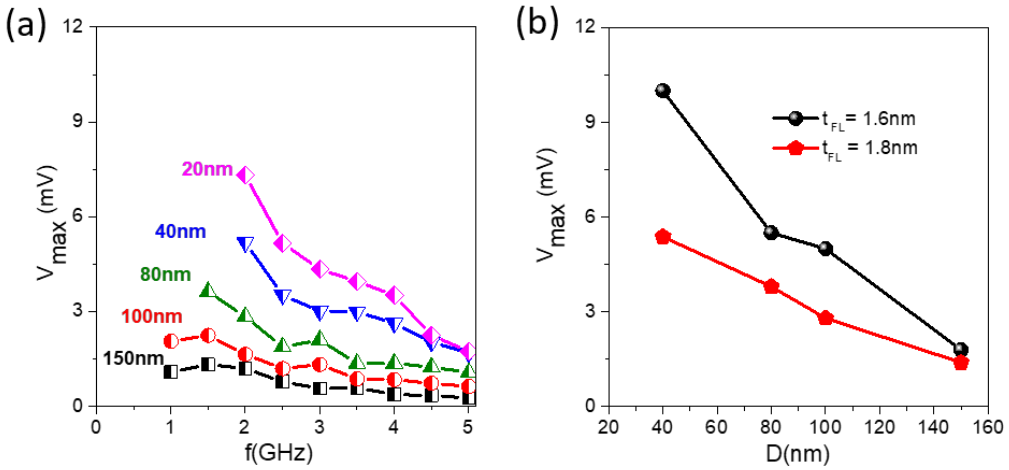

Figure 5.1.4 : (a) Maximum rectification voltage V_{max} for passive detection as a function of the rf excitation frequency f, measured at a source power of P_{rf} = –5 dBm and at zero dc bias current for five devices with different nominal diameters (20, 40, 80, 100 and 150nm) and a FL thickness of t_{FL} = 1.8nm. (b) Maximum voltage V_{max} for passive detection at f = 2 GHz as a function of the nominal diameter D_n for two different FL thicknesses t_{FL}= 1.6 nm and 1.8 nm.

The measurements for f_0 = 2 GHz, are shown in Figure *5.1.4*(b). They contain the maximum voltages from all available nominal pMTJ diameters, and the two free layer thicknesses of 1.6 nm and 1.8 nm. The enhancement of the dc maximum voltage with the reduction of the pMTJ diameter is present also in the free layer with a thickness of 1.6 nm, albeit with a generally higher dc voltage compared to the free layer with a thickness of 1.8 nm. Thus, the maximum of the output dc voltage, enhanced by reducing the pMTJ diameter, is further enhanced by reducing in addition the free layer thickness. These results provide important routes for the optimization of the spin-torque nano-diodes. Albeit, to be useful and for their generality, they have to be understood thoroughly first.

The approach used in this work starts first by investigating the diameter dependence, and then the thickness dependence.

For this we evaluate Eq. 5.1.2 at the resonance frequency $\omega = \omega_0$ for which V_{max} will be proportional to the inverse of the linewidth $\Delta\omega_0$.

Inserting the expression into 5.1.2 we get for V_{max} :

$$V_{max} \approx \frac{R_p}{R_0} * \underbrace{P_{rf}(1-\Gamma^2)}_{\Gamma} * \underbrace{\eta^2(1+\eta)^2}_{TMR} * \frac{\tilde{\alpha}}{\pi * r^2} * \underbrace{\frac{1}{\alpha((H_d - H_u) * (2m_{z0}^2 - 1) + 2H_{\parallel} m_{x0} + (H_{int\perp}) m_{z0})}}_{\delta m_z} \quad (5.1.3)$$

In Eq. 5.1.3, it can be seen that the maximum voltage depends inversely on the square of the diameter through the current density. From the susceptibility (through δm_z) it can be seen that at constant external field $H_{\parallel}$, the maximum enhancement of V_{max} is achieved when $H_u = H_d$. In particular the diameter affects the demagnetizing field H_d as was presented in Figure *4.2.4*(b) and Figure *4.2.5* in chapter 4. At smaller diameters H_d decreases, thus reducing $|H_u - H_d|$ and therefore leading to an increase of V_{max}. Furthermore, through the susceptibility, V_{max} depends on the interaction field $H_{int\perp}$ (from the SAF in case of the FL excitations) and the bias field $H_{\parallel}$. V_{max} can thus be further enhanced if both field components $H_{\parallel}$ and $H_{int\perp}$ are small or zero. Small $H_{int\perp}$means that the SAF stray field needs to be reduced. Finally, for the pMTJ stack studied here, the full TMR is partially masked by a serial resistance from the TaN bottom electrode, see section 4.2 of chapter 4. As a result, the measured effective TMR increases as the pMTJ diameter decreases. Since the output voltage depends also on the TMR through the TMR factor $\eta^2 = \frac{TMR}{2-TMR}$, the latter can also affect the maximum voltage when reducing the pMTJ diameter. Last, but not least, V_{max} also depends on the rf power P_{rf} and the spin torque amplitude $\tilde{a}$.

A variation of the diameter affects almost all of the terms contributing to V_{max}. In order to estimate the relative contributions of the different terms to V_{max} in Eq. 5.1.3, in Figure *5.1.5* they were plotted separately, where in each plot one of the contributions was kept size independent. The values of the parameters used are the same as those used to fit the data in Figure *5.1.1* and Figure *5.1.3*.

First, when keeping the TMR and the injected rf power size-independent, the diameter dependence of the magnetization oscillation amplitude (last factor in Eq. 5.1.3) leads to an enhancement of the maximum dc voltage V_{max} by a factor of ~ 7 when the diameter of the pMTJ is reduced from 150 nm to 40 nm (black line in Figure *5.1.5*). It is reminded here that the calculations were done using the real diameters ($D \approx D_n + 30$).

In addition, when including the diameter dependence of the effective TMR through $\eta^2 = \frac{TMR}{2+TMR}$ in Eq. 5.1.3, the total enhancement factor is ~ 10 (see Figure *5.1.5*, blue line). Thus, smaller pMTJ diameters are necessary to compensate for the TMR reduction due to the presence of the serial resistance. The latter, is better illustrated by the spin polarization ratio in Eq. 5.1.3 : $\frac{(\eta(1+\eta))^2|_{Dn=40nm}}{(\eta(1+\eta))^2|_{Dn=150nm}} = 1.5$. Therefore, the enhancement observed in the dc output signal as the diameter decreases are due to both, the magnetization dynamics and the effective TMR enhancement.

However, the diameter dependence of the resistance will also determine the actual rf power that is transmitted to the MTJ device, due to impedance mismatch. Notably, the increase of the resistance from 550 Ω to 2140 Ω, when reducing the nominal diameter from 150 nm to 40 nm increases the rf reflections (see *Tableau 5.1.2* below). The rf power transmitted to the device P_{rf_0} can be estimated from the reflection coefficient Γ with $P_{rf_0} = P_{rf} * (1 - \Gamma^2)$, where Γ is obtained from deembedding measurements (see section 2. 4. 1 in chapter 2), using a vector network analyzer. When the reflection coefficients are taken into account in Eq. 5.1.3, the total enhancement due to the diameter reduction drops from ~ 30 to ~ 15 (see Figure *5.1.5*, green line).

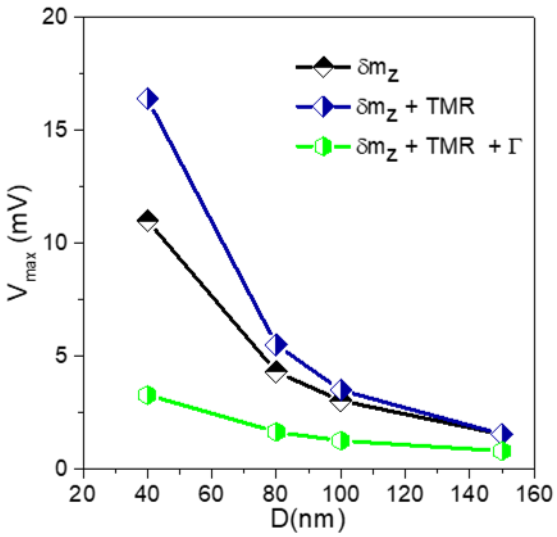

Figure 5.1.5 : The calculated rectification voltage V_{max} vs. the pMTJ diameter obtained using Eq. 5.1.3 for $P_{rf} = -5dBm$. The contribution due to only the variation of the internal magnetic fields, is shown by the black curve and is denoted by δm_z calculated from Eq. 3.3.10 in chapter 3. This contribution is due to the magnetic susceptibility and the STT excitation strength, and it scales the precession amplitude. The blue curve considers in addition the diameter dependence of the TMR due to the serial resistance, while the green curve takes in addition the impedance mismatch into account via the measured reflection coefficients Γ. TMR is the measured resistance changes with the serial resistance from the bottom electrode.

D_n (nm)	$R_0(\Omega)$	Γ @ 2 GHz	$(1-\Gamma^2)$
150	550	0.7	0.51
100	870	0.8	0.36
80	1180	0.84	0.29
40	2140	0.9	0.19

Tableau 5.1.2 : Measured values of the zero-field resistance R_0, reflection coefficient Γ, and portion of P_{rf} injected in the devices for the different nominal diameters D_n.

The predicted diameter dependence (in Fig. 5.1.5) is in good agreement with the experimental results and shows that the output voltage V_{max} can be optimized by reducing the device diameter. The predicted enhancement is attributed to a combination of : the STT excitation strength (via the current density), the precession amplitude via the susceptibility upon reducing $|H_u - H_d|$, and the serial resistance affecting the TMR.

In addition to the signal enhancement related to the reduction of the device diameter, the observed increase in signal when changing the thickness from $t_{FL} = 1.8$ nm to $t_{FL} = 1.6$ nm is also consistent with the theoretically calculated enhancement by a factor of ~1.8 (at f = 2 GHz, and D_n = 150 nm).

For a similar *rf* power and nominal diameter D_n, the resistance is the same for both thicknesses (see section 4. 2 of chapter 4), hence the voltage enhancement is mostly caused by the magnetization dynamics. A reduced FL thickness will increase the perpendicular anisotropy ($\propto 1/t_{FL}$) and thus reduce the magnitude of the effective anisotropy $|H_{ueff}| = |H_u - H_d|$ in Eq. 5.1.3. In consequence, it increases the precession amplitude and through this the maximum output voltage. Here a 10% change due to the increase of the spin transfer torque amplitude $\propto 1/t_{FL}$ is neglected.

Thus, in particular, for the MTJ configuration with iPMA, tuning the effective anisotropy H_{ueff} towards zero minimizes the FMR peak linewidth, and thus increases the magnetization oscillation amplitude. The reduction due to the impedance mismatch could be avoided when using an impedance matching network.

Finally, although, the analytic model developed here describes well the experimental results, it must be reminded that it does not take into account the thermal fluctuations (noise). Moreover, in the experiment, the thermal noise measured is not from the free layer solely. It is the total noise from all the constituents of the experimental setup, including the pMTJ. As a consequence, it buries a part of the output dc voltage, and therefore it reduces the sensitivity of the spin-torque nano-diode to rf currents with low powers. In the next section, this issue is addressed by characterizing the signal to noise ratio of the experimental results, for all the MTJ diameters and for t_{FL} = 1.4 nm.

5.1.3 The characterization of the signal to noise ratio and the sensitivity

The signal-to-noise ratio SNR_V for the voltage is here defined as the signal amplitude V_{max} divided by the *rms* noise background. The corresponding single-to-noise-ratio for the power in dB is given by $SNR_{dB} = 20\log(SNR_V)$. Figure *5.1.6*(a) shows the output voltage V_{max} (solid dots) and the corresponding *rms* noise levels (open dots), for all pMTJ diameters, and as a function of the input rf current power (P_{rf}) with a frequency of 2 GHz. The measurements are from a free layer with a thickness of t_{FL} = 1.8 nm. In Figure *5.1.6*(a), when P_{rf} increases from –25 dBm to –5 dBm, the signal amplitude increases linearly by a factor of 100, from 10 µV to 1 mV, for devices with nominal diameters D_n = 150 nm, and from 100 µV to 10 mV for devices with nominal diameters D_n = 40 nm. Moreover, for devices with nominal diameters D_n = 80, 100 and 150 nm, the noise level is of the order of 1 µV and is almost independent of rf current power P_{rf} (only a slight increase is observed for P_{rf} > –10 dBm). It is reminded here that the real diameters are around 30 nm larger than the nominal ones.

The devices with nominal diameters D_n = 40 and 20 nm show higher *rms* noise levels up to 10 µV for rf current power P_{rf} = –5 dBm. A possible origin of the increase in the noise level at low MTJ diameters is a current-induced heating due to their higher electrical resistances. With this the minimum signal-to-noise-ratio at P_{rf} = –25 dBm is SNR_V = 22 (SNR_{dB} = 26 dB) for D_n = 150 nm and SNR_V = 90 (SNR_{dB} =39 dB) for D_n = 20 nm. These values are above the recommended minimum SNR_V level of ~18 (SNR_{dB} = 25 dB) for wireless networks [141]. However, they do not take into account the impedance mismatch that leads to a reduced power at the device level. Including the correction of the impedance mismatch to determine the actual power seen by the pMTJ device, the SNR is much higher. An example is shown in Figure *5.1.6*(a) for a pMTJ device with a nominal diameter D_n = 40 nm, where for the corrected rf current power P_{rf} = -25 dBm, the

increases to SNR_V > 1030 (SNR_{dB} > 60 dB), while for a corrected power of P_{rf} = -40 dBm the SNR_V > 11 (SNR_{dB} > 20 dB).

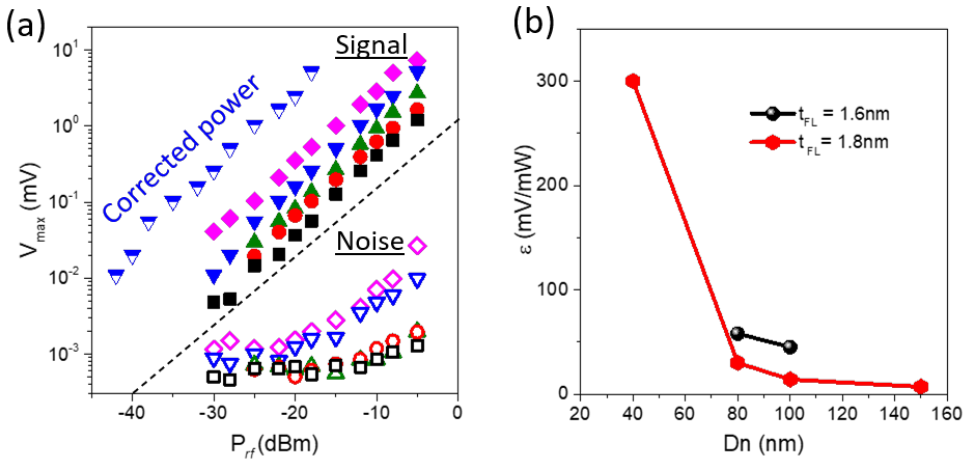

Figure 5.1.6 : (a) The power dependence of the maximum voltage (closed dots) and the *rms* noise (open dots) of the devices shown in Figure 5.1.4(a) at f = 2 GHz. Full dots are with respect to the rf source power. An example is shown for D_n = 40nm for the rf power seen by the device when correction due to impedance mismatch is taken into account (in blue, half-filled, inversed triangles). The correction results in a shift of the curve to lower power, which is largest for the smallest diameters. The dashed line is used to separate visually the signal data from the noise data. The color code correspond to the FL nominal diameters shown in Figure 5.1.4(a). (b) The sensitivity ε as a function of the nominal diameter D_n. Here the rf power has been corrected for the impedance mismatch for all diameters.

For the sensitivity to the rf power ε, it is defined as the slope of the maximum dc voltage V_{max} vs. P_{rfo}, where P_{rfo} is the corrected power due to impedance mismatch. As can be seen from Figure *5.1.6*(b) (for t_{FL}=1.8nm), the sensitivity increases from 7 mV/mW for a device with a nominal diameter D_n = 150 nm, to 300 mV/mW for D_n = 40 nm. These results indicate that the rf-to-dc property of the pMTJs can be optimized by adjusting the free layer thickness and diameter.

Comparing the results obtained here with the passive spin torque diode outputs from literature shows that the sensitivities are similar if the pMTJs impedance mismatch is corrected. The comparison is sketched in Figure *5.1.7*, for a pMTJ with a FL thickness of 1.8 nm and a nominal diameter of 20 nm (in pink). The sensitivity as defined above, is the slope of the voltage vs. rf power, and is illustrated in Figure *5.1.7* by the dashed line. It can be seen that the results from literature follow approximately this slope. However, the results from literature correspond to lower rf powers, which might be due to the lock-in amplifier in the setup. It should be noted that these literature results are from MTJs that use an in-plane polarizing layer, while the measurements from this work are from MTJs with an out-of-plane polarizing layer.

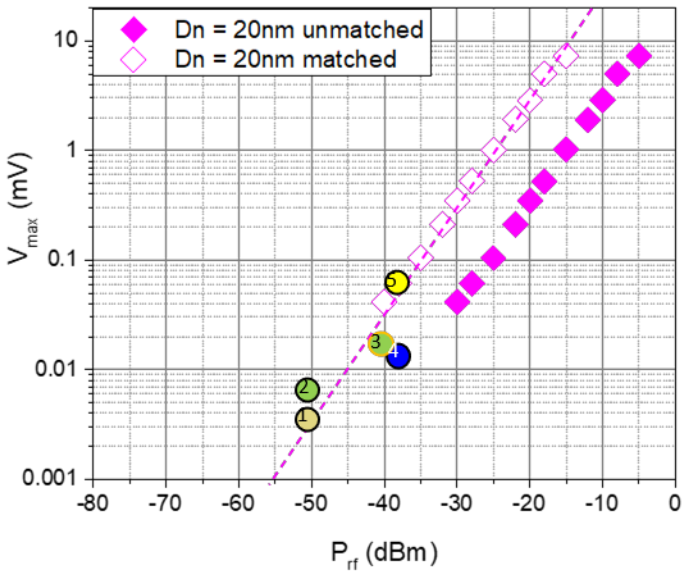

Figure 5.1.7 : V_{max} under in-plane field of a pMTJ with a FL thickness of 1.8 nm and a nominal diameter of 20 nm (pink Rhombus) compared to reported results from passive spin torque nano-diode experiments (colored circles with numbers). The reported results 1-5 are respectively from references *[63], [71], [100], [101], [142]*.

Motivated by these results, in the next section the pMTJ devices will be tested for wireless communication applications. Specifically, the demodulation of the type On-Off-Keying (OOK) [143].

5.1.4 Demonstration of On-Off-keying (OOK) demodulation in pMTJs

Demonstration of OOK modulation

In the previous section, it was shown that the rf-to-dc conversion is at the same time a band pass frequency filter that responds only to specific frequencies. Therefore, it can be used to demodulate information if "1" is coded in the resonance frequency and "0" by an off-resonance frequency.

The basic concept of the modulation/demodulation consists of mixing an input data signal that has a low frequency, with a signal that has much higher frequency called the carrier for efficient transmission (e.g smaller antennas) [144]. The latter, can be made more efficient by encoding the data in the frequency (FSK) or the phase (PSK) of the carrier, leading to a better immunity to noise [143].

For a pMTJ with a nominal diameter of 40 nm, and a free layer thickness of 1.8 nm, the demodulated signal is shown in Figure *5.1.9*(a)-(c) for different square signal (data) frequencies : 10 kHz, 50 kHz and 100 kHz respectively. The free layer resonance frequency was tuned to 2.4 GHz using an in-plane magnetic field of magnitude 20 mT. The original square signal used for OOK modulation is plotted in red in Figure *5.1.9*, it has an amplitude of 400 mV.

However, for an initial demonstration, here the pMTJs were tested for amplitude modulation of the sort OOK. An illustration of the OOK signal fed to the pMTJs is shown in Figure *5.1.8*. The rf frequency was fixed at 2.4 GHz and its power to -5 dBm. For the square modulation signal, its frequency is changed, in order to probe the limits at which the data frequency becomes too fast for the pMTJs to demodulate correctly.

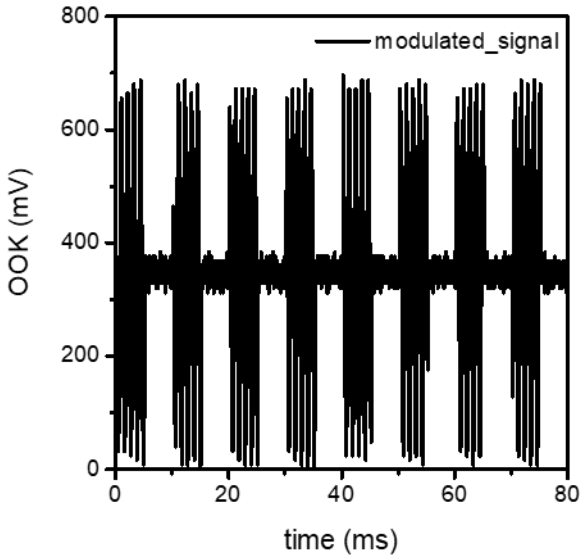

Figure 5.1.8 : An example of the OOK signal used in the demonstration. Its square signal frequency is set here to 100 Hz for illustration purposes.

For an OOK input (square signal) with a modulation frequency of 1 kHz, the demodulated signal at the output of the pMTJ is shown in Figure *5.1.9*(a). The output square signal reproduces well the original data in terms of frequency and phase. However, for the amplitude the demodulation efficiency is low $\frac{V_{MTJ}}{V_{data}} \approx 0.5$ %, and it has a noticeable background noise, which is a general feature of amplitude modulation [144].

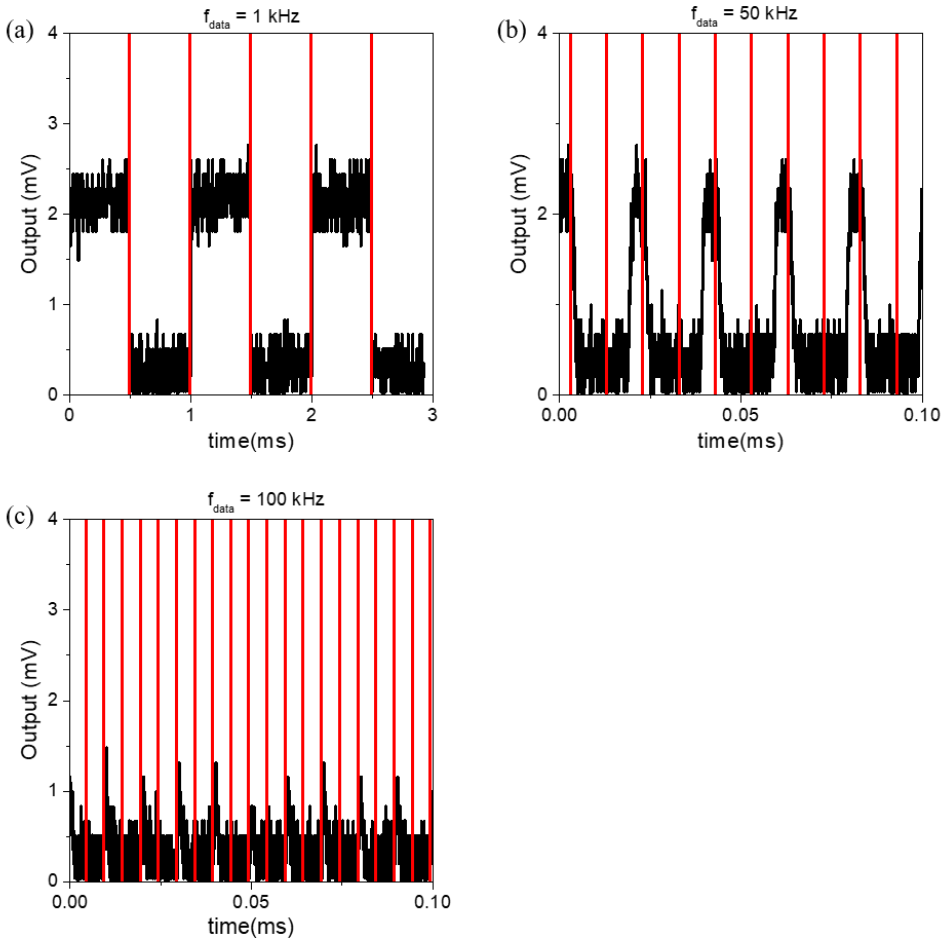

Figure 5.1.9 : OOK demodulation using a pMTJ with a nominal diameter of 40 nm and a free layer with a thickness of 1.8 nm. The carrier frequency of the input OOK signal is 2.4 GHz and its envelope square signal has a frequency of (a) 10 kHz, (b) 50 kHz and (c) 100 kHz.

Moreover, as the modulation frequency of the OOK signal increases, the demodulated signal starts to be distorted strongly until it almost disappears for a frequency of 100 kHz, see Figure *5.1.9*(b)-(c). The latter is not expected to be from the FL dynamics. It is attributed to the instruments of the setup. This is because for the pMTJs to be unable to demodulate the OOK, the modulation frequency must be in the range of the relaxation of the free layer magnetization. In this case, only the transient response of the forced free layer is present, not the steady state response required for the demodulation. Since, for these pMTJs, the relaxation rate of the free layer magnetization is estimated to be around 11 MHz (see section 3.2 of chapter 3), the output signal distortion is unlikely to be due to magnetization dynamics.

To investigate this assumption, the input signal was measured alone without the presence of the magnetic tunnel junction, for different OOK modulation frequencies. The results are shown in Figure *5.1.10* (a)-(b).

The measurements validate the assumption that the distortions in the signal are already present in the input OOK signal. Thus, even with distorted OOK inputs the spin-torque nano-diode was demodulating properly.

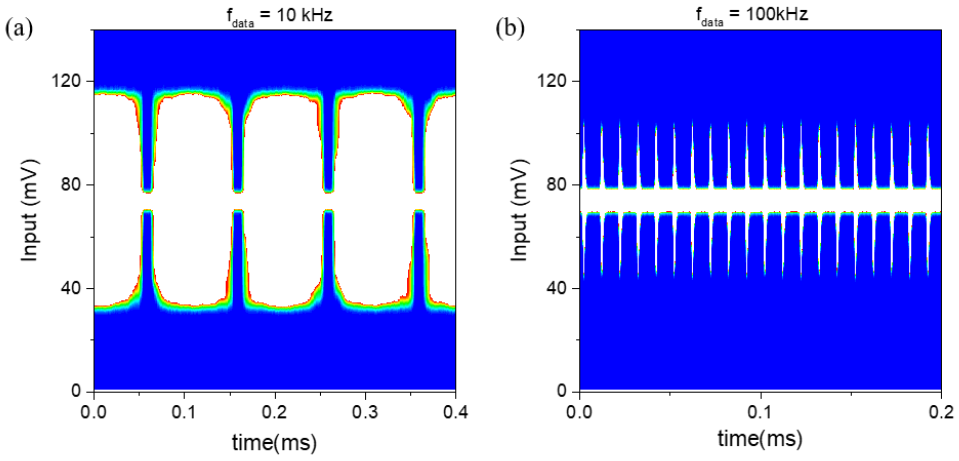

Figure 5.1.10 : (a) OOK square signal with a modulation frequency of 10 kHz. (b) the same as (a) but for 100 kHz

Unfortunately, this instrument-related issue prevents further experimental analysis of the demodulation properties of the pMTJs at higher modulation frequencies. This needs to be addressed in future experiments, in addition to the demonstration of FSK frequency demodulation instead of the amplitude to increase the signal to noise ratio.

Enhancing the SNR via filtering

In order to enhance the sensitivity to low input power, and the signal to noise ratio, one can use specific types of filters, either analog or digital. The latter can be more energy-efficient than lock-in-amplifiers to enhance the sensitivity, and much smaller in size compatible for integration with CMOS circuits. One specific type of digital filtering proposed here is based on the use of the correlation of the demodulated signal with the expected input, also called matched filters [145]. It permits to maximize the signal to noise ratio of the signal. The schematics of the process is illustrated in Figure *5.1.11*, adapted from [145].

To implement the matched filters the most energy efficient solution is to use analog filters [146]. Although, for physical demonstration, this can be done efficiently by using a second order digital filter such as Finite-impulse-response (FIR) filter [145].

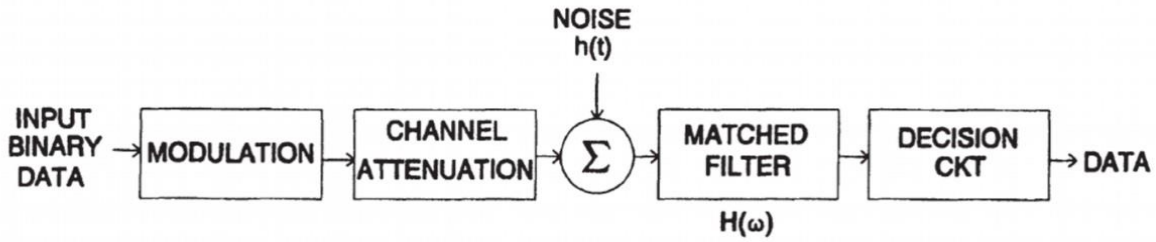

Figure 5.1.11 : Schematics to illustrate how to maximize the signal to noise ratio using matched filters and digitalization. Adapted from [145].

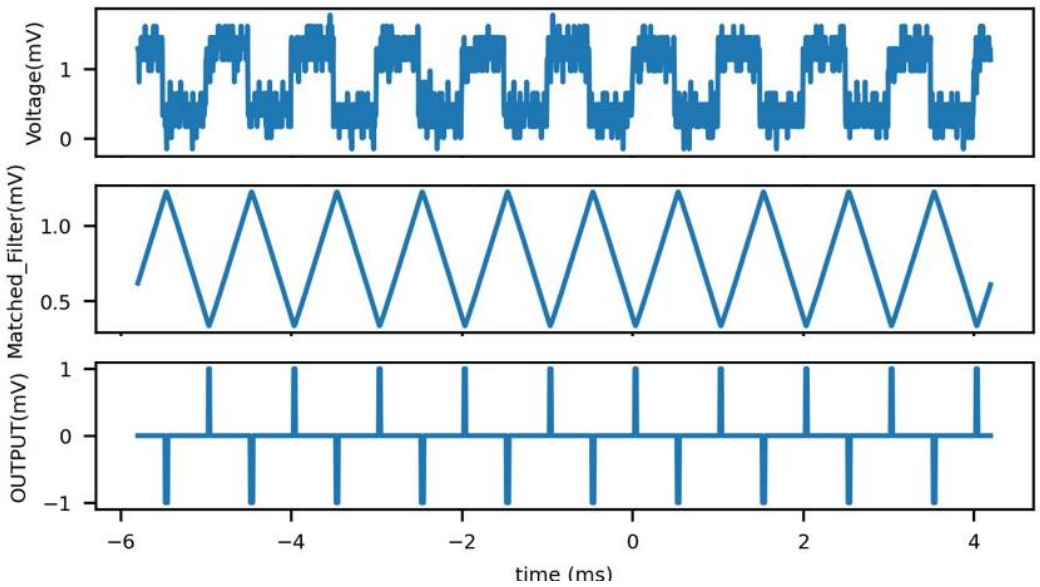

Figure 5.1.12 : (a) Experimental data for an OOK demodulated signal from a pMTJ with a nominal diameter of 40 nm, and a free layer thickness of 1.8 nm. (b) The output of a digitally implemented matched filter. (c) digitized version of (b) by setting a threshold of ~1.1 mV for "1" and ~0.6 mV for "-1".

Here, for a first demonstration of the feasibility of using a matched filter, it was implemented digitally, using a python software, and subsequently the maximized signal was sampled for a data stream of "1" and "-1" using a threshold detector, see Figure *5.1.12*. This is called decision CKT. The next step would be to implement such a filtering technique in a Field-programmable-gate-array (FPGA) to test the sensitivity of the spin-torque nano-diodes and explore how much the sensitivity can be enhanced using this technique.

So far all experiments presented above on the rf-to-dc conversion, were done under the in-plane magnetic bias fields. In the next section, the analysis will be extended to the characterizations using an out-of-plane magnetic field.

5.2 The spin-torque nano-diode effect under an out-of-plane magnetic field

For the perpendicular magnetic tunnel junctions (pMTJ), the characterization of the magnetization dynamics using an out-of-plane magnetic bias field is of great interest. For instance, once the rf-to-dc optimization is done under an external bias field, it is easy to generate this field locally in the pMTJ by adjusting the synthetic antiferromagnet thicknesses. This is more challenging to do for an in-plane magnetic bias field. However, understanding the measurements under an out-of-plane magnetic field are more complicated than those under in-plane magnetic field. This is because, under strong out-of-plane magnetic fields, both the FL and PL are orientated out-of-plane and therefore careful analysis must be conducted to distinguish between their FMR modes. Higher out-of-plane magnetic fields lead to an opening angle between the bottom SAF layer and the top SAF and polarizing layers, also called the spin flop effect [147]. The latter is present in the magnetoresistance measurements of all the FL thicknesses under an out-of-plane magnetic field, see Figure *5.2.1* (replotted from section 4.2 in chapter 4).

The measurements in Figure *5.2.1* were carried out using a PPMS setup that does not support high frequency measurements. To measure the rf detection we used a permanent magnet. Although, it limits the full range of characterization, it will allow a first understanding of the dynamics of the magnetic layers. The value of the magnetic field generated by the permanent magnet during the characterization is around 220 mT.

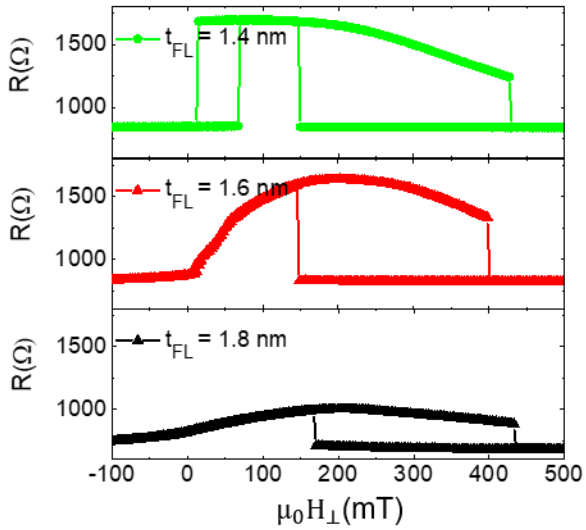

Figure 5.2.1 : The magnetoresistance as a function of an out-of-plane magnetic field, for pMTJs with nominal diameters of 100 nm, and free layer thicknesses of 1.4 nm (in green), 1.6 nm (in red), and 1.8 nm (in black). The measurements were done under a weak dc current magnitude I_{dc} = 10 µA.

The spin-torque nano-diode effect of the pMTJs, under an out-of-plane magnetic field and an rf current of a power of -10 dBm, is shown in Figure *5.2.2*(a)-(c). The measurements were done on pMTJs with nominal diameters of 80 nm and for all free layer thicknesses : 1.8 nm, 1.6 nm, and 1.4 nm.

The output voltage as a function of the rf frequency (Figure *5.2.2*), has a characteristic asymmetry in the corresponding resonance peak for all free layer thicknesses. Moreover, there are secondary resonance peaks, with lower amplitude, that are close to the main resonance peak, in the high frequency side.

In addition, the peak-to-peak maximum voltage obtained under an out-of-plane field (~ 4.5mV at -10 dBm) is in general higher than the ones reported under an in-plane magnetic bias fields (~1.5 at -10 dBm). The maximum voltage shows as well a trend to increase as the free layer thickness decreases. However, as will be discussed in the next section, the changes are mostly due to the reorientation of the free layer magnetization towards an out-of-plane easy axis. Thus, leading the free layer magnetization to be fixed and the polarizing layer magnetization to be the one that oscillates. Indeed, for an out-of-plane magnetic field larger than 200 mT the free layer with a thickness of 1.4 nm is saturated out-of-plane (see Figure *5.2.1*), and is unlikely to give large angle oscillations that are higher than the in-plane magnetic field case.

Moreover, the maximum output voltage exhibits a diameter dependence similar to that discussed in the previous section, see Figure *5.2.3*. For an rf power of -10 dBm and a frequency of 2.4 GHz, the enhancement is $\frac{V_{max}(D_n=40\ nm)}{V_{max}(D_n=150\ nm)} \approx 3$. The latter is attributed to the origins discussed before in the in-plane field case : the STT excitation strength, the competition of the PMA with the demagnetizing field that determines the susceptibility, the bottom layer serial resistance, and additionally for the polarizing layer the indirect exchange coupling to the SAF that is modeled as an interaction field $H_{int\perp}$.

Adding the best results obtained under the out-of-plane magnetic field to the comparison in Figure *5.1.7* under in-plane field, shows a promising enhancement of the V_{max} in out-of-plane fields as compared to in-plane fields. This is shown in Fig. 5.2.4 where the pMTJ's impedance mismatch is corrected. The results from the out-of-plane field, highlighted in red in Figure *5.2.4*, belongs to a device with a FL thickness of 1.4 nm, and a nominal diameter of 40 nm. It is reminded here that the different points in the comparison were selected for their sensitivity, however, they can have different frequencies and bias field orientations.

We now come back to the output signal shape and its asymmetry observed for all FL thicknesses for the rf-to-dc conversion under an out-of-plane field. It is noted that a similar asymmetry can also be observed for the detection under in-plane field as shown in Figure *5.1.1*(c) for the resonance peak that are attributed to the PL.

A thorough analysis of the signal shape will require numerical simulations that includes all magnetic layers and their possible interactions (via dipolar and/or interlayer exchange coupling). In the following a simplified analysis is attempted by focusing on the magnetization dynamics of the polarizing layer that is coupled to the SAF.

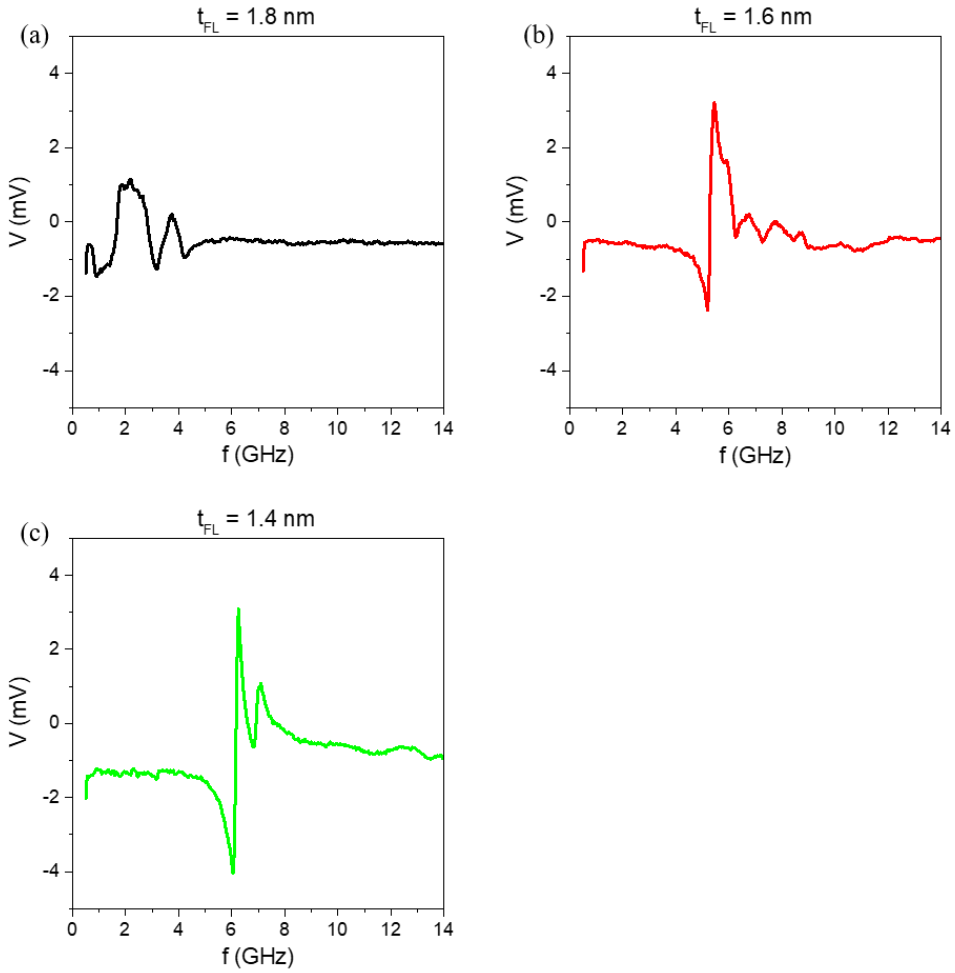

Figure 5.2.2 : The output voltage of the pMTJ as a function of the frequency of the injected rf current. The rf current has a power of -10 dBm. The pMTJs have a nominal diameter of 80 nm, and their thicknesses are : (a) 1.8 nm (black), (b) 1.6 nm (red), and (c) 1.4 nm (green). The applied out-of-plane magnetic field is around 220 mT.

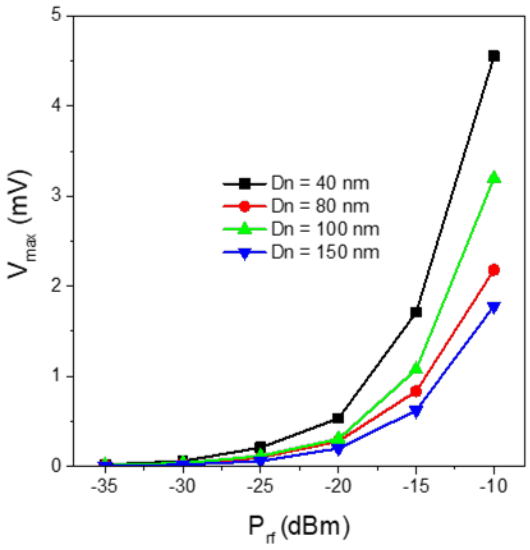

Figure 5.2.3 : The maximum output voltage V_{max} for pMTJs of a free layer thickness of 1.4 nm and different nominal diameters (as indicated in the legend). The injected rf current has a frequency of 2.4 GHz.

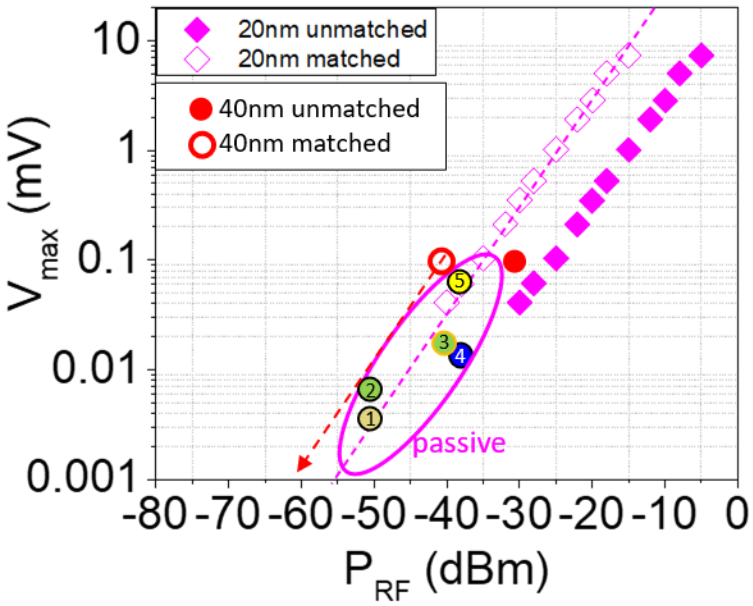

Figure 5.2.4: V_{max} of pMTJs compared to previous results for passive detection presented in Figure 5.1.7. The results under an out-of-plane magnetic field, illustrated by red points are from a pMTJ with a FL thickness of 1.4 nm and a nominal diameter of 40 nm. The comparison focuses on the best output signals (of pMTJs and literature results) and therefore the points are for different operating fields and frequencies.

5.2.1 On the antisymmetric shape of the ferromagnetic resonance under an out-of-plane magnetic field

In general, the asymmetry in the signal shape of a uniformly magnetized spin-torque nano-diode is attributed to the field-like torque [138], [139], or the non-collinearity of the bias field and the magnetization, or the VCMA [70], [100]. However, the field-like torque effect is unlikely to be the origin of the asymmetry here, because in the in-plane field measurements only the PL FMR is asymmetric. In addition, numerical simulations given in reference [95] demonstrate that for pMTJs the field-like torque effect on the free layer magnetization switching is negligible, unlike its effect in in-plane magnetic tunnel junctions reported in references [138] [139].

As for the VCMA effect, it was demonstrated from the PPMS measurements in section 4.4.1.3 from chapter 4, that it is weak in the pMTJs under investigation. In addition, since the free layer's interface perpendicular magnetic anisotropy is almost compensated by the demagnetizing field, the VCMA effect should be more recognizable in its magnetization resonance than the one of the polarizing layer. In Figure *5.1.1*(c), the free layer ferromagnetic resonance response shows a symmetric Lorentzian shape, which suggests a weak VCMA effect for the FL.

The above cited possible mechanisms on the origin of the signal asymmetry stem from considering a magnetic layer with a uniform magnetization, and that is not coupled to other magnetic layers. However, when considering the polarizing layer it is coupled via exchange interaction to the synthetic antiferromagnet (SAF). Furthermore, the PL will also experience dipolar interaction to the SAF and/or the FL. While quite generally it is known that the ferromagnetic resonance frequency is affected through coupling of different layers, an asymmetry in the resonance peak was reported in [89] for a coupled system of oscillating magnetic layers. For the SAF structures in general this is the case when the exchange coupling is not large enough for the optical and acoustic modes to be separated in a wide range of frequencies (the two modes are phase shifted by π).

Therefore, this maybe an origin for the asymmetry in the polarizing layer resonance. For instance, the PL FMR peak might be initially asymmetric due its coupling to the SAF, but its asymmetry is subject to changes due to other phenomena such as the field-like torque, the non-collinearity with the field, dipolar coupling, and the VCMA.

To investigate the SAF coupling effect on the PL detection signal shape, the macrospin model from section 3.3 of chapter 3 was extended to include the exchange coupling to the SAF (section 3.4). To simplify the calculations only the interlayer exchange coupling was considered as a coupling mechanism.

Earlier on, for the FMR frequency fitting (section 5.1), the model considered only one magnetic layer and the SAF effect was approximated by a fixed out-of-plane magnetic field. By including the exchange coupling between the PL and SAF to the model, the investigations of the FMR shape will be more accurate because the SAF oscillations are considered as well at least in first approximation. The layers considered in the calculations are illustrated in Figure *5.2.5*.

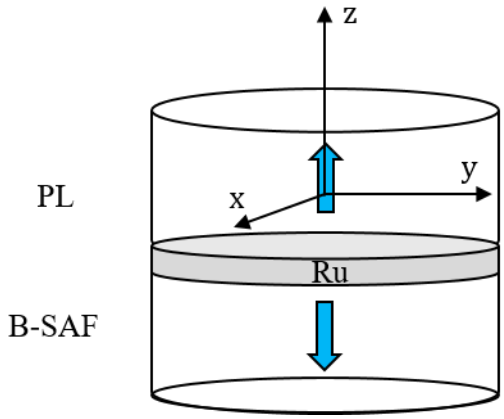

Figure 5.2.5: Illustration of the composite polarizing layer coupled to the magnetization of the bottom layer of SAF through a thin Ru layer.

For such a system of coupled layers, the magnetizations dynamics are given by two coupled LLG equations. The analytical solutions of this system, for damped oscillations are provided along with their derivations in section 3.4 of chapter 3. The solutions predict for the PL resonances an antisymmetric shape with the following frequencies, corresponding to the first (ω_-) and second (ω_+) peaks respectively :

$$\omega_- = \sqrt{\omega_0^2 - \gamma^2 \xi} \tag{5.2.1}$$

$$\omega_+ = \sqrt{\omega_0^2 + \gamma^2 \xi} \tag{5.2.2}$$

with the exchange coupling term $\xi = 2J_r(H_\perp - H_{ueff})$, with J_r the exchange energy coefficient. It must be noted here that the main difference between this model and the previous one used in section 5.1 is that only one of the two frequencies was considered as the PL FMR. It is reminded here that ω_0 is the FMR frequency in the absence of the interlayer coupling, ie Eq. 5.1.1.

The analysis of the solutions around ω_0 in section 3.4 of chapter 3, predicts that the FMR signal changes its sign as the rf excitation frequency changes from ω_- to ω_+. Thus, the two peaks make an asymmetric resonance response. The derived formulas are in good agreement with the analysis in ref. [89].

Combining these solutions with the spin-torque nano-diode voltage in Eq. 5.1.2, the predicted polarizing layer response is shown in Figure *5.2.6*. Here, the out-of-plane magnetic bias field was tuned to have the resonance frequencies similar to those observed experimentally in Figure *5.2.2*. It has a value of 400 mT almost twice of the field value used in the experiment. For the exchange coefficient $J_r = 10^{-3}\, J/m^2$, it's value was selected to be similar to the value used in other references to fit experimental measurements, such as [90], [148]. The values of the remaining parameters are in the figure caption of Figure *5.2.6*.

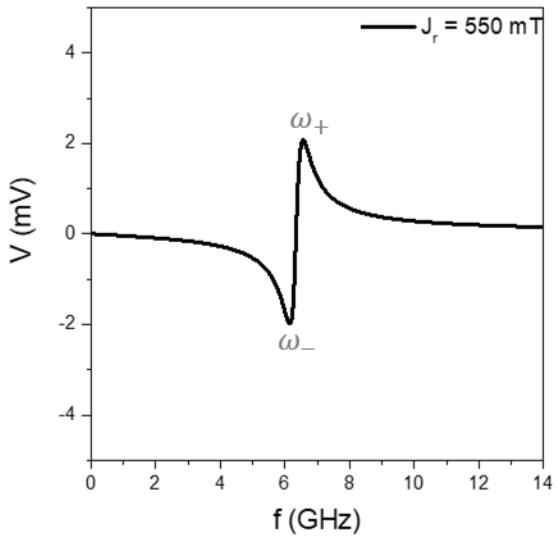

Figure 5.2.6 : The simulated output voltage of the polarizing layer vs. the frequency of the injected rf current. Here, the thickness of the polarizing layer is 1.8 nm and its nominal diameter is 80 nm. The power of the rf current is -10 dBm, the spin torque coefficient is $\tilde{a} \approx 1.8\, T/A$, and the out-of-plane magnetic field bias is $\mu_0 H_\perp \approx 400\, mT$.

The amplitude and the resonance frequencies are in agreement with the experimental results shown in Figure *5.2.2*. Therefore, these results suggest that the asymmetry in the output signal of the spin-torque nano-diode, maybe caused by the coupling of the polarizing layer to the SAF. Moreover, it highlights the importance of considering the coupling between the magnetic layers as a cause of the asymmetry in the resonance, among other possible reasons mentioned earlier.

However, the model derived here provides only a rough approximation of the magnetization dynamics under relatively small out-of-plane bias fields. A thorough analysis of the coupling between the magnetic layers requires numerical simulations, where the thicknesses and internal parameters of the two coupled layers are different. For instance, at higher out-of-plane magnetic fields when the synthetic antiferromagnet starts to rotate towards the bias field (spin flop), the opening angle between the polarizing layer and the free layer becomes larger. Thus, it can lead to higher output signals or different signal shapes that are not predicted by the model here.

Finally, an interesting feature of the signal shape in Figure *5.2.2* is the broadness after the second resonance maximum accompanied with small second order resonance peaks. The latter broadened signal shape, is similar to the signal shapes reported in ref [149]. It was attributed to the fusion of two magnons (spin flip). However, it is worth noting that using the model in section 3.4 of chapter 3, when the interlayer exchange coupling is reduced by 100 times, the ferromagnetic resonance has a similar broadened signal shape with secondary peaks, see Figure *5.2.7*. The latter though is still preliminary and requires further investigations, both in simulations and experiments.

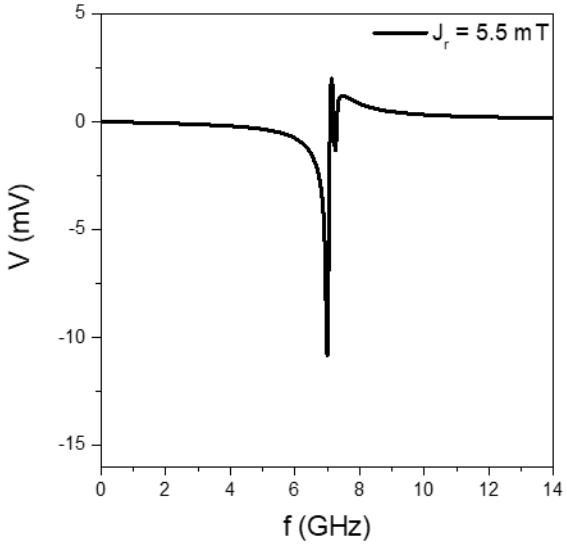

Figure 5.2.7 : Simulations of the polarizing layer output voltage vs. the rf signal frequency. The values of the parameters used for the simulations are the same as in Figure 5.2.6 except for the interlayer exchange coupling that is 100 times smaller.

Conclusion

In this chapter, the investigations were entirely focused on the passive rf-to-dc conversion using pMTJs. The experimental characterizations covered all free layer thicknesses (1.4 nm, 1.6 nm, and 1.8nm) under in-plane and out-of-plane magnetic field biases, in addition to the different device diameters (nominal 20 nm, 40 nm, 80nm, 100nm, and 150 nm). The results from both the free layer, and the polarizing layer were explained using the analytic model developed in chapter 3.

It was found experimentally, that reducing the diameter of the pMTJs enhances the maximum output voltage. For the in-plane bias field, the enhancement ratio is around 7 when reducing the nominal diameter from 150 nm to 20 nm. The origin of this enhancement was attributed to the combination of the higher current density, the compensation of the magnetic anisotropy by the demagnetizing field, and for the pMTJ devices studied here, to the presence of an ohmic serial resistance. This interpretation is well confirmed by modeling the voltage of the spin-torque nano-diode. In addition, it was found that by reducing the free layer thickness, the signal is further enhanced, by almost twice its value. This is attributed to the compensation of the interface perpendicular magnetic anisotropy field by the demagnetizing field.

Motivated by the results on the rectification signals, the pMTJs were tested for their demodulation capabilities using OOK modulation showing good preliminary results. Further improvement of the signal to noise ratio was proposed and simulated for the demodulation using a matched filter.

For the out-of-plane magnetic field measurements, excitations of the PL was detected. It shows a diameter dependence similar to the one observed for the in-plane field measurements. It is found that the out-of-plane field in general leads to higher rf-to-dc voltages compared to the in-plane field.

In the next chapter, the spin-torque nano-diode effect will be further explored by adding a dc current (active). The latter is expected to enhance the spin-torque nano-diode maximum voltage through the additional spin transfer torque (STT).

Active radiofrequency detection in pMTJs

As discussed in section 3.2 of chapter 3, the injection of a spin polarized dc current in a ferromagnetic layer affects the magnetization dynamics. Depending on the dc current sign, it can counteract or enhance the damping of the magnetization precession. For a magnetic layer, excited by a weak spin polarized rf current into FMR, this means that the dc current can increase or decrease its linewidth. Therefore, adding a spin polarized dc current, which compensates for the damping, will reduce the linewidth of this ferromagnetic resonance response. As a consequence, since the amplitude of oscillations, and with it the rf-to-dc conversion, depends inversely on the linewidth, the output voltage will be enhanced when adding a dc current. This is called here the active rf-to-dc conversion.

Such an enhancement of the rf-to-dc conversion signal amplitude, using a dc current, was demonstrated first in the paper on spin-torque nano-diodes in ref. [68]. Afterwards, it was used by S. Miwa et al. in ref. [71] to achieve high sensitivities surpassing those of semiconductor diodes at room temperature. Ever since its demonstration, the active rf-to-dc conversion is a well-established procedure to improve the spin-torque nano-diodes sensitivities for the uniform and non-uniform MTJs such as vortex based devices (see section 1.2 of chapter 1).

For sufficiently strong spin polarized dc currents, the magnetization becomes unstable and either switches between a parallel and antiparallel state or it can setup large angle steady state oscillations of the magnetization. An interesting feature of these self-sustained large angle oscillations is the ability to change the oscillations frequency by varying the dc current amplitude [62]. In this self-sustained oscillation state, the response of the MTJ dynamics to an additional external rf signal is different than in the passive and subcritical regime. Namely, the rf signal can injection lock the self-sustained oscillations and force the magnetization to oscillate at a given frequency, within a relatively large frequency range (locking range). It locks its phase leading to a drastic decrease of the oscillation phase noise. This strong reduction of the phase noise translates to smaller linewidth and higher output power at the oscillation frequency [99]. For the generation of rf signals using MTJs, injection locking is an active area in the quest for the reduction of their phase noise, see [150]–[154]. As for the spin-torque nano-diodes, which are the focus of this work, the injection locking was demonstrated to increase strongly their sensitivity to low power rf currents, see [100]–[102].

However, the signal enhancement using the active detection comes at the cost of more energy consumption, and needs to be evaluated for a given target application.

The active rf signal detection using pMTJs will be analyzed in this chapter. The investigation includes the different free layer thicknesses (1.8, 1.6, and 1.4 nm) and nominal diameters (40, 80, 100, and 150 nm), as well as studies for in-plane $H_{\parallel}$ and out-of-plane $H_{\perp}$ magnetic fields. For each FL thickness, first the magnetization dynamics is characterized for the dc current alone to understand its effect on the FMR frequency, and afterwards the rf current is added to investigate the spin-torque nano-diode effect.

6.1 The active detection under an in-plane magnetic field for t_{FL} = 1.8 nm

Following the structure of the passive detection chapter (chapter 5), here the investigations start for in-plane magnetic fields, and then proceed to out-of-plane fields. Furthermore, for each field orientation, the results from the FL thickness 1.8 nm are presented first, followed by those from 1.6 nm and 1.4 nm successively.

6.1.1 Spectral analysis of thermal FMR modes under dc current for t_{FL} = 1.8 nm

The aim of this subsection is to study experimentally the effect of the dc current on the magnetization dynamics of the pMTJ magnetic layers, in the absence of the rf current. This is important to understand the active rf-to-dc conversion, and to disentangle between the rf and dc current contributions to the output signal of the active spin-torque nano-diodes.

To investigate the dc current effect on the FMR frequency, as well as on its linewidth and power, the technique used here is based on the thermal FMR experiments described in section 2.4.3 of chapter 2. It consists of probing the magnetization dynamics through its resistive response (the TMR effect), by injecting a dc current in the pMTJ and measuring the resulting rf voltage signal using a spectrum analyzer.

The measurements of the FMR current dependence

In Figure *6.1.1*, the power spectral densities are shown for a device with a free layer thickness of 1.8 nm and nominal diameter of 80 nm, and under an in-plane magnetic field bias $\mu_0 H_{||} = 80$ mT. In Figure *6.1.1*(a)-(b) and Figure *6.1.1*(c)-(d) the dc currents have the same magnitudes but opposite signs. In addition, in Figure *6.1.1*(a) and Figure *6.1.1*(c), as in Figure *6.1.1*(b) and Figure *6.1.1*(d), the dc currents have the same sign but their magnitudes are different.

The power spectral densities in Figure *6.1.1*(a)-(d), in general, show two FMR modes, one at lower frequency and the other at higher frequency. In chapter 5 on the passive detection a similar result has been obtained, where the low frequency mode is attributed to the excitation of the free layer and the high frequency mode to the excitation of the PL. This identification is supported here by the current dependence of the oscillation power.

For instance, in Figure *6.1.1*(a)-(b) and Figure *6.1.1*(c)-(d), where the dc current has the same magnitude but the opposite sign, the two modes react differently to the current. Under a positive current, where the electrons flow from the polarizing layer to the free layer, the low frequency mode exhibits higher oscillation power compared to the mode at higher frequency. In addition, its oscillation power is further increased as the positive current amplitude increases, see Figure *6.1.1*(b) and Figure *6.1.1*(d). The opposite effect is noted for the negative current sign, where the electrons flow from the free layer to the polarizing layer.

In negative dc currents, the higher frequency mode builds up a higher oscillation power, which increases as the current magnitude increases. Furthermore, in Figure *6.1.1*(a)-(d), for higher dc current magnitudes, the noise level increases noticeably regardless of the current sign. This can be a manifestation of the Joule heating.

The power spectral density for the all the measured currents is depicted in Figure *6.1.2* as a contour plot of the power as a function of the frequency and dc currents, also called spectrogram. The latter permits to have a global view on the FMR response to the dc current sign and magnitude.

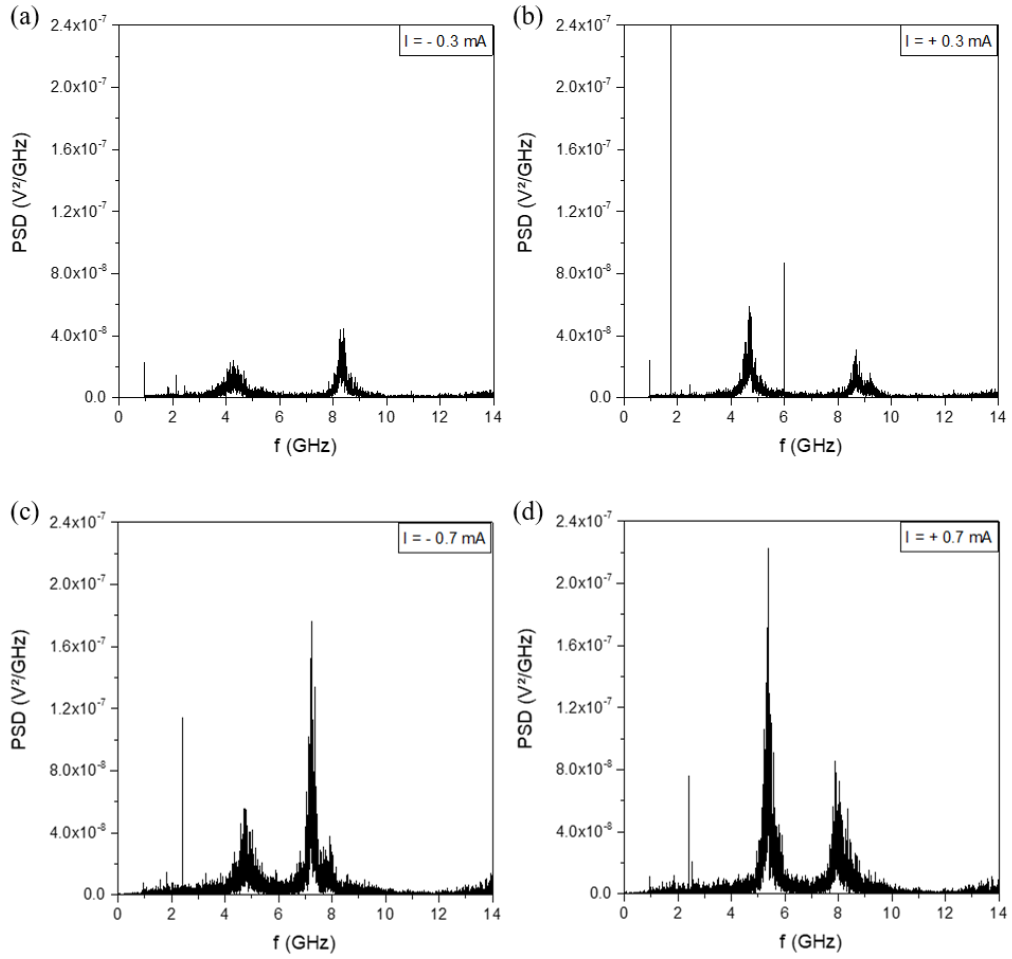

Figure 6.1.1: The power spectral densities of a pMTJ with a free layer thickness of 1.8 nm, a nominal diameter of 80 nm, under an in-plane magnetic bias field of magnitude $\mu_0 H_{\parallel} = 80\ mT$ and for different current values and signs : (a) I = -0.3 mA, (b) I = 0.3 mA, (c) I = -0.7 mA, (d) I = 0.7 mA

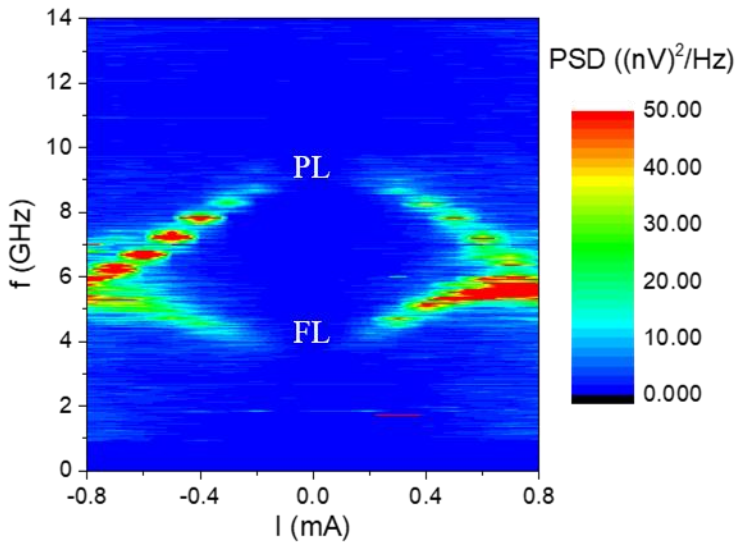

Figure 6.1.2: Contour plot of the power spectral density as a function the frequency and the input dc current. The figure is a summary for all PSDs taken at different currents, and otherwise under the same measurement conditions as in Figure 6.1.1.

Interestingly, in Figure *6.1.2*, the frequencies of the two FMR modes are both shifted by several GHz by the dc current, however, in an opposite manner. The polarizing layer mode frequency is reduced upon increasing the dc current (red shift), while the free layer mode frequency is increased (blue shift). Moreover, all FMR frequency shifts occur regardless of the dc current sign. This independence of the frequency shifts on the current sign in Figure *6.1.2*, and the noise in Figure *6.1.1* suggests strongly that this phenomenon is caused by Joule heating. The effect of a voltage controlled magnetic anisotropy (VCMA) or the spin transfer torque (damping-like) would both lead to an antisymmetric dependance on the current. For symmetric MTJs the field-like torque term of the STT could have a quadratic dependence on current [155], it is generally weaker than the damping-like torque and therefore unlikely to be the cause behind these relatively large frequency shifts.

It is noted that for MTJs with a perpendicular polarizer and an in-plane FL layer one can expect STT excitations that are symmetric with current sign as discussed in [97], however the asymmetry with the current sign of the observed peak power in Figure *6.1.2* suggests that this is not the case here. This might be due to the applied in-plane field leading to a more collinear configuration, and therefore the in-plane component of the PL can act as predicted from the current sign convention in Tableau 2.4.1 in section 2.4 of chapter 2.

These explanations are backed by the static characterizations of the switching diagrams done in section 4.4 of chapter 4. There it was found that the VCMA is weak for the pMTJs studied here, and that Joule heating in the FL is roughly ~24 K for $I = 0.4$ mA. Joule heating will reduce the saturation magnetization and the interface perpendicular anisotropy and thus affect the resonance frequency. To test this assumption, the resonance frequencies from the free and the polarizing layers were calculated using the macrospin model developed in the section 3.3 of chapter 3.

Theoretical analysis of the measured FMR current dependence

To analyze, first, the general effect of heating on the FMR frequency of a magnetic layer (FL or PL), in Figure *6.1.3*(a) the calculated FMR frequency is plotted for a constant in-plane field value, upon varying the out-of-plane field $H_\perp$ for different values of the iPMA expressed as a ratio of the anisotropy field H_u to the demagnetization field H_d. For the polarizing layer, the out-of-plane field $H_\perp$ represents the coupling to the SAF, while for the free layer it represents the dipolar field from the non-compensated SAF. The variation of the iPMA field H_u represents the effect of heating. The calculations in Figure *6.1.3*(a), predict that for a weak $H_\perp$, decreasing the iPMA leads to an increase in the FMR frequency (situation of the FL), while for a strong $H_\perp$, the reduction in the iPMA decreases the FMR frequency (situation of the PL). These tendencies are comparable to the FMR frequency behavior with the current amplitude in Figure *6.1.2*. Especially the FL layer experiences a weaker dipolar coupling field $H_\perp$ from the SAF (420 mT), as compared to the PL whose exchange coupling field is expected to be larger. Therefore assuming that the FMR frequency shifts in Figure *6.1.2* are caused by Joule heating explains the respective frequency shifts for the FL and PL modes with the dc current.

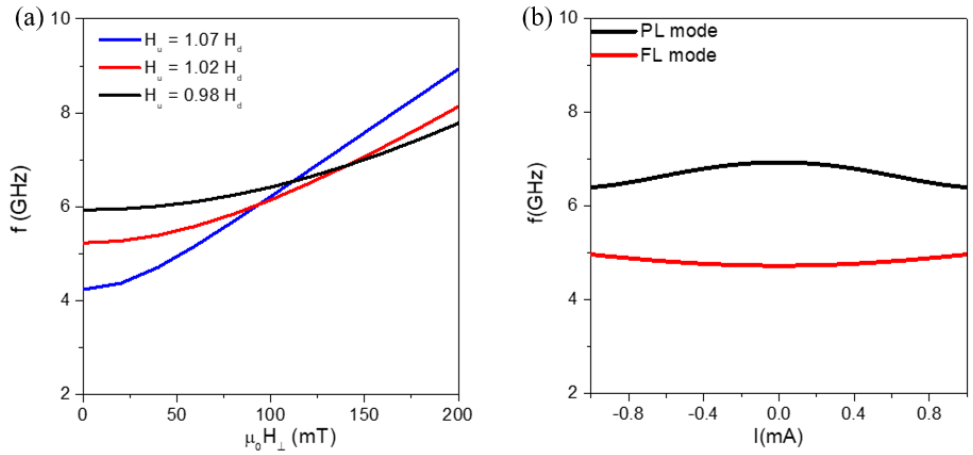

Figure 6.1.3: (a) Evaluation of the dependence of the FMR frequency on the value of iPMA field plotted as a function of the perpendicular interaction field $H_\perp$. The demagnetization field was taken as $H_d = 857.8\,mT$ corresponding to a pMTJ device of 80nm nominal diameter and 1.4nm thickness. (b) Simulations of the effect of Joule heating on the ferromagnetic resonance frequencies of the free and the polarizing layer. The current induced heating is defined as $\Delta T = 150(K/mA^2) * I^2(mA)$ for the FL, and $\Delta T = 300(K/mA^2) * I^2(mA)$ for the PL.

To substantiate further this analysis, using the fitted parameters from the section 4.4.1 in chapter 4, the Joule heating was included in the FMR frequency calculations through the respective temperature dependence of the anisotropy (Callen-Callen law) and of the saturation magnetization (Bloch law). The results are shown in Figure *6.1.3*(b).

They agree qualitatively with the experimental results in Figure *6.1.2*, especially for the frequency shifts with the dc current. The parameters used in the calculations are those from Table 4.2.4.1 in chapter 4.

Although the analysis done above hints to a noticeable presence of Joule heating and to its responsibility of the FMR frequency shifts, the spin transfer torque effect is still present. As mentioned above, it is observed in the non-symmetric behavior of the power spectral density (PSD) with the current sign in Figure *6.1.2*, the power of the FL mode is more intense in positive currents, and the power of the PL mode is more intense in negative currents.

Analysis of the measured FMR frequencies and linewidths

The action of the spin transfer torque is also measurable through the FMR linewidth. As predicted in Eq. 3.5.14 from chapter 3, the STT enhances the linewidth for one current sign and reduces it for the other. The linewidth and the power extracted from the experimental results in Figure *6.1.2*, are depicted in Figure *6.1.4*. Figure *6.1.4*(a) represents the FMR mode of the free layer magnetization, its linewidth appears to be reduced in both current signs, but with much stronger reduction in positive currents. The latter can be explained by the action of the spin transfer torque, where in positive current, the electrons flow from the polarizing layer to the free layer and reduce via STT the linewidth, whereas in the other current sign, the back reflected electrons, from the polarizing layer, reduce the free layer FMR linewidth as well, although the effect is smaller. These results, suggest that the spin-torque nano-diode output voltage, from the free layer FMR, should be enhanced in the positive current, and also slightly enhanced in the negative current.

For the polarizing layer FMR mode, shown in Figure *6.1.4*(b), its linewidth versus the dc current exhibit a linear behavior, and it agrees with the theoretical prediction in Eq. 3.5.14 from chapter 3. Here, the linewidth decreases in the negative current, where the electrons come from the free layer, and increases in positive current sign. Moreover, its linewidth does not seem to be fully-compensated, and therefore no clear signs of a transition to autonomous oscillations of the magnetization were observed. The magnetization of the polarizing layer seems to be in the stable damped precession regime for the different current ranges used here, higher currents were avoided for avoiding barrier breakdown.

The overall analysis done in this subsection allows to conclude that the dc current magnitude, likely because of the Joule heating, will shift the FMR frequency of the FL up and that of the PL down. In addition, the experimental evaluations of the linewidth dependence on the dc current, suggests that the output voltage of the active spin-torque nano-diodes will be enhanced by the negative current amplitude for the PL mode and by positive current for the FL mode.

These statements will be tested in the next subsection on the spin-torque nano-diode experiments for $t_{FL} = 1.8\,nm$.

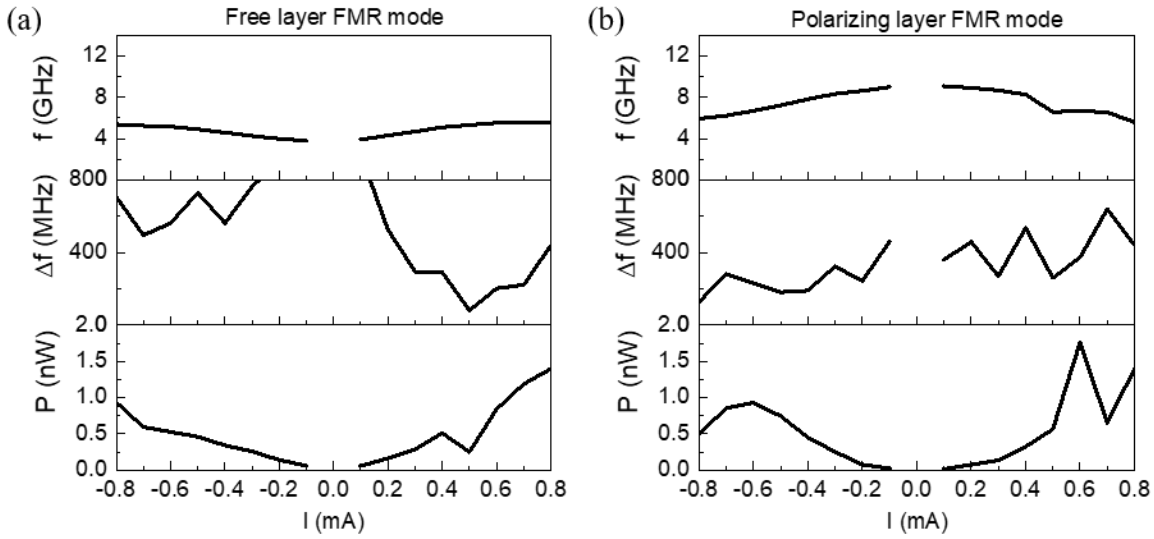

Figure 6.1.4 : The frequency f, linewidth Δf, and power P of the thermal FMR modes of Figure 6.1.2 as a function of the input dc current. (a) The FMR mode of the free layer magnetization. (b) the FMR mode of the polarizing layer magnetization.

6.1.2 Active spin-torque nano-diode experiments for t_{FL} = 1.8 nm

Active detection signal of the FL and PL modes

To explore the operation of the active spin-torque nano-diodes, the same experimental setup from section 2.4.2 in chapter 2 is used, however, with an additional dc current that is injected to the pMTJ simultaneously with the rf current.

The results of the active rf-to-dc conversion, for a device with a free layer of thickness 1.8 nm and a nominal diameter of 80 nm, are shown in Figure *6.1.5*(b)-(c). The injected dc current has a magnitude of |0.4| mA and the rf current has a power of -10 dBm. The measurements were done under an in-plane magnetic bias field of 50 mT.

In Figure *6.1.5*(a), the measurements are done without dc currents so that it can serve as a reference to compare with the active measurements. The first remark when comparing the passive rf-to-to-dc conversion in Figure *6.1.5*(a) and the active rf-to-dc conversion in Figure *6.1.5*(b)-(c) is that the signal noise is relatively high in the active measurements. The latter is partly attributed to the current source used here (Keithley 4200), that unfortunately produces relatively high electric noise with the dc current.

For the low frequency resonance mode arising from the free layer, it appears noisy in Figure *6.1.5*(b)-(c). Its independence on the current sign might be caused by the magnetic noise induced by the Joule heating in the free layer. Especially for the free layer thicknesses characterized here (1.8 nm) the perpendicular anisotropy almost compensates the demagnetizing fields.

Therefore the FL is highly sensitive to thermal fluctuations, which can be amplified by the presence of dc current through Joule heating. A good indication of the latter can be observed in the magnetoresistance curves for different current values shown in Figure *6.1.5*(d). For in-plane bias fields close to zero, the magnetoresistance shows an unexpected behavior with the dc current. As will be shown in chapter 7, these unexpected deviations are due to a superparamagnetic state (high magnetic noise).

For the higher frequency resonance mode, arising from the polarizing layer, the dc current magnitude and sign are clearly affecting the amplitude and the linewidth of the resonance response. For a negative current of magnitude -0.4 mA, where the electrons flow from the free to the polarizing layer, the signal is enhanced by a factor of ~ 1.7 compared to the passive case. Moreover, its linewidth is reduced by a value of ~200 MHz as compared to the passive case. For the positive current sign, Figure *6.1.5*(c) the polarizing layer mode is strongly reduced and hardly to be observed due to the increased noise.

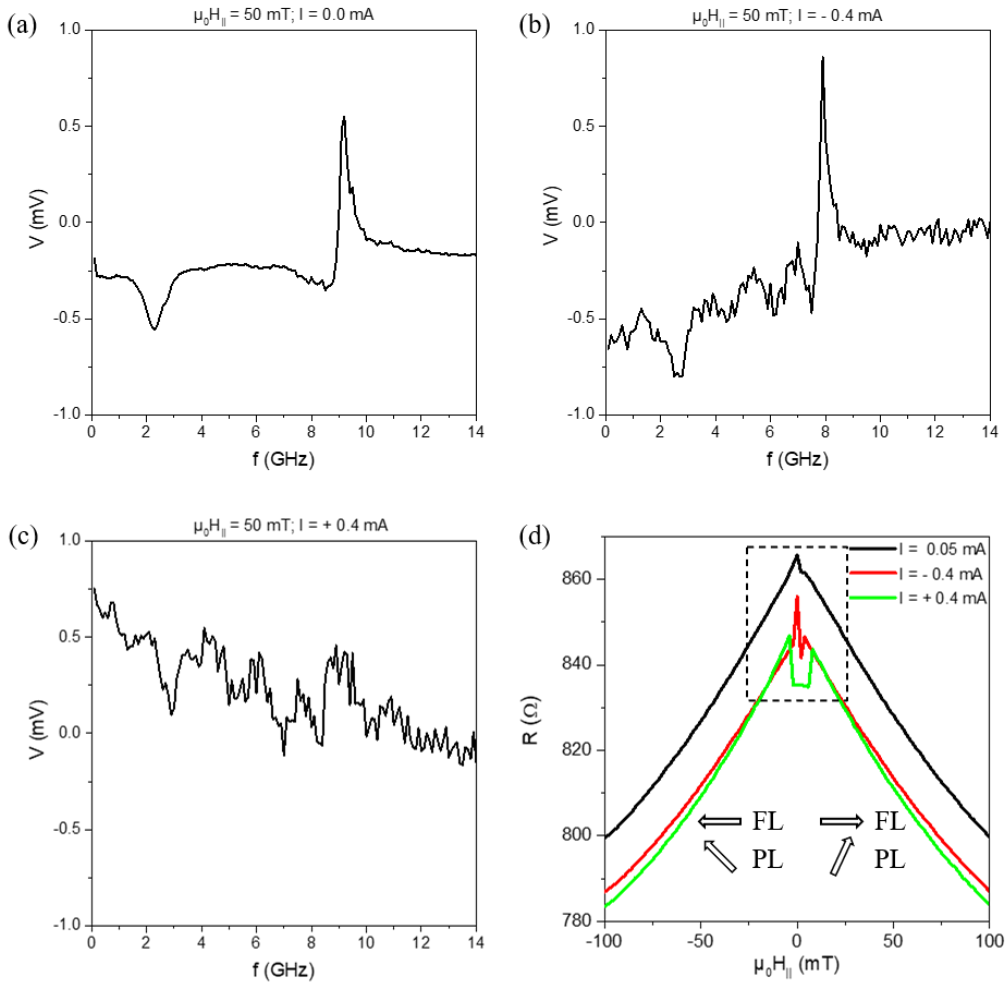

Figure 6.1.5 : Active rectification experiments showing the dc output voltage as a function of frequency for an rf current of power of -10 dBm, an in-plane magnetic field of magnitude 50 mT

and for (a) zero- dc current, (b) dc current of -0.4 mA and (c) dc current of +0.4mA. (d) The magnetoresistance as function of the in-plane magnetic field for the different dc currents 0.05 mA, 0.4 mA and -0.4 mA. The dashed box encloses the region where the resistance presents the distortions.

The overall active detection results from the polarizing layer mode are well understood in the light of the results presented for the thermal FMR modes in the previous subsection. Here, the spin transfer torque compensates the damping of the magnetization for the negative current sign, leading to smaller linewidth and thus higher output maximum voltages. For the opposite current sign, the spin transfer torque reinforces the magnetization damping, which leads to an increase in the linewidth as observed in Figure *6.1.4*(b), and therefore reduces the maximum amplitude.

For the FL layer mode, the measurements do not allow for a concrete conclusion on its behavior. Further investigations are required.

Active detection signal of the PL mode vs. diameter

Focusing on the polarizing layer mode for negative current, the general characteristics of the active detection in Figure *6.1.5*(a)-(b), were found also for all other nominal diameters : 40 nm, 80 nm, 100 nm, and 150 nm. The evolution of the maximum dc voltages obtained for devices of the different nominal diameters are shown in Figure *6.1.6* as a function of the dc current. Here, the rf current has a power of -5 dBm and the in-plane magnetic field has a magnitude of 80 mT. The rf power and the field magnitude were chosen such that they led to a good SNR for all nominal diameters.

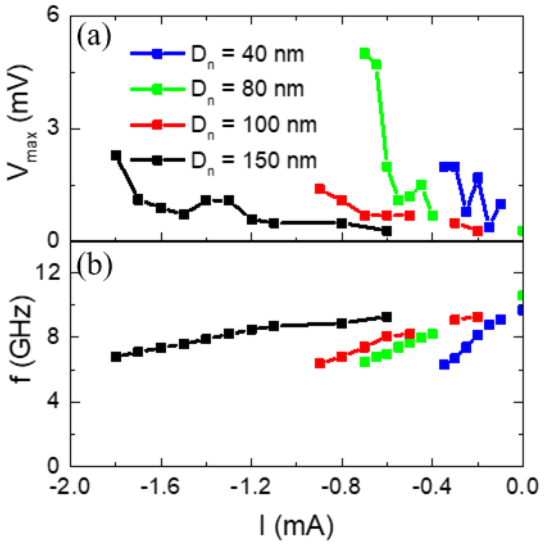

Figure 6.1.6 : (a) The maximum voltage V_{max} as a function of the input dc current for an rf current with a power of -5 dBm. (b) The frequency at which the largest maximum voltage is observed as a function of the input dc current.

As expected, in Figure *6.1.6*(a), the maximum detection voltage, for all nominal diameters, increases with the magnitude of the negative dc current. In addition, the dependence of the maximum voltage with diameter is the same as the one found for the passive detection in section 5.1.2 of chapter 5: V_{max} increases upon decreasing the diameter.

Moreover, the frequencies at which the maximum voltages occur, are monotonically shifted by the input dc current, see Figure *6.1.6* (b). The frequency red shifts in Figure *6.1.6* are consistent with the results from the thermal FMR modes in the previous subsection, where they were attributed to the Joule heating. In addition, the slope of the frequency shifts in Figure *6.1.6*, increases as the nominal diameter decreases, which is explained by both the higher current densities at smaller diameters, and the larger Joule heating due to the their higher resistances.

To conclude, it is demonstrated that the Joule heating via a DC current can be used to tune the detection frequency. In the next section these results will be extended to include the other free layer thicknesses (1.6 nm and 14 nm).

6.2 The active detection with an in-plane field for t_{FL} = 1.6 nm and t_{FL} = 1.4 nm

Active detection for t_{FL} = 1.6nm

Starting with the thermal FMR analysis, Figure *6.2.1*(a) depicts the spectrogram of a device with a free layer thickness of 1.6 nm and a nominal diameter of 100 nm, and under an in-plane bias field of magnitude $\mu_0 H_{||} = 80$ mT.

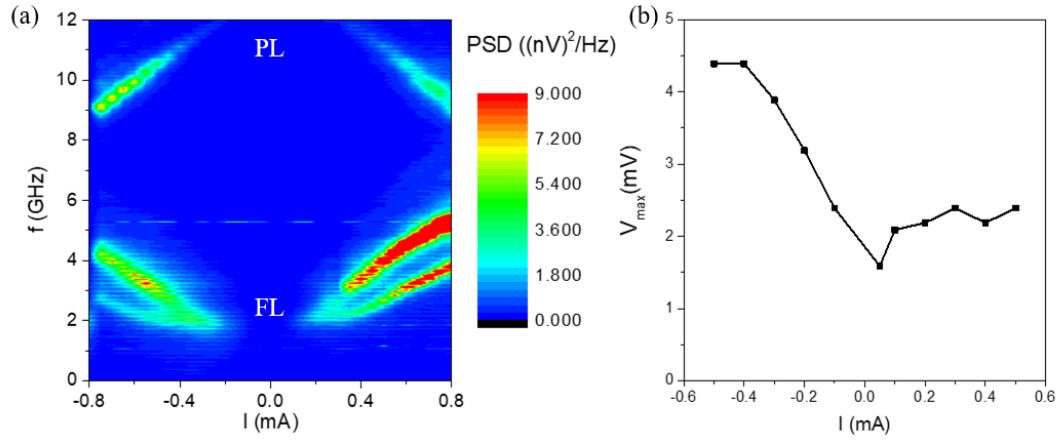

Figure 6.2.1 : (a) The contour plot of the power spectral density as a function the frequency and the input dc current for a device with a free layer thickness of 1.6 nm and a diameter of 100 nm, under an in-plane magnetic field bias of magnitude 80 mT. (b) The maximum rectification voltage from the PL mode plotted as a function of the input dc current, for a device with a FL thickness of 1.6 nm and a nominal diameter of 100 nm, and for an rf power of -5 dBm and in-plane field of 40 mT.

The spectrogram shows two FMR modes with an overall characteristics that is similar to the one from a device with a free layer thickness of 1.8 nm (Figure *6.1.2*). In both cases the polarizing layer mode frequency decreases with current, while the free layer mode frequency increases. In addition, the spin transfer torque in negative current enhances the power of the PL mode, while in the positive current it enhances the power of the FL mode. Therefore, the active rf-to-dc conversion for a FL thickness 1.6 nm is similar to that from 1.8 nm, and bears similar explanations, i.e. Joule heating is responsible for the frequency shifts, and the STT for the higher maximum rectification voltages. This is illustrated in the dependence of the maximum voltage corresponding to the PL layer mode plotted in Figure *6.2.1*(b) as a function of the dc current, under an in-plane field of 40 mT and an rf power of -10 dBm. The weak enhancements observed in the positive current might be due to the Joule heating reducing H_{ueff}.

Active detection for t_{FL} = 1.4nm

For a device with a free layer of thickness of 1.4 nm, under an in-plane magnetic field, the FL FMR mode behaves differently with the current as compared to the FL modes from the other thicknesses, see Figure 6.2.2. For t_{FL} = 1.4 nm, both the FL and the PL FMR frequencies decrease with current amplitude, independently of their sign. In addition, the FL FMR mode in Figure 6.2.2 is strongly excited by negative currents, which is opposite to the observations from the other FL thicknesses, see Figure *6.2.1*(a). This is caused by the difference on how the STT acts on FL magnetization. For t_{FL}=1.4nm the easy axis is oriented out-of-plane and quasi-co-linear with the PL. In addition due to the stray field from the uncompensated SAF, the FL magnetization is forced to be parallel to the PL. For such a configuration the positive current stabilizes the parallel state,

while for the negative current it destabilizes it through the back reflected electrons, see Table 2.4.1 in section 2.4.3 of chapter 2. Therefore, the FL excitations for t_{FL}=1.4 nm should occur in negative current as observed experimentally in Figure 6.2.2.

The decrease of the frequency for the FL mode with the dc current amplitude, instead of an increase is attributed to its out-of-plane easy axis. This assumption is tested in Figure *6.2.3* using the same Joule heating model exploited in Figure *6.1.3*(b), and the same parameters were only the FL thickness was varied (1.35 nm, 1.4 nm, and 1.45 nm). The model predicts that, for a layer with an out-of-plane easy axis, the dc current through the Joule heating keeps on reducing the FL FMR frequency until the easy axis switches in-plane. Then, the FMR frequency starts to increase with the current, similar to the observations from the other FL thicknesses 1.6 nm, and 1.8 nm.

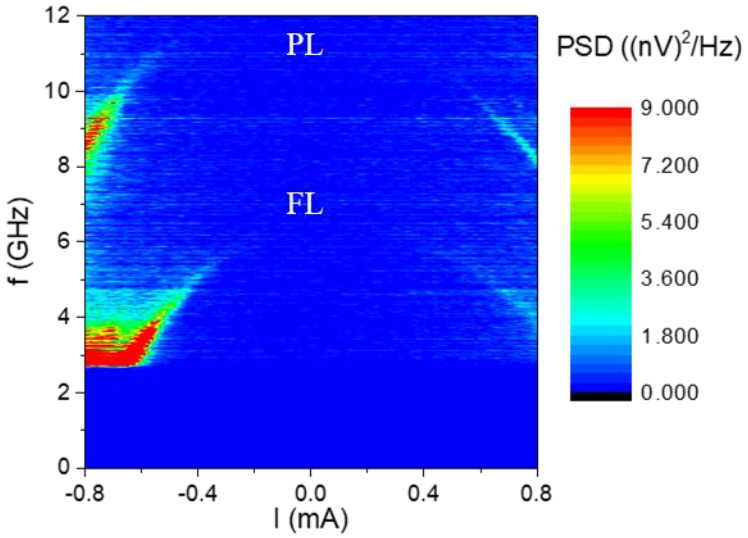

Figure 6.2.2 : The contour plot vs. current and frequency of a device with a free layer thickness of 1.4 nm and a nominal diameter of 100 nm, an under an in-plane magnetic field of magnitude 80 mT.

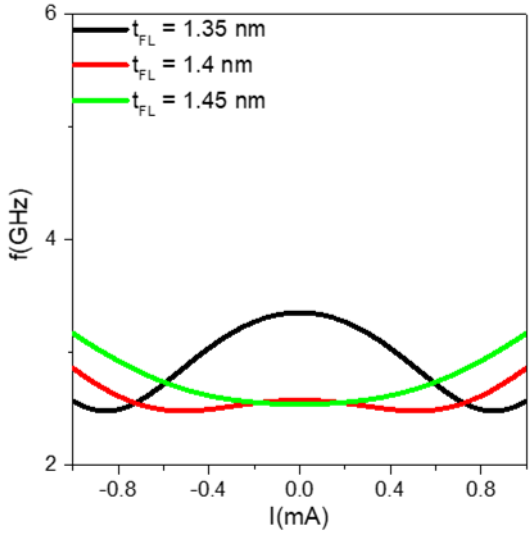

Figure *6.2.3* : Simulations of the effect of Joule heating on the ferromagnetic resonance frequencies vs. current for the free layer with thicknesses varying from 1.35 nm to 1.4 nm, i.e. for an out-of-plane easy axis. The effect of Joule heating is introduced as a temperature increase defined as $\Delta T = 150(K/mA^2) * I^2(mA)$ as is derived in section 4.4 in chapter 4.

To further investigate the behavior of the FMR modes corresponding to the FL thickness 1.4 nm, the spectrogram of a similar device (here D_n = 80 nm) is depicted in Figure *6.2.4*(a) for a constant dc current I = -0.58 mA, but for varying in-plane fields. The spectrogram helps to distinguish clearly the FL mode (low frequency) from that of the PL mode (high frequency).

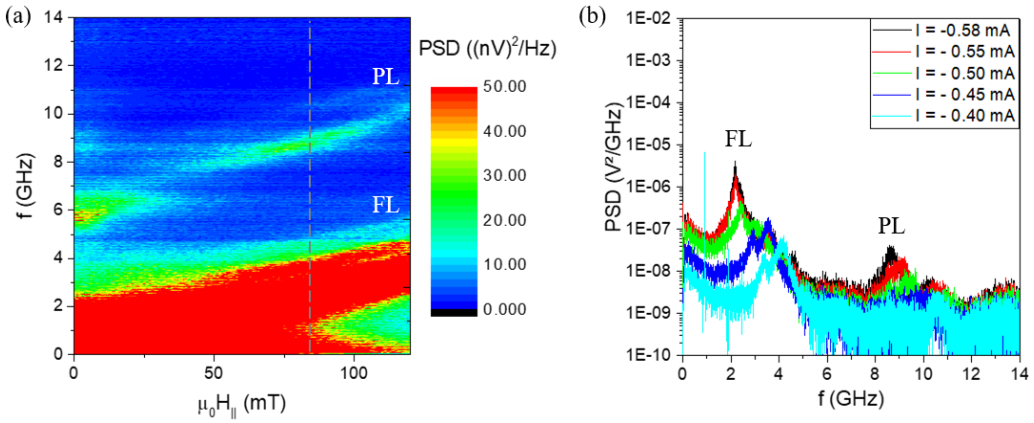

Figure 6.2.4 : FMR experiments for a pMTJ of a free layer thickness of 1.4 nm and a nominal diameter of 80 nm. (a) Contour plot of the power spectral density as a function the frequency and the in-plane field for an input dc current I = -0.58 mA. (b) Logarithmic plot of the power spectral

density under an in-plane magnetic field bias of magnitude $\mu_0 H_{\parallel} = 80\, mT$ and for different dc currents as indicated on the figure.

Despite the broadness of the FL mode, it produces FMR peaks with much stronger powers as compared to the PL mode. This is depicted in the logarithmic PSD plots in Figure *6.2.4*(b) for $\mu_0 H_{\parallel} = 80\, mT$ where the peaks at low frequency (~2.5 GHz) are much higher than those at high frequency (~ 9 GHz). The high power of the FL layer mode suggests that it may be undergoing a large angle steady state oscillation. Its power of oscillation is 10 times higher than that observed in the other thicknesses under similar conditions (see Figure *6.1.5*).

The active rf-to-dc conversion corresponding to the FL thickness of 1.4 nm, yields peaks that are similar to the those in Figure *6.2.4*(b). This is illustrated in Figure *6.2.5*(b) for the detection measurements of the same device evaluated in Figure *6.2.4*. It was measured under an rf current with a power of –10 dBm, a dc current of -0.45 mA, and an in-plane field $\mu_0 H_{\parallel} = 88\, mT$. Interestingly, unlike what was observed in the other FL thicknesses 1.6 nm and 1.8 nm where the FL layer rf-to-dc conversion voltage was weak ~ 0.3 mV, here in Figure *6.2.5*(b) it has a maximum voltage ~ 4 mV. This is 10 times higher. The dependence of V_{max} from the FL mode on the dc current is plotted in Figure *6.2.5*(b) for an in-plane field of 60 mT and an rf power of -10 dBm.

As for the PL layer mode that was dominant for the other thicknesses, for t_{FL}=1.4 nm, it produces the same maximum voltages ~ 1 mV but it is surpassed by the FL performance.

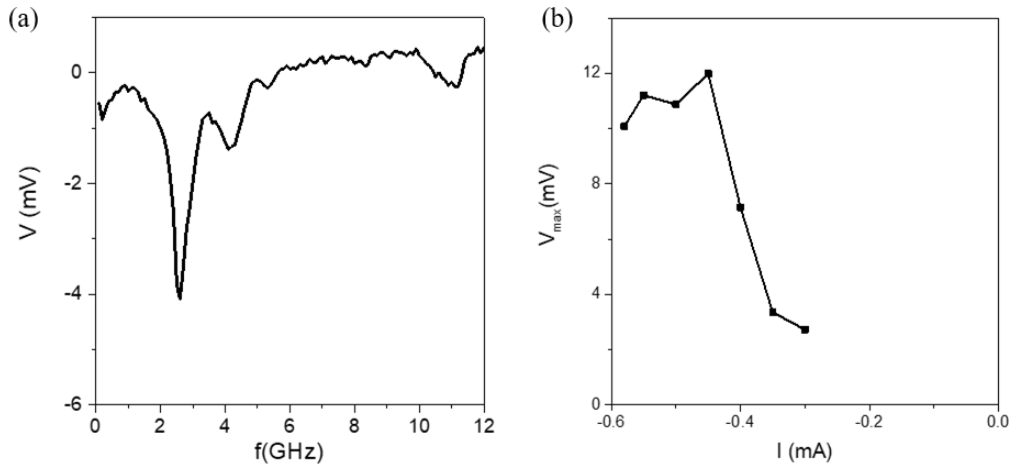

Figure 6.2.5: Experiments of the active rf-to-dc conversion for a pMTJ device with a FL thickness of 1.4 nm and a nominal diameter of 80 nm. (a) the detection voltage for a dc current I = - 0.45 mA as a function of the input rf signal frequency and with a power of -10 dBm. (b) The maximum rectification voltage from the mode in Figure 6.2.5(a) plotted as a function of the input dc current, for a device with a FL thickness of 1.4 nm and a nominal diameter of 80 nm, and for an rf power of -5 dBm and in-plane field of 60 mT.

6.3 Potential application of the wide range frequency tunability in the active detection

As presented above, the active detection under in-plane field for the pMTJs allows one to control via the dc current the detection frequency. It also allows for the increase of the detection signal as compared to the passive detection, but this increase will not be the same for all frequencies, since the enhancement scales with the dc current amplitude. The frequency tuning allows for interesting wireless applications. For instance, the frequency shift allows for the correction of frequency mismatches between an incoming and expected signal, for frequency hopping, as well as the ability to serve as a frequency multiplexer. The purpose of a frequency multiplexer is to allow only one frequency channel to be demodulated at a time. Using pMTJs, this channel can be selected by the dc current. A demonstration of such a multiplexer is shown in Figure *6.3.1*, for a device with a free layer of a thickness of 1.8 nm and nominal diameter of 40 nm, and under an in-plane magnetic field bias $\mu_0 H_{\parallel} = 80$ mT.

This is a first demonstration of its feasibility, but further detailed analysis of the spin-torque nano-diode multiplexer will be required to evaluate the linewidth and the rf current power dependencies for such an application. Moreover, the speed of the frequency tuning with current is an open question. If the speed is large enough it can as well be of interest for radar detection applications.

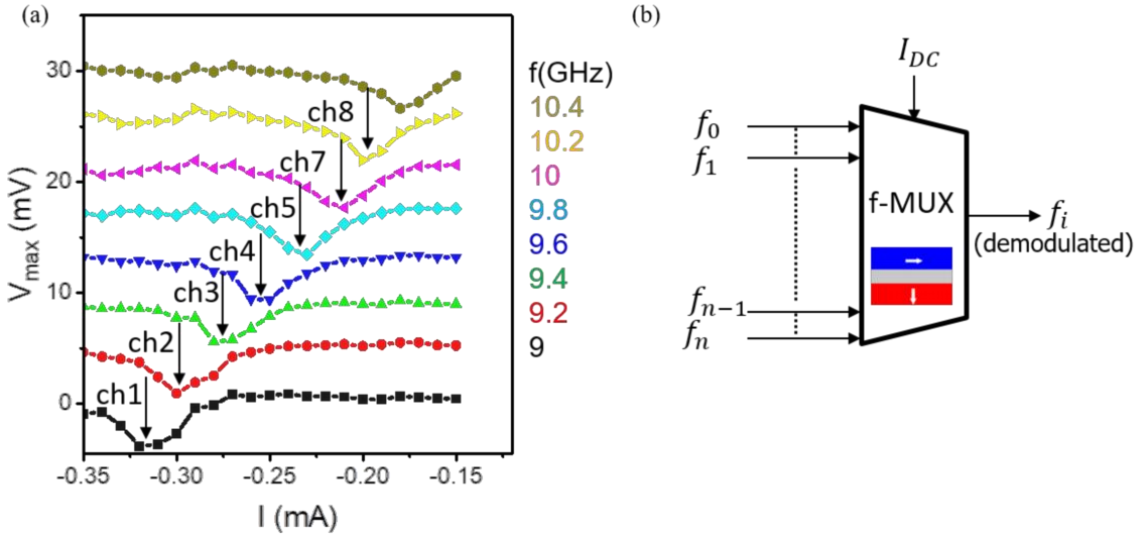

Figure 6.3.1 : Frequency multiplexer based on the active pMTJ spin-torque-nanodiode. (a) experimental results and (b) illustration of the multiplexer.

This concludes the discussion on the active detection under an in-plane magnetic bias field. In the next section the active detection will be considered for out-of-plane magnetic fields.

6.4 The active detection under an out-of-plane field for t_{FL} = 1.4 nm

For the characterization of the active rf signal detection under an out-of-plane magnetic field, in this work, a permanent magnet is used. Otherwise, the experimental setups are similar to those used in the previous sections. It is reminded as well that throughout this work (passive and active) the measurements under out-of-plane field were done for the antiparallel state of the FL and PL. For the parallel state no detection signals were observed in the out-of-plane field measurements.

Reflecting on the passive rf-to-dc conversion measurements under an out-of-plane field presented in section 5.2 of chapter 5, there was only one dominant FMR peak with an asymmetric shape. It was attributed to the polarizing layer, since at high out-of-plane fields, the FL is saturated out-of-plane, while the PL is tilted due to the SAF spin flop. Therefore the PL layer is softer and easier to excite than the FL that is stiffened by the field. Although, the possibility of the FMR mode to be from the FL or a coupling between the FL and PL is not yet completely ruled out.

In the following it will be shown that the active detection under out-of-plane fields supports the interpretation of the excitation of the PL.

Considering the FMR mode to be from the PL, it is more convenient to read the polarizing layer mode in a configuration where the free layer magnetization is fixed under out-of-plane field. This will render the evaluations of the results easier. Therefore, in this section the focus is on devices with free layer thicknesses of 1.4 nm, where the free layer magnetization is orientated out-of-plane. For the free layer thicknesses, 1.8 nm and 1.6 nm, they have a hard axis along the out-of-plane magnetic field direction, and their saturation requires fields larger than those available using a permanent magnet.

To start the characterization, first, the device is characterized in the presence of only the dc current, through the thermal FMR, to understand its effects on the polarizing layer magnetization dynamics. Thereafter, the experiments on the spin-torque nano-diode effect will be presented.

6.4.1 Spectral characterization of the pMTJ modes under dc current for t_{FL} = 1.4 nm

The spectrogram from the thermal FMR measurements of a device with a free layer thickness of 1.4 nm and a nominal diameter of 100 nm is shown in Figure *6.4.1*. The applied out-of-plane magnetic field has a magnitude of approximately $\mu_0 H_\perp = 230$ mT.

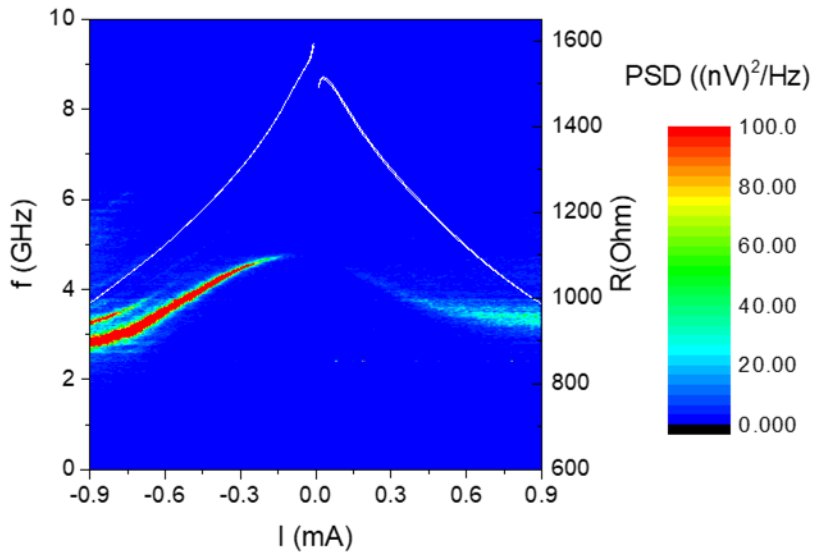

Figure 6.4.1 : The spectrogram of the power spectral density as a function of the frequency and the dc current, for a device with a free layer thickness of 1.4 nm and a nominal diameter of 100 nm, under an out-of-plane magnetic field bias of magnitude 230 mT. The magnetoresistance of the device as a function of the dc current is plotted on top of the PSDF plot (white lines, right scale) for comparison.

The spectrogram in Figure *6.4.1* contains as well the plot of the magnetoresistance as a function of the dc current (white line). The magnetoresistance shows a decrease with the current magnitude as expected from section 4.4.1.4 in chapter 4.

From the spectrogram in Figure *6.4.1*, only one FMR mode is observed that is strongly excited for negative current sign. Its frequency decreases with the dc current magnitude.

It is reminded here that the negative current correspond to the electrons flowing from the FL to the PL, and therefore the excitations, in Figure *6.4.1*, are more likely to be from the PL.

The excited modes in Figure *6.4.1* are visible starting from a relatively weak dc current of -0.3mA. This is similar to that observed for the in-plane field measurements (see Figure *6.2.2*). For the in-plane field measurements, it was independent of the current sign and the frequency shift was attributed to Joule heating. However, for the out-of-plane field measurements the observation of an excitation mode as well as the frequency shift is strongly dependent on the current sign.

This is illustrated in Figure *6.4.2*(a), where the mode frequency from a similar device is plotted as a function of the dc current. It can already be noticed that, despite the decrease of the mode frequency for both current signs, the slope is different. The latter is better depicted in Figure *6.4.2*(b), where the excitation frequencies for both current signs are plotted against each other. It is clearly seen that the mode frequency is more sensitive to the negative current, than it is to the positive one. Fitting linearly the slope of the frequency vs. current in Figure *6.4.2*(b) gives for the negative current a shift of $df/dI \sim -1.6\, GHz/mA$, and for the positive current a shift of $df/dI \sim -0.6\, GHz/mA$ (see Figure *6.4.2*(b) in green).

Moreover, the plots of the mode linewidth and power vs. current, in Figure *6.4.2*(c)-(d), show that the magnetization dynamics is different for the two current signs. In negative current, the linewidth keeps on deceasing with current until it saturates around I ~ -0.3 mA at a level of 50 MHz. This is a good indication that the oscillating magnetization is undergoing a transition to large angle auto-oscillations. It means that the spin transfer torque in the negative current was increasingly compensating for the damping until it reached the critical current, and the magnetization bifurcates from a stable spiral oscillation to a limit cycle. This conclusion is consistent with the measurements at positive current, where as expected the linewidth keeps on increasing with the current.

The observations from the linewidth are further supported by the plot of the power vs. current in Figure *6.4.2*(d). In negative current, and especially below -0.3 mA, the oscillation power grows with the current at a rate of $dP/dI \sim 3.5\ \mathrm{nW/mA}$, while for positive current, although it is growing, the growth rate it much smaller $dP/dI \sim 0.6\ \mathrm{nW/mA}$. These observations are illustrated in Figure *6.4.3* by the PSD spectra vs. frequency for different dc currents of similar magnitudes and different signs .

It should be noted here that the auto-oscillations of the PL and the absence of this regime for the FL oscillation might be related to the PL being coupled to the SAF. Similar oscillations have been observed for a pMTJ configuration where both the FL and the PL are coupled to a perpendicular biasing layer. In this case the FL was reported to have large angle auto-oscillation [156].

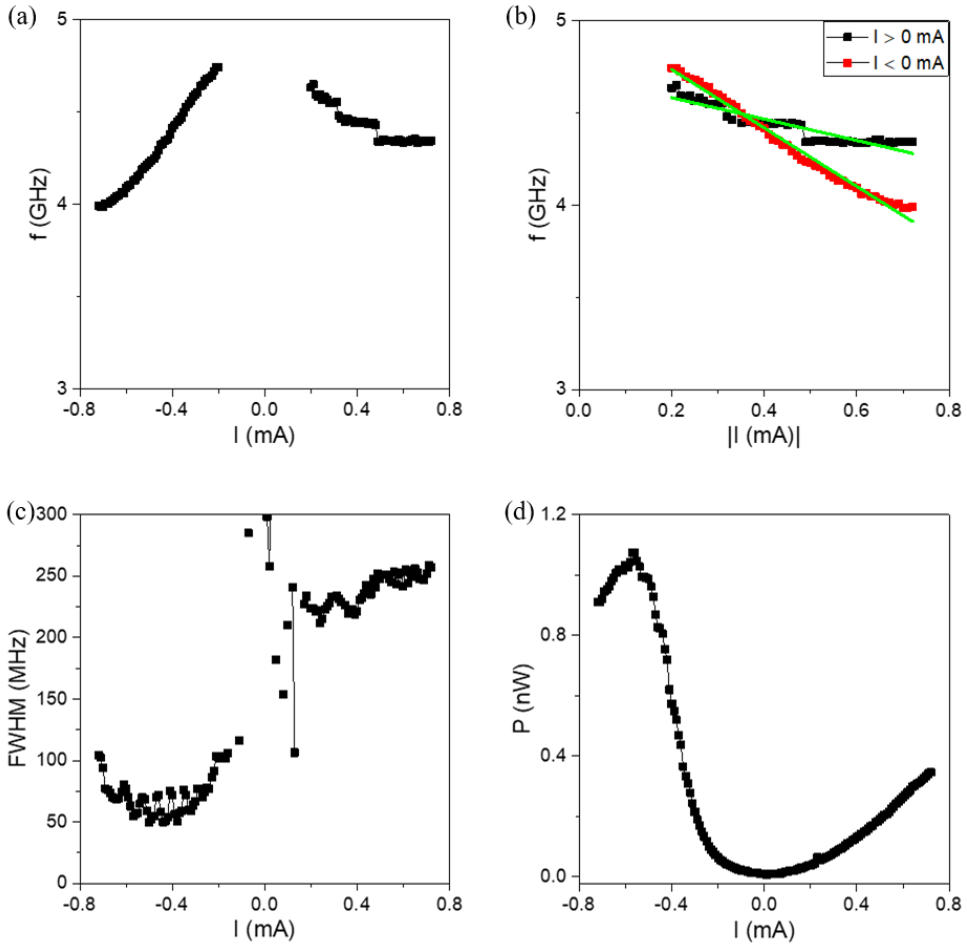

Figure 6.4.2: (a) The FMR frequency vs. current, extracted from a device with a FL thickness of 1.6 nm and a nominal diameter of 100 nm, and under an out-of-plane magnetic field of magnitude 230 mT. (b) The same as (a) but plotting the frequency for both current signs together as a function of the absolute value of the current. (c) The linewidths corresponding to results in (a) and d) the integrated peak power corresponding to results in (a).

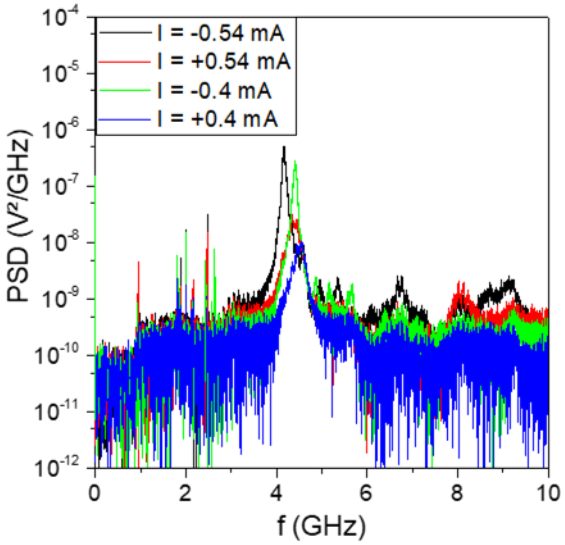

Figure 6.4.3 : Power spectral density in a logarithmic scale of the excitations for a pMTJ with a free layer thickness of 1.4 nm and a nominal diameter of 100 nm, under an out-of-plane magnetic field $\mu_0 H_\perp = 230\ mT$ and different dc currents as indicated on the figure.

For the frequency shift in Figure *6.4.2*(a), and its current sign dependence, it can be understood from the nonlinearity of the magnetization dynamics described by the LLG equation. A. Slavin and V. Tiberkevich [157]–[159] (see Annex C) mapped the LLG equation to a complex variable equation to describe the steady state oscillations of the magnetization. In their model the non-lienar frequency shifts of the steady state oscillation are approximated by :

$$f_p = f_0 + \frac{N}{2\pi} P \tag{6.4.1}$$

where f_0 is the linear (FMR) frequency, similar to the one in Eq. 5.1.1 in chapter 5 and N is the non-linear frequency shift coefficient while P is the oscillation power.

Combining Eq. 6.4.1, with the model on Joule heating developed in section 4.4 in chapter 4, the frequency shift by a dc current can be expressed as (using the chain rule) :

$$\frac{df_p}{dI} = \frac{df_0}{dT} * \frac{dT}{dI} + \frac{N}{2\pi}\frac{dP}{dI} \tag{6.4.2}$$

with $T = T_0 + \xi I^2$ (see section 4.4 of chapter 4). Eq. 6.4.2, predicts that the frequency shift by current has two additive components, the first term corresponding to the Joule heating, and the second one corresponding to the non-linearity of the magnetization dynamics. For the positive current sign, where the oscillation amplitude is weak $P \to 0$, the frequency in Eq. 6.4.1 is simply given by the FMR f_0, and its shifting is related to the Joule heating expressed by the first term in Eq. 6.4.2. The latter implies that the difference between the slope df/dI corresponding the positive and that corresponding to negative currents should give the STT-induced nonlinearity of the

frequency expressed in the second term of Eq. 6.4.2. This was done using the fits in Figure 6.4.2(b), and it yields :

$$\frac{df_{STT}}{dI} = \frac{N}{2\pi}\frac{dP}{dI} \approx 1.006\, GHZ/mA \tag{6.4.3}$$

Finally another feature of the PL STT excitation is discussed. It is observed in Fig. 6.4.2.d, where it can be seen that for negative dc currents above -0.6 mA, the oscillation power decreases strongly which is accompanied by an increase in the linewidth. This change is attributed to the approach to the critical current that switches the FL.

This switching is observed for another device (nominal diameter of 80nm) in the magnetoresistance vs. current shown in Figure *6.4.4* for a dc current of magnitude I = -0.8 mA. Here the FL switches from the antiparallel to the parallel state. This free layer switching is explained via STT from the back-reflected electrons. The PSD spectrogram corresponding to this device is shown together with the MR in Figure *6.4.4*, and its frequency, power, and linewidth in Figure *6.4.5*.

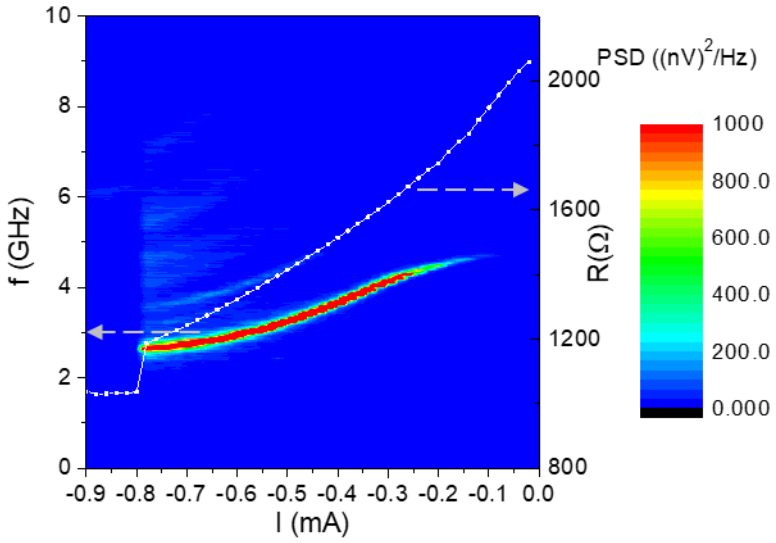

Figure 6.4.4 : The spectrogram of the PSD as a function of the frequency and the dc current, for a device with a free layer thickness of 1.4 nm and a nominal diameter of 80 nm, under an out-of-plane magnetic bias field of magnitude 230 mT. The spectrogram contains as well the magnetoresistance of the device as a function of the dc current (white line).

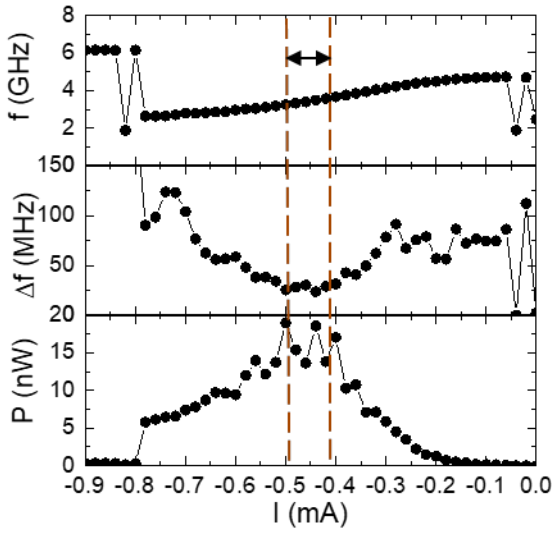

Figure 6.4.5 : The frequency f, linewidth Δf, and power P of the PL excitation shown in Figure 6.4.4, as a function of the input dc current.

The overall spectral measurements under an out-of-plane magnetic field done in this section suggest that the active spin-torque-nanodiode effect will be produced by the PL layer. In addition, its maximum voltage amplitude should be enhanced by negative dc currents, until it reaches a maximum at the "linewidth saturation" region above which it is expected to drop due to the FL switching.

6.4.2 The active detection under dc current and out-of-plane magnetic field

The measurements of the active spin torque diode effect are shown in Figure *6.4.6*(a)-(b). They are from the same device plotted in Figure *6.4.5*, with a FL thickness of 1.4 nm and a nominal diameter of 80 nm. The exciting rf current has a power of -12 dBm, and the out-of-plane magnetic field has a magnitude of ~ 230 mT.

As expected from the spectral measurements in Figure *6.4.5*, as the negative current magnitude approaches -0.4 mA, the rf-to-dc conversion maximum voltage increases noticeably. It reaches a maximum of around $V_{max} = 3$ mV. The input current -0.4 mA corresponds to the region for which the linewidth is smallest in Figure *6.4.5*. For larger current amplitudes the maximum voltage decreases, however, at a slower rate as compared to the subcritical currents. This is also illustrated in Figure *6.4.6*(b) in the spectrogram of the spin-torque nano-diode voltage as a function of the dc current and the FMR frequency. The results are in good agreement with the conclusions presented from the spectral mode measurements.

Another interesting remark from Figure *6.4.6*(a) is that the signal shape changes from being asymmetric Lorentzian at zero current to a symmetric Lorentzian as the negative current magnitude increases. This is due to the increase in the STT damping-like torque with the increasing negative the current, which favors the symmetric Lorentzian shape of the signal (see Eq. 3.5.9 in section 3.5.1 of chapter 3).

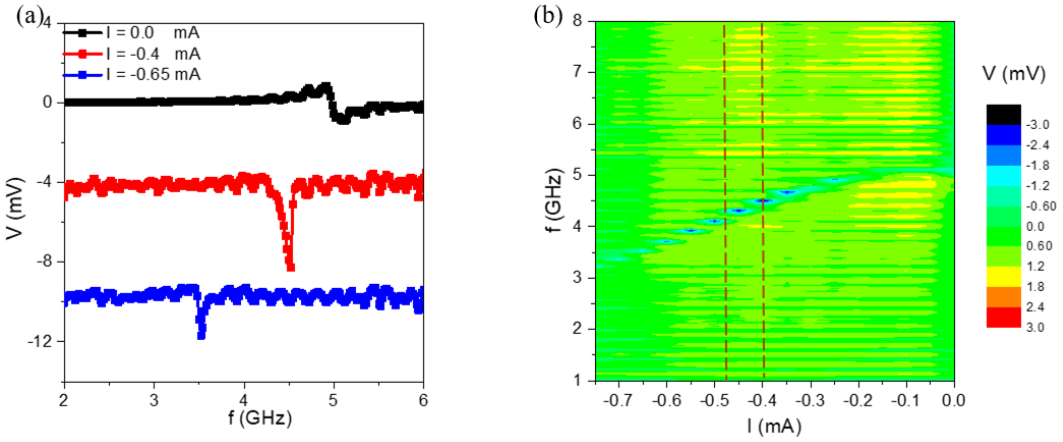

Figure 6.4.6 : The active spin-torque nano-diode measurements of the device in Figure 6.4.5. (a) The rectification voltage as a function of the input rf current frequency and the input dc current. The plots are offset to visualize the signal shapes. (b) The contour plot of the output voltage in (a) as a function of the frequency and the current.

A more detailed analysis of the autonomous oscillation region is still required to better understand the excitation and distinguish between a rectification of the steady state excitation and the possibility of injection locking via the rf signal. Such injection locking is expected to further enhance the maximum voltage [102].

Conclusion

In this chapter, the active spin-torque nano-diode effect was characterized and analyzed for in-plane and out-of-plane magnetic bias fields. It was found that the polarizing layer mode is the main contributor to the active detection. Its maximum amplitude was found to be relatively enhanced by the negative current in both in-plane and out-of-plane field orientations.

For the in-plane magnetic field measurements, the FL and PL FMR modes were found to be shifted by the dc current, independent of the current sign. This was attributed to the Joule heating in the devices, which reduces the PMA and M_s and therefore affects the frequency. In addition, the FL with a thickness of 1.4 nm, was found to be driven by the negative dc current, and the in-plane field into steady state auto-oscillations.

For the out-of-plane magnetic field, only one FMR mode was detected, and it was attributed to the PL oscillations. For dc currents above -0.3 mA, it undergoes a large angle steady state auto-oscillation, corresponding to the maximum enhancement of the active spin-torque nano-diode voltage signal by the dc current. The frequency shift with the dc current in the out-of-plane field measurements was found to be dominated by the STT in the negative current, while in the positive current only the Joule heating is acting.

Further simulation and experiments are still required to investigate the rectification of injection locked signals and its consequences on the active spin-torque nano-diode performance.

The active detection completes the characterization of the pMTJ-based spin-torque nano-diodes. The key points for the characterization were the maximum output dc signal, and the signal shapes. For the operation frequency, it is tunable through the field and was demonstrated here to be tunable via the dc current.

The measurements under the different conditions of currents and magnetic fields, and for the different FL thicknesses and pMTJ diameters suggest that the best detection signal corresponds to the PL mode from the pMTJs with nominal diameter of 40 nm, a FL thickness of 1.4 nm, in an antiparallel state, and under an out-of-plane field.

It produces the highest output dc voltages in the passive detection, and in the active detection its output is further improved by the negative current and reaches a maximum when it is driven into steady state oscillations. In addition to its higher dc outputs, its dependence on the out-of-plane field is easier to tune and can be implemented in real devices through the tuning of the SAF stray fields. Moreover, its asymmetric signal shape in the passive detection gives it an additional advantage for wireless applications such as FSK demodulation where it can double the output signal. Furthermore, its signal shape was demonstrated to be tunable by negative current and can be changed from being antisymmetric in the passive case to being symmetric in the active one.

These different advantages makes it the optimal case for a wake-up receiver based on a pMTJ when compared to other measured devices. Although, it has a disadvantage of working in the antiparallel state where the resistance is at its highest value leading to strong impedance mismatches. This can be overcome by implementing an impedance matching network.

For the FL mode based-detection, in general, it holds over this optimal mode the advantage of being explainable via the derived formulas and its behavior is predictable with good certainty. For the PL mode, however, the understanding of its dynamics it not yet fully completed and still requires additional measurements and simulations to conclude on.

Field-free perpendicular superparamagnetic tunnel junctions fully operated by dc current

So far in this manuscript, the main focus was the investigation of the magnetization dynamics in the presence of an rf current excitation and its use as a pMTJ-based spin-torque nano-diode. For this purpose pMTJs with different thicknesses and diameters were characterized statically in chapter 4 to determine the equilibrium states of the magnetization and to evaluate the dc current effects on the magnetization, such as the STT, the Joule heating, and the VCMA. Subsequently, in chapter 5 and chapter 6, the spin-torque nano-diode effect was studied for passive and active detection respectively. The results obtained demonstrated that the pMTJs, in addition to their memory and sensor functionalities, can function as rf detectors and generators.

In this chapter, it will be demonstrated that in addition to all these functionalities observed in one single pMTJ, it also can operate as a current controlled random number generator, and more interestingly at zero bias field. The phenomenon behind this additional function is the super-paramagnetism.

The field-free superparamagnetism in the pMTJs studied in this work was first observed during the static characterization in chapter 4. In Figure 4.6.1 in section 4.6 of chapter 4, it was shown that the in-plane magnetoresistance under dc current exhibits an unusual behavior near zero magnetic field. For a device with a FL thickness of 1.4 nm, in the same section, a strong resistance peak centered at zero field becomes visible above a certain current value, and the peak amplitude increases with current. This magnetoresistance distortion near zero field was observed for all free layer thicknesses : 1.4 nm, 1.6 nm, and 1.8 nm. But they were more pronounced for 1.4 nm.

In this chapter, using real-time measurements, it will be demonstrated that the origin of these resistance distortions is a random telegraph noise corresponding to the magnetization being in a superparamagnetic state [112], [160]. To the best of our knowledge, the results are the first demonstration of superparamagnetic pMTJs operating at zero bias field, and fully controlled by a dc current. The latter is of interest for non-conventional computing [9], [161]–[163] and artificial intelligence [164]. The main advantages of these superparamagnetic tunnel junctions, for these applications, lie in their nano-size, low energy consumption, and current-control of their switching probability. The additional advantage for the pMTJs studied here, is that they do not require any external magnetic field to function. Thus, they further reduce the energy consumption by saving the energy needed to generate the external magnetic field bias.

In the following sections, the investigations are carried out by first discussing the static magnetoresistance loops of the different free layer thicknesses and diameters, to provide a general view on the observed features. Thereafter, the time domain measurements will be presented to

characterize the stochastic switching of the resistance in time. Finally, the experimental results will be discussed within the Neel-Brown model introduced in section 3.6 of chapter 3.

7.1 The magnetoresistance distortions under dc current and in-plane magnetic field

The magnetoresistance loops of the perpendicular magnetic tunnel junctions have been discussed in detail in section 4.2 of chapter 4 for low dc current values. They were presented for all the free layer thicknesses (1.4 nm, 1.6 nm, and 1.8 nm) and for all available nominal diameters (40 nm, 80 nm, 100 nm, and 150 nm). Examples for in-plane fields were shown in Figure 4.2.2(b) of chapter 4, for a pMTJ with a nominal diameter of 100 nm and FL thicknesses of 1.6 nm and 1.8 nm (see Figure 4.2.1 for 1.4 nm). When repeating these in-plane field magnetoresistance measurements with dc currents of larger and larger amplitude, strong magnetoresistance distortions start to appear around zero field. These distortions are shown in more detail in Figure *7.1.1*(b)-(d) for the three free layer thicknesses : 1.4 nm, 1.6 nm, and 1.8 nm respectively for devices with a nominal diameter of 100 nm. Depending on the FL thickness, the distortion manifests itself differently in the hysteresis loop. In addition, the measurements were conducted for both current signs (positive and negative), at the same current amplitude. It be can be seen in Figure *7.1.1*(b)-(d) that the distortion is observed only for one current sign.

In pMTJs with a free layer thickness of 1.4 nm, Figure *7.1.1*(b), the positive current sign seems to have negligible effect on the magnetoresistance when compared to the low current measurements in Figure *7.1.1*(a). However, for the negative current sign, a prominent peak is observed in the magnetoresistance plot, with a maximum at zero field, and a resistance change of $\Delta R_{max} \approx 150$ **Ω** (54% TMR). Moreover, the magnetoresistance drops rapidly with the in-plane field until it reaches the parallel resistance state for field magnitudes larger than 50 mT. For the other free layer thicknesses (1.6 nm and 1.8 nm), in Figure *7.1.1*(c)-(d), similar current sign dependencies are observed, but the magnetoresistance modifications have a different shape and are much smaller in magnitude about $\Delta R_{max} \approx 20$ **Ω**. For a free layer thickness of 1.6 nm, the distortions occur for lower current values as compared to the other free layer thicknesses. Its distortion appears for negative dc currents of magnitude |0.3| mA, while for the other thicknesses it requires negative currents of magnitudes |0.7| mA. The latter is attributed to the high sensitivity to the thermal fluctuations for pMTJs of a free layer thickness of 1.6 nm. For these devices the iPMA cancels the demagnetization energy so that the effective magnetic anisotropy field goes to zero $|H_u - H_d| \rightarrow 0$. In consequence, the system is more sensitive to fluctuations.

Since the magnetoresistance modifications are largest for the devices with a free layer thickness of 1.4 nm, in the coming sections they will be the focus of the analysis. The obtained conclusions can be generalized to the free layer thicknesses of 1.6 nm and 1.8 nm.

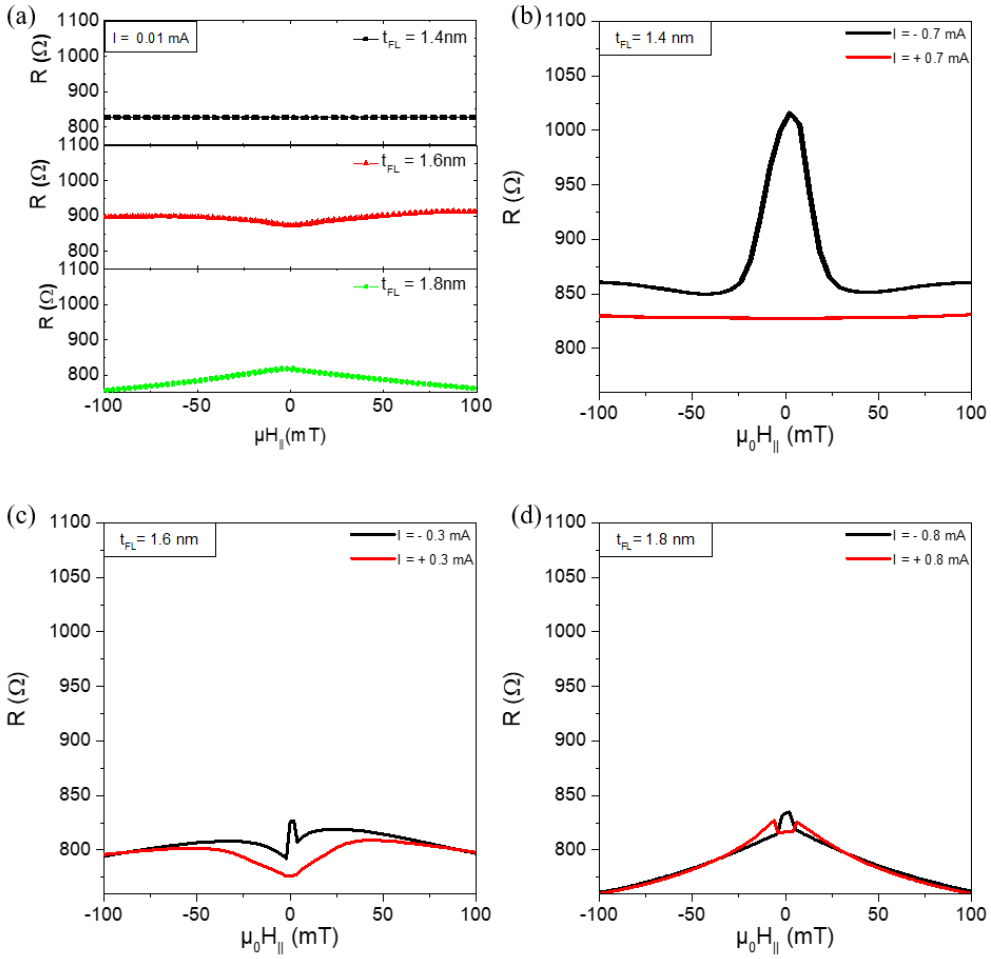

Figure 7.1.1 : Magnetoresistance measurements of a pMTJ with a nominal diameter of 100 nm, and under an in-plane magnetic bias field. (a) The magnetoresistances for all the three free layer thicknesses (1.4nm, 1.6 nm, and 1.8 nm), under weak dc current (10 μA). (b) The magnetoresistances of a device of a free layer thickness of 1.4 nm under dc current of magnitude |0.7| mA, where the positive current is in red and the negative current is in black. (c) The same as in (b) but for a free layer thickness of 1.6 nm and a dc current amplitude of |0.3| mA. (d) The same as (b), but for a free layer thickness of 1.8 nm.

7.1.1 Current dependence of the magnetoresistance peak for t_{FL} = 1.4 nm

Figure *7.1.2* shows the evolution of the magnetoresistance resistance peak for increasing dc current amplitude. It is seen that the maximum of the magnetoresistance peak at zero field increases with current amplitude. For the case in Figure *7.1.2* this increase is 175 Ω when the negative current amplitude increases from |0.5| mA to |0.7| mA.

Possible explanations for this magnetoresistance peak can be advanced, as already mentioned in previous chapters: Joule heating, the STT effect or a VCMA. In section 4.4.1.3 of chapter 4 and

section 6.1 of chapter 6, the VCMA was proved to be weak for the pMTJs used here, using different methods. The asymmetry in current sign therefore points to the spin transfer torque (STT), since Joule heating would occur for both current signs (but it cannot be excluded that joule heating contributes to the effect by reducing M_s and K_u). As a first test, it was checked whether the increase in magnetoresistance is related to the excitation of steady state oscillations and the signal output was measured with a spectrum analyzer. However no excitation peaks could be detected, which leads to the conclusion that other effects must be at the origin.

As a reminder from the previous chapters, it must be noted that at zero external magnetic field the magnetization of the free layer with a thickness of 1.4 nm is oriented out-of-plane, parallel to that of the polarizing layer magnetization.

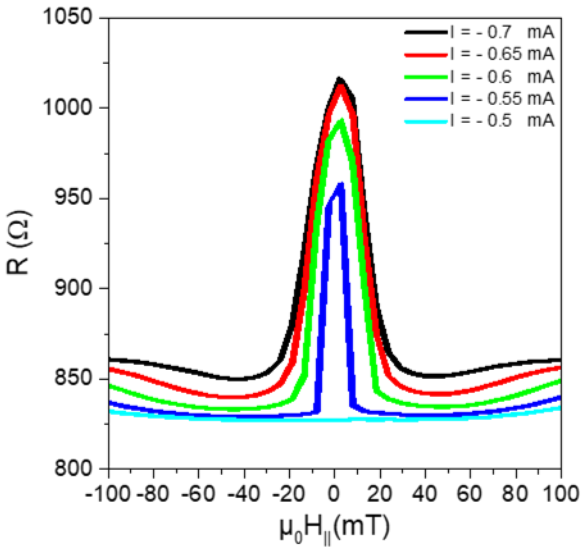

Figure 7.1.2 : The PPMS magnetoresistance as a function of the in-plane bias magnetic field for different negative current magnitudes, from a device with a nominal diameter of 100 nm and a free layer with a thickness of 1.4 nm.

Since the negative current refers to the flow of electrons from the free layer to the polarizing layer, the free layer magnetization state can be de-stabilized by the STT via the back-reflected electrons whose spin polarization is opposite to the FL magnetization (see Tableau 2.4.1 of section 2.4 of chapter 2 for the current convention). Since STT steady state excitations are excluded (see above), then the magnetoresistance distortions must be attributed to another effect that is enhanced or induced by the STT. Before discussing this in detail (section 7.2), we present the temperature and diameter dependence of the magnetoresistance distortions.

7.1.2 Temperature dependence of the magnetoresistance peak for t_{FL} = 1.4 nm

To further analyze the magnetoresistance peaks, besides the current dependence, we measured also their temperature dependence to see whether the peak at zero field is affected. The corresponding results are shown in Figure *7.1.3*. As can be seen, for the same negative dc current of magnitude |0.7| mA, the magnetoresistance peak at zero field is absent at a temperature of 200 K, while it is clearly visible at 300K. Actually, for lower temperatures, a higher current amplitude is required to induce the magnetoresistance peak at the same total ΔR change ($\sim$120 Ω). This is because upon cooling down, the interfacial perpendicular anisotropy (iPMA) becomes stronger making the magnetization more stable, and thus larger current amplitudes are needed to destabilize the magnetization. This was discussed in section 4.3 of chapter 4.

The ensemble of these observations, along with the current sign dependence, are reliable hints for the fact that the observed phenomenon is induced by the spin transfer torque, and that it might be enhanced by Joule heating (via M_s and H_u).

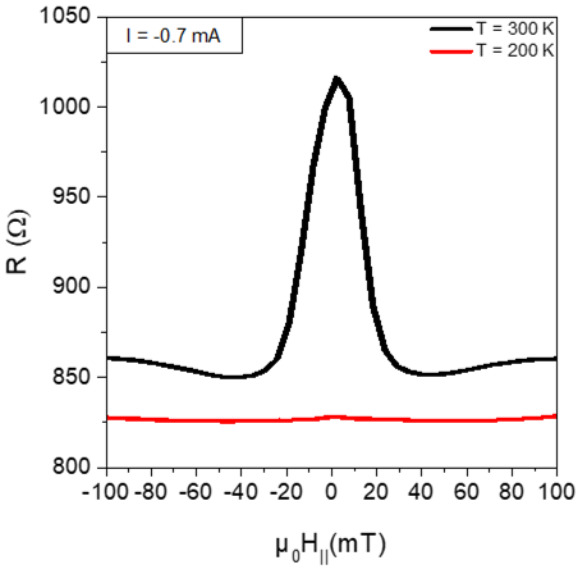

Figure 7.1.3 : The same as in Figure 7.1.2 but with a constant dc current magnitude of -0.7 mA and for two different temperatures 300 K and 200 K (black and red).

7.1.3 Diameter dependence of the magnetoresistance peak for t_{FL} = 1.4 nm

The magnetoresistance peak around zero field was observed for pMTJ devices of different nominal diameters (150 nm, 100 nm, 80 nm, and 40 nm). Figure *7.1.4*(a)-(b) summarizes the maximum resistance changes (ΔR_{max}) vs. the nominal diameter, where for each diameter the corresponding dc currents are different (see Figure *7.1.4*(b)). It can be seen from Figure *7.1.4*(a) that generally ΔR_{max} increases whenever the diameter decreases.

These diameter-resistance dependencies are all familiar from the previous chapters, where it was demonstrated that they are due to the combination of : the STT strength, the reduction of the effective magnetic anisotropy $H_{ueff} = (H_u - H_d)$, and the presence of a serial resistance in the pMTJ stack.

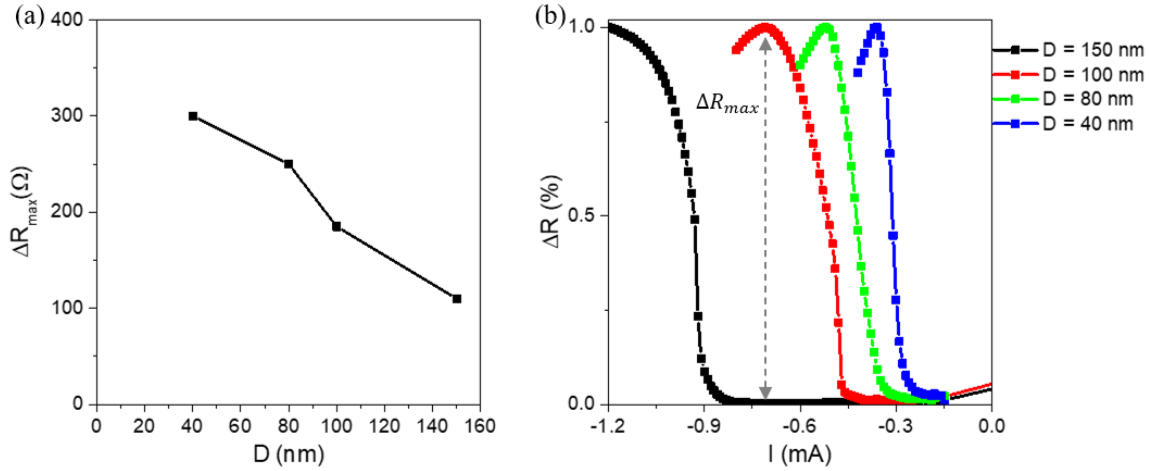

Figure 7.1.4 : Zero field $\mu_0 H_{||} = 0\ mT$ measurements summarizing (a) the maximum resistance change ΔR_{max} as a function of the MTJ nominal diameter; (b) the normalized magnetoresistance changes as a function of the input dc current for all nominal diameters : 150 nm, 100 nm, 80 nm, and 40 nm (black, red, green, blue respectively).

In Figure 4.2.4(b) of chapter 4, it was already shown that for a device with a FL thickness of 1.4 nm reducing the diameter increases the effective anisotropy leading to a more stable magnetic state. Therefore, as such, it is expected that for lower diameters more current is required to switch the magnetization, and hence ΔR_{max} is expected to be lower through the TMR-voltage dependence (see Figure 4.4.1.4 in chapter 4). However, this is clearly not the dominant effect in Figure *7.1.4*(b), since an opposite behavior is observed. The absence of an increase of the critical current due to the effective anisotropy can be explained by being counteracted by the higher STT amplitude occurring at smaller diameters. For instance, from Eq. 3.2.11 in section 3.2 of chapter 3, the critical current was demonstrated to be :

$$I_{c_{P\to Ap}}(A) \propto \frac{\frac{\pi}{4} * D^2}{\tilde{a}} * H_{ueff} \qquad (7.1.1)$$

with D is the pMTJ diameter, and $\tilde{a}$ the STT amplitude.

The opposite diameter dependencies of H_{ueff} and STT, suggest that their overall contribution to ΔR_{max} in Figure *7.1.4*(a) is weakened. The last expected contributor to the diameter-resistance changes $\Delta R_{max}(D)$ in Figure *7.1.4*(a) is the serial resistance from the TaN bottom electrode. The latter masks a portion of the TMR and its effect decreases as the resistance of the pMTJ increases with at diameters reduction. The latter was discussed in section 4.1.2 of chapter 4, where the resistance change affected by the serial resistance is expressed by :

$$\Delta R \propto (R_{ap} - R_p) * \frac{1}{1 + \frac{R_s}{\rho_p * t_{FL}} * \frac{\pi}{4} * D^2} \quad (7.1.2)$$

with ρ_p is the resistivity of the parallel resistance.

7.1.4 Diameter dependence of the critical current for t_{FL} = 1.4 nm

Apart from the larger ΔR_{max} for smaller diameters, the measurements show as well that smaller diameters require lower dc currents to drive the magnetoresistance peak. This is illustrated in Figure *7.1.4*(b), where the normalized magnetoresistance changes are plotted as a function of the dc current, and at zero bias magnetic field. For instance, to drive the resistance peak for a pMTJ with a nominal diameter of 150 nm a minimum dc current of magnitude |0.9| mA is required, while for a pMTJ with a nominal diameter of 40 nm only a dc current of magnitude |0.2| mA is needed. This is attributed, for reasons discussed next, to the higher current densities at smaller diameters, and thus higher spin transfer torque.

In the previous subsection 7.1.3, it was mentioned that the effective magnetic anisotropy H_{ueff} increases at lower diameters D, and that the critical current is proportional to both H_{ueff} and D^2 (see Eq. 7.1.1). Therefore, since the critical current in Figure *7.1.4*(b) is decreasing upon decreasing the diameter, this indicates that the increase of the strength of the STT ~D^2 dominates the increase due to the diameter dependence of H_{ueff}.

To verify this assumption, in Figure *7.1.5* the resistance changes are plotted as a function of the current density for all the diameters (i.e. Eq. 7.1.1 divided by $\frac{\pi}{4} * D^2$). This allows one to normalize to the same STT, leaving behind the possible dependence on H_{ueff}. Interestingly, the diameter dependence observed in Figure *7.1.4*(b) reverses completely in Figure *7.1.5* for the current densities. In the latter, it is the larger diameters that require less current densities. Hence, this confirms the prediction in Figure *4.2.5* in chapter 4 that smaller diameters increase H_{ueff}, and thus higher current densities are required to switch the magnetization.

The overall observations suggest strongly that the critical current dependence on diameter is dominated by the STT strength, although the effect of the effective anisotropy is present and measurable.

Finally, it should be noted that for all diameters, upon increasing the dc current the Joule heating is reducing the effective anisotropy and the TMR as well. The latter can be noted, since upon increasing the current density, the magnetoresistance reduction reaches its maximum and then reduces again. The reduction is attributed to the TMR-voltage dependence discussed in section 4.4.1.4 of chapter 4.

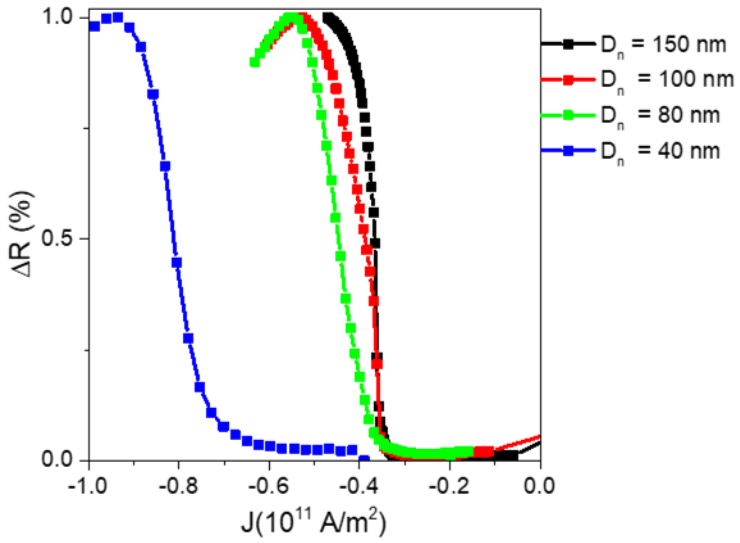

Figure 7.1.5 : The normalized magnetoresistance changes from Figure 7.1.4(b) plotted at zero field as a function of the input dc current density J (A/m^2) for all the measured nominal diameters : 150 nm, 100 nm, 80 nm, and 40 nm (black, red, green, blue respectively).

Before investigating the physical mechanisms behind these magnetoresistance peaks, in the next section the discussion will be extended to include the out-of-plane field characterizations. These measurements will help to link more accurately the magnetoresistance distortions to the parallel and anti-parallel states through the analysis of the hysteresis loops.

7.2 Characterization of the magnetoresistance distortions under a dc current and an out-of-plane magnetic field bias

The magnetoresistance measurements as a function of the out-of-plane field are shown in Figure *7.2.1*, for a device with a FL thickness of 1.4 nm and a nominal diameter of 100 nm. For negative dc currents below |0.5| mA, the hysteresis loops follow the behavior discussed in section 4.2 of chapter 4, where the combined effect of the STT and the Joule heating reduce the coercive field of the magnetization for currents of negative sign. Consequently, the stability of the magnetization is reduced, and at small or zero coercive field, thermal fluctuations can switch the magnetization randomly between the two states (parallel and antiparallel). This correspond to a superparamagnetic state.

The macrospin assumption used so far explains well the behavior of the hysteresis loops in the negative current in Figure *7.2.1*. However, once the coercive field is reduced to zero, which occurs for current values larger than |0.5| mA in Figure *7.2.1*, it does not explain the observed results. Besides the reduction of the coercive fields, it can be seen in Figure *7.2.1*, that for current values larger than |0.5| mA further modifications of the magnetoresistance loop manifest themselves. In

particular three distinct resistance levels appear, with the first one at high negative fields corresponding to the antiparallel state, the second one at high positive field corresponding to the parallel state, and the third level around zero field with an intermediate resistance. This third state occurs in the region were the resistance distortions were observed Figure *7.1.1* under the in-plane magnetic field.

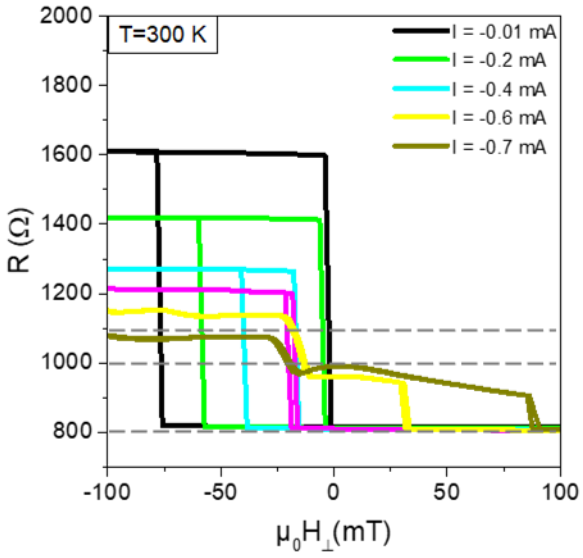

Figure 7.2.1 : The magnetoresistance of a pMTJ with a FL layer thickness of 1.4 nm and a nominal diameter of 100 nm, plotted as a function of an out-of-plane magnetic field, and for different dc currents.

The presence of this intermediate resistance state suggests that the FL magnetization, for negative currents higher than |0.5| mA, is not switching uniformly as predicted by the macrospin model but more likely through the nucleation of a reversed magnetic domain. Once nucleated, it propagates with increasing current amplitude until it has completely reversed the anti-parallel state. The switching through the nucleation and the propagation of magnetic domain is illustrated in Figure *7.2.2*.

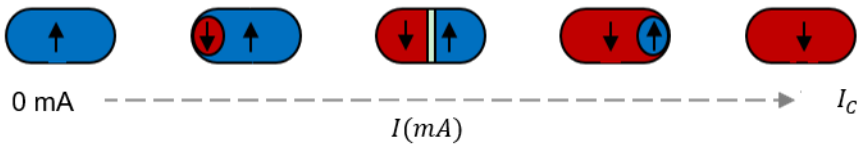

Figure 7.2.2 : The process of the magnetization switching through the nucleation and the propagation of a magnetic domain wall, as a function of the dc current; with I_c the critical switching current.

Such a process was predicted in the literature [165] using Mumax3 micromagnetic simulations to occur whenever the pMTJ diameter is larger than 20 nm.

Therefore, it is plausible to have such a domain nucleation process in the pMTJs used in this work whose real diameters are $D = D_n + 30$ = 70 nm, 110 nm, 130 nm, and 180 nm.

7.2.1 The temperature dependence of the magnetoresistance loop under an out-of-plane field

To further investigate the intermediate magnetization state observed in *Figure 7.2.1*, it was characterized at different temperatures to see how it is affected. The magnetoresistance measurements are shown in *Figure 7.2.3* for the same device measured in *Figure 7.2.1*, and for a dc current of -0.6 mA. The measurements show that the magnetoresistance loops respond to the temperature in a similar manner as it response to the current.

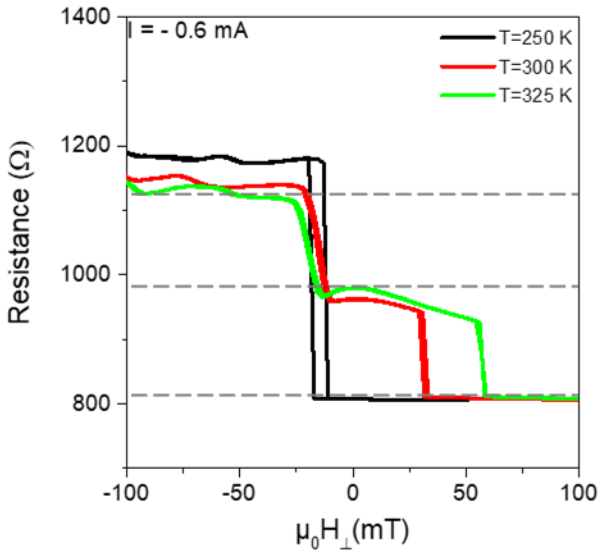

Figure 7.2.3 : The magnetoresistance of a pMTJ with a FL layer thickness of 1.4 nm and a nominal diameter of 100 nm, plotted as a function of an out-of-plane magnetic field at I = -0.6 mA, and for different temperatures. The measurements were done using the PPMS.

For instance, at higher temperatures (325 K) the intermediate state becomes more stable and higher fields are required to switch to the other states (AP / P), while at a lower temperatures (250 K) it disappears and only a square hysteresis loop remains without intermediate resistance level. The latter is similar to the response to the current in the sense that adding or subtracting 0.1 mA from I = -0.6 mA leads to the increase of the stability of the intermediate state or its disappearance respectively.

For the temperature measurements, and assuming the presence of the nucleated domain, this behavior can be explained by the increase of the perpendicular magnetic anisotropy at lower temperatures leading to smaller domain wall widths and finally resulting in a single domain [25].

These measurements and their similarity with the current dependence, suggest that the domain is nucleated and propagated through the combination of both the STT and the Joule heating.

7.2.2 The current dependence of the magnetoresistance distortions

The assumed magnetic domain nucleation can explain the increase of the intermediate resistance levels towards the antiparallel resistance with the current amplitude, see Figure *7.2.1* for I = -0.6 mA and I = -0.7 mA. To investigate this point in this subsection the magnetoresistance was characterized as a function of the current for a device with a nominal diameter of 150 nm at zero field and the obtained results are plotted against the antiparallel resistance for comparison, see Figure *7.2.4* black and red plots respectively.

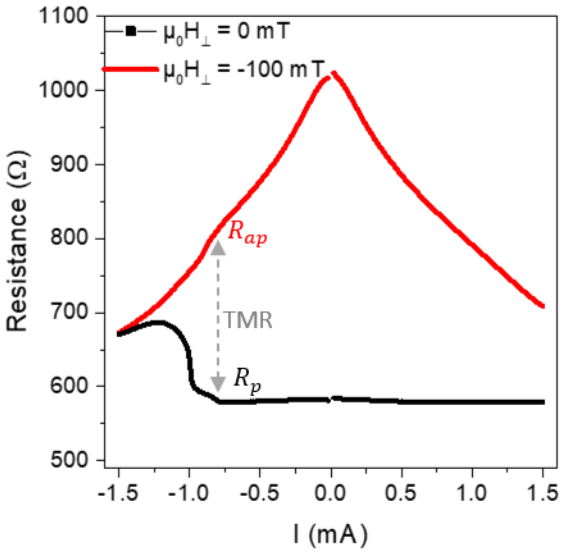

Figure 7.2.4 : The magnetoresistance of a device with a nominal diameter of 150 nm plotted as a function of the dc current (a) for the parallel state at zero external magnetic field bias (black line) and (b) for the anti-parallel state at $\mu_0 H_\perp = -100\ mT$ (red line), enough to saturate the free layer magnetization.

Figure 7.2.4 shows that at zero field and at a current value of -0.9 mA the intermediate resistance appears and its value grows with the current until -1.2 mA where it reaches a maximum resistance

that is below the antiparallel resistance. The latter might be the case because a domain wall is present in the junction for these currents. Furthermore, as the current increases, the intermediate resistance keeps on evolving until it reaches at -1.4 mA the antiparallel resistance value, which can correspond to the propagation of the nucleated domain wall.

Hence, these different observations from the magnetoresistance measurements conducted in the out-of-plane field suggest that the STT and the Joule heating nucleate a reversed domain in the FL. Moreover, it demonstrates that near zero field the device is in an intermediate resistance state different from the antiparallel or the parallel states. The negative current at zero field switches the magnetization from the parallel to this intermediate state. As will be discussed in the next section this switching is superparamagnetic.

It should be noted here that these measurements correspond to devices with nominal diameters of 100 nm and 150 nm, and these conclusions apply mostly to them. For the smaller diameters similar measurements are still required to generalize on them (this was challenging to do with the PPMS).

In the following the intermediate state of the magnetoresistance will be referred to as R'_{AP} (effective anti-parallel state).

7.3 Real-time characterization of the magnetoresistance distortions in the absence of an external magnetic field

The static measurements presented so far gave a good hint that in near zero field the FL is undergoing an unexpected behavior. At the beginning of the advanced analysis, this behavior was first characterized using a spectrum analyzer to see if it is related to magnetization oscillations. The results from a device with a FL thickness of 1.4 nm and a nominal diameter of 80 nm are plotted in Figure *7.3.1*(a)-(b).

In Figure 7.3.1(a) no resonance or excitation peaks were observed, instead the power spectral density starts with a high power at low frequencies, and decreases monotonically and rapidly at higher frequencies, by f = 2 GHz it is already negligible. This inverse dependence of the power spectral density on the frequency is usually a strong hint of random noise, which can be gaussian or non-gaussian such as the random telegraph noise, all of them have a dependence $\propto f^{-\alpha}$ [166].

The power spectral densities (PSD) from all measured currents are presented in the contour plot in Figure 7.3.1(b). For negative currents higher than |0.4| mA, where the resistance distortions appears, the PSD increases with the current amplitude at low frequencies and drops rapidly at higher frequencies similar to the one discussed in Fig. 7.3.1 for – 0.5 mA.

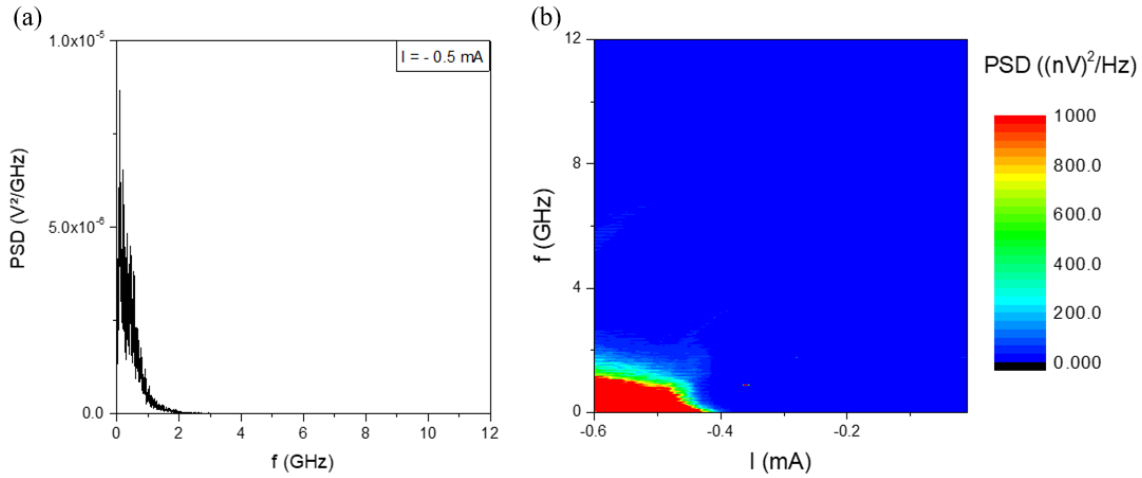

Figure 7.3.1: (a) The power spectral density of a pMTJ device with a free layer thickness of 1.4 nm and a nominal diameter of 80 nm, at zero bias field, and for a dc current of magnitude I = -0.5 mA. (b) The contour plot of the power spectral density at zero field. It is plotted as a function the frequency and different negative dc currents.

The frequency measurement in this section indicate that a random noise is involved in the magnetoresistance distortions. To investigate this suggestion, in the following the magnetoresistance will be analyzed in real-time using an oscilloscope and the setup from section 2.5 of chapter 2.

7.3.1 Time traces of the magnetoresistance at zero field

For the real-time characterizations of the magnetoresistance, a pMTJ with a free layer thickness of 1.4 nm and a nominal diameter of 150 nm was selected. This choice stems from the time constant analysis, where it was found that at zero magnetic bias field, and with the present setup, only devices with this diameter show stochastic switching on time scales slow enough to be measured. The magnetoresistances of the smaller diameters were found to change much faster than the time constant of the setup (~100 ns) and thus they require a more sophisticated setup with higher frequency bandwidth.

Moreover, in the real time analysis for convenience the measurements are conducted as a function of voltage instead of current.

Typical results of the real-time measurements of the magnetoresistance are shown in Figure *7.3.2* for an applied voltage of -0.575 V. As can be seen, the resistance switches stochastically between two well defined resistance levels : the parallel state R_p and the intermediate state R'_{AP}. This type of stochastic fluctuations between two levels are well known for a wide range of physical phenomena [166], it is called random telegraph noise [167]. For the pMTJs this large random telegraph noise in the resistance is a confirmation of the existence of a superparamagnetic state.

Another confirmation of the superparamagnetic state in these pMTJ comes from the voltage dependence of the random telegraph noise via the STT effect. This is explored next.

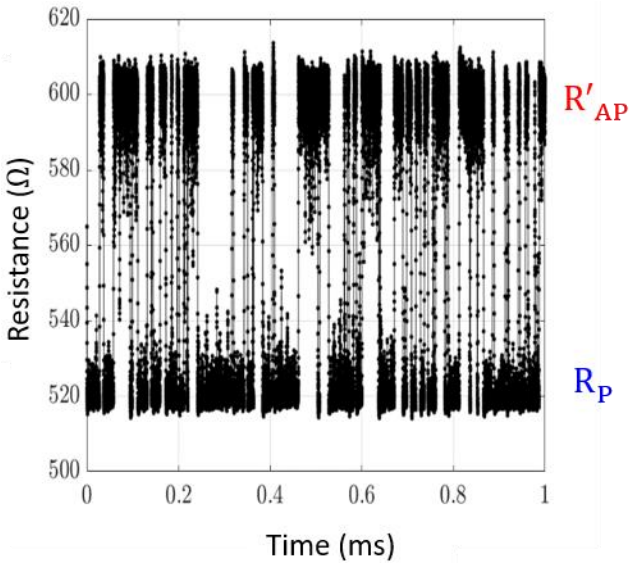

Figure 7.3.2 : Real-time measurements of the magnetoresistance under dc voltage of magnitude |0.575| V, and in zero external magnetic field. Here the maximum resistance is referred to as R'_{AP} corresponding the intermediate resistance level.

7.3.2 Voltage dependence of the stochastic magnetization fluctuations at zero field

In this subsection, the results of Figure *7.3.2* were extended to different applied dc voltages to analyze their effect on the measured time traces. Typical time traces are shown in Figure *7.3.3*(a)-(c). It can be seen that the time that the magnetization spends in one state before it randomly switches is strongly dependent on the applied voltage. This waiting time is called the dwell-time. For instance, at lower voltages such as $V_{app} = -0.572$ V (Figure *7.3.3*(a)) the magnetization spends on average more time in the low resistance state (parallel) than in the high (i.e. intermediate) resistance state, while for higher voltages such as $V_{app} = -0.577$ V (Figure *7.3.3*(c)) the inverse is observed. In between these two voltages, such as depicted in Figure *7.3.3*(b), the magnetization in average spends equal times in the two resistance states, while switching randomly. This is confirmed through the corresponding histogram of Figure *7.3.3*b, shown in Figure *7.3.3*(d).

In this histogram the high resistance state (R'_{ap}) appears to be broader than the low resistance state (R_p). This is possibly due to the intermediate magnetoresistance state being created by the nucleation and propagation of a domain wall, as discussed in section 7.2. The propagation of the domain can add additional fluctuations that would not be present in the R_p state and the uniform switching.

In the next subsection, the time traces from all the measured voltages will characterized through their dwell-times using the method described in section 2.5 of chapter 2.

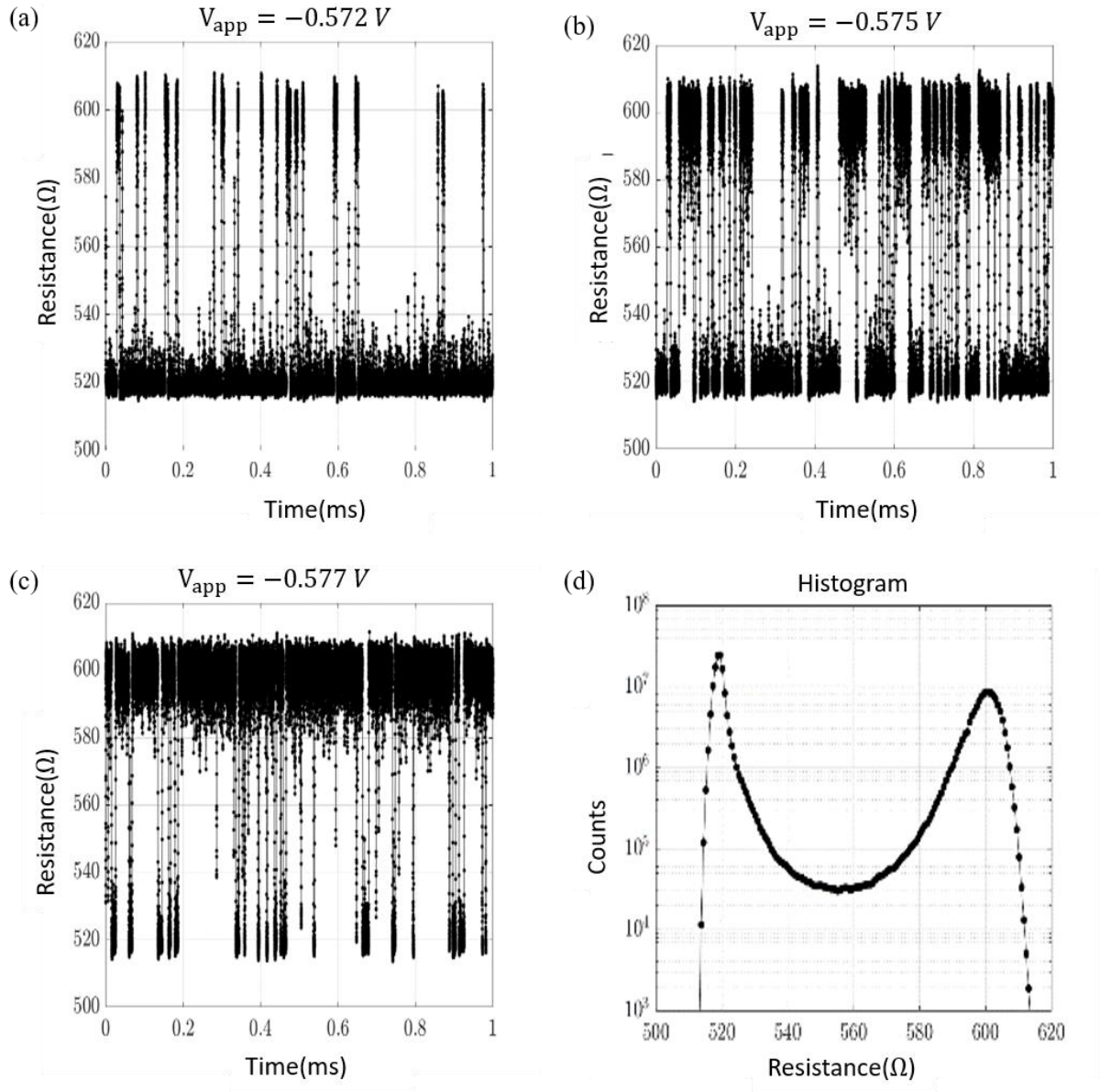

Figure 7.3.3 : Time-domain measurements of the magneto-resistance in zero applied field for the same device as in Figure 7.3.2 and for an applied voltage of (a) V_{app} = -0.572 V, (b) V_{app} = -0.575 V and (c) V_{app} = -0.57 V. (d) The histogram of the magnetoresistance plot in (b).

7.3.3 Experimental analysis of the dwell times as a function of the dc voltage

The presence of a well-defined two level magnetic state in Figure *7.3.3*(d) allows the analysis of the time traces by the transition state theory (TST) [108], also called Kramer's theory. For this the dwell times were extracted from the time traces using a matlab code, see Figure 2.5.2 of chapter 2.

The voltage dependence of the magnetization dwell-time is depicted in Figure *7.3.4*(a). The plot is equivalent to the probability of the magnetization being in the high resistance state, and is defined as :

$$P(AP') = \frac{< \tau'_{ap} >}{< \tau'_{ap} > + < \tau_p >} \tag{7.3.1}$$

where $< \tau'_{ap} >$ is the average dwell-time of the intermediate state, $< \tau_P >$ the average dwell-time of the low (parallel) resistance state, and $P(AP')$ is the probability of the magnetization to be in the intermediate state.

The probability as a function of the applied voltage in Figure *7.3.4*(a) has a form of a logistic regression function, where the voltage clearly tunes the probability of the effective anti-parallel state (high resistance state R'_{ap}) between 0 and 1 within a small voltage range of $\Delta V \approx 20$ mV. This is a well known response of superparamagnetic tunnel junctions when controlled by a dc voltage [112], [168], [169]. It is as well its main advantage for applications such as neuromorphic computing [164].

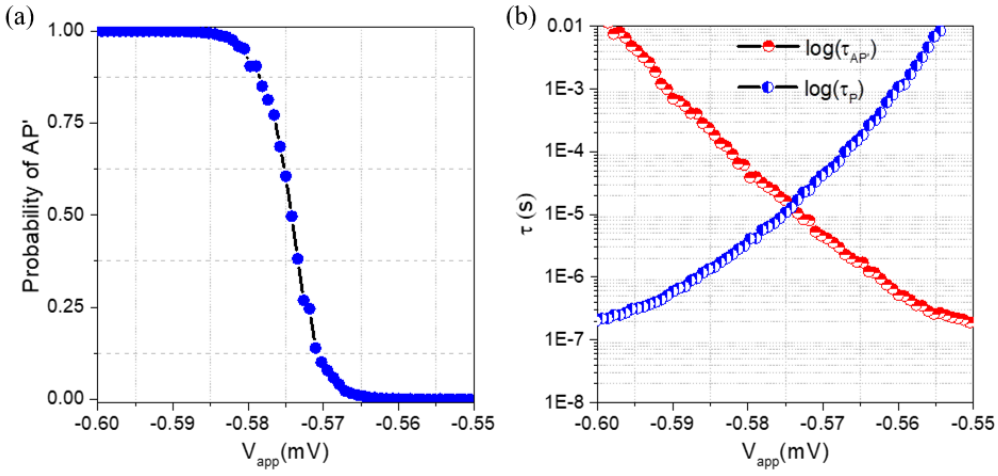

Figure 7.3.4: (a) The probability P of the effective anti-parallel state R'_{ap} as a function of the applied voltage. It was extracted from the experimental results using Eq. 7.3.1. (b) The logarithmic plot of the average dwell-times as a function of the applied voltage, with the parallel state in blue and the effective antiparallel state in red.

The logarithmic plot of the dwell-times is depicted in Figure *7.3.4*(b), where for both magnetoresistance states, it shows a quasi-linear dependence. The latter hints at an exponential dependence of the dwell-times with the voltage, also called the Arrhenius law, which is expected for the superparamagnetic tunnel junction operated via a dc voltage [112]. Interestingly, even though the switching here occurs between the parallel state and an intermediate one it follows the reported predictions from a macrospin model where the magnetization switches between the parallel and the antiparallel states (see section 3.6 of chapter 3).

In addition, in Figure *7.3.4*(b) the minimum average dwell-time of the magnetization switching is $< \tau_{av} > \sim 10^{-5}\ s$, given by the crossing point between the two dwell times plots $< \tau_p >$ and $< \tau_{AP}, >$. It appears to be around 10 times faster than the ones reported for perpendicular magnetic tunnel junctions in [168], [169]. On the other hand, it is relatively slow compared to recent reports on in-plane magnetized tunnel junctions, where the average time of the magnetization switching was reported to be in the sub-nanosecond range [170], [171].

However, so far in-plane superparamagnetic tunnel junctions (i-SMTJ) were operated only under an external magnetic field. Therefore, the pMTJs hold over the i-SMTJs the advantage of zero field operation. However, for the results reported here the power consumption is relatively high (~ 0.6 V), with the majority of it needed just to drive the system into superparamagnetic state.

The different results from this section confirm that the random switching of the magnetoresistance corresponds to a superparamagnetic state. It gathers many properties of superparamagnetism in the MTJs such as: large resistance changes, random telegraph noise, and the dependence on the voltage amplitude and sign via the STT.

In the next sections using the Néel-Brown model discussed in section 3.6 of chapter 3, the focus will be on the exploration of the origin of this effect, why it occurs at zero external magnetic field, and how it can be further improved to have faster switching and lower energy consumption.

7.4 Theoretical analysis of the mean dwell-times of the perpendicular superparamagnetic tunnel junctions

To theoretical analysis of the mean dwell times in this section are carried out using the Néel-Brown model developed for a coherent macrospin switching. This is because, despite the difference in the magnetization switching mechanism here, the Arrhenius law of the mean dwell-times predicted by the macrospin model was observed here as well as a function of the magnetic field, the temperature, and the voltage. Moreover, studies on superparamagnetism using spin-polarized scanning tunneling microscopy (SP-STM) and Monte-Carlo simulations in [172] reported that the nucleation switching only adds an extra energy offset to the total magnetic energy barrier, and makes the attempt time dependent on the diameter of the magnetic layer. Thus, even for the nucleation switching the Arrhenius law from the Néel-Brown model [112] can be roughly used to approximate the magnetization switching, with the awareness that the fitted parameters do not

reflect the real macrospin ones, because they contain the modifications added by the nucleation process.

In general, the Néel-Brown model presented in Eq. 3.6.16 of chapter 3 predicts that if the ferromagnetic layer is in a superparamagnetic state (low energy barrier), it should operate in the absence of the external magnetic bias field and dc voltage (current). Their presence will only tune the magnetization dwell-times to favor one of the metastable states. Therefore, field-free operation is not expected to be a challenging task.

However, the difficulty lies in fabricating magnetic tunnel junctions that meet the theoretical requirements. There exist often non-intended stray fields arising from the different layers in the stack and resulting in some magnetic coupling between the layers. The most dominant one is the stray field from the non-compensated synthetic antiferromagnet (SAF). These extra magnetic fields affect the symmetry of the energy wells and thus require external magnetic bias fields to compensate for them. The latter is illustrated in Figure *7.4.1*, where Figure *7.4.1*(a) corresponds to a zero applied field symmetric energy well where the probability of the magnetization to be switched by the thermal fluctuations is equal for the two states parallel/ anti-parallel. The addition of the extra field from the stack stabilizes one of the two metastable states and therefore weakens the random switching of the magnetization, see Figure *7.4.1*(b).

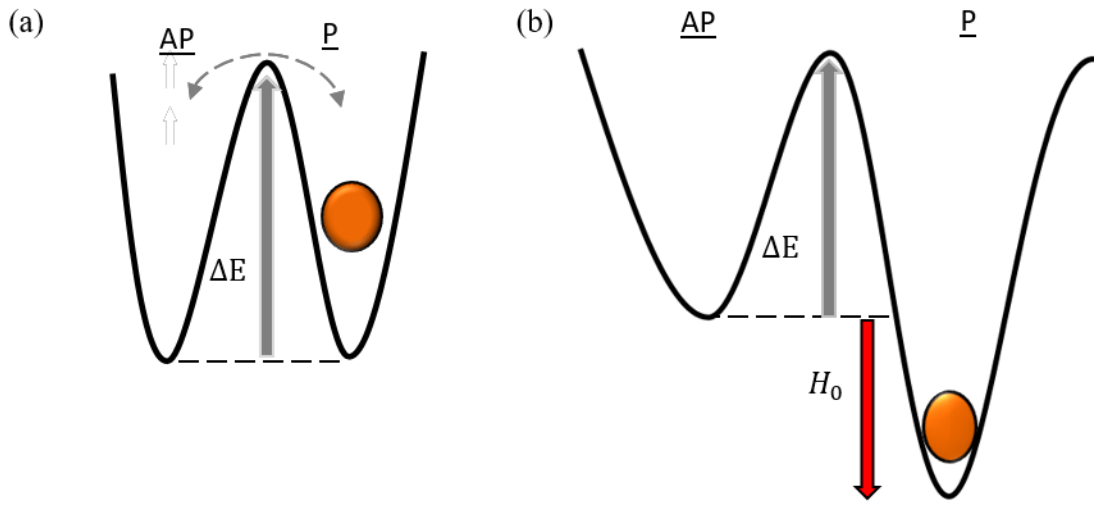

Figure 7.4.1 : (a) Illustration of the superparamagnetism in a symmetric energy well were the random switching is equiprobable between the two metastable states. (b) The illustration of the effect of the non-compensated stray field from the SAF denoted here H_0 and corresponding for the pMTJs to $H_{int\perp}$.

The solutions to solve this problem are usually bias-field based, where the extra magnetic fields are compensated by (i) an external one which increases drastically the power consumption, or (ii) through nanofabrication of permanent magnets which is challenging to do. However, the Néel-

Brown model in Eq. 3.6.16 of chapter 3 has a voltage dependent term as well, and therefore it can act to balance the asymmetry in the energy well created by the extra magnetic fields. For instance, if the SAF stray field stabilizes the parallel state, the voltage (current) through the spin transfer torque can be tuned to favor the anti-parallel state and therefore for certain voltage values balance the asymmetry in the energy well.

While the spin transfer torque does not change the energy landscape, it acts by pumping energy into the system until it reaches an effective energy level at which the superparamagnetic state is restored. An illustration of this is shown in Figure *7.4.2*.

Interestingly, the balance of an asymmetrical energy well by voltage leads to an effective energy barrier ($\Delta\tilde{E}$) that is smaller than the initial intrinsic energy barrier (ΔE). Therefore, it can increase the tuning rate of the superparamagnetic tunnel junction.

The use of the voltage to effectively balance the asymmetry of the energy well has a crucial condition, however. It requires that the voltage needed to drive the system into superparamagnetism is smaller than the barrier-breakdown voltage of the MTJ. The latter is usually around $V_B = 1\,V$ [14], [17]. This condition, most likely is what made it harder for this STT-based solution to work, because the critical switching voltages in the absence of an external magnetic field were higher than the barrier-breakdown voltage (V_B). Therefore, the reduction of the critical switching voltage is the main key to using this solution. In the latter lies the advantage of the perpendicular magnetic tunnel junctions (pMTJ). They have generally smaller critical switching voltages when compared to in-plane MTJs[14].

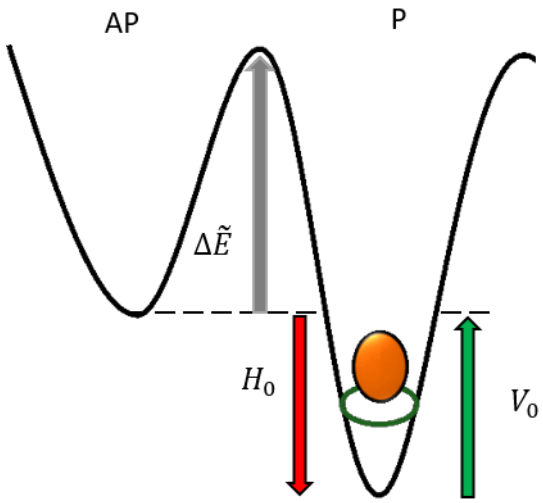

Figure 7.4.2 : Illustration of the effect of the spin transfer torque on the metastable state and how it can balance the asymmetry in the energy well caused by the SAF stray field $H_{int\perp} = H_0$.

Moreover, it is easier to further reduce the critical switching voltage of the pMTJs via the thickness of the free layer. The critical switching voltage for the pMTJs is given by (see section 2.2 of chapter 2 for the derivation and the full expression) :

$$V_c \propto \alpha * (H_u - H_d) \tag{7.4.1}$$

where α is the damping constant, H_u the perpendicular anisotropy field ($\propto 1/t_{FL}$), and H_d is the demagnetizing field. Hence, V_c of the pMTJs is easily tunable through their geometry. Therefore, they are most likely to operate in the absence of an external field if the energy barrier is small enough and the non-compensated stray field of the SAF is not too strong.

Consequently, it is expected from the pMTJ devices studied in this work that they can fully operate in the absence of an external magnetic field because their SAF stray field is intermediate (~ 40 mT). Their effective energy barrier will be extracted in the following sub-section using the Néel-Brown model.

7.4.1 Fitting of the dwell times from the field-free SMTJs using the Néel-Brown Model

In the absence of an external magnetic field, the Néel-Brown model is simplified and takes the following form :

$$\tau_p = \tau_0 * \exp\left(\beta * \Delta E * \left(1 + \frac{V_{app}}{V_c}\right)\right) \tag{7.4.2.a}$$

$$\tau_{ap} = \tau_0 * \exp\left(\beta * \Delta E * \left(1 - \frac{V_{app}}{V_c}\right)\right) \tag{7.4.2.b}$$

Therefore using Eq. 7.4.2 the fitting of the dwell time and the extraction of the parameters is straightforward. However, for the pMTJ devices studied here, the situation is different. The superparamagnetism certainly happens in the absence of any external magnetic field, but the non-compensated stray field from the synthetic antiferromagnet (SAF) is present and it is acting out-of-plane along the axis of the magnetization. Thus, adding the field to Eq. 7.4.2 is more appropriate for the fitting of the experimental results obtained in this work. Including the SAF field the equation takes the form :

$$\tau_p = \tau_0 * \exp\left(\beta * \Delta E * \left(1 + \frac{V_{app}}{V_c}\right)\left(1 + \frac{H_{int\perp}}{H_{ueff}}\right)^2\right) \tag{7.4.3.a}$$

$$\tau_{ap} = \tau_0 * \exp\left(\beta * \Delta E * \left(1 - \frac{V_{app}}{V_c}\right)\left(1 - \frac{H_{int\perp}}{H_{ueff}}\right)^2\right) \tag{7.4.3.b}$$

The fitting including the SAF- stray field $H_{int\perp}$ is a bit more complicated due to the quadratic dependence on the field in Eq. 7.4.3. Therefore, since here only the voltage is changed, the Néel-Brown model is further simplified to take a simpler form, similar to the one in Eq. 7.4.2. The simplification starts, first, by assuming that the system has been balanced by the voltage V_0 so that it has an equiprobable random switching. This balance voltage V_0 corresponds to the point where the dwell-times in Eq. 7.4.3 are equal ($\tau_p = \tau_{ap}$), and it takes the following form :

$$\left(1 + \frac{V_0}{V_c}\right)(1+h)^2 = \left(1 - \frac{V_0}{V_c}\right)(1-h)^2 \tag{7.4.4}$$

with $h = \frac{H_{int\perp}}{H_{ueff}}$, $H_{int\perp}$ the stray field from the SAF, it can as well be any magnetic field along the axis of the magnetization, and H_{ueff} is the effective anisotropy field defined in the previous chapters.

Next, Eq. 7.4.4 is solved for V_0, which gives :

$$V_0 = V_c * \left(-\frac{2h}{1+h^2}\right) \tag{7.4.5}$$

The importance of Eq. 7.4.5 is that it provides an analytical formula for the STT balance voltage required to induce superparamagnetism. Experimentally it is equivalent to the voltage at the crossing point of the two dwell-times in Figure *7.3.4*(b).

Inserting the formula of V_0 back to the Néel-Brown Eq. 7.4.2, gives an expression for the effective energy barrier $\Delta\tilde{E}$ created by the STT:

$$\Delta\tilde{E} = \Delta E * \frac{(1-h^2)^2}{1+h^2} \tag{7.4.6}$$

For applied voltages higher or smaller than V_0, they can be expressed in Eq. 7.4.6 as $V_\epsilon = V_{app} - V_0$, with V_ϵ the additional voltage needed to be higher or smaller than V_0. Developing the algebra yields the following simplified model :

$$\tau_p = \tau_0 * \exp\left(\beta * \Delta\tilde{E} * \left(1 - \frac{V_{app} - V_0}{V_c + V_0}\right)\right) \tag{7.4.7}$$

$$\tau_{ap} = \tau_0 * \exp\left(\beta * \Delta\tilde{E} * \left(1 - \frac{V_{app} - V_0}{V_c - V_0}\right)\right) \tag{7.4.7.b}$$

The simplification here consists in the derivation of an expression for the compensation voltage V_0, and the effective energy barrier $\Delta\tilde{E}$ that are independent of the energy minimum P or AP'. Therefore, it allows flexibility in fitting using Eq. 7.4.6 as a function of the applied voltage.

The fitting of the experimental results from Figure *7.3.4*(b) is depicted in Figure *7.4.3*. It is in good agreement with the measurements, although, the linear fitting in Figure *7.4.3* seems to break down if the applied voltages are far from the balance voltage V_0. In these voltage regions, the logarithmic plot of the mean dwell-time is distorted, but it is not expected to be due to an intrinsic effect.

It is mostly the time constant of the setup in these regions RC~ 100 ns.

The extracted parameters and their values are the following :

- From the experiment : V_0 = -0.575 mV, $\mu_0 H_{int\perp} = 40$ mT.
- From the fitting : $\Delta\tilde{E} = 15$ K_BT, $\Delta E = 16$ K_BT, and $\mu_0 H_{ueff} = 27\,mT$.

The attempt time was taken as τ_0 = 1 ns, this value is generally accepted in literature for the attempt time [112]. Although it should be noted that it was reported theoretically to be variable with the internal parameters, see ref. [173].

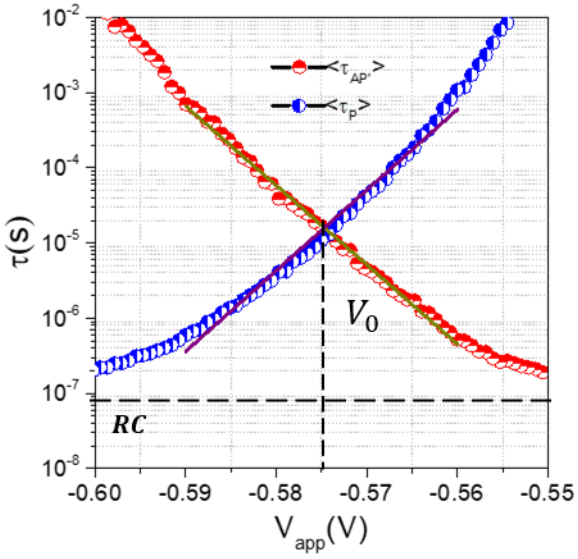

Figure 7.4.3: The fitting of the logarithmic plot of the mean dwell-times from Figure 7.3.4(b).

The STT balancing voltage V_0 is relatively high, and therefore to be more adequate for low energy applications it should be reduced. From its analytical formula in Eq. 7.4.4, it is clear that it can be reduced through two procedures, the first one by further reducing the critical switching voltage, and the other one by reducing the stray field from the SAF. Both cases are possible for pMTJs by varying the free layer thickness, and by tuning the SAF multilayers, respectively. The other important condition for low power applications is the speed to reach nanosecond dwell-times. As discussed above, the results reported here are relatively slow compared to the actual state-of-the-art especially compared to in-plane MTJs [170], [171]. However, the analysis of the simplified model in Eq. 7.4.5 allows the prediction of how the pMTJs can be further improved to reach much smaller mean dwell-times. The key to increase their speed, interestingly, lies in the tuning of the SAF stray field and not as expected in canceling it. This is illustrated in Figure *7.4.4*, where the effective energy barrier (normalized by the real one) is plotted as a function of the SAF stray field (normalized by the effective anisotropy field H_{ueff}). It can be noted that the effective energy barrier can be minimized by tuning the SAF stray field. Moreover, it can be done without the need to change the intrinsic parameters of the real energy barrier ΔE or the magnetic anisotropy field

H_{ueff}. The only requirement is to tune the SAF stray field to be equal to the magnetic anisotropy field H_{ueff} :

$$H_{int\perp} \rightarrow H_{ueff} \tag{7.4.8}$$

Nevertheless, if the SAF stray field is fixed, the magnetic anisotropy field can as well be tuned to meet the requirement in Eq. 7.4.8 through the FL thickness and the diameter.

It should be noted that the model developed here is derived from the Fokker-Planck equation (see chapter 3, section 3.6) by assuming a large energy barrier ($\Delta E > 5\ K_B T$). Therefore it fails in describing intermediate and small energy barriers. For those cases, the Langer method is more suitable [173]–[175].

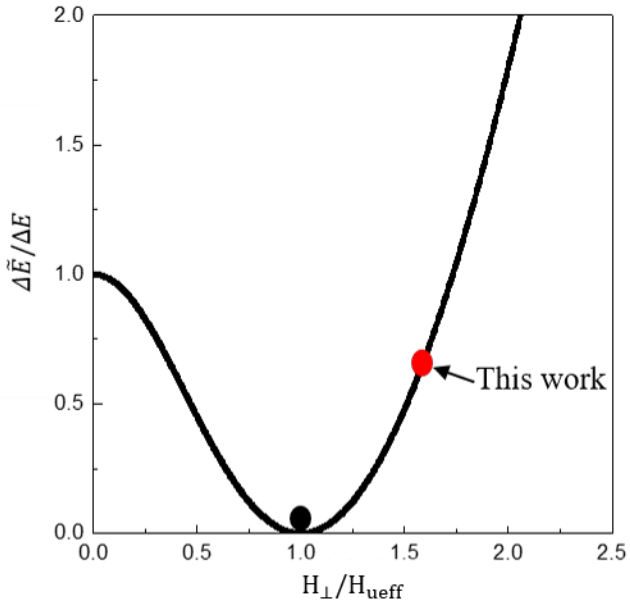

Figure 7.4.4 : The ratio of the effective to the real energy barrier as a function of the ratio of the SAF stray field to the effective anisotropy field.

It must be reminded that the extracted parameters here are phenomenological ones, they don't necessarily reflect the actual device parameters because they might contain offsets caused by the nucleation and propagation switching.

Conclusion

In this chapter, the observed magnetoresistance distortions in the absence of an external magnetic field were demonstrated to be a result of the emergence of a superparamagnetic state. Real-time measurements showed that when the magnetoresistance has distortions near zero field, the magnetization is switching randomly between two discrete states. The latter is of interest for applications for it represents the first demonstration of a perpendicular superparamagnetic tunnel junction that operates fully in the absence of a magnetic field.

Furthermore, the magnetization random switching was found to be only 53% of the full TMR at zero voltage. This is attributed to the presence of a magnetic domain that might be nucleated by Joule heating and spin transfer torque. The random switching then occurs between the P state and the domain state.

The mean dwell-times were found to follow an Arrhenius law, and have similar behavior to the one from superparamagnetic tunnel junctions with a full switching of TMR. Accordingly, they were analyzed using the Néel-Brown model to extract the effective parameters of the measured device. Moreover, developing the Néel-Brown model allowed to predict further enhancements of the device performance to obtain faster switching and lower energy consumption. It was predicted that the switching will be fastest if the SAF stray field is equal to the magnetic effective anisotropy field H_{ueff}.

The next step will be to further characterize the stochastic properties of the pMTJs devices in zero and non-zero fields, and to verify the predictions of this chapter to improve their switching speed and energy consumption.

Summary and perspectives

8.1 General conclusion

This thesis focuses on perpendicular magnetic tunnel junctions (pMTJ) whose magnetic layers are characterized by a perpendicular magnetic anisotropy. This allows the tuning of the free layer magnetization orientation via its thickness and the device diameter, which can be as small as 20 nm. Two distinct functionalities were investigated : (i) the conversion of an rf current to a dc voltage and (ii) the stochastic switching when driven into a superparamagnetic state. The objective was to define the experimental conditions that lead to the largest output voltages for the rf-to-dc conversion, and a field-free stochastic switching for the superparamagnetic state. The experiments were carried out under in-plane and out-of-plane fields, and with rf and dc currents, for three free layer thicknesses (1.4 nm, 1.6 nm, and 1.8 nm) and for 5 nominal diameters (20 nm, 40 nm, 80 nm, 100 nm, and 150 nm).

The pMTJs studied here are standard bottom pinned MTJs with a resistance-area (RA) product of $\sim 10\ \Omega.\mu m^2$ and a TMR of ~ 100 %. Their stack composition was presented in chapter 2 with a description of its different major blocks, such as : FL, PL, T-SAF, B-SAF, and top and bottom electrodes.

To characterize the pMTJs, different experimental setups were used for the static and the dynamic measurements: the VSM for the continuous films, the automatic tester and PPMS for the static MR of the nanopillars, the deembedding and the ST-FMR for the rf-to-dc conversion, the generation setup for the FMR spectral densities, and the time resolved experiments for the superparamagnetic state. All these setups were presented in chapter 2.

In chapter 3, preparing for the analysis of the experimental results, all required theoretical formalisms and equations were derived using an analytic macrospin model. The first task was to determine the free layer equilibrium state under an out-of-plane stray field from the SAF and an external in-plane field. For this, via the total energy minimization, an exact analytic formula was derived to account for both fields simultaneously. The next task was to derive an analytic formula for the rf-to-dc voltage for the pMTJ where the PL is oriented out-of-plane. This was done in chapter 3 through the linearization of the LLG equation. The derivations were extended to include the effects of an additional dc current (for active detection) and the coupling to another magnetic layer. In the last part of chapter 3, a presentation of the analytic derivations of the Neel-Brown was included to account for the superparamagnetic state.

The analysis of the experimental results started with chapter 4. In this chapter the focus was to determine the equilibrium magnetic states of both the free and the polarizing layers. For this, the three free layer thicknesses (t_{FL} =1.4 nm, 1.6 nm and 1.8 nm) were characterized under out-of-plane and in-plane magnetic fields, and for variable temperatures and dc currents. The measurements combined with the theoretical formalisms from chapter 3 helped to identify the equilibrium orientation of the free layer magnetization.

It was found that for $t_{FL} = 1.4$ nm the free layer magnetization is orientated out-of-plane, while for $t_{FL} = 1.6$ nm and $t_{FL} = 1.8$ nm it is orientated in zero field at an intermediate angle and in-plane respectively. Moreover it was found that under dc current the dominant effect is the spin transfer torque, followed by the Joule heating by $\zeta \approx 150\ \mathrm{K/mA^2}$, and probably a weak voltage controlled anisotropy (VCMA).

The polarizing layer was demonstrated to be out-of-plane at equilibrium and reorients by an in-plane field. The characterization of the polarizing layer reversal revealed that its AP-to-P reversal is dependent on the free layer thickness, while its P-to-AP is almost independent of temperature and current amplitude and sign. The quantification of the Joule heating gives an approximate value of $\zeta \approx 300\ \mathrm{K/mA^2}$.

The understanding of the static behavior of the pMTJs layers will be the background on which the coming chapters are build. In the next chapter, it will be used to investigate the magnetization dynamics under an oscillating electric current, for the passive spin-torque nano-diode effect. Subsequently, it will be used for the investigations of the magnetization dynamics under both dc and oscillating current (active detection), and finally for the stochastic behavior of the magnetization reversal.

In chapter 5, the investigations were entirely focused on the passive rf-to-dc conversion of the pMTJs. The experimental characterizations covered all the free layer thicknesses (1.4 nm, 1.6 nm, and 1.8nm) under in-plane and out-of-plane magnetic bias fields, in addition to the different nominal diameters (20 nm, 40 nm, 80nm, 100nm, and 150 nm). The results from both the free layer, and the polarizing layer were explained using the analytic model developed in chapter 3.

It was found experimentally, that reducing the diameter of the pMTJs enhances the maximum output voltage. For the in-plane bias field, the enhancement ratio is around 7 when reducing the nominal diameter from 150 nm to 20 nm. The origin of this enhancement was attributed to the combination of the higher current density, the compensation of the magnetic anisotropy by the demagnetizing field, and for the pMTJ devices studied here, to the presence of an ohmic serial resistance. This interpretation is well confirmed by modeling the voltage of the spin-torque nano-diode. In addition, it was found that by reducing the free layer thickness, the signal is further enhanced, by almost twice its value. This is attributed to the compensation of the interface perpendicular magnetic anisotropy field by the demagnetizing field.

Motivated by the results on the rectification signals, the pMTJs were tested for their demodulation capabilities using OOK modulation showing good preliminary results. Further improvement of the signal to noise ratio was proposed and simulated for the demodulation using a matched filter.

For the out-of-plane magnetic field measurements, excitations of the PL was detected. It shows a diameter dependence similar to the one observed for the in-plane field measurements. It is found that the out-of-plane field in general leads to higher rf-to-dc voltages compared to the in-plane field.

The investigations conducted in the passive rf-to-dc conversion were extended in chapter 6 to include the active rf-to-dc conversion. It was found that the polarizing layer FMR mode is the main

contributor to the active detection. In addition, the maximum output voltage was found to be relatively enhanced by the negative current in the in-plane and the out-of-plane bias fields.

Moreover, for the in-plane magnetic field measurements, the FL and PL FMR modes were found to be shifted by the dc current, independent of the current sign. This was attributed to the Joule heating in the devices that strongly affects M_s and the iPMA. The effect due to Joule heating was evaluated using the derived macrospin model. In addition, the FL with a thickness of 1.4 nm was found to be driven by the negative dc current into steady state auto-oscillations.

For the out-of-plane magnetic field measurements, only one FMR mode was detected, and it was attributed to the PL oscillations. For dc currents above -0.3 mA, it undergoes a large angle steady state auto-oscillations, corresponding to the maximum enhancement of the active rf-to-dc conversion by the dc current. The frequency shift with the dc current in the out-of-plane field measurements was found to be dominated by the STT in the negative current, while in the positive current only the Joule heating is acting.

The active detection completed the characterization of the pMTJ-based spin-torque nano-diodes that were carried throughout this thesis. The key points for the characterization were the maximum output dc signal, and the signal shapes. For the operation frequency, it is tunable through the field and was demonstrated here to be tunable via the dc current.

The measurements under the different conditions of currents and magnetic fields, and for the different FL thicknesses and pMTJ diameters suggest that the best detection signal corresponds to the PL mode from the pMTJs with nominal diameter of 40 nm, a FL thickness of 1.4 nm, in an antiparallel state, and under an out-of-plane field.

It produces the highest output dc voltages in the passive detection, and in the active detection. Its output is further improved by applying a negative dc current, reaching a maximum when it is driven into steady state oscillations. In addition to its higher dc output voltage, its dependence on the out-of-plane field is easier to tune and implement through the SAF multilayers than the in-plane field. Moreover, its asymmetric signal shape in the passive detection gives it an additional advantage for wireless applications such as FSK demodulation where it can double the output signal. Furthermore, its signal shape was demonstrated to be tunable by negative current and can be changed from being antisymmetric in the passive case to being symmetric in the active one.

These different advantages makes it the optimal case for a wake-up receiver based on pMTJs when compared to other measured devices. Although, it has a disadvantage of being working in the antiparallel state where the resistance is at its highest value leading to strong impedance mismatch.

For the FL mode based-detection, in general, it holds over this optimal mode the advantage of being explainable via the derived formulas and its behavior is predictable with good certainty. For the PL mode, however, the understanding of its dynamics it not yet fully completed and still requires additional measurements and simulations to conclude on.

Following the active rf-to-dc characterization, the discussions were oriented in chapter 7 towards an STT induced superparamagnetic state. The aim of the studies in chapter 7 was to understand some magnetoresistance distortions that were observed under a dc current and in the absence of an

external magnetic field. The real-time measurements showed that at these distortions near zero field, the magnetization is switching randomly between two discrete states.

Furthermore, the random magnetization switching was found to be only 53% of full TMR. It was attributed to the presence of a magnetic domain that might be nucleated by the Joule heating and the spin transfer torque.

The mean dwell-times were found to follow an Arrhenius law, and have a similar behavior to the one from the superparamagnetic tunnel junctions that switch in full-TMR. Accordingly, they were analyzed using the Néel-Brown model to extract the effective parameters of the measured device. The average dwell-time was found to be $\sim 10^{-5}\ s$, and the voltage required to induce the stochastic switching at zero field is $V_0 \sim 0.6$ V. The presence of the superparamagnetic state was argued to be due to the STT balancing effectively the asymmetry in the energy barrier caused by the SAF stray field.

These results on the stochastic switching are the first demonstration of a field-free current controlled stochastic perpendicular magnetic tunnel junction.

8.2 Perspectives

Further possible studies to be realized on these pMTJs for the detection and the superparamagnetic state can be divided into short and long term goals respectively. The short term part concerns the studies to be done on these specific devices and focuses on additional experimental schemes. The long term part, on the other hand, concerns the modification of the pMTJ stack and the possible enhancements that can results from it.

- ***Short term*** :

  For the passive detection, what remains to be studied in more detail is the polarizing layer FMR mode. Its physics is not yet fully understood and therefore a thorough numerical simulation study is needed to investigate its nature and how it is affected by its coupling to the SAF. In addition, for the measurements under the out-of-plane field, they were done here using a permanent magnet, but a new setup with an electromagnet was developed after this work, and therefore it will be of interest to characterize fully the field dependence of the PL mode.

  For the passive detection and considering the application as a wake-up receiver, implementing an impedance matching network would further enhance the sensitivity to low rf powers. Moreover, implementing the proposed matched filter will maximize the signal to noise ratio and therefore it will improve the reading of the output. An additional interesting experiment that was not possible during this work, and that should be done, is to test the FSK demodulation in particular for devices with an asymmetric peak.

  For the active detection characterizing the injection locking at f and 2f is an important step to further enhance the signal and reduce strongly its linewidth. As for the applicative part of the active detection, in addition to the injection locking, the current-swept frequency range and the

linewidth of the current peaks remain still to be determined, as well as the highest speed at which the frequency can be tuned via the dc current.

For the field-free superparamagnetic tunnel junctions, one of the main step to be done is the reduction of the RC of the setup so that the stochastic response of the devices with smaller diameters can be measured at zero bias fields. In addition, the analysis presented in this work suggested that a domain wall is involved in the switching and therefore some micromagnetic simulations are needed to understand the underlying process. As for the reduction of the dwell times and the power consumption at zero field they will require long term goals.

- ***Long term*** :

For the detection, in general, for both passive and active detection, developing a stack with lower damping, smaller H_{ueff}, and higher TMR will lead to more optimized signals. Moreover when co-integrating the devices with CMOS, in order to be less bothered by the serial resistance from the bottom electrode, the devices should have the smallest diameters possible. This will give them high resistances and thus help them to overcome the signal degradation caused by the serial resistance. However, the impedance matching circuit needs to cope for the increased resistance.

Furthermore, to better understand the PL layer mode varying the SAF multilayers and the Ru thickness will help to acquire deeper understanding of the undergoing magnetization dynamics.

For the field-free superparamagnetic tunnel junctions, it was predicted that a faster stochastic switching is achieved when the effective magnetic anisotropy H_{ueff} is equal to the stray field from the SAF. The latter can be tested by either tuning the SAF stray field through variation of its layer thicknesses, or by tuning the iPMA via the FL thickness. It was also predicted that lower energy consumption can be achieved if the critical switching current was minimized, which can be done by minimizing H_{ueff} through the FL thickness.

An additional part of the perspectives is the development of demonstrators for the applications of the pMTJ-based detection and the field-free superparamagnetic tunnel junctions. For the detection the goal is to build a wake-up receiver using these devices. This will be addressed within an upcoming European based collaborative project (Swan-on-chip, coordinated by INL) and the results presented here will provide the basis and guidelines to achieve this goal. As for the field-free superparamagnetic pMTJs the goal is to couple several of them in order to demonstrate their capabilities to solve problems using unconventional computing methods. The work on this is continued by another PhD student at Spintec, and a first demonstration of coupling of 2 devices was already achieved !

Annexes

A. Exact analytic solution to determine the critical points for the total energy density

The goal of this annex is to present the exact solution for the derivation of the energy minima for the total energy density when simultaneously an out-of-plane field and an in-plane magnetic field are taken into account. In chapter 3, section 3.1, the problem was transformed to a polynomial of 4th order, with the critical points corresponding to it roots.

The solution from section 3.1 of chapter 3 is the following :

$$\theta_{(1,2,3,4)} = \text{acos}\left(X_{(1,2,3,4)}\right) \qquad (A.1)$$

where,

$X_{(1,2,3,4)} = Y_{1,2,3,4} - \frac{\alpha}{4}$ (Depressed quartic),

$Y_{(1,2)} = \frac{U \pm \sqrt{\Delta_I}}{2}$, and , $Y_{(3,4)} = \frac{-U \pm \sqrt{\Delta_{II}}}{2}$;

$\Delta_I = U^2 - 4 * (t_0^2 - V)$,

$\Delta_{II} = U^2 - 4 * (t_0^2 + V)$,

$U = \sqrt{(2 * t_0 - P)}$,

$V = -\frac{q}{2*U}$,

$t_0 = W_0 - \frac{L}{3}$,

$W_0 = \left[\left(\frac{n}{2}\right) + \sqrt{\left(\frac{n}{2}\right)^2 - \left(\frac{m}{3}\right)^3}\right)^{\frac{1}{3}} + \left[\left(\frac{n}{2}\right) - \sqrt{\left(\frac{n}{2}\right)^2 - \left(\frac{m}{3}\right)^3}\right)^{\frac{1}{3}}$,

$n = -\frac{2}{27}L^3 + L * r * \frac{2}{3} + \frac{q^2}{8}$,

$m = \frac{L^2}{3} + r$,

$L = -\frac{P}{2}$,

$P = -\frac{3}{8} * \alpha^2 + \beta$,

$$q = \frac{1}{8}\alpha^3 - \alpha * \frac{\beta}{2},$$

$$r = -\frac{3}{256} * \alpha^4 + \beta * \frac{\alpha^2}{16} - \gamma * \frac{\alpha}{4} + \lambda.$$

B. TMR effective diameter dependence due to a serial resistance

Looking at the TMR statistics shown in section 4.2 of chapter 4, it can be seen that a linear fit of the TMR is a good approximation to its dependence on the squared diameter. Thus, it can be simplified by using a Taylor expansion, where the second order terms are neglected;

$$TMR \approx TMR_0 \left(1 - \frac{R_s}{\rho_p * t_{FL}} * \frac{\pi}{4} * D_n^2\right) \quad (B.1)$$

As a consequence, using Eq. B.1, a linear fit of the TMR distributions (average) allows the extraction of the intrinsic TMR of the devices, as well the approximate value of the serial resistance. The extracted parameters are presented below in Eq. B.2, with R_{p_m} the measured resistance of the parallel state, and the intrinsic tunneling magnetoresistance $TMR_0 \approx 124$ %.

$$\begin{cases} TMR_0(\%) = 124 & (I) \\ \dfrac{R_s}{\rho_p * t_{FL}} * \dfrac{\pi}{4} * D_n^2 = \dfrac{R_s}{R_p} = 18 * D_n^2 & (II) \\ R_{p_m} = R_p + R_s = R_p(1 + 18 * D_n^2) & (III) \end{cases} \quad (B.2)$$

Finally, by merging the equation Eq. B.2(II) and Eq. B.2(III) one obtains a formula for the serial resistance as function of the MTJ nominal diameter and the measured parallel resistance. It takes the following form :

$$R_s = \frac{R_{p_m}}{1 + 0.05 * D_n^{-2}} \quad (B.3)$$

An important point here is that Eq. B.3 represents the part of the real serial resistance seen through the measured parallel resistance (R_{p_m}). It represents the real value of the serial resistance only when the diameter is large ($\lim_{D_n \to \infty} R_s = R_{p_m}$). Therefore the best approximation of the serial resistance is obtained by the MTJs with the largest diameters, for this case $D_n = 150$ nm. The calculations, using Eq. B.3, give a serial resistance of the value $R_s \approx 180\ \Omega$.

C. Self-sustained oscillations of the magnetization under ac current forcing

Once the free layer magnetization is in the self-sustained precession regime, the magnetic tunnel junction is called a spin torque nano-oscillator (STNO)[62]. The injected dc current multiplied by the oscillating magnetization, via the TMR generates microwave voltages. Moreover, the frequency of the generated microwave voltage is tunable via the input dc current [21]. These properties and the nano-sizes of the STNO made them of interest for microwave applications. They were the focus of numerous studies in the past decades, where, they were demonstrated for a wide range of applications such as : microwave modulation (amplitude, frequency, and phase)[176]–[179], ultrafast spectral analysis [156], [180], and neuromorphic computing [181].

Therefore, in the stable precession regime the formalism developed in chapters 3 does not hold anymore. Here, the spin-torque nano-diode is replaced by an autonomous oscillator that would interact differently with the forcing rf current. The phenomenon that governs this type of interaction between the autonomous oscillators is called synchronization [98]. It forces the oscillators to oscillate at the same frequency, within a relatively large frequency range (locking range), and it locks their phases leading to a drastic decrease of their phase noise. This strong reduction of the oscillator phase noise, translates to less energy dissipation, and thus smaller linewidth and higher power of the oscillator frequency spectrum [99]. For the STNOs, the synchronization is still an active area in the quest for the reduction of their relatively strong phase noise, see [150]–[154]. In addition, for spin-torque nano-diodes measurements, the synchronization was found to increase strongly their sensitivity to low rf current powers, see [100]–[102].

Understanding the mechanism by which the magnetization synchronizes to the forcing rf current, requires solving the LLG equation. Nevertheless, this task is complicated to do analytically, due to the strong nonlinearity of the LLG equation. Moreover, the complex trajectory of the magnetization undergoing a stable limit cycle, rendering the approximation methods such as the perturbation and the linearization difficult to apply. However, Slavin and Tiberkevich (ST) in [157]–[159] found a good approximation to the magnetization dynamics by transforming the LLG equation into a generalized equation of autonomous oscillators. Their approach consists of transforming the magnetization components (m_x, m_y, m_z), into complex ones (c, c*) through canonical transformations. It is inspired by the spin waves formalism [182], and specifically the Holstein-Primakoff transformation [183]. The details of the derivation of the Slavin-Tiberkevich equation from the LLG equation are presented in detail in [184], [185].

Here, the model is introduced briefly to highlight its simplification of the problem. But, for readers interested in a more detailed analysis of the subject, they are referred to more adequate references such as [157], [184], [185].

The major transformations to get to the complex variable "c" are summarized in the following table :

Holstein-Primakoff [183]	Bogoliubov [186]	Normalization
$\boldsymbol{a} = \frac{\boldsymbol{m_x + i m_y}}{\sqrt{\boldsymbol{2(1+m_z)}}}$ $\bar{\boldsymbol{a}} = \frac{\boldsymbol{m_x - i m_y}}{\sqrt{\boldsymbol{2(1+m_z)}}}$	$\boldsymbol{b} = \boldsymbol{ua} + \boldsymbol{v}\bar{\boldsymbol{a}}$ $\bar{\boldsymbol{b}} = \boldsymbol{va} + \boldsymbol{u}\bar{\boldsymbol{a}}$	$\boldsymbol{c} = \boldsymbol{\beta}\, \boldsymbol{b}$

Table C.1 : The group of transformations used to transform the magnetization components (m_x, m_y, m_z) to the complex variable "c".*[184]*

The Bogoliubov transformation and its normalization, serve to make the magnetization trajectory circular. The final equation takes the following form :

$$\frac{dc}{dt} + i\omega(|c|^2)\, c + \Gamma_+(|c|^2)\, c - \Gamma_-(|c|^2)\, c = 0 \qquad (C.1)$$

where $c = \sqrt{p}e^{i(\omega(p)t + \phi)}$, with $p = |c|^2$ the power of the magnetization oscillations, and $\phi = \arg(c)$ their phase. $\Gamma_+(|c|^2)$ and $\Gamma_-(|c|^2)$ stand for the Gilbert damping and the Slonszewski spin transfer torque terms respectively. Separating the real and the imaginary parts of the equation yields a separate equations for the power and the phase, given by [157]:

$$\frac{dp}{dt} = -2[\Gamma_+(p) - \Gamma_-(p)]p \qquad (C.2)$$

$$\frac{d\phi}{dt} = \omega(p) \qquad (C.3)$$

For small oscillation power p, the different terms in Eq. C.1 and Eq. C.3 can be expanded to the following form :

$$\omega(p) \approx \omega_0 + Np \qquad (C.4)$$

$$\Gamma_+(p) \approx \Gamma_G(1 + Qp) \qquad (C.5)$$

$$\Gamma_-(p) \approx \sigma I_{dc}(1 - p) \qquad (C.6)$$

where ω_0 the ferromagnetic resonance frequency, $N = \frac{d\omega(p)}{dp}$ the nonlinearity coefficient (see [157]), $\Gamma_G \propto \alpha$, Q phenomenological parameter, and $\sigma \propto \tilde{\alpha}$.

Interestingly, Eq. C.4, shows that the magnetization oscillation frequency is tunable by the oscillations amplitude p. Moreover, the solutions of Eq. C.2 for small amplitude perturbation δp reflects the stability of the magnetization precessions. It is expressed by :

$$p = p_0\left(1 + \delta p\, e^{-\Gamma_p t}\right) \qquad (C.7)$$

where the perturbed magnetization relaxes back to its previous stable precessions power (p_0) with a relaxation time $t_p = \frac{1}{\Gamma_p}$. For a weak rf current force $f_e e^{-i\omega_e t}$, the equations in Eq. C.2-C.3 take the following form [157], [184]:

$$\frac{dp}{dt} + 2[\Gamma_+(p) - \Gamma_-(p)]p = 2f_e\sqrt{p}\cos(\omega_e t + \phi - \psi_e) \qquad (C.8)$$

$$\frac{d\phi}{dt} + \omega(p) = -\frac{f_e}{\sqrt{p}}\sin(\omega_e t + \phi - \psi_e) \qquad (C.9)$$

The solutions of Eq.C.8-C.9, when the frequency difference between the source and the STNO is relatively small, are approximately :

$$\phi = \arcsin\left(\frac{\delta}{\Delta}\right) + cst \qquad (C.10)$$

$$p \approx p_0 + N\delta \qquad (C.11)$$

where $\delta = \omega_e - \omega_g$ is the detuning frequency, with ω_g the frequency of the STNO and ω_e the frequency of the forcing rf current. $\Delta \approx \frac{Nf_e}{\Gamma_p p_0\sqrt{p_0}}$, represents the locking range, where the phase of the STNO is locked.

The synchronization mechanism occurring here can be described, simply, by inserting Eq. C.11 in the frequency equation Eq. C.4, giving :

$$\omega_p \approx \omega_g + N\delta \qquad (C.12)$$

with ω_g the STNO frequency at a constant dc current. Here, the detuning creates a feedback loop on the frequency by reducing or increasing it until it becomes equal to the rf current frequency. In addition, at the same frequency the STNO phase in Eq. C.10 becomes approximately constant (locked), and thereby its noise is strongly reduced.

References

[1] P. J. Nahin, *The Science of Radio: with MATLAB® and Electronics Workbench® Demonstrations*. Springer Science & Business Media, 2001.

[2] G. Thirunavukkarasu and G. Murugesan, "A Comprehensive Survey on Air-Interfaces for 5G and beyond," in *2019 10th International Conference on Computing, Communication and Networking Technologies (ICCCNT)*, 2019, pp. 1–7.

[3] J. A. Stankovic, "Wireless sensor networks," *computer*, vol. 41, no. 10, pp. 92–95, 2008.

[4] J.-H. Chang and L. Tassiulas, "Energy conserving routing in wireless ad-hoc networks," in *Proceedings IEEE INFOCOM 2000. Conference on Computer Communications. Nineteenth Annual Joint Conference of the IEEE Computer and Communications Societies (Cat. No. 00CH37064)*, 2000, vol. 1, pp. 22–31.

[5] J. Blobel, "Energy Efficient Communication using Wake-Up Receivers," p. 135.

[6] F. Engmann, F. A. Katsriku, J.-D. Abdulai, K. S. Adu-Manu, and F. K. Banaseka, "Prolonging the lifetime of wireless sensor networks: a review of current techniques," *Wireless Communications and Mobile Computing*, vol. 2018, 2018.

[7] D. D. Wentzloff, A. Alghaihab, and J. Im, "Ultra-low power receivers for IoT applications: A review," in *2020 IEEE Custom Integrated Circuits Conference (CICC)*, 2020, pp. 1–8.

[8] G. Finocchio *et al.*, "Perspectives on spintronic diodes," *Applied Physics Letters*, vol. 118, no. 16, p. 160502, 2021.

[9] M. W. Daniels, A. Madhavan, P. Talatchian, A. Mizrahi, and M. D. Stiles, "Energy-efficient stochastic computing with superparamagnetic tunnel junctions," *Physical review applied*, vol. 13, no. 3, p. 034016, 2020.

[10] M. N. Baibich *et al.*, "Giant magnetoresistance of (001) Fe/(001) Cr magnetic superlattices," *Physical review letters*, vol. 61, no. 21, p. 2472, 1988.

[11] G. Binasch, P. Grünberg, F. Saurenbach, and W. Zinn, "Enhanced magnetoresistance in layered magnetic structures with antiferromagnetic interlayer exchange," *Physical review B*, vol. 39, no. 7, p. 4828, 1989.

[12] B. Dieny, V. S. Speriosu, S. S. Parkin, B. A. Gurney, D. R. Wilhoit, and D. Mauri, "Giant magnetoresistive in soft ferromagnetic multilayers," *Physical Review B*, vol. 43, no. 1, p. 1297, 1991.

[13] J. S. Moodera, L. R. Kinder, T. M. Wong, and R. Meservey, "Large magnetoresistance at room temperature in ferromagnetic thin film tunnel junctions," *Physical review letters*, vol. 74, no. 16, p. 3273, 1995.

[14] D. Apalkov, B. Dieny, and J. M. Slaughter, "Magnetoresistive Random Access Memory," *Proceedings of the IEEE*, vol. 104, no. 10, pp. 1796–1830, Oct. 2016, doi: 10.1109/JPROC.2016.2590142.

[15] J. C. Slonczewski, "Current-driven excitation of magnetic multilayers," *Journal of Magnetism and Magnetic Materials*, vol. 159, no. 1–2, pp. L1–L7, 1996.

[16] L. Berger, "Emission of spin waves by a magnetic multilayer traversed by a current," *Physical Review B*, vol. 54, no. 13, p. 9353, 1996.

[17] R. B. Goldfarb, B. Dieny, and K.-J. Lee, *Introduction to Magnetic Random-Access Memory*. John Wiley & Sons, 2016.

[18] S. I. Kiselev *et al.*, "Microwave oscillations of a nanomagnet driven by a spin-polarized current," *nature*, vol. 425, no. 6956, pp. 380–383, 2003.

[19] M. Tsoi *et al.*, “Excitation of a magnetic multilayer by an electric current,” *Physical Review Letters*, vol. 80, no. 19, p. 4281, 1998.
[20] W. H. Rippard, M. R. Pufall, S. Kaka, S. E. Russek, and T. J. Silva, “Direct-current induced dynamics in C o 90 F e 10/N i 80 F e 20 point contacts,” *Physical review letters*, vol. 92, no. 2, p. 027201, 2004.
[21] J.-V. Kim, “Spin-Torque Oscillators,” in *Solid State Physics*, vol. 63, Elsevier, 2012, pp. 217–294. doi: 10.1016/B978-0-12-397028-2.00004-7.
[22] D. C. Ralph and M. D. Stiles, “Spin transfer torques,” *Journal of Magnetism and Magnetic Materials*, vol. 320, no. 7, pp. 1190–1216, 2008.
[23] M. D. Stiles and A. Zangwill, “Anatomy of spin-transfer torque,” *Phys. Rev. B*, vol. 66, no. 1, p. 014407, Jun. 2002, doi: 10.1103/PhysRevB.66.014407.
[24] T. Shinjo, *Nanomagnetism and Spintronics*. Elsevier, 2013.
[25] S. Chikazumi, S. Chikazumi, and C. D. Graham, *Physics of ferromagnetism*. Oxford University Press, 1997.
[26] “Orbital Magnetic Moment.” http://hyperphysics.phy-astr.gsu.edu/hbase/quantum/orbmag.html (accessed May 24, 2022).
[27] J. J. Sakurai and J. Napolitano, “Modern Quantum mechanics, 2: nd edition,” *Person New International edition*, 2011.
[28] D. J. Griffiths and D. F. Schroeter, *Introduction to quantum mechanics*. Cambridge university press, 2018.
[29] N. F. Mott, “Electrons in transition metals,” *Advances in Physics*, vol. 13, no. 51, pp. 325–422, 1964.
[30] I. A. Campbell and A. Fert, “Transport properties of ferromagnets,” *Handbook of Ferromagnetic Materials*, vol. 3, pp. 747–804, 1982.
[31] A. Purbawati, “Frequency modulation of spin torque nano-oscillators (STNOs) for wireless communication applications,” p. 203.
[32] M. Julliere, “Tunneling between ferromagnetic films,” *Physics letters A*, vol. 54, no. 3, pp. 225–226, 1975.
[33] S. Yuasa and D. D. Djayaprawira, “Giant tunnel magnetoresistance in magnetic tunnel junctions with a crystalline MgO (0 0 1) barrier,” *Journal of Physics D: Applied Physics*, vol. 40, no. 21, p. R337, 2007.
[34] J. C. Slonczewski, “Conductance and exchange coupling of two ferromagnets separated by a tunneling barrier,” *Phys. Rev. B*, vol. 39, no. 10, pp. 6995–7002, Apr. 1989, doi: 10.1103/PhysRevB.39.6995.
[35] W. H. Butler, X.-G. Zhang, T. C. Schulthess, and J. M. MacLaren, “Spin-dependent tunneling conductance of Fe| MgO| Fe sandwiches,” *Physical Review B*, vol. 63, no. 5, p. 054416, 2001.
[36] J. Mathon and A. Umerski, “Theory of tunneling magnetoresistance of an epitaxial Fe/MgO/Fe (001) junction,” *Physical Review B*, vol. 63, no. 22, p. 220403, 2001.
[37] S. Ikeda *et al.*, “Tunnel magnetoresistance of 604% at 300 K by suppression of Ta diffusion in Co Fe B/ Mg O/ Co Fe B pseudo-spin-valves annealed at high temperature,” *Applied Physics Letters*, vol. 93, no. 8, p. 082508, 2008.
[38] J. Z. Sun, “Current-driven magnetic switching in manganite trilayer junctions,” *Journal of Magnetism and Magnetic Materials*, vol. 202, no. 1, pp. 157–162, 1999.
[39] M. Manfrini *et al.*, “Agility of vortex-based nanocontact spin torque oscillators,” *Applied Physics Letters*, vol. 95, no. 19, p. 192507, 2009.

[40] A. Zangwill, *Modern Electrodynamics:*, 1st ed. Cambridge University Press, 2012. doi: 10.1017/CBO9781139034777.
[41] S. Monso *et al.*, "Crossover from in-plane to perpendicular anisotropy in Pt/CoFe/AlO x sandwiches as a function of Al oxidation: A very accurate control of the oxidation of tunnel barriers," *Applied physics letters*, vol. 80, no. 22, pp. 4157–4159, 2002.
[42] W. B. Zeper, F. Greidanus, P. F. Carcia, and C. R. Fincher, "Perpendicular magnetic anisotropy and magneto-optical Kerr effect of vapor-deposited Co/Pt-layered structures," *Journal of Applied Physics*, vol. 65, no. 12, pp. 4971–4975, 1989.
[43] A. Aharoni, *Introduction to the Theory of Ferromagnetism*, vol. 109. Clarendon Press, 2000.
[44] D. E. Laughlin, K. Srinivasan, M. Tanase, and L. Wang, "Crystallographic aspects of L10 magnetic materials," *Scripta Materialia*, vol. 53, no. 4, pp. 383–388, Aug. 2005, doi: 10.1016/j.scriptamat.2005.04.039.
[45] B. D. Cullity and C. D. Graham, *Introduction to magnetic materials*. John Wiley & Sons, 2011.
[46] J. Chatterjee, "Engineering of magnetic tunnel junction stacks for improved STT-MRAM performance and development of novel and cost-effective nano-patterning techniques," p. 180.
[47] J.-C. A. Huang, A. C. Hsu, Y. H. Lee, T.-H. Wu, and C. H. Lee, "Influence of crystal structure on the perpendicular magnetic anisotropy of an epitaxial CoPt alloy," *Journal of applied physics*, vol. 85, no. 8, pp. 5977–5979, 1999.
[48] S. Iwata, S. Yamashita, and S. Tsunashima, "Perpendicular magnetic anisotropy and magneto-optical Kerr spectra of MBE-grown PtCo alloy films," *IEEE Transactions on Magnetics*, vol. 33, no. 5, pp. 3670–3672, 1997.
[49] D. Weller, Y. Wu, J. Stöhr, M. G. Samant, B. D. Hermsmeier, and C. Chappert, "Orbital magnetic moments of Co in multilayers with perpendicular magnetic anisotropy," *Physical review B*, vol. 49, no. 18, p. 12888, 1994.
[50] N. Nakajima *et al.*, "Perpendicular magnetic anisotropy caused by interfacial hybridization via enhanced orbital moment in Co/Pt multilayers: Magnetic circular x-ray dichroism study," *Physical Review Letters*, vol. 81, no. 23, p. 5229, 1998.
[51] S. Ikeda *et al.*, "A perpendicular-anisotropy CoFeB–MgO magnetic tunnel junction," *Nature materials*, vol. 9, no. 9, pp. 721–724, 2010.
[52] L. Néel, "Anisotropie magnétique superficielle et surstructures d'orientation," *Journal de Physique et le Radium*, vol. 15, no. 4, pp. 225–239, 1954.
[53] J. G. Gay and R. Richter, "Spin anisotropy of ferromagnetic films," *Physical review letters*, vol. 56, no. 25, p. 2728, 1986.
[54] P. Bruno, "Tight-binding approach to the orbital magnetic moment and magnetocrystalline anisotropy of transition-metal monolayers," *Phys. Rev. B*, vol. 39, no. 1, pp. 865–868, Jan. 1989, doi: 10.1103/PhysRevB.39.865.
[55] P. Bruno, "Magnetic surface anisotropy of cobalt and surface roughness effects within Neel's model," *Journal of Physics F: Metal Physics*, vol. 18, no. 6, p. 1291, 1988.
[56] L. Nistor, "Jonctions tunnel magnétiques à aimantation perpendiculaire: anisotropie, magnétorésistance, couplages magnétiques et renversement par couple de transfert de spin," p. 219.

[57] H. X. Yang, M. Chshiev, B. Dieny, J. H. Lee, A. Manchon, and K. H. Shin, "First-principles investigation of the very large perpendicular magnetic anisotropy at Fe| MgO and Co| MgO interfaces," *Physical Review B*, vol. 84, no. 5, p. 054401, 2011.
[58] A. Manchon *et al.*, "Analysis of oxygen induced anisotropy crossover in Pt/Co/M Ox trilayers," *Journal of Applied Physics*, vol. 104, no. 4, p. 043914, 2008.
[59] L. Landau and E. Lifshits, "ON THE THEORY OF THE DISPERSION OF MAGNETIC PERMEABILITY IN FERROMAGNETIC BODIES," vol. 53, p. 9.
[60] T. L. Gilbert, "A phenomenological theory of damping in ferromagnetic materials," *IEEE transactions on magnetics*, vol. 40, no. 6, pp. 3443–3449, 2004.
[61] D. Houssameddine, "Dynamique de l'aimantation de nano-oscillateurs micro-ondes à transfert de spin," p. 194, 2009.
[62] T. Chen *et al.*, "Spin-torque and spin-Hall nano-oscillators," *Proceedings of the IEEE*, vol. 104, no. 10, pp. 1919–1945, 2016.
[63] B. Fang *et al.*, "Experimental demonstration of spintronic broadband microwave detectors and their capability for powering nanodevices," *Physical Review Applied*, vol. 11, no. 1, p. 014022, 2019.
[64] D. Marković *et al.*, "Detection of the microwave emission from a spin-torque oscillator by a spin diode," *Physical Review Applied*, vol. 13, no. 4, p. 044050, 2020.
[65] N. Leroux *et al.*, "Radio-frequency multiply-and-accumulate operations with spintronic synapses," *Physical Review Applied*, vol. 15, no. 3, p. 034067, 2021.
[66] L. Zhang *et al.*, "Dual-band microwave detector based on magnetic tunnel junctions," *Applied Physics Letters*, vol. 117, no. 7, p. 072409, 2020.
[67] L. Mazza *et al.*, "Computing with injection-locked spintronic diodes," *arXiv:2201.04724 [cond-mat]*, Jan. 2022, Accessed: Feb. 24, 2022. [Online]. Available: http://arxiv.org/abs/2201.04724
[68] A. A. Tulapurkar *et al.*, "Spin-torque diode effect in magnetic tunnel junctions," *Nature*, vol. 438, no. 7066, pp. 339–342, 2005.
[69] C. Wang, Y.-T. Cui, J. Z. Sun, J. A. Katine, R. A. Buhrman, and D. C. Ralph, "Sensitivity of spin-torque diodes for frequency-tunable resonant microwave detection," *Journal of Applied Physics*, vol. 106, no. 5, p. 053905, 2009.
[70] J. Zhu *et al.*, "Voltage-Induced Ferromagnetic Resonance in Magnetic Tunnel Junctions," *Phys. Rev. Lett.*, vol. 108, no. 19, p. 197203, May 2012, doi: 10.1103/PhysRevLett.108.197203.
[71] S. Miwa *et al.*, "Highly sensitive nanoscale spin-torque diode," *Nature materials*, vol. 13, no. 1, pp. 50–56, 2014.
[72] R. Sharma *et al.*, "Electrically connected spin-torque oscillators array for 2.4 GHz WiFi band transmission and energy harvesting," *Nature communications*, vol. 12, no. 1, pp. 1–10, 2021.
[73] O. V. Prokopenko *et al.*, "Spin-torque microwave detector with out-of-plane precessing magnetic moment," *Journal of Applied Physics*, vol. 111, no. 12, p. 123904, 2012.
[74] A. S. Jenkins *et al.*, "Spin-torque resonant expulsion of the vortex core for an efficient radiofrequency detection scheme," *Nature nanotechnology*, vol. 11, no. 4, pp. 360–364, 2016.
[75] S. Tsunegi, T. Taniguchi, K. Yakushiji, A. Fukushima, S. Yuasa, and H. Kubota, "Achievement of high diode sensitivity via spin torque-induced resonant expulsion in vortex magnetic tunnel junction," *Applied Physics Express*, vol. 11, no. 5, p. 053001, 2018.

[76] P. N. Skirdkov and K. A. Zvezdin, “Spin-Torque Diodes: From Fundamental Research to Applications,” *Annalen der Physik*, vol. 532, no. 6, p. 1900460, 2020.
[77] M. Quinsat, “Etude d’un auto-oscillateur non-isochrone: Application à la dynamique non-linéaire de l’aimantation induite par transfert de spin,” p. 232.
[78] A. Chavent *et al.*, “A multifunctional standardized magnetic tunnel junction stack embedding sensor, memory and oscillator functionality,” *Journal of Magnetism and Magnetic Materials*, vol. 505, p. 166647, Jul. 2020, doi: 10.1016/j.jmmm.2020.166647.
[79] W. Skowroński, S. Łazarski, P. Rzeszut, S. Ziętek, J. Chęciński, and J. Wrona, “Influence of a composite free layer structure on thermal stability of perpendicular magnetic tunnel junction,” *Journal of Applied Physics*, vol. 124, no. 6, p. 063903, Aug. 2018, doi: 10.1063/1.5032148.
[80] L. Cuchet, “Magnetic and transport properties of single and double perpendicular magnetic tunnel junctions,” p. 209.
[81] M. Mansueto, “Memristive magnetic memory for spintronic synapses,” p. 127.
[82] S. A. H. Shah, D. M. S. Anwar, and D. A. Khaliq, “Vibrating Sample Magnetometery: Analysis and Construction,” p. 45.
[83] “Vibrating-sample magnetometer,” *Wikipedia*. Jun. 10, 2022. Accessed: Jun. 24, 2022. [Online]. Available: https://en.wikipedia.org/w/index.php?title=Vibrating-sample_magnetometer&oldid=1092515805
[84] T. Guillet, “Tuning the spin-orbit coupling in Ge for spin generation, detection and manipulation,” p. 224.
[85] D. M. Pozar, *Microwave engineering*. John wiley & sons, 2011.
[86] A. Hubert and R. Schäfer, *Magnetic Domains: The Analysis of Magnetic Microstructures*. Springer Science & Business Media, 2008.
[87] P. RHODES, “Demagnetising Energies of Uniformly Magnetised Rectangular Blocks,” *Proc. Leeds Phil. Liter. Soc*, vol. 6, pp. 191–210, 1954.
[88] D. J. Griffiths, *Introduction to electrodynamics*, Fourth edition. Boston: Pearson, 2013.
[89] O. G. Udalov, A. A. Fraerman, and E. S. Demidov, “Definition of the interlayer interaction type in magnetic multilayers analyzing the shape of the ferromagnetic resonance peaks,” *Journal of Applied Physics*, vol. 125, no. 10, p. 103902, Mar. 2019, doi: 10.1063/1.5050916.
[90] X. Chen, C. Zheng, S. Zhou, Y. Liu, and Z. Zhang, “Ferromagnetic resonance modes of a synthetic antiferromagnet at low magnetic fields,” *J. Phys.: Condens. Matter*, vol. 34, no. 1, p. 015802, Jan. 2022, doi: 10.1088/1361-648X/ac2a79.
[91] *Single and Multivariable Calculus*. David R. Guichard.
[92] N. Krvavica, “Explicit expressions for real roots of a quartic equation,” *arXiv:1902.08807 [math]*, Feb. 2019, Accessed: Feb. 21, 2022. [Online]. Available: http://arxiv.org/abs/1902.08807
[93] J. Grollier *et al.*, “Field dependence of magnetization reversal by spin transfer,” *Physical Review B*, vol. 67, no. 17, p. 174402, 2003.
[94] K. Bernert, V. Sluka, C. Fowley, J. Lindner, J. Fassbender, and A. M. Deac, “Phase diagrams of MgO magnetic tunnel junctions including the perpendicular spin-transfer torque in different geometries,” *Phys. Rev. B*, vol. 89, no. 13, p. 134415, Apr. 2014, doi: 10.1103/PhysRevB.89.134415.
[95] A. A. Timopheev, R. Sousa, M. Chshiev, L. D. Buda-Prejbeanu, and B. Dieny, “Respective influence of in-plane and out-of-plane spin-transfer torques in magnetization

switching of perpendicular magnetic tunnel junctions," *Phys. Rev. B*, vol. 92, no. 10, p. 104430, Sep. 2015, doi: 10.1103/PhysRevB.92.104430.
[96] G. Strang, *Linear algebra for everyone*. Wellesley-Cambridge Press, 2020.
[97] U. Ebels *et al.*, "Macrospin description of the perpendicular polarizer-planar free-layer spin-torque oscillator," *Physical Review B*, vol. 78, no. 2, p. 024436, 2008.
[98] A. Pikovsky and M. Rosenblum, "Synchronization," *Scholarpedia*, vol. 2, no. 12, p. 1459, 2007.
[99] P. Maffezzoni and D. D'Amore, "Phase-Noise Reduction in Oscillators via Small-Signal Injection," *IEEE Transactions on Circuits and Systems I: Regular Papers*, vol. 58, no. 10, pp. 2498–2507, Oct. 2011, doi: 10.1109/TCSI.2011.2123610.
[100] B. Fang *et al.*, "Giant spin-torque diode sensitivity in the absence of bias magnetic field," *Nat Commun*, vol. 7, no. 1, p. 11259, Sep. 2016, doi: 10.1038/ncomms11259.
[101] L. Zhang *et al.*, "Ultrahigh detection sensitivity exceeding 105 V/W in spin-torque diode," *Applied Physics Letters*, vol. 113, no. 10, p. 102401, 2018.
[102] D. Tiwari, N. Sisodia, R. Sharma, P. Dürrenfeld, J. Åkerman, and P. K. Muduli, "Enhancement of spin-torque diode sensitivity in a magnetic tunnel junction by parametric synchronization," *Applied Physics Letters*, vol. 108, no. 8, p. 082402, 2016.
[103] L. Néel, "Théorie du traînage magnétique des ferromagnétiques en grains fins avec applications aux terres cuites," *Ann. géophys.*, vol. 5, pp. 99–136, 1949.
[104] W. F. Brown Jr, "Thermal fluctuations of a single-domain particle," *Physical review*, vol. 130, no. 5, p. 1677, 1963.
[105] H. Risken, "Fokker-planck equation," in *The Fokker-Planck Equation*, Springer, 1996, pp. 63–95.
[106] M. C. Wang and G. E. Uhlenbeck, "On the Theory of the Brownian Motion II," *Rev. Mod. Phys.*, vol. 17, no. 2–3, pp. 323–342, Apr. 1945, doi: 10.1103/RevModPhys.17.323.
[107] A. Einstein, "Über die von der molekularkinetischen Theorie der Wärme geforderte Bewegung von in ruhenden Flüssigkeiten suspendierten Teilchen," *Annalen der Physik*, vol. 322, no. 8, pp. 549–560, 1905, doi: 10.1002/andp.19053220806.
[108] H. A. Kramers, "Brownian motion in a field of force and the diffusion model of chemical reactions," *Physica*, vol. 7, no. 4, pp. 284–304, 1940.
[109] W. Coffey and Y. P. Kalmykov, *The Langevin equation: with applications to stochastic problems in physics, chemistry and electrical engineering*, vol. 27. World Scientific, 2012.
[110] Z. Li and S. Zhang, "Thermally assisted magnetization reversal in the presence of a spin-transfer torque," *Phys. Rev. B*, vol. 69, no. 13, p. 134416, Apr. 2004, doi: 10.1103/PhysRevB.69.134416.
[111] T. Taniguchi, Y. Utsumi, M. Marthaler, D. S. Golubev, and H. Imamura, "Spin torque switching of an in-plane magnetized system in a thermally activated region," *Phys. Rev. B*, vol. 87, no. 5, p. 054406, Feb. 2013, doi: 10.1103/PhysRevB.87.054406.
[112] W. Rippard, R. Heindl, M. Pufall, S. Russek, and A. Kos, "Thermal relaxation rates of magnetic nanoparticles in the presence of magnetic fields and spin-transfer effects," *Phys. Rev. B*, vol. 84, no. 6, p. 064439, Aug. 2011, doi: 10.1103/PhysRevB.84.064439.
[113] N. Strelkov *et al.*, "Impact of Joule heating on the stability phase diagrams of perpendicular magnetic tunnel junctions," *Phys. Rev. B*, vol. 98, no. 21, p. 214410, Dec. 2018, doi: 10.1103/PhysRevB.98.214410.
[114] K. Yakushiji, A. Fukushima, H. Kubota, M. Konoto, and S. Yuasa, "Ultralow-Voltage Spin-Transfer Switching in Perpendicularly Magnetized Magnetic Tunnel Junctions with

Synthetic Antiferromagnetic Reference Layer," *Appl. Phys. Express*, vol. 6, no. 11, p. 113006, Nov. 2013, doi: 10.7567/APEX.6.113006.
[115] H. Sato *et al.*, "Properties of magnetic tunnel junctions with a MgO/CoFeB/Ta/CoFeB/MgO recording structure down to junction diameter of 11 nm," *Appl. Phys. Lett.*, vol. 105, no. 6, p. 062403, Aug. 2014, doi: 10.1063/1.4892924.
[116] S.-E. Lee, Y. Takemura, and J.-G. Park, "Effect of double MgO tunneling barrier on thermal stability and TMR ratio for perpendicular MTJ spin-valve with tungsten layers," *Appl. Phys. Lett.*, vol. 109, no. 18, p. 182405, Oct. 2016, doi: 10.1063/1.4967172.
[117] H. B. Callen and E. Callen, "The present status of the temperature dependence of magnetocrystalline anisotropy, and the l (l+ 1) 2 power law," *Journal of Physics and Chemistry of Solids*, vol. 27, no. 8, pp. 1271–1285, 1966.
[118] V. Drewello, J. Schmalhorst, A. Thomas, and G. Reiss, "Evidence for strong magnon contribution to the TMR temperature dependence in MgO based tunnel junctions," *Phys. Rev. B*, vol. 77, no. 1, p. 014440, Jan. 2008, doi: 10.1103/PhysRevB.77.014440.
[119] S. Zhang, P. M. Levy, A. C. Marley, and S. S. P. Parkin, "Quenching of Magnetoresistance by Hot Electrons in Magnetic Tunnel Junctions," *Phys. Rev. Lett.*, vol. 79, no. 19, pp. 3744–3747, Nov. 1997, doi: 10.1103/PhysRevLett.79.3744.
[120] J. S. Moodera and G. Mathon, "Spin polarized tunneling in ferromagnetic junctions," *Journal of Magnetism and Magnetic Materials*, vol. 200, no. 1–3, pp. 248–273, Oct. 1999, doi: 10.1016/S0304-8853(99)00515-6.
[121] C. W. Miller and D. D. Belyea, "The impact of barrier height distributions in tunnel junctions," *Journal of Applied Physics*, vol. 105, no. 9, p. 094505, May 2009, doi: 10.1063/1.3122600.
[122] R. Stratton, "Volt-current characteristics for tunneling through insulating films," *Journal of Physics and Chemistry of Solids*, vol. 23, no. 9, pp. 1177–1190, 1962.
[123] W. Greiner, L. Neise, and H. Stöcker, *Thermodynamics and Statistical Mechanics*. Springer Science & Business Media, 2012.
[124] F. P. Incropera and F. P. Incropera, Eds., *Fundamentals of heat and mass transfer*, 6th ed. Hoboken, NJ: John Wiley, 2007.
[125] C.-G. Duan *et al.*, "Surface Magnetoelectric Effect in Ferromagnetic Metal Films," *Phys. Rev. Lett.*, vol. 101, no. 13, p. 137201, Sep. 2008, doi: 10.1103/PhysRevLett.101.137201.
[126] M. Tsujikawa and T. Oda, "Finite Electric Field Effects in the Large Perpendicular Magnetic Anisotropy Surface Pt / Fe / Pt (001) : A First-Principles Study," *Phys. Rev. Lett.*, vol. 102, no. 24, p. 247203, Jun. 2009, doi: 10.1103/PhysRevLett.102.247203.
[127] K. Nakamura, R. Shimabukuro, Y. Fujiwara, T. Akiyama, T. Ito, and A. J. Freeman, "Giant Modification of the Magnetocrystalline Anisotropy in Transition-Metal Monolayers by an External Electric Field," *Phys. Rev. Lett.*, vol. 102, no. 18, p. 187201, May 2009, doi: 10.1103/PhysRevLett.102.187201.
[128] S. Zhang, "Spin-Dependent Surface Screening in Ferromagnets and Magnetic Tunnel Junctions," *Phys. Rev. Lett.*, vol. 83, no. 3, pp. 640–643, Jul. 1999, doi: 10.1103/PhysRevLett.83.640.
[129] W. Kang, Y. Ran, Y. Zhang, W. Lv, and W. Zhao, "Modeling and Exploration of the Voltage-Controlled Magnetic Anisotropy Effect for the Next-Generation Low-Power and High-Speed MRAM Applications," *IEEE Transactions on Nanotechnology*, vol. 16, no. 3, pp. 387–395, May 2017, doi: 10.1109/TNANO.2017.2660530.

[130] S. S. P. Parkin *et al.*, “Exchange-biased magnetic tunnel junctions and application to nonvolatile magnetic random access memory (invited),” *Journal of Applied Physics*, vol. 85, no. 8, pp. 5828–5833, Apr. 1999, doi: 10.1063/1.369932.
[131] A. Conca *et al.*, “Low spin-wave damping in amorphous $Co_{40}Fe_{40}B_{20}$ thin films,” *Journal of Applied Physics*, vol. 113, no. 21, p. 213909, Jun. 2013, doi: 10.1063/1.4808462.
[132] S. Iihama, S. Mizukami, H. Naganuma, M. Oogane, Y. Ando, and T. Miyazaki, “Gilbert damping constants of Ta/CoFeB/MgO(Ta) thin films measured by optical detection of precessional magnetization dynamics,” *Phys. Rev. B*, vol. 89, no. 17, p. 174416, May 2014, doi: 10.1103/PhysRevB.89.174416.
[133] J. Lindner *et al.*, “Two-magnon damping in thin films in case of canted magnetization: Theory versus experiment,” *Phys. Rev. B*, vol. 80, no. 22, p. 224421, Dec. 2009, doi: 10.1103/PhysRevB.80.224421.
[134] P. Roschmann, “Separation of anisotropy and porosity contributions to inhomogeneous broadened FMR linewidth in polycrystalline YIG,” *IEEE Transactions on Magnetics*, vol. 11, no. 5, pp. 1247–1249, Sep. 1975, doi: 10.1109/TMAG.1975.1058912.
[135] S. Mizukami, Y. Ando, and T. Miyazaki, “The Study on Ferromagnetic Resonance Linewidth for NM/80NiFe/NM (NM=Cu, Ta, Pd and Pt) Films,” *Jpn. J. Appl. Phys.*, vol. 40, no. Part 1, No. 2A, pp. 580–585, Feb. 2001, doi: 10.1143/JJAP.40.580.
[136] S. T. Purcell, H. W. van Kesteren, E. C. Cosman, W. B. Zeper, and W. Hoving, “Magnetic properties of ultrathin epitaxial Co films on a Pd (111) single crystal,” *Journal of Applied Physics*, vol. 69, no. 8, pp. 5640–5642, Apr. 1991, doi: 10.1063/1.348940.
[137] V. Kambersky and C. E. Patton, “Spin-wave relaxation and phenomenological damping in ferromagnetic resonance,” *Phys. Rev. B*, vol. 11, no. 7, pp. 2668–2672, Apr. 1975, doi: 10.1103/PhysRevB.11.2668.
[138] H. Kubota *et al.*, “Quantitative measurement of voltage dependence of spin-transfer torque in MgO-based magnetic tunnel junctions,” *Nature Physics*, vol. 4, no. 1, pp. 37–41, 2008.
[139] J. C. Sankey, Y.-T. Cui, J. Z. Sun, J. C. Slonczewski, R. A. Buhrman, and D. C. Ralph, “Measurement of the spin-transfer-torque vector in magnetic tunnel junctions,” *Nature Physics*, vol. 4, no. 1, pp. 67–71, 2008.
[140] T. Devolder, S. Couet, J. Swerts, S. Mertens, S. Rao, and G. S. Kar, “Effect of Tantalum Spacer Thickness and Deposition Conditions on the Properties of MgO/CoFeB/Ta/CoFeB/MgO Free Layers,” *IEEE Magnetics Letters*, vol. 10, pp. 1–4, 2019, doi: 10.1109/LMAG.2019.2940572.
[141] D. D. Coleman and D. A. Westcott, *CWNA Certified Wireless Network Administrator Study Guide: Exam CWNA-108*. John Wiley & Sons, 2021.
[142] X. Cheng, J. A. Katine, G. E. Rowlands, and I. N. Krivorotov, “Nonlinear ferromagnetic resonance induced by spin torque in nanoscale magnetic tunnel junctions,” *Applied Physics Letters*, vol. 103, no. 8, p. 082402, 2013.
[143] G. Smillie, *Analogue and digital communication techniques*. Elsevier, 1999.
[144] J. F. White, *High frequency techniques: An introduction to rf and microwave design and computer simulation*. John Wiley & Sons, 2004.
[145] M. Frerking, *Digital signal processing in communications systems*. Springer Science & Business Media, 2013.

[146] P. M. Grant, “The potential application of analogue matched and adaptive filters in spread-spectrum communications,” *Radio and Electronic Engineer*, vol. 52, no. 5, pp. 246–258, 1982.
[147] B. Negulescu, D. Lacour, M. Hehn, A. Gerken, J. Paul, and C. Duret, “On the control of spin flop in synthetic antiferromagnetic films,” *Journal of Applied Physics*, vol. 109, no. 10, p. 103911, May 2011, doi: 10.1063/1.3583584.
[148] A. S. Jenkins *et al.*, “Current driven magnetization dynamics of a self-polarised synthetic ferrimagnet,” *Journal of Applied Physics*, vol. 115, no. 8, p. 083911, Feb. 2014, doi: 10.1063/1.4866871.
[149] C. T. Boone *et al.*, “Resonant Nonlinear Damping of Quantized Spin Waves in Ferromagnetic Nanowires: A Spin Torque Ferromagnetic Resonance Study,” *Phys. Rev. Lett.*, vol. 103, no. 16, p. 167601, Oct. 2009, doi: 10.1103/PhysRevLett.103.167601.
[150] S. Urazhdin, P. Tabor, V. Tiberkevich, and A. Slavin, “Fractional synchronization of spin-torque nano-oscillators,” *Physical review letters*, vol. 105, no. 10, p. 104101, 2010.
[151] S. Sani *et al.*, “Mutually synchronized bottom-up multi-nanocontact spin–torque oscillators,” *Nature communications*, vol. 4, no. 1, pp. 1–7, 2013.
[152] A. Slavin, “Spin-torque oscillators get in phase,” *Nature nanotechnology*, vol. 4, no. 8, pp. 479–480, 2009.
[153] S. Tamaru, H. Kubota, K. Yakushiji, S. Yuasa, and A. Fukushima, “Extremely Coherent Microwave Emission from Spin Torque Oscillator Stabilized by Phase Locked Loop,” *Sci Rep*, vol. 5, no. 1, p. 18134, Nov. 2016, doi: 10.1038/srep18134.
[154] S. Wittrock *et al.*, “Stabilization of phase noise in spin torque nano oscillators by a phase locked loop,” *arXiv:2110.13073 [cond-mat, physics:physics]*, Oct. 2021, Accessed: Apr. 05, 2022. [Online]. Available: http://arxiv.org/abs/2110.13073
[155] S.-C. Oh *et al.*, “Bias-voltage dependence of perpendicular spin-transfer torque in asymmetric MgO-based magnetic tunnel junctions,” *Nature Phys*, vol. 5, no. 12, pp. 898–902, Dec. 2009, doi: 10.1038/nphys1427.
[156] A. Litvinenko *et al.*, “Ultrafast GHz-Range Swept-Tuned Spectrum Analyzer with 20 ns Temporal Resolution Based on a Spin-Torque Nano-Oscillator with a Uniformly Magnetized ‘Free’ Layer,” *Nano Lett.*, vol. 22, no. 5, pp. 1874–1879, Mar. 2022, doi: 10.1021/acs.nanolett.1c04031.
[157] A. Slavin and V. Tiberkevich, “Nonlinear Auto-Oscillator Theory of Microwave Generation by Spin-Polarized Current,” *IEEE Transactions on Magnetics*, vol. 45, no. 4, pp. 1875–1918, Apr. 2009, doi: 10.1109/TMAG.2008.2009935.
[158] A. N. Slavin and V. S. Tiberkevich, “Nonlinear self-phase-locking effect in an array of current-driven magnetic nanocontacts,” *Phys. Rev. B*, vol. 72, no. 9, p. 092407, Sep. 2005, doi: 10.1103/PhysRevB.72.092407.
[159] A. N. Slavini and P. Kabos, “Approximate theory of microwave generation in a current-driven magnetic nanocontact magnetized in an arbitrary direction,” *IEEE Transactions on Magnetics*, vol. 41, no. 4, pp. 1264–1273, Apr. 2005, doi: 10.1109/TMAG.2005.845915.
[160] C. P. Bean and undJ D. Livingston, “Superparamagnetism,” *Journal of Applied Physics*, vol. 30, no. 4, pp. S120–S129, 1959.
[161] W. A. Borders, A. Z. Pervaiz, S. Fukami, K. Y. Camsari, H. Ohno, and S. Datta, “Integer factorization using stochastic magnetic tunnel junctions,” *Nature*, vol. 573, no. 7774, pp. 390–393, 2019.

[162] N. A. Aadit *et al.*, “Massively parallel probabilistic computing with sparse Ising machines,” *Nature Electronics*, pp. 1–9, 2022.
[163] K. Y. Camsari, R. Faria, B. M. Sutton, and S. Datta, “Stochastic p-bits for invertible logic,” *Physical Review X*, vol. 7, no. 3, p. 031014, 2017.
[164] A. Mizrahi *et al.*, “Neural-like computing with populations of superparamagnetic basis functions,” *Nature communications*, vol. 9, no. 1, pp. 1–11, 2018.
[165] P. Bouquin, S. Rao, G. S. Kar, and T. Devolder, “Size dependence of spin-torque switching in perpendicular magnetic tunnel junctions,” *Appl. Phys. Lett.*, vol. 113, no. 22, p. 222408, Nov. 2018, doi: 10.1063/1.5055741.
[166] M. B. Weissman, “1/f noise and other slow, nonexponential kinetics in condensed matter,” *Rev. Mod. Phys.*, vol. 60, no. 2, p. 35, 1988.
[167] Y. Yuzhelevski, M. Yuzhelevski, and G. Jung, “Random telegraph noise analysis in time domain,” *Review of Scientific Instruments*, vol. 71, no. 4, pp. 1681–1688, Apr. 2000, doi: 10.1063/1.1150519.
[168] M. Bapna and S. A. Majetich, “Current control of time-averaged magnetization in superparamagnetic tunnel junctions,” *Appl. Phys. Lett.*, vol. 111, no. 24, p. 243107, Dec. 2017, doi: 10.1063/1.5012091.
[169] B. Parks, M. Bapna, J. Igbokwe, H. Almasi, W. Wang, and S. A. Majetich, “Superparamagnetic perpendicular magnetic tunnel junctions for true random number generators,” *AIP Advances*, vol. 8, no. 5, p. 055903, May 2018, doi: 10.1063/1.5006422.
[170] K. Hayakawa *et al.*, “Nanosecond Random Telegraph Noise in In-Plane Magnetic Tunnel Junctions,” *Phys. Rev. Lett.*, vol. 126, no. 11, p. 117202, Mar. 2021, doi: 10.1103/PhysRevLett.126.117202.
[171] C. Safranski, J. Kaiser, P. Trouilloud, P. Hashemi, G. Hu, and J. Z. Sun, “Demonstration of Nanosecond Operation in Stochastic Magnetic Tunnel Junctions,” *Nano Lett.*, vol. 21, no. 5, pp. 2040–2045, Mar. 2021, doi: 10.1021/acs.nanolett.0c04652.
[172] S. Krause *et al.*, “Magnetization Reversal of Nanoscale Islands: How Size and Shape Affect the Arrhenius Prefactor,” *Phys. Rev. Lett.*, vol. 103, no. 12, p. 127202, Sep. 2009, doi: 10.1103/PhysRevLett.103.127202.
[173] L. Desplat and J.-V. Kim, “Entropy-reduced retention times in magnetic memory elements: a case of the Meyer-Neldel compensation rule,” *Physical Review Letters*, vol. 125, no. 10, p. 107201, 2020.
[174] J. S. Langer, “Statistical theory of the decay of metastable states,” *Annals of Physics*, vol. 54, no. 2, pp. 258–275, 1969.
[175] G. Duff, “Langer’s Method for the Calculation of Escape Rates and Its Application to Systems of Ferromagnets,” p. 180.
[176] P. K. Muduli, Ye. Pogoryelov, S. Bonetti, G. Consolo, F. Mancoff, and J. Åkerman, “Nonlinear frequency and amplitude modulation of a nanocontact-based spin-torque oscillator,” *Phys. Rev. B*, vol. 81, no. 14, p. 140408, Apr. 2010, doi: 10.1103/PhysRevB.81.140408.
[177] Ye. Pogoryelov, P. K. Muduli, S. Bonetti, E. Iacocca, F. Mancoff, and J. Åkerman, “Frequency modulation of spin torque oscillator pairs,” *Appl. Phys. Lett.*, vol. 98, no. 19, p. 192501, May 2011, doi: 10.1063/1.3588218.
[178] M. Quinsat *et al.*, “Modulation bandwidth of spin torque oscillators under current modulation,” *Appl. Phys. Lett.*, vol. 105, no. 15, p. 152401, Oct. 2014, doi: 10.1063/1.4898093.

[179] A. Litvinenko *et al.*, “Analog and Digital Phase Modulation and Signal Transmission with Spin-Torque Nano-Oscillators,” *Physical Review Applied*, vol. 16, no. 2, p. 024048, 2021.
[180] A. Litvinenko *et al.*, “Ultrafast sweep-tuned spectrum analyzer with temporal resolution based on a spin-torque nano-oscillator,” *Nano letters*, vol. 20, no. 8, pp. 6104–6111, 2020.
[181] M. Romera *et al.*, “Vowel recognition with four coupled spin-torque nano-oscillators,” *Nature*, vol. 563, no. 7730, pp. 230–234, 2018.
[182] J. Van Kranendonk and J. H. Van Vleck, “Spin Waves,” *Rev. Mod. Phys.*, vol. 30, no. 1, pp. 1–23, Jan. 1958, doi: 10.1103/RevModPhys.30.1.
[183] T. Holstein and H. Primakoff, “Field Dependence of the Intrinsic Domain Magnetization of a Ferromagnet,” *Phys. Rev.*, vol. 58, no. 12, pp. 1098–1113, Dec. 1940, doi: 10.1103/PhysRev.58.1098.
[184] J. Hem, “Mécanismes de synchronisation dans les oscillateurs à transfert de spin,” p. 305.
[185] C. Dieudonne, “Synchronization of a Spin Transfer oscillator to a RF current: mechanisms and room-temperature characterization.,” p. 184.
[186] S. N. M. Ruijsenaars, “On Bogoliubov Transformations. II. The General Case,” *Department of Mathematics and Statistics University of Ottawa*.

Publications and conferences

Publications

In preparation (2022)	**Field-Free stochastic perpendicular superparamagnetic tunnel junctions** A. Sidi El Valli, G. Lezier, J. Langer, J. Wrona, R. Sousa, B. Dieny, U. Ebels and P. Talatchian
Published by NanoLetter (2022). Preprint, arXiv:2110.02618	**Ultra-fast GHz-range swept-tuned spectrum analyzer with 20 ns temporal resolution based on a spin-torque nano-oscillator with a uniformly magnetized'free'layer.** A. Litvinenko, A. Sidi El Valli, V. Iurchuk, S. Louis, V. Tyberkevych, B. Dieny, A. Slavin, U. Ebels
Published In Applied Physics Letters (2021). Preprint, arXiv: 2110.14501	**Size-dependent enhancement of passive microwave rectification in magnetic tunnel junctions with perpendicular magnetic anisotropy.** A. Sidi El Valli, V. Iurchuk, G. Lezier, I. Bendjeddou, R. Lebrun, N. Lamard, A. Litvinenko, J. Langer, J. Wrona, L. Vila, R. Sousa, I.L. Prejbeanu, B. Dieny, U. Ebels.
Published In IEEE International New Circuits and Systems Conference (NEWCAS) (2021). 50681.2021.9462731	**Radio Receivers based on Spin-Torque Diodes as Energy Detectors.** I. Bendjeddou, A. Sidi El Valli, A. Litvinenko, Y. Le Guennec, F. Podevin, S. Bourdel, E. Pistono, D. Morche, A. JENKINS, R. Ferreira, M. Jotta Garcia, R. Lebrun, V. Cros, P. Bortolotti, U. EBELS.
Published In Electronics letters (2021). *57*,6, 264-266	**Microwave functionality of spintronic devices implemented in a hybrid complementary metal oxide semiconductor and magnetic tunnel junction technology**. Rui Ma, A. Sidi El Valli, M. Kreißig, G. Pendina, F. Protze, U. Ebels, G. Prenat, A. Chavent, V. Iurchuk, R. Sousa, L. Vila, F. Ellinger, J. Langer, J. Wrona, I.L. Prejbeanu.

Talks (contributed)

Joint Magnetism and Magnetic Materials MMM and Intermag 2022
New Orlean, USA
Jan. 2022

Current controlled perpendicular superparamagnetic tunnel junctions operating at zero bias field.
A. SIDI EL VALLI, G. Lezier, J. Langer, J. Wrona, R. Sousa, B. Dieny, U. Ebels and P. Talatchian

Intermag 2021
Lyon, France
Jan. 2022

Current induced broadband microwave rectification in perpendicular anisotropy magnetic tunnel junctions.
A. Sidi El Valli, V. Iurchuk, A. Litvinenko , N. Lamard, J. Langer, J. Wrona, L. Vila, R. Sousa, I.L. Prejbeanu, B. Dieny, U. Ebels.

Joint Magnetism and Magnetic Materials MMM and Intermag 2019
Washington, USA
Jan. 2019

Demonstration of rf functions for spin torque oscillators based on fully perpendicular magnetic tunnel junctions.
V. Iurchuk, A. Sidi El Valli, N. Lamard, J. Langer, J. Wrona, L. Vila, R. Sousa, I.L. Prejbeanu, U. Ebels.

Poster presentation

Magnonics
Carovigno, Italy
July. 2019

Size-dependent enhancement of passive microwave rectification in magnetic tunnel junctions with perpendicular magnetic anisotropy.
A. Sidi El Valli, V. Iurchuk, I. Bendjeddou, R. Lebrun, N. Lamard, A. Litvinenko, J. Langer, J. Wrona, L. Vila, R. Sousa, I.L. Prejbeanu, B. Dieny, U. Ebels

Colloque Louis Neel
Toulouse, France
Mai. 2019

Microwave rectification in magnetic tunnel junctions with perpendicular anisotropy.
A. Sidi El Valli, V. Iurchuk, I. Bendjeddou, R. Lebrun, N. Lamard, J. Langer, J. Wrona, L. Vila, R. Sousa, I.L. Prejbeanu, B. Dieny, U. Ebels

Summer school

Aug-2019 **European summer on magnetism,** Brno, Czech**.**

June-2019 **IEEE magnetics society summer school**, Richmond, USA.